論文 / 著書情報
Article / Book Information

題目(和文)	
Title(English)	Uncertainty in shallow S-wave velocity model from surface-wave inversion using the Markov-chain Monte Carlo method for estimation of variability in soil amplification
著者(和文)	SAIFUDDINfuddin
Author(English)	Fuddin Sai
出典(和文)	学位:博士(学術), 学位授与機関:東京工業大学, 報告番号:甲第11317号, 授与年月日:2019年9月20日, 学位の種別:課程博士, 審査員:山中 浩明,田村 哲郎,盛川 仁,松岡 昌志,淺輪 貴史,海江田 秀志
Citation(English)	Degree:Doctor (Academic), Conferring organization: Tokyo Institute of Technology, Report number:甲第11317号, Conferred date:2019/9/20, Degree Type:Course doctor, Examiner:,,,,,
学位種別(和文)	博士論文
Type(English)	Doctoral Thesis

Uncertainty in shallow S-wave velocity model from surface-wave inversion using the Markov-chain Monte Carlo method for estimation of variability in soil amplification

A doctoral thesis presented by

Saifuddin

Supervised by

Prof. Hiroaki Yamanaka

Department of Environmental Science and Technology

Tokyo Institute of Technology

June 2019

Acknowledgments

First and foremost, it is my pleasure to thank my supervisor, *Professor Hiroaki Yamanaka* at Department of Environmental Science and Technology, Tokyo Institute of Technology for accepting me as his student and directing me throughout my study. Nevertheless, I could not complete my study within three years, then I decided to conduct my remaining works and write my thesis in Indonesia. Therefore, I am deeply grateful again to *Professor Hiroaki Yamanaka* as he still believes in me and encourages me to finish the remaining works and the thesis. I am also deeply grateful to *Assistant Professor Kosuke Chimoto* at Department of Environmental Science and Technology, Tokyo Institute of Technology for his advice and help during my research.

I am deeply thankful to Ph.D. thesis reviewers, *Professor Hitoshi Morikawa*, *Professor Masashi Matsuoka, Professor Tetsuro Tamura, Professor Takashi Asawa* from Tokyo Institute of Technology, and also *Professor Hideshi Kaieda* from Central Research Institute of Electric Power Industry Japan, for helpful comments and suggestions in this thesis.

I am sincerely grateful to *the Ministry of Education, Culture, Sports, Science and Technology (MEXT), Japan* for a generous scholarship during my study as Research and Doctoral students at Tokyo Institute of Technology.

I thank *Professor Nozomu Yoshida* at Kanto Gakuin University for providing the open-source code of DYNEQ. I also indebted to *the National Research Institute for Earth Science and Disaster (NIED), Japan* for providing strong motion data and soil column that I used in this study.

I deeply indebted to members of Yamanaka laboratory: *Dr. Hussam Eldein, Dr. Koichiro Saguchi, Rama, Ozlem, Selene, Mohamed, Shun, Nogami san, Yuny, Tsuchiya san,*

Imai san, Sorimachi san, Kojima san, Noyori san, Hirose san, Liu san, Ishihara san, Ishige san, Shimizu san, Seita san, Chujo san, and *Miyanaga san* for their help in the last four years. I also indebted to the secretary, *Shimamoto san* for her kind assistance during my stay in Japan.

I am grateful to *Shun Harigaya* and *Harigaya's family* for letting me have experiences in Japanese homestays and delightful dinners.

I thank my best friends and roommates, *Samratul Fuady* and *Haeruman Azam* for wonderful memories: hilarious chatting, traveling, cooking, and many other activities. I also thank *all Indonesian friends* who I sincerely indebted during my stay in Japan.

I am profoundly grateful to my beloved father and mother, *Moch. Chamim* and *Asifah*, my late little sister, *Nur Hasanah*, and my little sister, *Rofiatul Adawiyah* for continuous support in my study and life. I am also grateful to my father and mother in law, *Priyo Hutomo* and *Lusi Yuwantari* for their encouragement in my education and life. Finally, I am grateful to my wife, *Eritrina Putri Ekantari* for the love, and she keeps believing in me that I am able to complete my thesis. Moreover, my daughter, *Zamzami Febriani* as one of the sources of my happiness.

~To all of you, I am eternally grateful~

Abstract

Chapter 1 reviews previous researches and points out the difficulty in a surface-wave phase velocity inversion using the least square methods, genetic algorithm, and simulated annealing. In this study, I examine the Markov-chain Monte Carlo (MCMC) inversion for estimation of uncertainty in an S-wave velocity (*Vs*) profile from observational error in a phase velocity in numerical experiments and application to real data. Furthermore, soil amplification variability is also estimated due to the *Vs* profile uncertainty.

Chapter 2 explain a computational procedure of the MCMC method for estimation of uncertainty in a *Vs* profile. I also depict a computational procedure of soil amplification variability due to the uncertainty in the *Vs* model. An equivalent linear method is used to calculate a nonlinear soil response.

In Chapter 3, numerical experiments are conducted. I generate synthetic observed phase velocities of Rayleigh waves for two- and three-layer models of shallow soil. It is found that multiple chains converge faster than a single chain in the MCMC sampling. I show that my final inverted models and calculated phase velocities from sampling can explain well the true *Vs* profiles and the phase velocities, respectively. I estimate the uncertainty of each model parameter from its distribution. Moreover, a trade-off-relationship among model parameters can be examined from the sampled models. It is shown that the incompleteness of the phase velocity at the high frequency rises the uncertainties in the *Vs* and thickness at the top layer while the absence of phase velocity at the low frequency increases the uncertainty in the *Vs* in the half-space. It is also depicted that the observational errors of the phase velocities are linearly associated with the resolutions of the *Vs* and thickness.

In Chapter 4, a synthetic strong motion is applied to the engineering bedrock of the sampled models from Chapter 3, to obtain the surface motion assuming linear and nonlinear

amplifications. It is shown that the uncertainty in the *Vs* models can smooth spectral shapes of the linear and nonlinear soil amplifications at high frequencies due to averaging of peaks. I find that the nonlinear amplification shows less variability and also has a flatter spectral shape than the linear amplification, particularly at high frequencies. The distributions of ground motion proxies generally have less uncertainty for the nonlinear amplification as well. Furthermore, it is shown that soil amplification variability due to the absence of phase velocity at the high frequencies, is more critical than the lack of phase velocity at the low frequencies. I also find that the higher peak ground accelerations of input motions produce the lower nonlinear amplification variability, while different phase angles of input motions have slight effects into the nonlinear amplification variability. These results are profoundly caused by the high damping factor applied in the nonlinear soil response.

Chapter 5 shows deconvolved bedrock motion variability due to *Vs* profile uncertainty from Chapter 3. The deconvolved spectral acceleration and ground motions proxies at bedrock with their uncertainties can explain well their corresponding true values. Accuracy of the deconvolved bedrock motions may be increased by giving thickness information during the inversion.

In Chapter 6, I apply the MCMC method to obtain uncertainty in a *Vs* profile from a Rayleigh wave phase velocity around the K-NET Tsukidate station (MYG004) attained by microtremor explorations during the 2011 off Pacific Coast of Tohoku Earthquake. I estimate the engineering bedrock's motion variability due to the main shock, deconvolved from the observed surface motions, considering the uncertainty in the shallow *Vs* profile. The *Vs* profile uncertainty at the strong motion station is estimated with observed Rayleigh wave phase velocities. It is indicated that some parameters have non-Gaussian distributions at different sites. The estimated bedrock peak ground acceleration ranges are 610–930 cm/s^2 and 2000–3100 cm/s^2 for the east-west (EW) and north-south (NS) directions, respectively. Meanwhile, the ranges of the peak ground velocities are about 35–40 cm/s and 90–120 cm/s for the EW and

NS components, respectively. The results indicate that the minimum and maximum possible values of the deconvolved spectral acceleration and the ground motion proxies are affected by *Vs* profile uncertainty. Moreover, the upper and lower possible values of the spectral acceleration and the ground motion proxies are also influenced by their nonlinear soil characteristics. Furthermore, the spectral velocities at stations in the main part of Tsukidate Town are also estimated with the observed phase velocities. They have predominant peaks at periods shorter than 0.5 s, suggesting only minor structural damage around Tsukidate Town.

Chapter 7 summarizes my findings in the surface-wave phase velocity inversion using the MCMC method in numerical experiments and the application to actual data. I also outline my results in relation to the seismic motion characteristics variability due to the uncertainty in model parameters from the surface-wave inversion. Moreover, future works are depicted in this chapter.

Keywords: *Uncertainty, S-wave velocity profile, MCMC method, variability, linear amplification, nonlinear amplification, the 2011 off Pacific Coast of Tohoku Earthquake, microtremor exploration, MYG004, deconvolved engineering bedrock motions*.

Contents

Chapter 1 Introduction

1.1 Background

The properties of seismic waves like spectral shape and amplitude can be altered during seismic wave propagation in near-surface layers. Soil amplification is used to quantify the modification of seismic waves due to local site effects. It is known an S-wave velocity (*Vs*) profile of a soil mostly controls the soil amplification. Therefore, the *Vs* profile at a site of engineering interest must be known for design building, liquefaction, and microzonation of earthquake disaster mitigation.

To acquire a *Vs* profile, an *in-situ* measurement using either invasive or non-invasive techniques can be applied. PS logging is one of the invasive methods commonly used. It is one of the best approaches to obtain a *Vs* profile since wave velocities are directly measured in ground (Yoshida, 2015). Though, the non-invasive methods like surface wave surveys have gained popularity in recent years due to cost-effective, environment-friendly, and simplicity in field operation as compared to invasive techniques. Moreover, surface wave investigation has been shown to have similar results for site characterization as compared to downhole methods (e.g., Xia et al., 2002).

A *Vs* profile obtained by either invasive or non-invasive measurement will have uncertainty. It is commonly assumed the resolution of the *Vs* profile from an invasive method is higher than that of a non-invasive technique because it is a direct estimation of the wave velocities. Therefore, the uncertainty in the *Vs* profile from the surface wave survey is raised more concern than that of invasive one for ground motion estimation. During the surface-wave measurement, observational error mainly arises from noise in recorded signals. The observational error will generate uncertainty in the *Vs* profile during inversion of surface-wave phase velocity. Since the *Vs* profile mainly affects soil amplification, the uncertainty in the *Vs* profile may also cause inaccuracy in ground motion estimations in engineering design. Hence, it is important to understand the effect of uncertainty in the *Vs* profile derived from surface-wave inversions and its effect on the variability of the soil amplification.

1.2 Reviews on previous studies

1.2.1 Surface wave survey

In the seismological community, the propagation of surface waves caused by an earthquake has been widely employed to deduce crust and upper mantle structure in different regions of the Earth since the 1950s (e.g., Brune et al., 1961; Ewing et al., 1957). It has been important methods for global and regional scales for seismologists. In the global case, earthquakes with magnitudes higher than 6.5 with very long periods of 150 to 320 s are employed, while earthquakes with magnitudes less than 4.5 and period interests of 10 to 60 s are used for the regional scale (e.g., Romanowicz, 2002). Examples of estimation of the Earth's crust and upper mantle profiles in the global scales were conducted by Montagner and Tanimoto (1991) and Trampert and Woodhouse (1995). For the regional instances, the surface wave methods are used to estimate *Vs* structures of the crust and upper mantel in central Eurasia (Villaseñor et al., 2001), and applied to study *Vs* profiles in China and adjacent regions (e.g., Huang et al., 2003).

Most of the instruments for analysis of the seismic record, forward, and inversion analyses in a dispersion curve for engineering practice are adopted from the field of seismology (e.g., Foti, 2014). The surface wave method has been extensively used to delineate *Vs* profile in engineering purpose in the early 1980s, since the introduction of spectral analysis surface wave (SASW) by Nazarian and Stokoe (1984). Two receivers are used during surface wave measurement in SASW approach. Improvement of SASW was done by Park et. al (1999) by using multiple stations during the measurement known as multichannel analysis of surface waves (MASW) technique. Currently, MASW is a common method to be used for active source tests. Artificial sources like a sledgehammer and drop weights are often used in the active source survey.

Passive source methods using microtremors (ambient noises) are also widely used to deduce *Vs* profiles for engineering application. The microtremors are produced by natural phenomena (e.g., ocean waves, wind, and rain) and human activities (e.g., machinery in factories, motor cars, and people walking) (Okada, 2003). The microtremors are abundance, weak, and low amplitude vibrations on the surface of the earth. It was pioneered by Japanese Seismologists (Aki, 1957; Kanai et al., 1954). Aki (1957) proposed the Spatial Autocorrelation (SPAC) technique, which is an important foundation to be used for estimation of subsurface structure (Okada, 2003). Moreover, the microtremor's spectral ratio of the horizontal component to the vertical component (*H*/*V*), proposed by Nakamura (1989) are widely applied for microzonation of earthquake mitigation. In the microtremor technique, the frequency range of the phase velocity cannot be controlled. Thus, we sometimes obtain incompleteness of phase velocity data at frequencies higher than about 10 Hz (e.g., Yamanaka, 2005). Therefore, it may lead to uncertainty in a *Vs* profile from a phase velocity inversion.

There are two types of surface-waves which are Rayleigh and Love waves. However, in engineering practice, Rayleigh waves are assumed mainly in the surface wave survey. Surface wave methods are based on a phase velocity dispersion of Rayleigh waves during its propagation in a vertically heterogeneous medium. The phase velocity of the Rayleigh waves depends on the properties of a subsurface material such as S-wave velocity, P-wave velocity, thickness, and density of each layer. Figure 1.1 shows an example of a three-layer model (two layers of soil over a half-space). The figure indicates vertical particle motion in the first layer related to a high frequency (short wavelength) of Rayleigh waves. Therefore, the material properties of the first layer control the velocity of Rayleigh waves. The figure also shows the amplitude in depth associated with a low frequency (long wavelength) of Rayleigh waves.

Hence, the low frequency of Rayleigh waves is controlled by some mixture of material properties of all three layers.

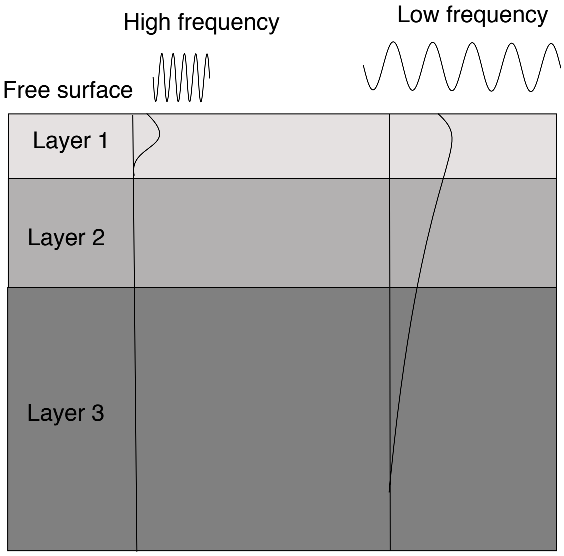

Figure 1.1 Geometric dispersion of Rayleigh waves. Vertical particle motions associated with a high frequency (short wavelength) and low frequency (long wavelength) in a vertically heterogeneous layered medium (modified after Foti et al., 2014)

The standard procedure for the surface-wave survey can be divided into three main steps as shown in Figure 1.2: acquisition of field data, data processing to obtain a dispersion curve of phase velocity, and also an inversion of the phase velocity into a *Vs* profile. Different methods for each step can be conducted depending on the scale of the task, the objective, the complexity of the subsurface characteristics, and the available apparatus and funds (Socco et al., 2010). For example, the acquisition of the surface-wave explorations could be performed using active or passive sources for shallow and deep structures, respectively. The passive source generally has more energy in low-frequency range than that of the active source while the active source has more information in high-frequency range than that of the passive sources (Foti et al., 2018). Additionally, a combination of active and passive techniques can be also conducted (e.g., Park et al., 2005; Zor et al., 2010) to improve the resolution of dispersion curves. In term of signal data processing to obtain a dispersion curve of phase velocity, a frequency-wavenumber (*f-k*) is commonly used for active-source data, while SPAC (e.g., Aki, 1957) and *f-k* (e.g., Horike, 1985) are can be employed for passive-source data.

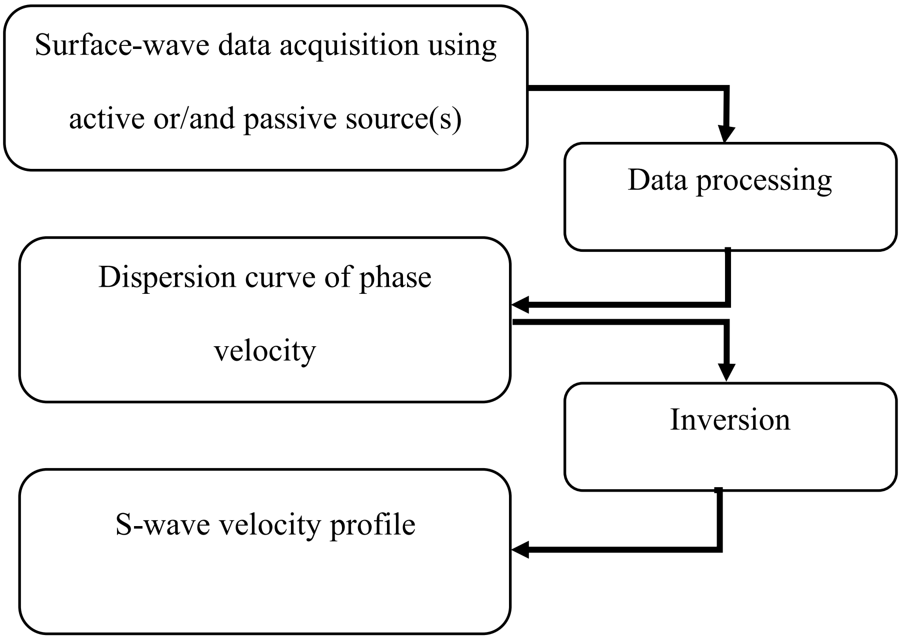

Figure 1.2 Flowchart of data acquisition to S-wave velocity profile.

1.2.2 Inversions of dispersion curves

A least squared method has been conventionally used in a phase velocity inversion into a *Vs* profile (e.g., Horike, 1985; Yuan and Nazarian, 1993). It is well understood that the inversion of the surface-wave phase velocity is a nonlinear problem. Therefore, a linearized least square method is required to solve the nonlinear inversion problem by neglecting higher-order term in the Taylor series expansion. A general relationship between the *i*-th datum (d_i) and model parameter vector (**m**) can be written (Richardson and Zandt, 2003) as follows

$$d_i = g_i(\mathbf{m}). \tag{1.1}$$

Where $g_i(\mathbf{m})$ is a nonlinear function that shows the relationship of the *i*-th given datum and the parameter. I can present in this equation a matrix term assuming initial model (m_0) as follows

$$\Delta\mathbf{E} = \mathbf{G}\Delta\mathbf{m}\,, \tag{1.2}$$

Where the matrix **G** is sometimes stated as the kernel or data kernel, $\Delta\mathbf{E}$ is misfit between calculated phase velocity and observed data, while $\Delta\mathbf{m}$ is the difference between initial and *i*-th models. A final inverted model can be acquired using iterations until $\Delta\mathbf{m}$ becomes adequately small (convergence is obtained) or until $\Delta\mathbf{E}$ becomes sufficiently small (acceptable misfit). Although the least-squares method conventionally used in an inversion of a phase velocity into a *Vs* profile (final inverted model) and generally converged fast. It is well understood that the linearized least square method requires a derivative function of $g_i(\mathbf{m})$ and an inverse of matrix **G** during the inversion. Moreover, a proper initial model is also necessary.

Figure 1.3 shows the relationship between the iterative evolution of models versus the misfit function ($E(\mathbf{m})$). The figure indicates the effect of different initial models into final inverted models. If the initial model is located near the global minimum, the final model will be easily converged in nearby of the global minimum as shown in Figure 1.3(a). However, inversion in a phase velocity is a nonlinear problem so it has multiple local minima. Hence, it is often that the final inverted model is trapped in the local minimum as presented in Figure 1.3(b). Besides, it is difficult to prepare a suitable initial model in a site of interest during the inversion of a dispersion curve. Furthermore, an inverse of the matrix **G** is necessary that may affect a numerical instability.

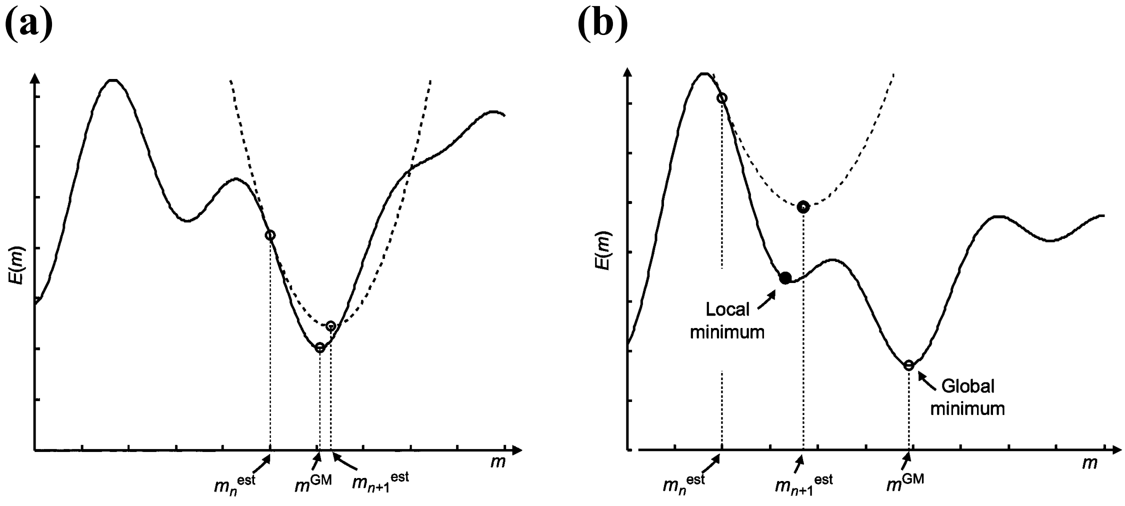

Figure 1.3 (a) The iterative method locates the global minimum (m^{GM}) of the error ($E(m)$, solid curve) by determining the paraboloid (broken curve) tangent to $E(m)$ at the m_n^{est} (m_0, initial model). The final inverted solution m_{n+1}^{est} is at the minimum of this paraboloid and, under favorable conditions, can be closed to the global minimum. (b) If the trial solution/initial model (m_n^{est}) is too far from the global minimum, the method may converge to a local minimum (Menke, 2012).

Global search algorithms, also known as heuristic search methods, mostly used for artificial intelligence and many engineering optimizations since the 1980s (e.g., Pearl, 1984). Two of global search methods, the Genetic Algorithm (GA) and the Simulate Annealing (SA) are commonly used for the inversion of geophysical data, including surface-wave inversions (e.g., Yamanaka, 2005). Unlike*,* the above linearized least-square inversion. It requires a forward calculation that does not need a proper initial model and calculation of matrices as used in the least square method. The GA finds an optimal model from the lowest misfit function during a phase velocity inversion based on principles of biological evolution such as selection, mutation, and crossover (Dal Moro et al., 2007; Yamanaka and Ishida, 1996). Meanwhile, the SA finds an optimal model by mimicking physical annealing. It generates an initial random model with a large temperature and then slowly drops it as more trial solutions are tested (e.g., Menke, 2012; Yamanaka, 2005). Moreover, a hybrid (GA and SA) technique can be also performed to reduce computational effort (Yamanaka, 2007).

1.2.3 Application of surface wave explorations

As previously stated, active or/and passive measurement(s) can be performed to deduce a *Vs* profile using the surface wave methods. The active source measurements are commonly used to obtain a shallow *Vs* profile of the soil. For examples, MASW was used to obtain a shallow *Vs* profile for seismic microzonations in Lorca City, Spain (Martínez-Pagán et al., 2014) and Dinar region, Turkey (Ismet Kanli et al., 2006). MASW also used to delineate shallow *Vs* profiles around the city of Port-au-Prince, during the 2010 Haiti Earthquake (Rathje et al., 2011). They found that the most heavily damaged areas in downtown Port-au-Prince have average shear wave velocities over the top 30 m (*AVS30*) about 350 m/s. Meanwhile, passive explorations such as microtremor measurements have been widely applied to estimate shallow (e.g., Karagoz et al., 2015; Pramatadie et al., 2016) and deep *Vs* profiles (e.g., Kuo et al., 2016; Satoh et al., 2001). Furthermore, the microtremor explorations have been also broadly employed to deduce a *Vs* profile for estimation of ground motion features around damaged areas in the past large earthquakes. For instances, Satoh et al. (2004) suggested that a thick sediment layer was responsible for long-period velocity pulses at the sites in the footwall during the 1999 Chi-Chi, Taiwan Earthquake with an Mw of 7.6. Recently, Chimoto et al. (2016) found a top layer of a *Vs* profile has low velocity and thick layer that might affect heavy damages around Mashiki city during the 2016 Kumamoto Earthquake, Japan with an Mw of 7.1. These studies indicate the importance of shallow and deep *Vs* profiles from surface wave explorations to estimate ground motion characteristics and damage.

Furthermore, Socco et al. (2010) indicated that the increasing use of surface wave methods in practice and research in the scientific and engineering communities. In addition, international benchmarks of a *Vs* profile from a surface-wave phase velocity inversion have been also performed by experts (Garofalo et al., 2016a, 2016b). Garofalo et al. (2016b) found that regardless of different approaches had been used by those experts, the characteristics of phase velocity were similar. However, the variability of *Vs* profiles increased in relation to major stratigraphic. Moreover, it was found that the *Vs* profiles from the surface-wave inversion were comparable to down-hole results (Garofalo et al., 2016a). As shown in these studies that the *Vs* profiles from the surface-wave inversion have been extensively used and examined. Yet, observational error in a phase velocity is generally neglected during inversion of phase velocity.

1.2.4 Uncertainty of model parameters from phase velocity inversion

Observational errors in phase velocities caused by random and systematic errors during surface-wave measurements. The systematic errors are affected by procedural and instrumental errors. Meanwhile, the random errors in an active source are caused noises (e.g. body waves) in the signals (Rayleigh waves). In a passive source (microtremors), the frequency ranges of the phase velocity cannot be controlled. Additionally, in both active and passive sources, random errors are caused by the presence of incoherent noises since surface-waves are assumed as coherent noises. In this study, I assumed that the observational errors are only caused by random errors.

Assuming that observational error ($\sigma\left(f_i\right)$) is normally distributed in a dispersion curve. $\sigma\left(f_i\right)$ is the standard deviation of the phase velocity at frequency-*i*. To fit the calculated phase velocity ($C(f_i)$) into observed data ($O(f_i)$), I have to minimize the sum of squared errors ($E(\mathbf{m})$). The sum of square error/misfit function (e.g., Aster et al., 2013; Yamanaka, 2011) can be written as

$$E\left(\mathbf{m}\right)=\sum_{i=1}^{n}\left[\frac{O\left(f_i\right)-C\left(f_i\right)}{\sigma\left(f_i\right)}\right]^2 \qquad 1.3$$

In the linearized square inversion, the quality of the inverted parameters can be estimated using the resolution matrix (e.g., Wiggins, 1972). Therefore, the standard deviation of the inverted S-wave velocity models can be calculated using the standard deviations of the observed phase velocity. However, GA and SA do not provide any evaluation of the uncertainty in a final inverted model (Dal Moro et al., 2007; Yamanaka, 2005).

The Markov-chain Monte Carlo (MCMC) method is also a heuristic approach and widely used for artificial intelligence and optimization problems (e.g., Ghahramani, 2015). Moreover, the method has been extensively applied in different fields of sciences and technologies (Gilks et al., 1995). In the MCMC sampling, a random model is used to estimate the probability density function (pdf) for the target distribution. Uncertainty in a model parameter can be estimated from the pdf of the model parameter. Few studies had been conducted to verify the applicability of the MCMC method for phase velocity inversions (e.g., Molnar et al., 2013, 2010; Yamanaka, 2014, 2013, 2011). The MCMC method had been previously used to estimate the uncertainty of shallow *Vs* (Yamanaka, 2014) and deep *Vs* (Yamanaka, 2013, 2011) profiles from inversions of synthetics and microtremor phase velocities. Moreover, Molnar et al. (2013, 2010) also applied the MCMC method to obtain a variation of *Vs* profiles from inversions of microtremor phase velocities. They also estimated the variability of the linear response due to the uncertainty of the *Vs* models. However, their studies did not discuss the variability of a nonlinear soil amplification due to the uncertainty in the *Vs* models. It is important to discuss the variability of the nonlinear soil responses due to the *Vs* profile uncertainty in engineering application, particularly for earthquakes with large peak amplitudes. Therefore, in this study, I examined the applicability of the MCMC method for inversions of surface-wave phase velocities, with special attention paid to the nonlinear seismic response of shallow soil.

1.2.5 Variability in soil amplification

Soil amplification is commonly used to understand the seismic response of a soil deposit primarily caused by horizontally polarized shear-wave (*SH*) waves vertically propagating from the underlying bedrock (e.g., Kramer, 1996). The soil will be amplified for a low impendence ratio of a surface layer over a bedrock layer. The impedance ratio is mainly affected by *Vs* profile of the soil. Consequently, a *Vs* profile is an important parameter for estimation of soil amplification at site interest.

The behavior of soil during earthquake shaking can be defined as linear and nonlinear soil responses. During weak motion, the soil will behave linearly, while many studies suggest the soil will behave nonlinearly during strong shaking with a peak ground acceleration (PGA) exceeding 100 cm/s^2 (e.g., Beresnev and Wen, 1996; Wen et al., 1994).

Furthermore, a lateral variation of *Vs* profiles could be also included during the estimation of 2D soil amplification (e.g., Amrouche et al., 2014). Moreover, material heterogeneity and topography play a major role in the spatial variability of the seismic wave (Assimaki et al., 2005). Furthermore, 2D/3D soil amplifications are sometimes employed to incorporate basin effect due to trapped surface-wave in surficial layers (e.g., Semblat, 2006). Hence, several factors may also affect the variability of soil amplification such as soil heterogeneity, horizontal variation, topography, and uncertainty in *Vs* profiles. However, in engineering practice, the soil is commonly assumed to be 1D homogeneous horizontal layers. Thus, the uncertainty in the *Vs* profile is the most concern that affects the variability of soil amplification. In this study, I focus on the effect of observational error in a phase velocity to uncertainty in a *Vs* profile from a surface-wave inversion and its effect on the variability of 1D soil amplification for engineering purpose.

Some studies (e.g., Foti et al., 2009; Jakka et al., 2014; Molnar et al., 2013; Yamanaka, 2014, 2013, 2011) have been devoted to understanding the effects of the uncertainty in *Vs* profiles from surface-wave inversion into 1D soil responses. However, it seems there is still no consensus on the effect of the uncertainty in *Vs* profiles on the variation of soil response. Thus, I will, in a later section, discuss the reasons for these differences in later discussion.

1.3 Objective of this research

In this study, my main interest is an inversion of a dispersion curve into an S-wave velocity profile. Therefore, my main concern is to understand the effect of observational error in a phase velocity into uncertainty in the S-wave velocity profile. Hence, I start the discussion of errors in the phase velocity in this study. Thus, I conducted numerical experiments to examine the performance of the MCMC method, for inversions of shallow phase velocities with observational errors into uncertainties in *Vs* profiles. Moreover, the uncertainties of the *Vs* models were used to estimate the variability in 1D linear and nonlinear soil amplifications. Furthermore, I also applied the MCMC inversion to actual phase velocities around Tsukidate station (MYG004) during massive accelerations of the 2011 off Pacific Coast of Tohoku Earthquake with an Mw of 9.0.

1.4 Thesis organization

This thesis discusses the effect of observational error in a phase velocity into uncertainty of a *Vs* profile. Furthermore, the effect of the uncertainty in the *Vs* profile into the variability of 1D linear and nonlinear soil amplification are also estimated. Numerical experiments and application to real data are conducted in this study. The flow chart of the thesis is shown in Figure 1.4.

Chapter 1 presents the background concerning the effect of observational error in a surface-wave phase velocity to uncertainty in a *Vs* profile and its effect on the variability of soil amplification. Previous studies related to these topics are also discussed. This chapter also includes the objective of the research.

Chapter 2 describes the methodology that is used for obtaining uncertainty in *Vs* profile and variability of soil amplification. This chapter explains the overview of computational procedures of the MCMC inversion and soil amplification.

Chapter 3 explains numerical experiments to obtain uncertainties in *Vs* profiles from surface-wave inversions using the MCMC method for two- and three-layer models. This chapter shows generation of synthetic phase velocities. I also portray a comparison between a single chain and multiple chains during the MCMC sampling. The uncertainties in *Vs* profiles for two and three-layer models are depicted. Moreover, the trade-off-relationship between the inverted model parameters and improvement of resolutions of *Vs* profiles from inversion by giving thickness information in advance are discussed. Furthermore, this chapter covers uncertainties of *Vs* profiles because of absences of phase velocities in low or high frequency range, different observational errors in phase velocities, and frequency-dependent errors in the phase velocities.

Chapter 4 shows estimation of the variability of linear and nonlinear soil amplification from sampled models for two- and three-layers models in Chapter 3. This chapter presents a generation of a synthetic motion at engineering bedrock. Moreover, estimation of amplification, spectral acceleration, and ground motion proxies for linear and nonlinear cases are shown in this chapter. The reasons for different variability in the linear and nonlinear soil responses are described. I also explain the variability of the soil amplifications related to the absences of phase velocities in low or high frequency range, the different observational errors in phase velocities, and the frequency-dependent errors in the phase velocities from Chapter 3. Moreover, I also discuss a comparison with previous studies in relation to the variability in the soil amplification. Additionally, this chapter also discusses effects of different PGAs and phase angles of input motions to nonlinear soil amplification variability.

Chapter 5 presents numerical tests on a comparison between the variability of nonlinear soil responses obtained from SHAKE91 and DYNEQ. The variability in deconvolved bedrock motions assuming a nonlinear soil response is discussed for two- and three-layer models. Furthermore, the variability in the bedrock motion for a given thickness during inversion is also depicted.

Chapter 6 depicts uncertainty in a *Vs* profile and variability in bedrock motions beneath Tsukidate station (MYG004) during the main shock of the 2011 off Pacific Coast of Tohoku Earthquake. Moreover, uncertainties in *Vs* profiles and variability in surface motions around MYG004 during the mainshock are also described. The reasons for low structural damages during the mainshock around Tsukidate city are also examined.

Chapter 7 concludes my study and suggests possible future works.

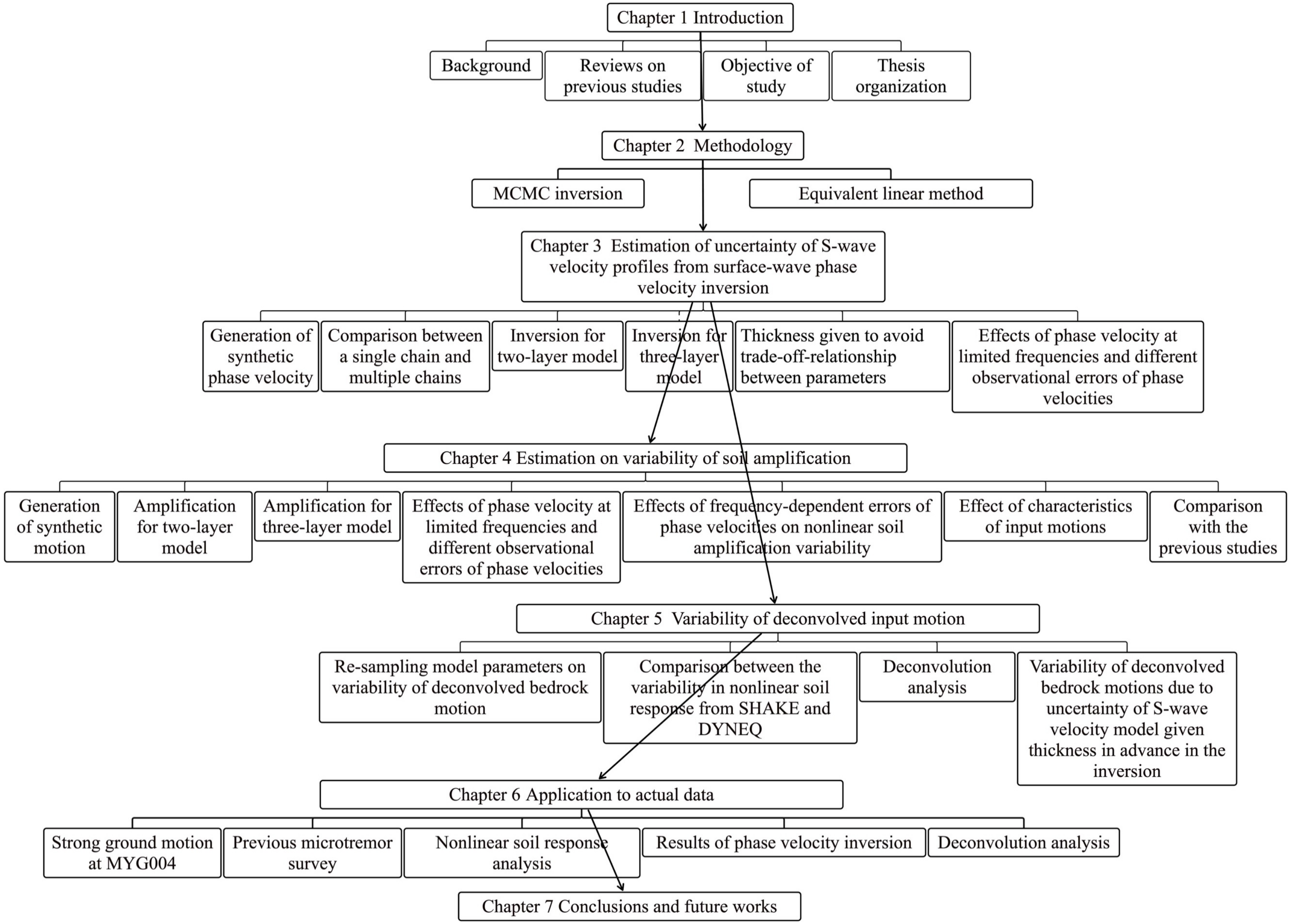

Figure 1.4 A flowchart of the thesis

Chapter 2 Methodology

2.1 The Markov-chain Monte Carlo inversion

2.1.1 Forward calculation

2.1.2 Inversion calculation

2.2 Equivalent linear method

2.1 The Markov-chain Monte Carlo inversion

2.1.1 Forward calculation

Before I explain a computational procedure of a phase velocity inversion using the Markov-Chain Monte Carlo (MCMC) method, I like to describe a calculation of a theoretical phase velocity. The calculation of the theoretical phase velocity (C) of Rayleigh waves for a horizontally layered model is estimated using the Haskell's method (Haskell, 1953). The dispersive characteristics of a Rayleigh wave phase velocity for n-1 homogeneous, isotropic, and elastic layers over a half-space (n) is affected by P-wave velocity (α_i or Vp_i), S-wave velocity (β_i or Vs_i), density (ρ_i), and thickness (H_i) as shown in Figure 2.1.

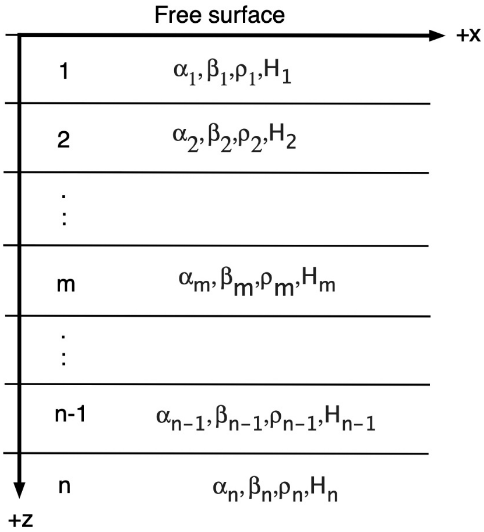

Figure 2.1 Heterogeneous vertically soil layers in x- and z-axis. The dispersive Rayleigh waves are controlled by S-wave velocity (β), P-wave velocity (α), density (ρ), and thickness (H).

Rayleigh waves propagate horizontally in the x-direction with phase velocity (C=$C(k)$) is dependent on its wavenumber (k). Hence, it is also depending on the frequency since the frequency is given by $f = Ck/2\pi$. I seek the phase velocity for different wavenumbers or frequencies, $C = C(k)$ or $C = C(f)$ in the forward calculation of the dispersion curve.

The general computational procedure in estimation of a theoretical phase velocity is to find the zero of a characteristic equation ($F(C,k)$). It is depending on the phase velocity, wave number, and the elastic constants (α_i, β_i, ρ_i, and H_i) of the layers as following

$$F(C,k)=(J_{13}-J_{14})(J_{22}-J_{21})-(J_{11}-J_{12})(J_{24}-J_{34}). \tag{2.1}$$

The elements of a matrix **J** with a size of 4 by 4 in Equation 2.1 are formed by transfer matrices with a size of 4 by 4 ($\mathbf{A_i}$) from n-1 to 1st layer and multiplied by an inverse matrix in the half-space with a size of 4 by 4 ($\mathbf{E_n^{-1}}$). The relationship of matrix **J** to matrices **A** and $\mathbf{E_n^{-1}}$ is expressed as

$$\mathbf{J}=\mathbf{E_n^{-1}A_{n-1}A_{n-2}\cdots A_2A_1}, \tag{2.2}$$

where the inverse matrix in the half-space is

$$\mathbf{E_n^{-1}}=\begin{bmatrix} -2\left(\alpha_n/\beta_n\right)^2 & 0 & \left(\rho_n\alpha_n\right)^{-1} & 0 \\ 0 & C^2\left(\gamma_n-1\right)/\alpha_n r_{\alpha n} & 0 & \left(\rho_n\alpha_n^2 r_{\alpha n}\right)^{-1} \\ \left(\gamma_n-1\right)/\gamma_n r_{\beta n} & 0 & -\left(\rho_n C^2\gamma_n r_{\beta n}\right)^{-1} & 0 \\ 0 & 1 & 0 & \left(\rho_n C^2\gamma_n\right)^{-1} \end{bmatrix}, \tag{2.3}$$

and the transfer matrix at m-layer is

$$\mathbf{A}_m=\begin{bmatrix} \gamma_m\cos P_m-(\gamma_m-1)\cos Q_m & -i\left[\gamma_m r_{\alpha m}\sin P_m+(\gamma_m-1)r_{\beta m}^{-1}\sin Q_m\right] & \rho_m C^2\gamma_m(\gamma_m-1)(\cos P_m-\cos Q_m) & i\rho_m C^2\gamma_m^2 r_{\alpha m}\sin P_m+\gamma_m^2 r_{\beta m}\sin Q_m \\ i\left[(\gamma_m-1)r_{\alpha m}^{-1}\sin P_m+\gamma_m r_{\beta m}\sin Q_m\right] & -(\gamma_m-1)\cos P_m+\gamma_m\cos Q_m & i\rho_m C^2(\gamma_m-1)r_{\alpha m}^{-1}\sin P_m-\gamma_m^2 r_{\beta m}\sin Q_m & -\left(\rho_m C^2\right)^{-1}(\cos P_m-\cos Q_m) \\ -\left(\rho_m C^2\right)^{-1}(\cos P_m-\cos Q_m) & i\left(\rho_m C^2\right)^{-1}\left(r_{\alpha m}\cos P_m-r_{\beta m}^{-1}\sin Q_m\right) & -(\gamma_m-1)\cos P_m+\gamma_m\cos Q_m & i\left[(\gamma_m-1)r_{\alpha m}^{-1}\sin P_m+\gamma_m r_{\beta m}\sin Q_m\right] \\ i\left(\rho_m C^2\right)^{-1}\left(r_{\alpha m}^{-1}\cos P_m-r_{\beta m}\cos Q_m\right) & -\left(\rho_m C^2\right)^{-1}(\cos P_m-\cos Q_m) & i\left[(\gamma_m-1)r_{\alpha m}^{-1}\sin P_m+\gamma_m r_{\beta m}\sin Q_m\right] & \gamma_m\cos P_m-(\gamma_m-1)\cos Q_m \end{bmatrix}. \tag{2.4}$$

Where

$$\gamma_m = 2\left(\beta_m / C\right)^2 , \tag{2.5}$$

$$r_{\alpha m} = \begin{cases} +\sqrt{\left(C/\alpha_m\right)^2 - 1} & C > \alpha_m \\ -i\sqrt{1-\left(C/\alpha_m\right)^2} & C < \alpha_m \end{cases} , \tag{2.6}$$

$$r_{\beta m} = \begin{cases} +\sqrt{\left(C/\beta_m\right)^2 - 1} & C > \beta_m \\ -i\sqrt{1-\left(C/\beta_m\right)^2} & C < \beta_m \end{cases} , \tag{2.7}$$

$$P_m = kr_{\alpha m} H_m , \tag{2.8}$$

and

$$Q_m = kr_{\beta m} H_m . \tag{2.9}$$

To find $C(k)$ or $C(f)$ at given wavenumber or frequency from a function of $F(C,k) \approx 0$, an initial phase velocity and an initial wavenumber are given in the first iteration. For example, the initial phase velocity is obtained from C_n root in the following equation of a phase velocity related to a P-wave velocity (α_n) and an S-wave velocity (β_n) in the half-space as

$$\left(\frac{C_n}{\beta_n}\right)^6 - 8\left(\frac{C_n}{\beta_n}\right)^4 + 8\left(\frac{C_n}{\beta_n}\right)^2\left[1+2\left(1-\frac{\beta_n^2}{\alpha_n^2}\right)\right] - 16\left(1-\frac{\beta_n^2}{\alpha_n^2}\right) = 0 . \tag{2.10}$$

Iterative evaluation is conducted for different wave number so I can obtain phase velocity for different frequencies ($C(f)$). I also use this computational procedure to generate synthetic phase velocities assuming a fundamental mode in the next chapter. Moreover, I also employ this approach in the forward calculation of the dispersion curve for the MCMC inversion. The computational procedure in the theoretical dispersion curve of the phase velocity can be found in Figure 2.2.

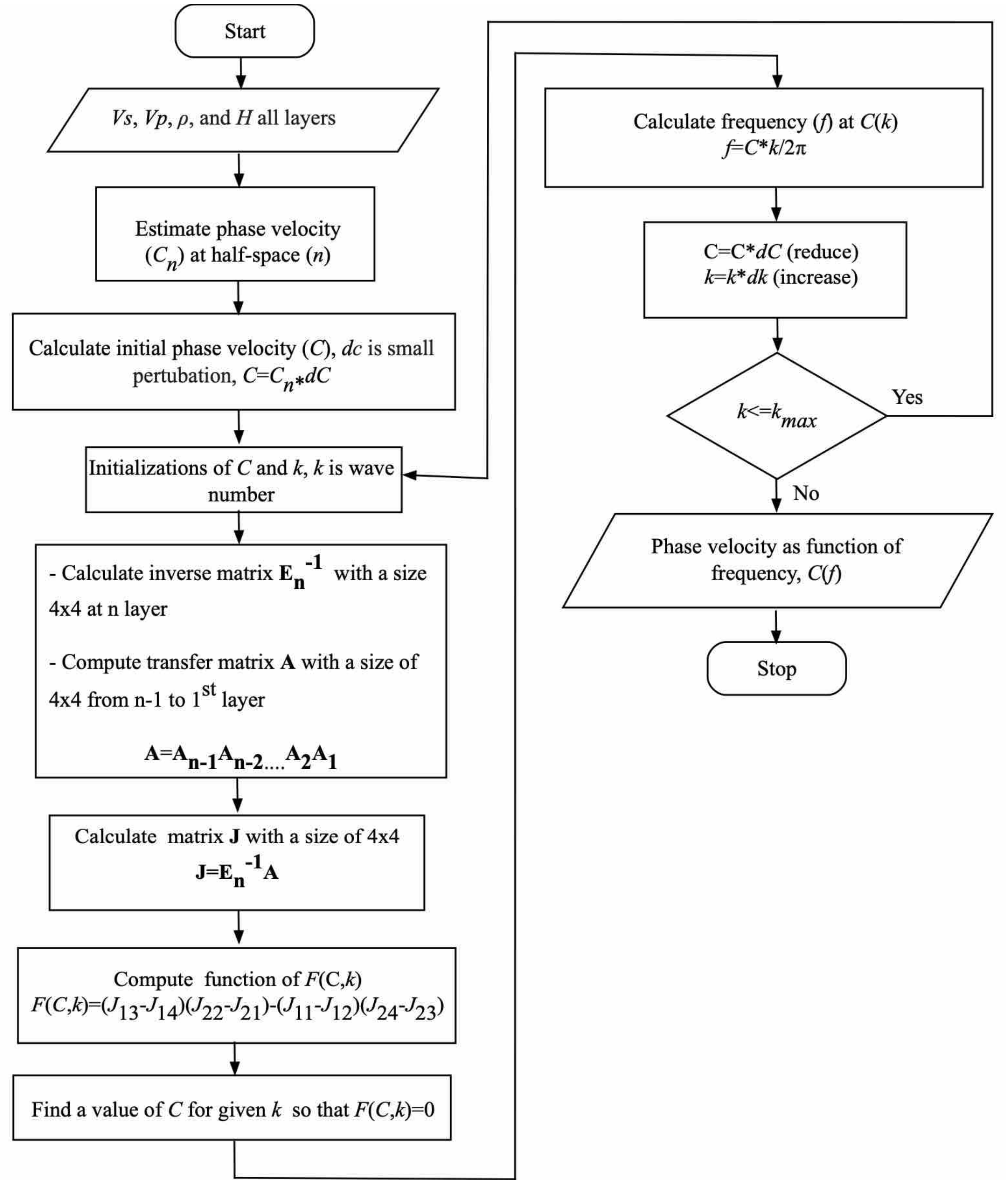

Figure 2.2 Computational process of forward calculation in the dispersion curve of phase velocity for stratified layers.

2.1.2 Inversion calculation

The MCMC inversion (Yamanaka, 2014, 2013, 2011) samples models in the model spaces based on misfit values ($E(\mathbf{m})$) for a model parameter ($\mathbf{m}$). The model parameters denote S-wave velocity and thickness of each layer in a layered model in this study. The misfit value as previously mentioned in Equation 1.3 can be also defined in the following

$$E(\mathbf{m}) = \sum_{i=1}^{n} \left[\frac{O(f_i) - C(f_i)}{\sigma(f_i)} \right]^2, \qquad 2.11$$

where $O(f_i)$, $C(f_i)$, and $\sigma(f_i)$ are the observed phase velocity, the calculated phase velocity, and the standard deviation of the observed phase velocity at frequency f_i, respectively. Additionally, n is the number of observed phase velocities.

The calculation of the theoretical phase velocity for a horizontally layered model in the MCMC inversion is also estimated using the Haskell's method (Haskell, 1953) assuming the fundamental mode. Besides the thickness and S-wave velocity, it also requires information on a density and a P-wave velocity, which are less sensitive to the phase velocity than the thickness and S-wave velocity (Horike, 1985). Moreover, I used the following empirical relationship (Kitsunezaki et al., 1990)

$$V_P = 1.11V_S + 1290, \qquad 2.12$$

to calculate a P-wave velocity from an S-wave velocity (m/s). This relation has been used in several previous studies (e.g., Yamanaka, 2014, 2013, 2011, 2005).

In the MCMC method, a posterior probability distribution, $p(\mathbf{m}|\mathbf{d})$ is formulated based on the Bayes' theorem for a model parameter (**m)** and a given data (**d**). The given data denote the observed phase velocity. The theorem is expressed as

$$p(\mathbf{m}\,|\,\mathbf{d}) = \frac{p(\mathbf{d}\,|\,\mathbf{m})p(\mathbf{m})}{p(\mathbf{d})}. \qquad 2.13$$

Here, $p(\mathbf{m}|\mathbf{d})$ is a conditional probability distribution of the model parameters given the observed phase velocity. Moreover, $p(\mathbf{m})$ and $p(\mathbf{d})$ are a prior probability distribution of the model and the probability distribution of the data, respectively. I assume that the distribution of the data and a prior distribution of the model parameters are constant, because I typically have the data before the inversion, and I do not have prior information on the model parameters. $p(\mathbf{d}|\mathbf{m})$ is a conditional probability distribution related to a likelihood function $L(\mathbf{m})$, and it can be written as

$$p(\mathbf{d}\,|\,\mathbf{m}) \propto L(\mathbf{m}) = \exp\left[-E(\mathbf{m})\right]. \qquad 2.14$$

I regard the posterior distribution of the model parameters as a solution to my inversion considering their uncertainties. From the above assumption, I can write the posterior distribution as:

$$p(\mathbf{m}\,|\,\mathbf{d}) \propto \exp\left[-E(\mathbf{m})\right]. \qquad 2.15$$

To find a stationary sampling from the posterior distribution in Equation 2.15, I apply the Metropolis-Hastings (MH) algorithm (Hastings, 1970). This algorithm constructs a Markov chain to estimate a stationary sampling condition of the models. The sampling process in the MCMC method uses a series of iterations to generate a stationary sampling from a random initial model ($\mathbf{m_0}$). Assuming $\mathbf{m_{i-1}}$ is the current model at i-th iteration of the chain. A candidate model ($\mathbf{m}'$) is produced using a proposal distribution $q(.|\mathbf{m_{i-1}})$. The proposal distribution is a normal distribution with an average of $\mathbf{m_{i-1}}$ and a standard deviation of $\boldsymbol{\sigma_{pi}}$. The new model is controlled by the standard deviation. The acceptance of the generated model is based on an acceptance probability of the MH algorithm (r), expressed as

$$r = \min\left\{ \frac{L(\mathbf{m}')q(\mathbf{m}_{\text{i-1}} \mid \mathbf{m}')}{L(\mathbf{m}_{\text{i-1}})q(\mathbf{m}' \mid \mathbf{m}_{\text{i-1}})}, 1 \right\}. \qquad 2.16$$

In this study, a symmetric proposal distribution is used, so that $q(\mathbf{m}_{\text{i-1}} \mid \mathbf{m}') = q(\mathbf{m}' \mid \mathbf{m}_{\text{i-1}})$. Hence, Equation 2.16 can be rewritten as

$$r = \min\left\{ \frac{L(\mathbf{m}')}{L(\mathbf{m}_{\text{i-1}})}, 1 \right\}. \qquad 2.17$$

The next model in the chain is $\mathbf{m}_\mathbf{i} = \mathbf{m}'$, if the candidate model ($\mathbf{m}'$) is accepted. Otherwise, the new model is equal to the current model, $\mathbf{m}_\mathbf{i} = \mathbf{m}_\mathbf{i-1}$. The numerical procedure in this acceptance is similar to that of the Metropolis simulated annealing (e.g., Yamanaka, 2005). The illustration of the acceptance probability of models using the MH algorithm can be found in Figure 2.3. The figure shows the evolution of model parameters until reaching a stationary state.

The sampled models are depending on the assumed initial model at an early stage of the iterations. Therefore, I need to discard sampled data before reaching a stationary state; this is known as a burn-in period. I employ Geweke's convergence criteria (Geweke, 1992) to determine the burn-in period by using a *Z*-value. The *Z*-value for each parameter is calculated as

$$Z = \frac{|g_1 - g_2|}{\sqrt{s_1 + s_2}}, \qquad 2.18$$

where g_1 and s_1 are the average and the variance for the first p data, while g_2 and s_2 are the average and the variance for q data from the end of the iteration. Assuming that the number of data after the burn-in period is L, the p and q were set to be 10% and 50% of L, respectively. I calculated different burn-in periods until the maximum *Z*-values of all the parameters were less than 1.96. This *Z*-value shows stationarity at a significance level of 5%. Computational procedures in estimations of sampled models from the MCMC inversion and burn-period are depicted in Figure 2.4.

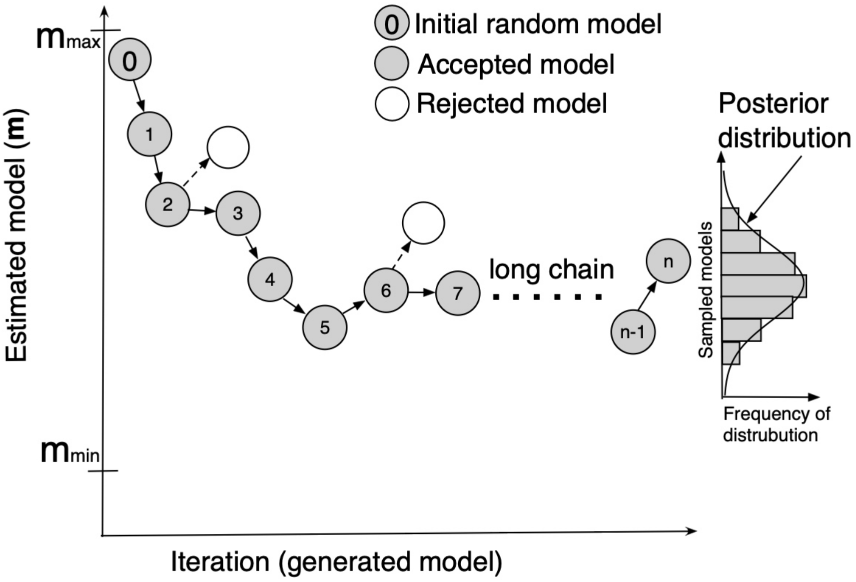

Figure 2.3 Visualization of model generation using the acceptance probability of the MH algorithm within search limits of estimated models (m_{min}-m_{max}). Generated models from an initial random model until *n*-model. Some models are accepted or rejected based on the acceptance probability until reaching a stationary state. Posterior distribution of estimated models can be evaluated after a burn-in period.

Unlike, in the previous studies by Yamanaka (2014;2013;2011) that used only one initial random model during inversion of a phase velocity using the MCMC method. In this study, I applied five different initial random models so that if the multiple chains have arrived at a similar distribution, then I can be more certain of convergence state.

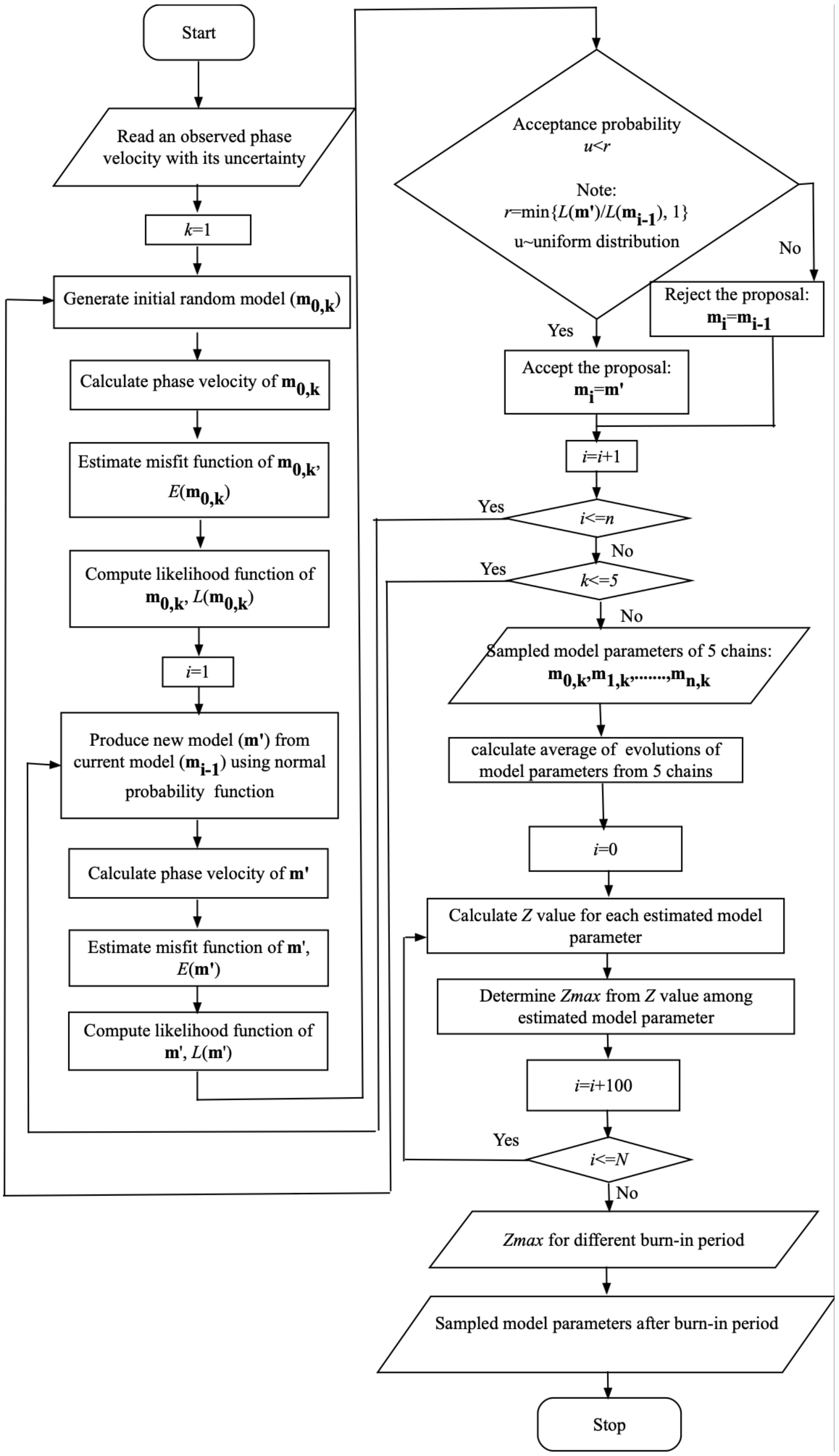

Figure 2.4 A flowchart of the MCMC sampling in a phase velocity inversion generates a random initial model ($\mathbf{m}_{0,k}$) until *n*-model ($\mathbf{m}_{n,k}$) using *k-th* different random number and estimation of different burn-in periods at iterations of 100 to *N* using Geweke's technique. *N* is about 50-80% of *n* in this study. The model parameters after burn-in periods are obtained by Geweke's procedure. Model parameters (**m**) represent the S-wave velocity and the thickness in each layer of the model. In this study, I use five different random numbers to generate initial models.

2.2 Equivalent linear method

Sampled model parameters beyond a burn-in period are used for estimation of variability in linear and nonlinear soil amplifications. In this study, the nonlinear soil response is approximated by an equivalent linear method.

Unlike other structural materials such as steel and concrete, nonlinear behavior of soil occurs from the very small strain (e.g., Yoshida, 2015). The behavior of soil under cyclic loading such as seismic loads might exhibit a hysteresis loop as shown in Figure 2.5. The hysteresis loop can be explained either by an actual path of the loop represented by a tangent shear modulus (G_{tan}) or by parameters that depict its common pattern characterized by a secant shear modulus (G_{sec}) (e.g., Kramer, 1996). Parameter G_{tan} changes during a cycle of loading, however, its average value over the whole loop can be estimated by the secant shear modulus as

$$G_{sec} = \frac{\tau_c}{\gamma_c}, \qquad 2.19$$

where τ_c and γ_c represent the shear stress and shear strain amplitudes, respectively. Thus, parameter G_{sec} describes the typical inclination of the hysteresis loop. Energy dissipated (W_D) is equal to the area of the hysteresis loop (A_{loop}). The dissipated energy can conveniently be explained by the damping ratio as

$$h = \frac{W_D}{4\pi W_S} = \frac{1}{2\pi}\frac{A_{loop}}{G_{sec}\gamma_c^2}, \qquad 2.20$$

where W_S is the maximum strain energy, which is equal to the area of a triangle, $W_s = \frac{1}{2}G_{sec}\gamma_c^2$. The parameters G_{sec} and h are often referred to as equivalent linear materials. These parameters are applied in SHAKE code (Schnabel et al., 1972) and newer version code, SHAKE91 (Idriss and Sun, 1992). It is known as an equivalent linear method where the stress-strain relationship is represented in linear in order to solve the equation of motion in the frequency domain, which are based on the multiple reflection theory and nonlinearity of soil behavior.

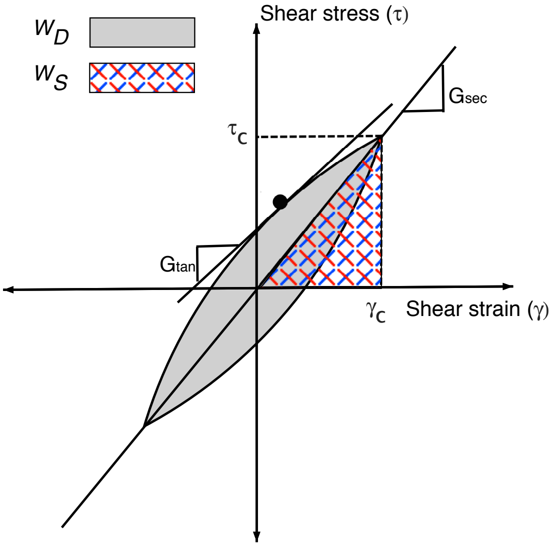

Figure 2.5 Secant shear modulus (G_{sec}) and tangent shear modulus (G_{tan}) (Kramer, 1996; Yoshida, 2015).

The multiple reflection theory expressed a soil response associated with the vertical propagation of shear waves through the linear viscoelastic system shown in Figure 2.6. The system consists of *n* horizontal layers, which extend to infinity in the horizontal direction and has a half-space as the bedrock layer. Each layer is homogeneous and isotropic and is defined by the thickness, mass density, shear modulus (rigidity) (*G*) and damping factor (*h*). The shear modulus is related to an S-wave velocity ($G = \rho V_S$).

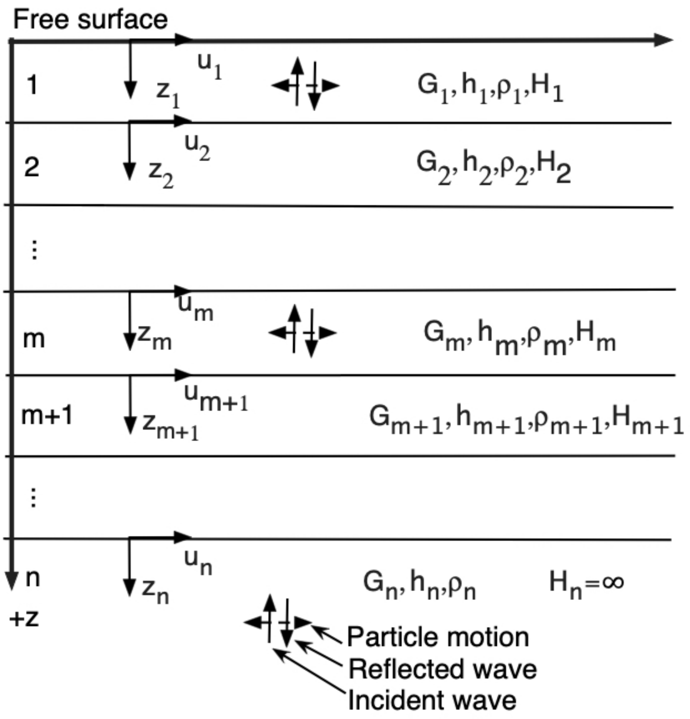

Figure 2.6 Layered soil deposit over elastic bedrock (Modified after Kramer, 1996; Schnabel et al., 1972).

Vertical propagation of shear waves through the system in Figure 2.6 causes only horizontal displacements. Assuming the soil in all layers works as a Kelvin-Voigt solid, 1D equation of motion for vertically propagating shear waves can be presented as

$$\rho \frac{\partial^2 u}{\partial t^2} = G \frac{\partial^2 u}{\partial z^2} + \eta \frac{\partial^3 u}{\partial z^2 dt}. \qquad 2.21$$

Where η is viscosity and it is related to damping, the solution of displacement wave ($u(z,t)$) for a harmonic motion with angular frequency (ω) is expressed as

$$u(z,t) = Ee^{i(kz+\omega t)} + Fe^{-i(kz-\omega t)}, \qquad 2.22$$

where E and F represent amplitudes of waves traveling in the $-z$ (upward) and $+z$ (downward) directions, respectively. It is also possible to estimate velocity ($\dot{u}(z,t)$) and acceleration ($\ddot{u}(z,t)$) waves from the displacement wave as the following equation

$$\dot{u}(z,t) = \frac{\partial u(z,t)}{\partial t} = i\omega u(z,t) \text{ and } \ddot{u}(z,t) = \frac{\partial^2 u(z,t)}{\partial t^2} = -\omega^2 u(z,t). \qquad 2.23$$

Experiments on many soil materials indicated that G and h are approximately constant over the frequency range as it was applied in SHAKE (Schnabel et al., 1972) and SHAKE91 (Idriss and Sun, 1992). The complex shear modulus (G^*) is expressed in terms of damping ratio instead of the viscosity,

$$G^* = G + i\omega\eta = G(1 + 2ih). \qquad 2.24$$

Equation 2.24 is used in original SHAKE while in SHAKE91, G^* is equal to,

$$G^* = G\left(1 - 2h^2 + 2ih\sqrt{1 - h^2}\right). \qquad 2.25$$

G^* is supposed to be written as in Equation 2.25. However, for small h, the h^2 terms can be can neglected so that G^* are assumed as in Equation 2.24 (Kramer, 1996). In my study, G^* in Equation 2.25 was applied since I used SHAKE91 for nonlinear analysis.

Recursion formulas for the amplitudes, E_{m+1} and F_{m+1}, of the incident and reflected wave in layer-m+1, expressed in terms of the amplitudes in layer-m as

$$E_{m+1} = \frac{1}{2}E_m\left(1 + \alpha_m^*\right)e^{ik_m^* H_m} + \frac{1}{2}F_m\left(1 - \alpha_m^*\right)e^{-ik_m^* H_m}, \qquad 2.26$$

$$F_{m+1} = \frac{1}{2}E_m\left(1 - \alpha_m^*\right)e^{ik_m^* H_m} + \frac{1}{2}F_m\left(1 + \alpha_m^*\right)e^{-ik_m^* H_m} \qquad 2.27$$

Where k_m^* is a complex wave number and α_m^* is the complex impedance ratio at the boundary between layer-m and m+1 expressed as

$$\alpha_m^* = \frac{k_m^* G_m^*}{k_{m+1}^* G_{m+1}^*} = \frac{\rho_m Vs_m^*}{\rho_{m+1} Vs_{m+1}^*}. \qquad 2.28$$

Vs_m^* is a complex shear wave velocity at layer-*m*. The transfer function $A_{m,n}$ between the motion at layer-*m* and *n* is defined by

$$A_{m,n}(f)=\frac{u_m(f)}{u_n(f)}=\frac{\dot{u}_m(f)}{\dot{u}_n(f)}=\frac{\ddot{u}_m(f)}{\ddot{u}_n(f)}=\frac{E_m(f)+F_m(f)}{E_n(f)+F_n(f)} \qquad 2.29$$

Based on Equation 2.29, if a motion is known in any one layer or layer-interface in the system, then a motion can be calculated in any other layer or layer-interface. This equation is important for convolution and deconvolution analyses. The convolution analysis is used to estimate a surface motion from a known bedrock motion, while the deconvolution is employed to calculate a bedrock motion from a recorded surface motion. The transfer function is often stated as soil amplification. The impedance ratio is mostly controlled by velocity contrast since the difference of densities between two layers is generally small as indicated in Equation 2.28. The impedance ratio controls a peak of soil amplification. Meanwhile, layer thicknesses are related to attenuation of amplitudes of the incident and reflected waves as shown in Equations 2.26 and 2.27, respectively. Therefore, the S-wave velocity and thickness of a layered model are important parameters for estimation of soil response. In my study, I assumed that soil amplification as a transfer function of the surface motion (free surface of layer 1) to the outcrop motion (free surface of layer-*n*) is defined as

$$A_{1,n}(f)=\frac{u_1(f)}{u_n(f)}=\frac{\dot{u}_1(f)}{\dot{u}_n(f)}=\frac{\ddot{u}_1(f)}{\ddot{u}_n(f)}=\frac{2E_1(f)}{2E_n(f)}. \qquad 2.30$$

The nonlinearity of a shear modulus and damping is accounted by use of an equivalent linear procedure based on an effective strain level computed for each layer. The effective shear is generally assumed as 65% of the maximum shear strain. Iterative procedures in the equivalent linear can be found in Figure 2.7. The number of iterations is presented by a cycle with a number. An initial rigidity (G_0) and initial damping (h_0) in the lowest strain level are used to predict the first effective shear strain (γ_{eff1}) as depicted in the figure. Because the G_0 and h_0 are greater than the given *G* and *h* curves (black curve), next iteration is required until estimated *G* and *h* (third iteration) getting close to the given *G* and *h* curve. It is commonly assumed that the estimated *G* and *h* converged if the difference between the target curve and the estimated *G* and *h* is less than 5%.

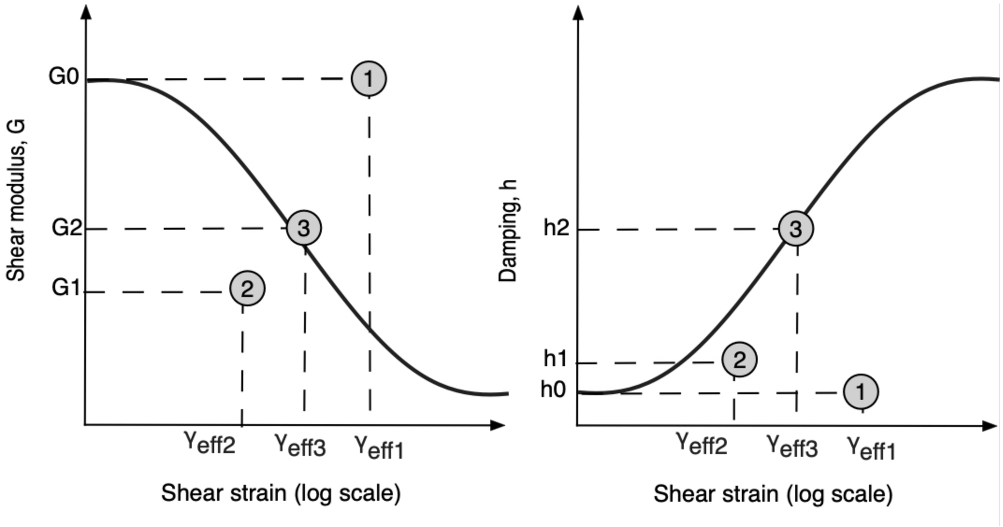

Figure 2.7 Iterative routine to find compatible shear modulus and damping ratio in the equivalent linear method. Cycle with a number indicates the iterative number while the black curve shows target *G* and *h* curves.

Many studies have shown that conventional equivalent linear methods such as SHAKE, give reasonable results for estimation of a nonlinear soil response as compared to nonlinear methods, for moderate strain levels up to 0.3-0.4% (e.g., Kaklamanos et al., 2015, 2013). However, SHAKE may have significant over-damping effects at high frequencies if the strain level is too large, particularly for soft soil (Hartzell et al., 2004; Yoshida et al., 2002). An enhanced equivalent linear method is often used for high strain level (larger than 1%) such as DYNEQ code (e.g., Yoshida, 2015; Yoshida et al., 2002). The multiple reflection theory as above explained is also applied in DYNEQ code as similar to that of SHAKE. Unlike SHAKE, DYNEQ treats frequency-dependent effective strain to avoid overdamping effect in high frequency range. The effective strain (γ_{eff}) is expressed as

$$\gamma_{eff} = \begin{cases} \gamma_{\max} & f < f_p \\ \gamma_{\max} - \left(\frac{\log f - \log f_p}{\log f_e - \log f_p} \right)^m & f_p \le f \le f_e \\ 0 & f > f_e \end{cases} . \qquad 2.31$$

Where $\gamma_{\max}$ is the maximum shear strain and f_p is a frequency at the largest shear strain. Moreover, f_e is the frequency above which linear behavior is assumed. The effective strain controls the shear modulus and damping in the equivalent linear method. Hence, the shear modulus and damping are also frequency-dependent. The effective strain is constant at frequencies lower than f_p ($f<f_p$). In middle frequency region ($f_p \leq f \leq f_e$), a parabolic equation is used in logarithm expression (practically $m=2$). The effective strain is zero at a high frequency higher than f_e ($f>f_e$). Moreover, f_e is a key frequency in this method. Yoshida (2015) mentioned that the parameter f_e lies between 5 and 15 Hz. In this research, I used f_e equal to 10 Hz as suggested by Yoshida (2015).

In this study, I used SHAKE91 to estimate 1D nonlinear soil response in the numerical study, while DYNEQ was applied in real data due to the large motion. I used sampled models after the burn-in period from the MCMC inversion to estimate a variation of soil response using the equivalent linear technique. Figure 2.8 indicates a computational procedure to estimate the variation of ground motion response from sampled models.

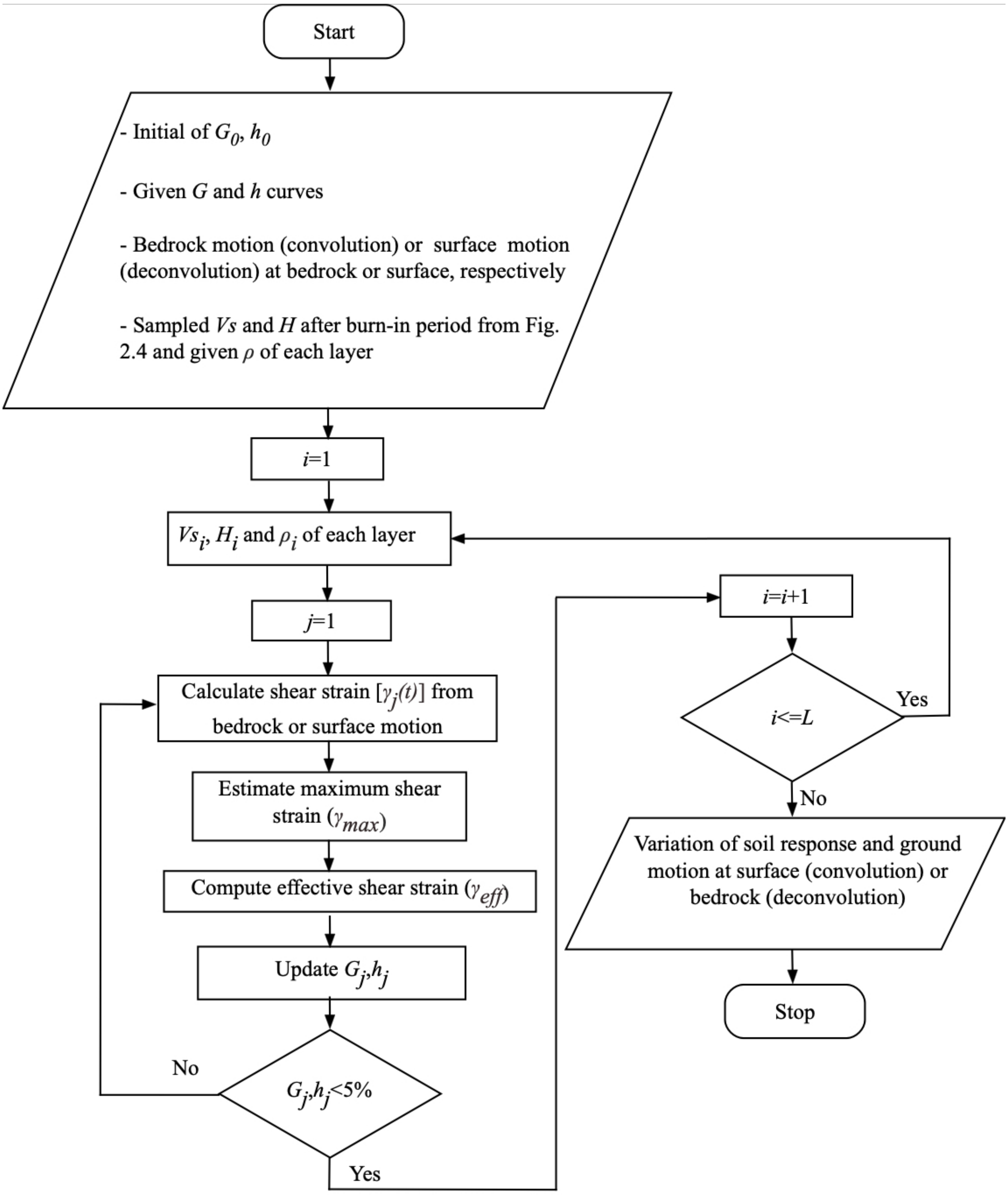

Figure 2.8 Computational procedure in the estimation of soil response variation using an equivalent linear method from sampled models from MCMC inversion. *L* is the number of models after the burn-in periods.

Chapter 3 Estimation of uncertainty in S-wave velocity profile from surface-wave phase velocity inversion

3.1 Objective

3.2 Generation of synthetic phase velocity

3.3 Comparison between a single chain and multiple chains

3.4 Inversion for two-layer model

3.5 Inversion for three-layer model

3.6 Thickness given to avoid trade-off-relationship between parameters

3.7 Effects of phase velocity at limited frequencies and different observational errors of phase velocities on uncertainty of S-wave velocity models

3.8 Effect of frequency-dependent error of phase velocity on uncertainty of sampling parameters

3.9 Summary

3.1 Objective

In this chapter, numerical experiments are conducted to verify performances of the Markov-chain Monte Carlo (MCMC) method for an inversion of surface-wave phase velocity. First, I compare convergence speeds of a single chain and multiple chains of the MCMC sampling in two- and three-layer models, in order to find a burn-in period of sampled models. Then, I estimate uncertainty in an S-wave velocity model from sampled models after the burn-in period for both models. I also discuss a trade-off-relationship between model parameters from the inversion. Additionally, effects of given thickness in the inversion into the resolution of the S-wave velocity model are shown in this chapter. Furthermore, I also present the uncertainty in the S-wave velocity profile due to phase velocities at a limited frequency, different observational errors in phase velocities, given thickness for different observational errors in phase velocities, and frequency-dependent errors of phase velocities.

3.2 Generation of synthetic phase velocity

I generated phase velocities of a fundamental Rayleigh wave in two models with the two- and three-layer models of shallow soil, as shown in Figure 3.1(a). In the first experiment, I start with a simple model that has two layers (a single soil layer over a half-space). I set the two-layer model to have a soft and thick soil layer, so the soil model has a pronounced nonlinear effect in amplification. Its phase velocity can be found in Figure 3.1(b). Then, I extend my model into a three-layer model (two soil layers over a half-space). The S-wave velocity for each layer in the three-layer model was generated based on an actual borehole at Echujima in the Tokyo Bay area (Iida et al., 2005). However, I modified the thicknesses of the first and second layers of the model. The second layer of the three-layer model is thicker than that of the first layer to make its phase velocity has a plateau at frequencies of 3 to 7 Hz as depicted in

Figure 3.1(c). Therefore, the shape of the phase velocity of the three-layer model is different from that of the two-layer model as shown in Figure 3.1(b) and (c).

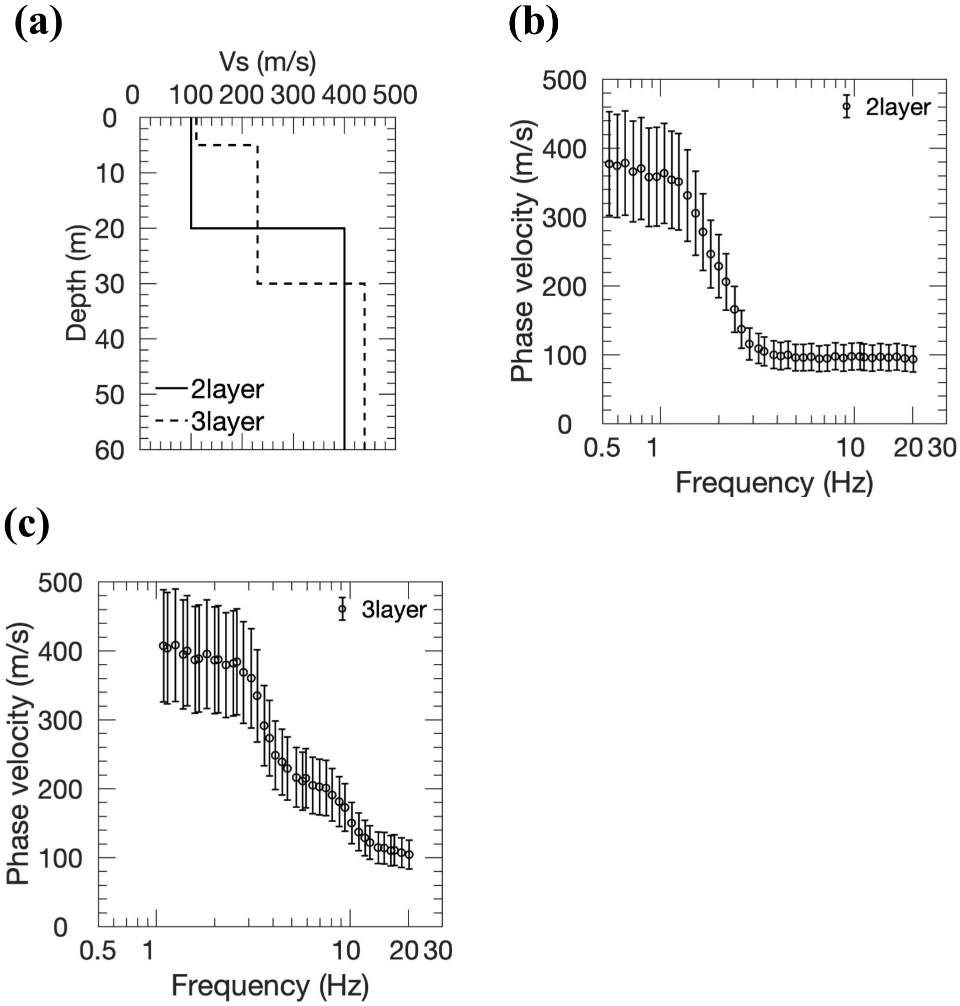

Figure 3.1 (a) True S-wave velocity profiles of two- and three-layer models. Synthetic phase velocities with observational errors of (b) two- and (c) three-layer models.

Synthetic phase velocities were calculated using Haskell's method (Haskell, 1953) as previously explained. Then, I perturbed the phase velocities by 5% of their amplitudes using uniform random numbers. The variation coefficient (SD/AVE) of the phase velocity is assumed to be 20% at each frequency. The variation coefficient represents a standard deviation (SD) over an average (AVE) of an estimated parameter. The frequency ranges of the phase velocities are 0.5 to 20 Hz and 1 to 20 Hz for two- and three-layer models, respectively. I chose the frequency ranges for the models by considering the results of typical microtremor measurements in previous studies (e.g., Özmen et al., 2017; Pramatadie et al., 2016). Figure 3.1(b) shows that the phase velocity of the two-layer model has enough coverage in a low and high frequency range. It is indicated that S-wave velocities at the top layer and half-space are similar to phase velocities at high frequency ranges (about more than 10 Hz) and low frequency range (about less than 1 Hz), respectively. Figure 3.1(c) shows that the phase velocity of the three-layer model has decent coverage. These phase velocities were used as synthetic data in the following numerical studies.

3.3 Comparison between a single chain and multiple chains

Before I estimate sampled models of the two- and three-layer models, I compare the results of a single chain and multiple chains of the MCMC sampling. In the MCMC inversion, if I make very long chains (e.g., infinite iterations), the stationary state will be reached eventually. However, I use a realistic number of iterations to find the stationary sampling considering the computational cost. As previously mentioned, Yamanaka (2014, 2013, 2011) applied the MCMC method to invert a phase velocity into an S-wave velocity. He only used a single chain with 100,000 iterations. I cannot be sure if the single chain with 100,000 iterations is enough to find the stationary state for many cases. Therefore, in this study, I used multiple chains of the MCMC sampling. The multiple chains should converge faster than a single chain. Moreover, if the different chains from different initial models have similar chains, so I may have better confidence in convergence state of chains than that of a single chain.

3.3.1 Different number of chains in two-layer model

In this study, I ran ten tests to generate sampling using different random numbers as initial models within the search limits in Table 3.1. Randomly generated initial models were developed during the MCMC sampling. Moreover, the density values were given in advance, as shown in the table, while *V*p for each layer was calculated by Equation 2.12.

Table 3.1 Two-layer model parameters and search limits for inversion.

No	True model			Search limits	
	Vs (m/s)	*H* (m)	ρ (g/cm^3)	*Vs* (m/s)	*H* (m)
1	100	20	1.7	70-150	0.5-50
2	400	-	1.9	250-600	-

Figure 3.2(a) indicates evolutions of the S-wave velocities and thickness in the MCMC sampling from ten chains using different initial models with 50,000 iterations each examination. Different initial models have similar evolutions after iterations about higher than 1,000. I averaged the evolutions of the parameters for a number of chains more than one to estimate maximum *Z*-values of model parameters (*Zma*x). The stationary state is quantitatively estimated by the *Zmax* among those examined parameters that have a value less than 1.96 in the early stages of the iteration process, as shown in Figure 3.2(b). The figure depicts that the one, five, and ten chain(s) have *Zmax* less than 1.96 at early iteration. It is indicated that the sampling parameters reach a stationary state at early iteration, caused by the two-layer model has a sufficient phase velocity information at low and high frequencies as shown in Figure 3.1(b).

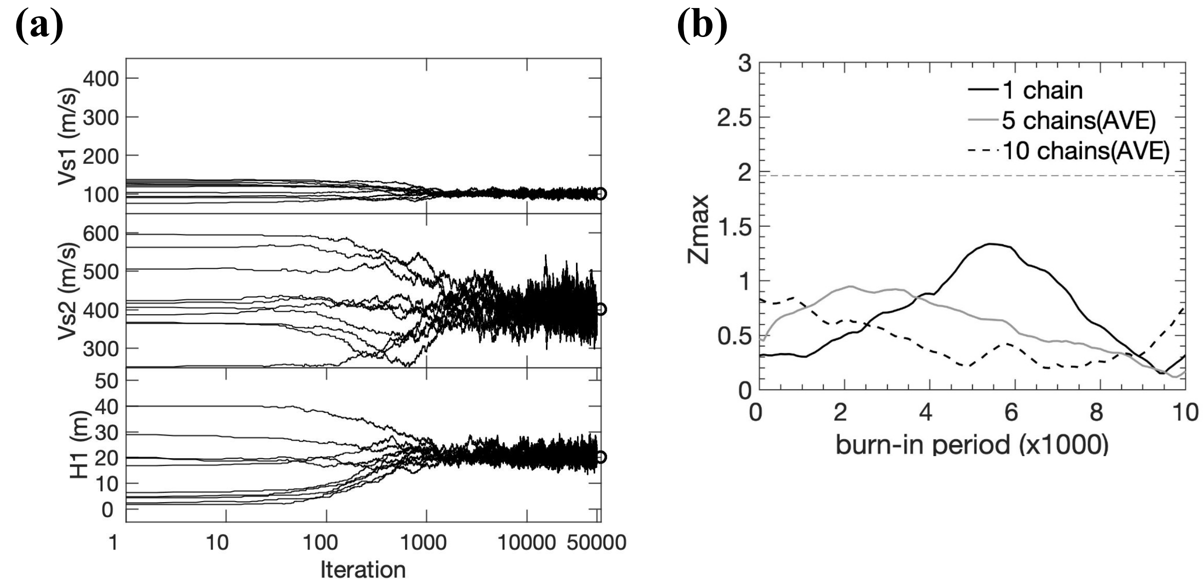

Figure 3.2 Ten chains of the MCMC sampling with different initial models for two-layer model. (a) Evolutions of S-wave velocity at the first and second layer and thickness at the first layer from top to bottom, respectively. True value for each parameter presented by open cycle at end of iteration. If a number of chains more than one, the chains are averaged. (b) Relationship of maximum *Z*-values and different burn-in periods using a different number of chains. A broken horizontal line indicates a *Z*-value of 1.96.

3.3.2 Different number of chains in three-layer model

In this section, I also examine a single chain and multiple chains of the MCMC sampling in a three-layer model. I ran 100,000 iterations each examination. The search limits of each model parameter can be seen in Table 3.2. Furthermore, the assumed density for each layer can be also found in the table, while *V*p for each layer is predetermined by Equation 2.12.

Table 3.2 The three-layer model parameters and search limits for inversion.

No	True model			Search limits	
	Vs (m/s)	*H* (m)	ρ (g/cm^3)	*Vs* (m/s)	*H* (m)
1	110	5	1.7	80-200	0.5-50
2	230	25	1.7	120-400	0.5-60
3	440	-	1.9	300-600	-

Figure 3.3(a) shows the evolutions of the model parameters from the MCMC sampling using ten chains. The figure portrayed that model parameters for different initial random models have similar evolution after iterations of higher than about 10,000. I also used the Geweke's technique to quantitively estimate burn-in periods for different number of chains as shown in Figure 3.3(b). I averaged evolutions of parameters if a number of chains are higher than one, as similar to the two-layer model. The evolutions of model parameters from five and ten chains are faster to reach the stationary states than that of the single-chain as portrayed in the figure. Moreover, it is also indicated that five chains are sufficient for estimation of a stationary state in the MCMC sampling considering the convergence speed and computational cost. Therefore, in the next calculation of the MCMC inversion, I will use five chains for estimation of model parameters. It is obvious that computational time for five chains is longer than that of a single chain. I used a laptop with Intel Core i7-2760QM 2.4 GHz with quad-core processors during the MCMC sampling in this study. It took about 10 minutes for a single chain with 50,000 iterations in the two-layer model and about 20 minutes with 100,000 iterations for a single chain in the three-layer model. Therefore, the computational time of five chains were 50 and 100 minutes for the two- and three-layer models, respectively. It is still possible to calculate in

reasonable computational time considering the advantages of multiple chains as I mentioned before.

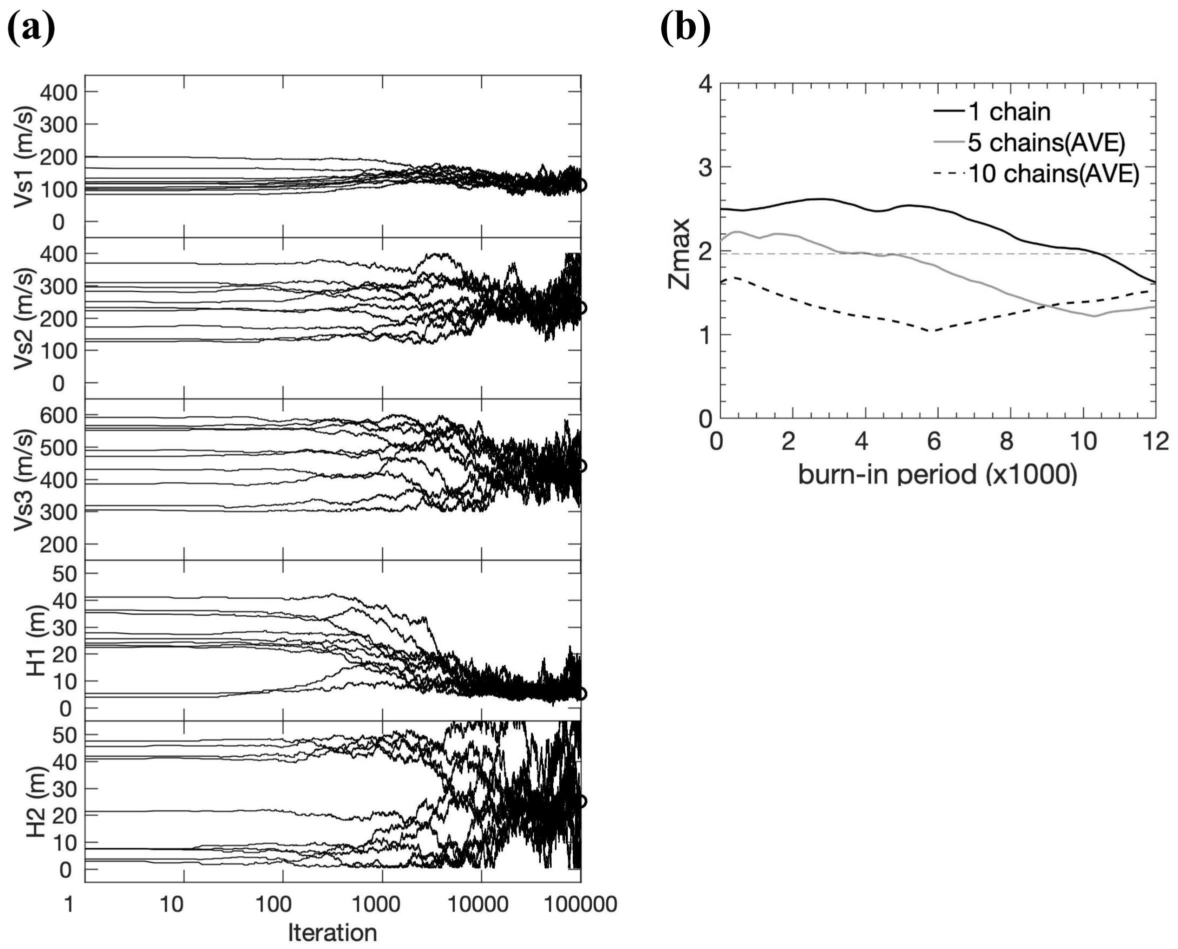

Figure 3.3 Ten chains of the MCMC sampling using different initial random model for three-layer model. (a) Evolutions of S-wave velocities and thicknesses at different layers. If a number of chains more than one, the chains are averaged (AVE). True value for each parameter presented by open cycle at end of iteration. (b) Relationship of maximum *Z*-values and different burn-in periods using one, five, and ten chain(s). A broken horizontal line indicates a *Z*-value of 1.96.

3.4 Inversion for two-layer model

3.4.1 Determination of burn-in period

Here, I discussed the determination of burn-in periods using five chains of the MCMC sampling for the two-layer model. Figure 3.4(a) shows the evolutions of the S-wave velocities and the thicknesses using 50,000 iterations each in the five tests, giving 250,000 sampled models in total. As mentioned before, I averaged the five chains in Figure 3.4(a) to estimate *Zmax*. The stationary state is quantitatively estimated by the *Zmax* among those examined parameters that have a value less than 1.96 in the early stages of the iteration process due to sufficient coverage of the phase velocity, as mentioned before, as shown in Figure 3.4(b). The *Z*-value for individual model parameter is also depicted in Figure 3.4(b). Therefore, I decided to use a burn-in period of 4,000 to avoid dependency of the sampled models on the initial models, resulting in 20,000 total discarded sampled models. The 230,000 sampled models from beyond the burn-in periods can be used to evaluate the distributions of the model parameters.

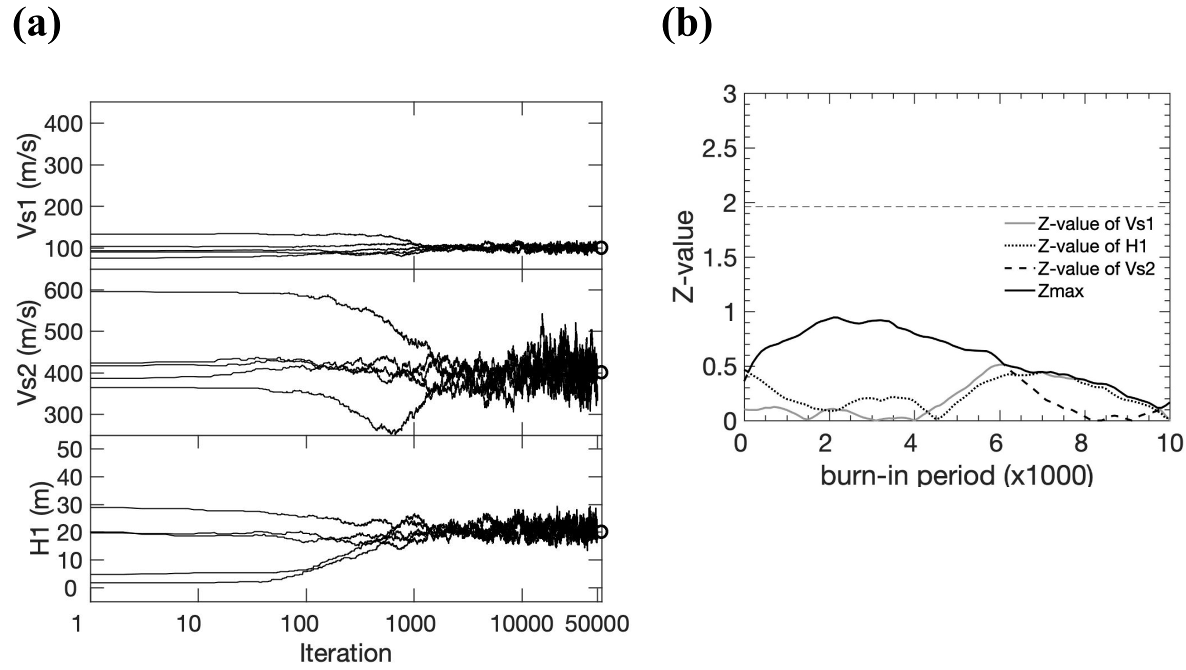

Figure 3.4 Results of sampling of parameters in two-layer model. (a) Evolutions of S-wave velocity at the first and second layer and thickness at the first layer obtained from five tests. Five chains are averaged (AVE) for Zmax estimation. True value for each parameter presented by open cycle at end of iteration. (b) Relationship of Z-values of model parameters/maximum Z-values and different burn-in periods using five random numbers. A broken horizontal line indicates a Z-value of 1.96.

Eventually, I determined a final model and its uncertainty value from the average and standard deviation of the sampled model distributions, respectively.

3.4.2 Distributions of model parameters

The distributions of the S-wave velocities and the thicknesses are evaluated for the models sampled after the burn-in period, as shown in Figure 3.5. The frequency distribution of each parameter is normalized to its area as shown in the figure for a probability density function. The average, standard deviation, and true value for each parameter are also indicated in the figure. The distributions of the S-wave velocity and the thickness of the top layer are very narrow, indicating a high resolution, while the S-wave velocity for the second layer has a wider distribution. The relatively low resolution in the second layer is due to a larger standard deviation of the phase velocity at low frequencies.

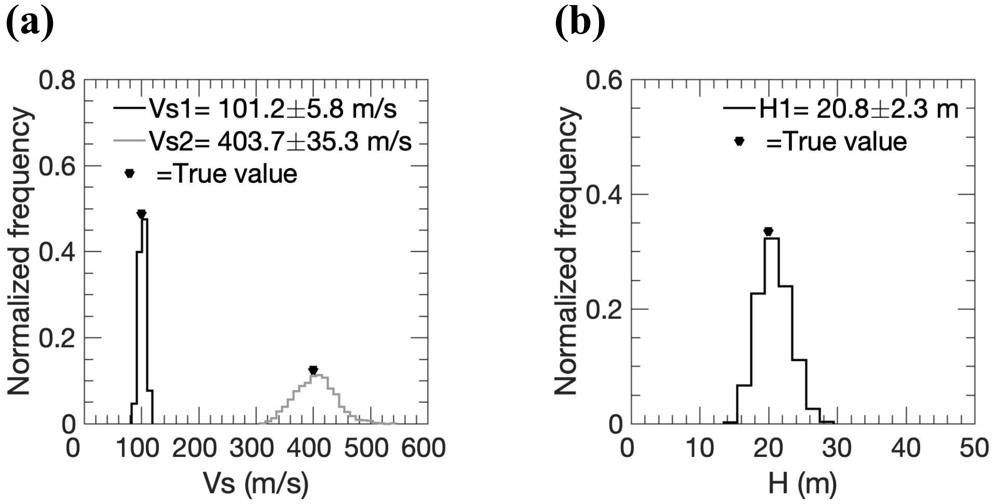

Figure 3.5 Distributions of (a) velocities and (b) thickness of sampled models after the burn-in period in two-layer model. The triangle shows true value for each parameter.

Next, these model parameters are used to determine the final inverted model and its uncertainty, as presented in Figure 3.6(a). The inverted model and the true model are quite similar, and the observed synthetic phase velocities at all frequencies are also well explained by the calculated phase velocity for the inverted model as shown in Figure 3.6(b).

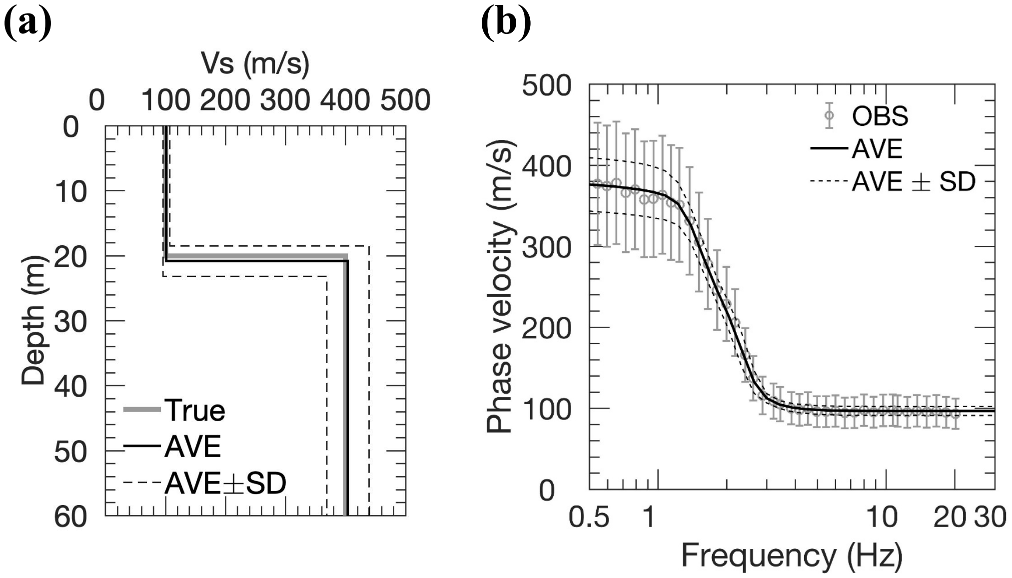

Figure 3.6 (a) Comparison between the true and final inverted model (AVE) with its uncertainty (SD) S-wave velocity profile for the two-layer model. (b) Their comparison between synthetic observed phase velocities (OBS) and inverted phase velocities (AVE) with its standard deviations (SD) are also shown.

3.4.3 Trade-off-relationship between model parameters in the two-layer model

I can also use the sampled models from the inversions to understand a trade-off-relationship between the model parameters. The trade-off-relationship portrays a resolution of one model parameter depends on other model parameters. The trade-off-relationship can be identified with a correlation coefficient between the model parameters from sampled models and it is essentially inevitable in the inversions of phase velocity. Therefore, the search limits of S-wave velocity and thickness are usually required to be carefully chosen (Yamanaka, 2014). For example, the search limit of an S-wave velocity can be narrower than that of the thickness considering existing subsurface data.

I present the trade-off-relationships for the two-layer models as depicted in Figure 3.7. The S-wave velocity and the thickness of the first layer have a high correlation coefficient of approximately 0.8 in Figure 3.7(a). However, Figure 3.7(b) indicates that the weak correlation between S-wave velocities or thickness at the first and second layers in the two-layer model.

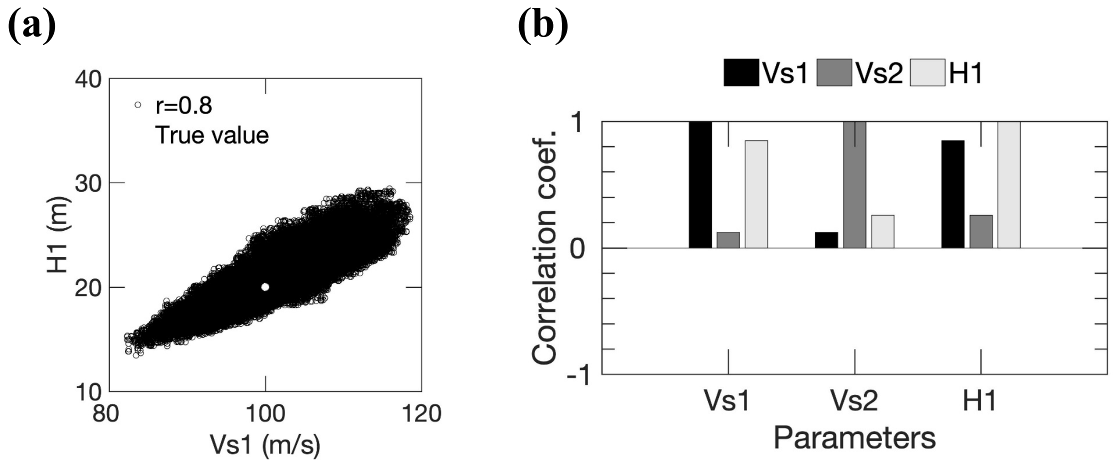

Figure 3.7 (a) Relationship of S-wave velocity and thickness of the first layer in two-layer model. A white circle indicates the parameter for the true model and *r* means correlation coefficient. (b) Correlation coefficients between model parameters in two-layer model.

I also did sensitivity tests of the phase velocity in relation to the model parameters at the first and second layers as depicted in Figure 3.8. The sensitivity of the phase velocity to the S-wave velocity ($\frac{\partial C}{\partial Vs_i}$) at the *i*-layer is calculated by

$$\frac{\partial C}{\partial Vs_i} = \frac{C\left(Vs_i, H_i\right) - C\left(Vs_i + \Delta Vs_i, H_i\right)}{\Delta Vs_i} \, , \tag{3.1}$$

where ΔVs_i is a perturbation in the S-wave velocity at the *i*-layer. Meanwhile, the sensitivity of the phase velocity to the thickness ($\frac{\partial C}{\partial H_i}$) at the *i*-layer is estimated by

$$\frac{\partial C}{\partial H_i} = \frac{C\left(Vs_i, H_i\right) - C\left(Vs_i, H_i + \Delta H_i\right)}{\Delta H_i} \, , \tag{3.2}$$

where ΔH_i is a perturbation in the thickness at the *i*-layer. ΔVs_i and ΔH_i are assumed to be 10% of corresponding parameters. Regardless of the high correlation coefficient of the S-wave velocity and the thickness at the first layer, the phase velocity in frequencies higher than 3 Hz (high-frequency) is only controlled by the S-wave velocity at the first layer as displayed in

Figure 3.8(a) and (b). It is suggested that the prominent correlation coefficient of the S-wave velocity and thickness of the first layer is caused by the high sensitivities of the phase velocity to the S-wave velocity and thickness of the first layer at frequencies of 1-3 Hz (mid-frequency), as depicted in Figure 3.8(a) and (b), respectively. Meanwhile, the S-wave velocity at the second layer controls the phase velocity in frequencies less than 2 Hz (low-frequency).

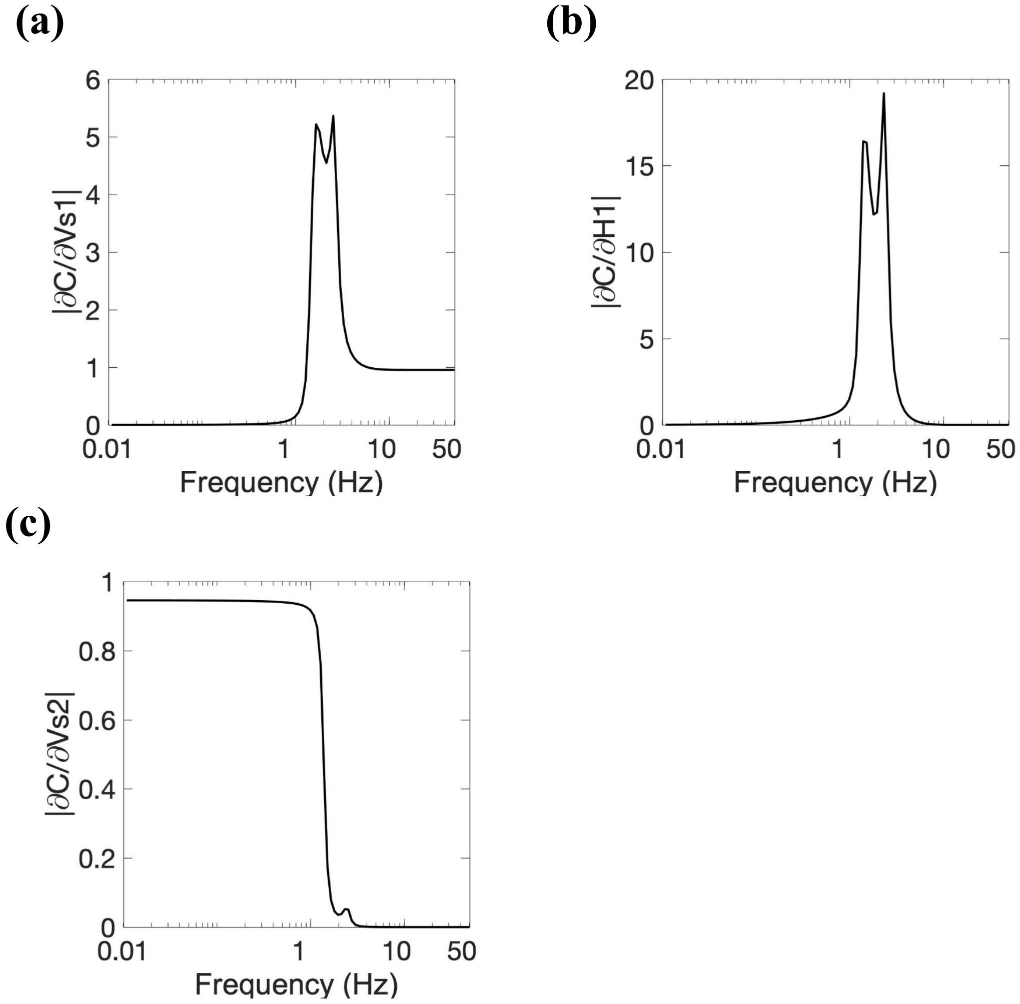

Figure 3.8 Sensitivities of a phase velocity to S-wave velocity ($\frac{\partial C}{\partial Vs_i}$) and thickness ($\frac{\partial C}{\partial H_i}$) at the *i*-layer. The phase velocity (*C*) to (a) S-wave velocity (*Vs*1), (b) thickness (*H*1) at the first layer, and (c) S-wave velocity (*Vs*2) at the second layer. $\Delta Vs1$, $\Delta H1$, and $\Delta Vs2$ are given 10% of their corresponding parameters.

3.5 Inversion for three-layer model

3.5.1 Estimation of burn-in period

In this section, I also present the MCMC sampling in the three-layer model in Figure 3.9(a). I ran five examinations with 100,000 iterations for each examination, giving a total of 500,000 models. I also used Geweke's technique to estimate the burn-in period from the averaged evolutions of the model parameters in Figure 3.9(a). Figure 3.9(b) indicates that the number of deleted models is 30,000. Therefore, I used the 470,000 sampled models after the burn-in periods for assessment of the uncertainties of the S-wave velocity profiles for the three-layer model.

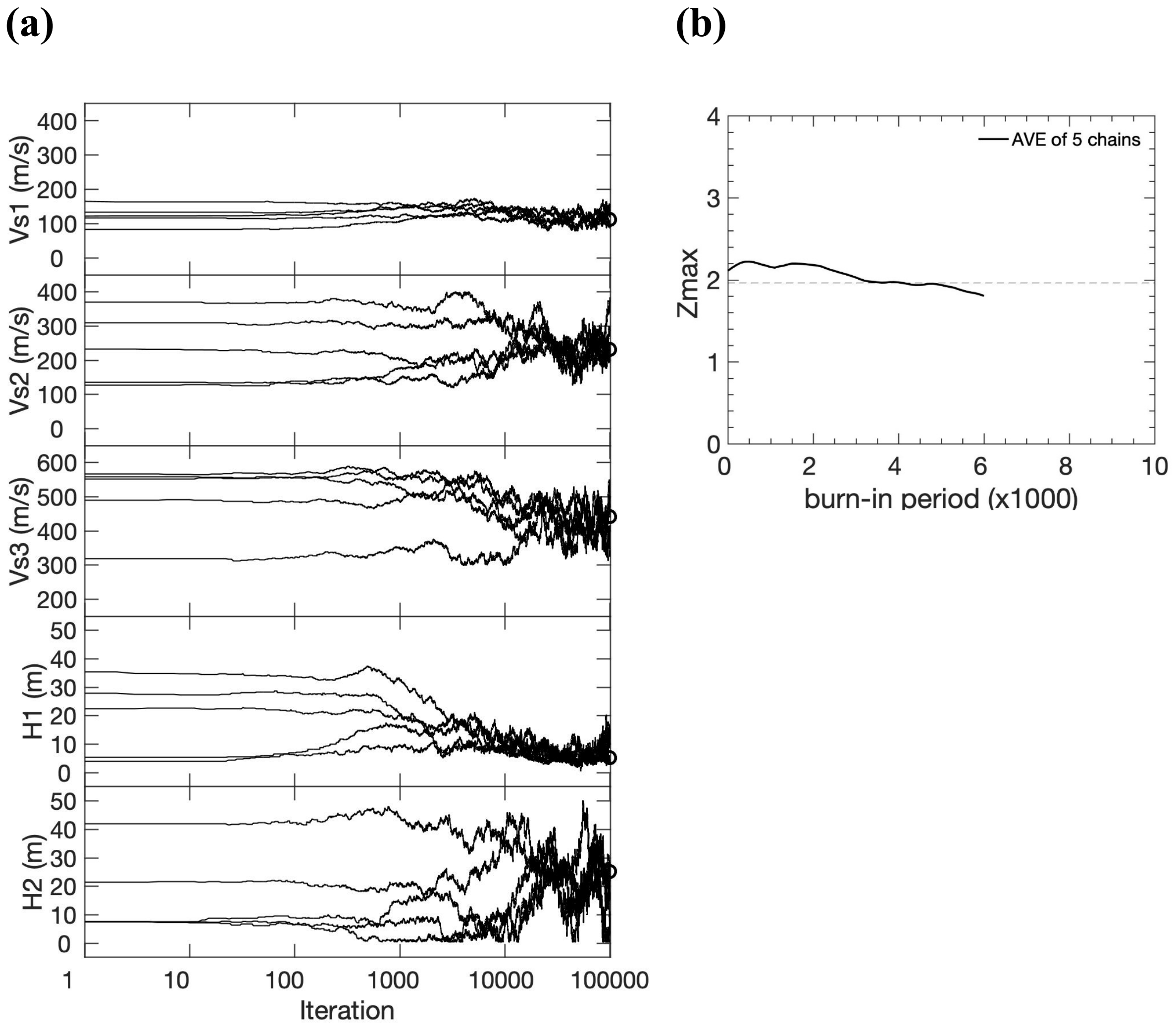

Figure 3.9 Results of sampling in three-layer model. (a) Evolutions of S-wave velocities at first, second, and third layers, and thicknesses at first and second layers obtained from five tests (from top to bottom, respectively). True values for parameters presented by open cycles at ends of iterations. (b) Relationship of maximum Z-values and burn-in period from the average evolution of model parameters. A broken horizontal line indicates a Z-value of 1.96.

3.5.2 Distributions of parameters of sampling models

The distributions of the model parameters in the first layer (*Vs*1 and *H*1) have the lowest uncertainties than those of the second and third layers, as shown in Figure 3.10(a) and (b), respectively, since there is enough coverage of the phase velocity in high frequency range (> 15 Hz), as depicted in Figure 3.1(c). However, the distributions of the parameters in the second layer (*Vs*2 and *H*2) are wider than those of the first layer, because the standard deviation of the phase velocity in a mid-frequency (3-8 Hz) is higher that of in the high frequency as displayed in Figure 3.1(c). Furthermore, the resolution of the S-wave velocity at the third layer is lower than that of the first layer since the uncertainty of the phase velocity in the low frequency (< 2 Hz) is higher that of in the high frequency.

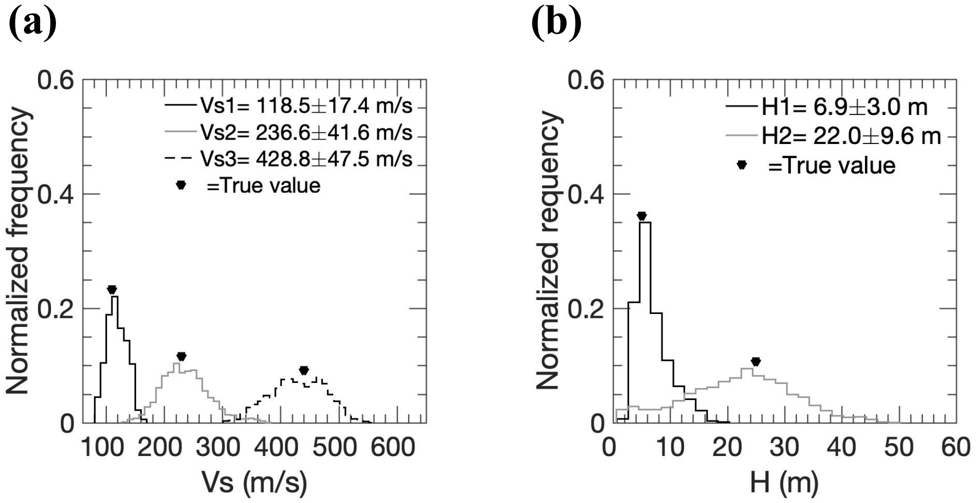

Figure 3.10 Distributions of (a) velocities and (b) thicknesses of sampled models after burn-in periods for three-layer model. A triangle shows true value for each parameter.

Afterward, the final model and its uncertainty are assessed from the distributions of the model parameters. The inverted model is similar to the actual model as presented in Figure 3.11(a), since the phase velocity has sufficient coverage in the low and the high frequencies as depicted in Figure 3.11(b). Similarly, the calculated phase velocity can explain quite well the observed one, as shown in Figure 3.11(b).

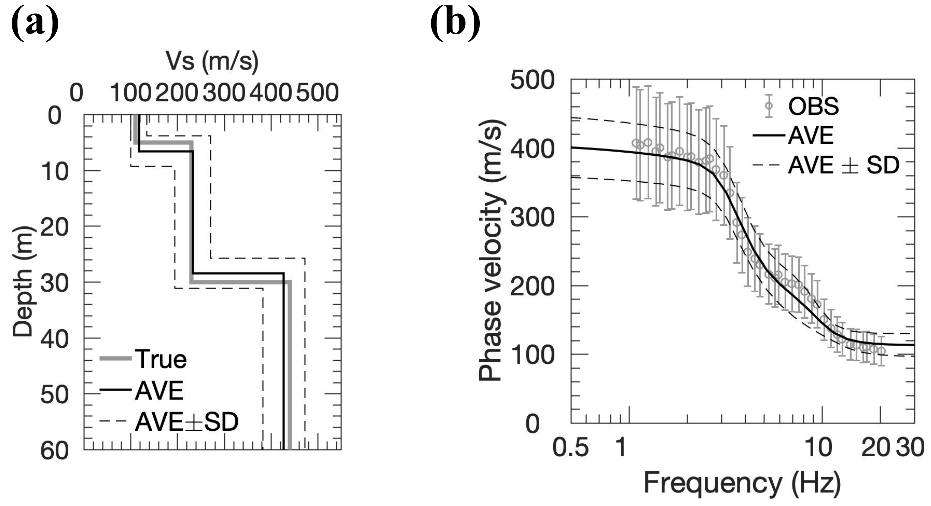

Figure 3.11 (a) Comparison between the true and final inverted model (AVE) with its uncertainty (SD) S-wave velocity profile for the three-layer model. (b) Their comparison between synthetic observed phase velocities (OBS) and inverted phase velocities (AVE) with its standard deviations (SD) are also shown.

3.5.3 Trade-off-relationship between model parameters in three-layer model

I also present the trade-off-relationships for the three-layer model in Figure 3.12. The S-wave velocity and the thickness of the first layer have high correlations of approximately 0.8 as depicted in Figure 3.12(a). Figure 3.12(b) indicates that the correlation coefficient of the S-wave velocity and the thickness at the second layer is about 0.5. Moreover, the figure also shows that the correlation coefficients of model parameters at the first ($Vs1$ and $H1$) and second ($Vs2$ and $H2$) layers are about 0.3. However, the correlation coefficient of the S-wave velocity of the third layer and the model parameters of the first or the second layer are small as depicted in the figure.

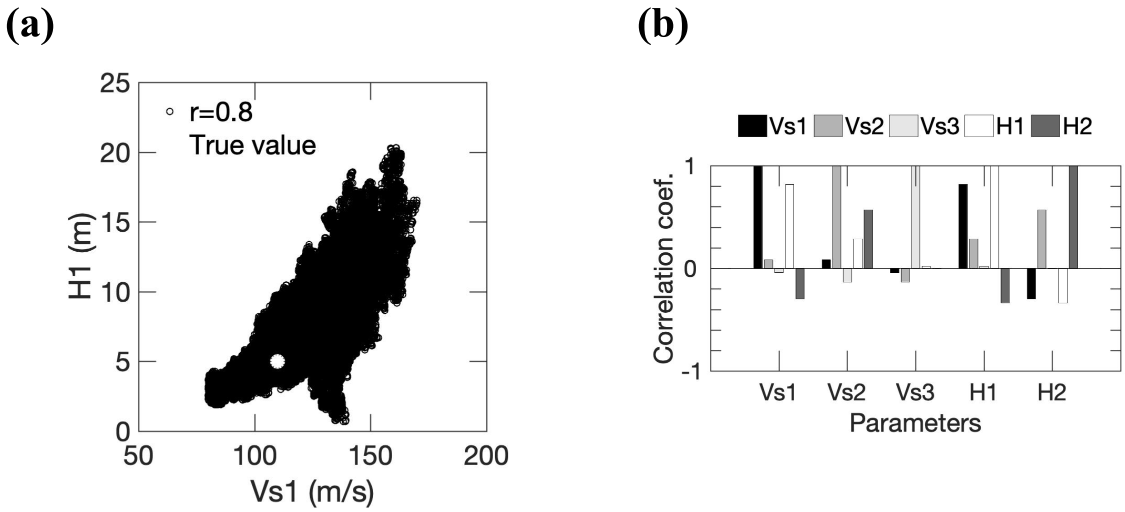

Figure 3.12 (a) Relationship of S-wave velocity and thickness of the first layer in the three-layer models. A white circle indicates the parameter for the true model and *r* means correlation coefficient. (b) Correlation coefficients between model parameters in the tree-layer model.

I also examined sensitivities of the phase velocity due to the S-wave velocity and thickness at different layers as shown in Figure 3.13. Figure 3.13(a) shows the phase velocity is only controlled by the S-wave velocity of the first layer at frequencies higher than 20 Hz, while the S-wave velocity and the thickness of the first layer affect the phase velocity at frequencies of about 2-20 Hz. This causes the high correlation coefficient of the first layer's S-wave velocity and thickness as depicted in Figure 3.12(a). The S-wave velocity and thickness at the second layer affect the phase velocity at frequencies of about 2-10 Hz and 2-6 Hz, as shown in Figure 3.13(b) and (c), respectively. It is shown that the phase velocity in a mid-frequency is affected by mixtures of parameters in the first, second, and third layers as portrayed in Figure 3.13(b) to (d). Furthermore, the S-wave velocity of the third layer controls the phase velocity at frequencies less than 3 Hz as depicted in Figure 3.13(e).

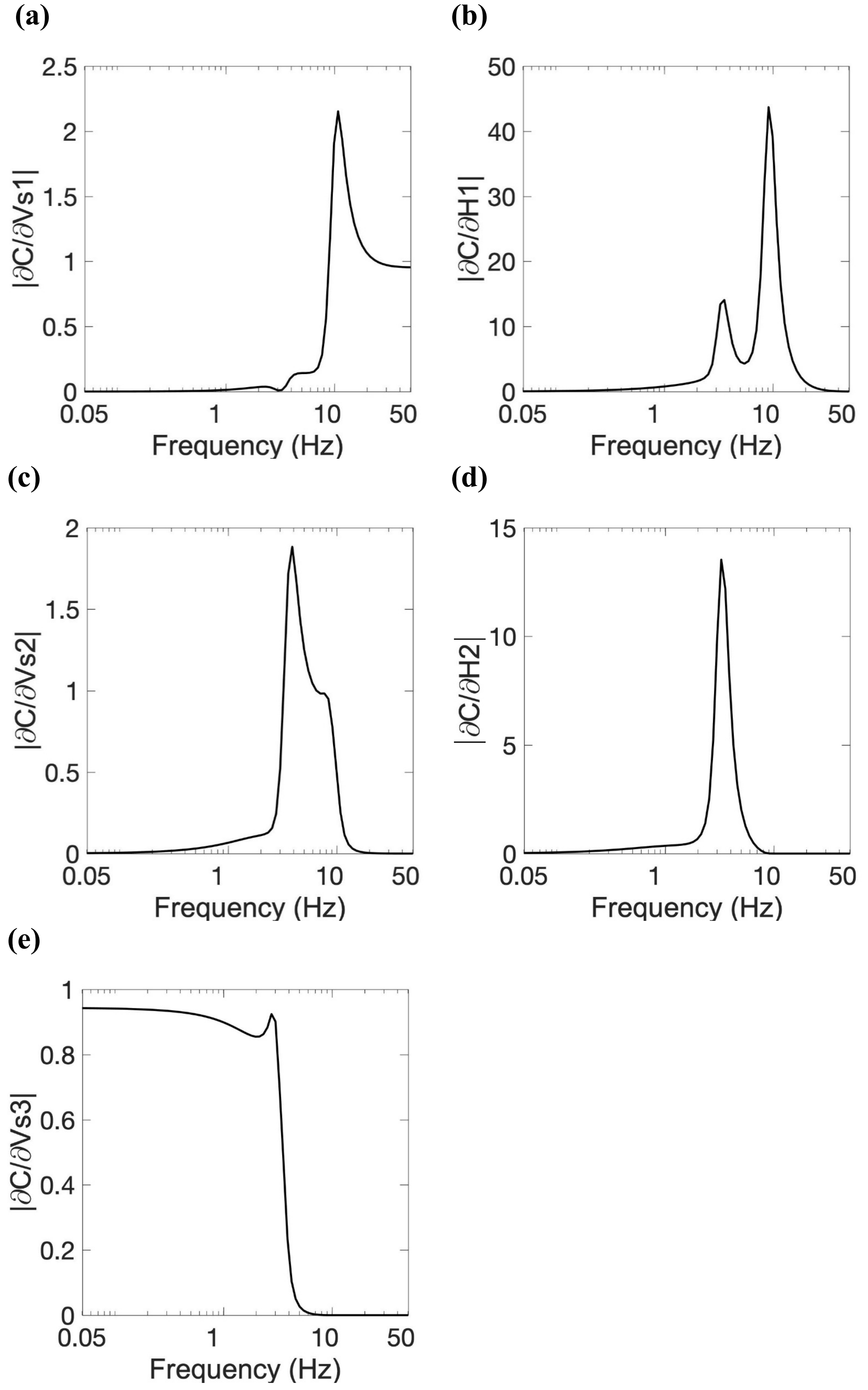

Figure 3.13 Sensitivity tests of a phase velocity to S-wave velocity ($\frac{\partial C}{\partial Vs_i}$) and thickness ($\frac{\partial C}{\partial H_i}$) at the *i*-layer in three-layer model. The phase velocity (*C*) to (a) S-wave velocity (*Vs*1), (b) thickness (*H*1) at the first layer. The phase velocity (*C*) to (c) S-wave velocity (*Vs*2) and (d) thickness (*H*2) at the second layer. The phase velocity (*C*) to (c) S-wave velocity (*Vs*3) at third layer. $\Delta Vs1$, $\Delta H1$, $\Delta Vs2$, $\Delta H2$, and $\Delta Vs3$ are given 10% of their corresponding parameters.

3.6 Given thickness to avoid trade-off-relationship between parameters

Either *Vs* or *H* can be given in advance during the MCMC inversion to improve resolutions of model parameters by avoiding the trade-off-relationship. Here, I gave the value of thickness at the first layer in the two-layer model to enhance the resolutions of the S-wave velocities. During surface wave measurement at a site interest, the measurement site may be close to a borehole. It is common that information of borehole thickness are used for the surface wave inversion to improve the resolutions of S-wave velocities.

Figure 3.14 shows a comparison between the distributions of S-wave velocities in the inversion with and without thickness constraint in the two-layer model. Figure 3.14(a) shows that the given thickness slightly reduces uncertainty in the S-wave velocity of the first layer regardless of dependency decreasing of the S-wave velocity to the first layer's thickness. It is caused by the phase velocity of the two-layer model in frequencies higher than 3 Hz, is mostly sensitive to the S-wave velocity at the first layer, as depicted in Figure 3.8(a) and (b). Meanwhile, the distribution of the S-wave velocity at the second layer is similar for the given and unknown thicknesses, since a weak correlation between the thickness at the first layer and the S-wave velocity at the second layers.

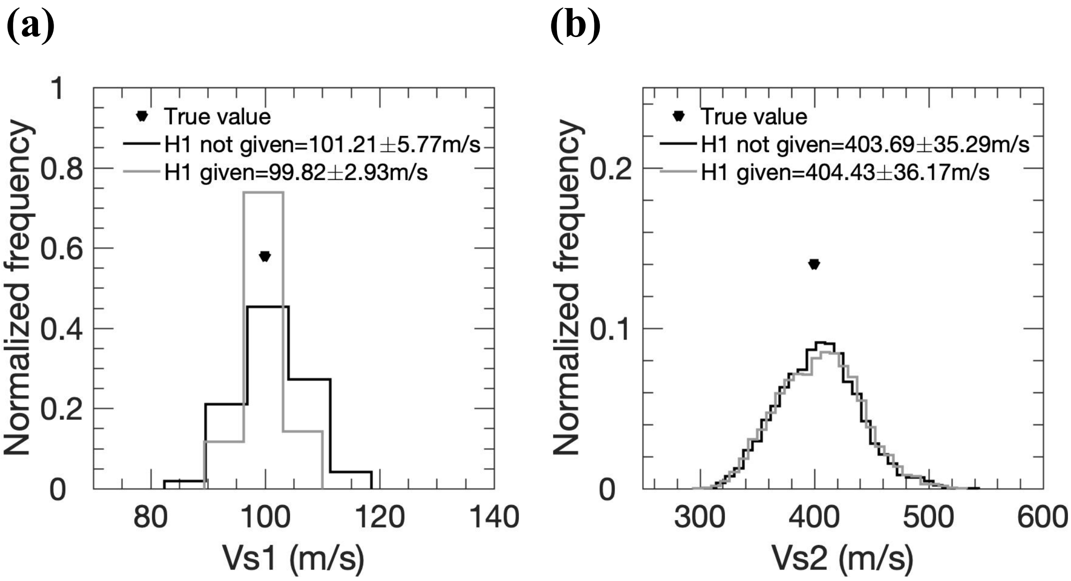

Figure 3.14 Comparison between distributions of model parameters from given (given *H*) and varied (varied *H*) thicknesses for the two-layer model. S-wave velocities at (a) the first and (b) second layers.

Furthermore, I also compared the distributions of the S-wave velocities of given and unknown thicknesses, for the three-layer models as depicted in Figure 3.15. The figure shows the distributions of the S-wave velocities of the first and second layers from the given thicknesses, have higher resolutions than those of the unknown thicknesses. It is caused by the high correlation coefficient of the S-wave velocity and the thickness of the first layer. Moreover, the moderate correlation coefficient of the S-wave velocity and the thickness of the second layer. However, the distribution of the S-wave velocity at the third layer from known thicknesses is similar to that of the unknown thicknesses due to the weak correlation coefficient of the S-wave velocity of the third layer and the thickness of the first or the second layer.

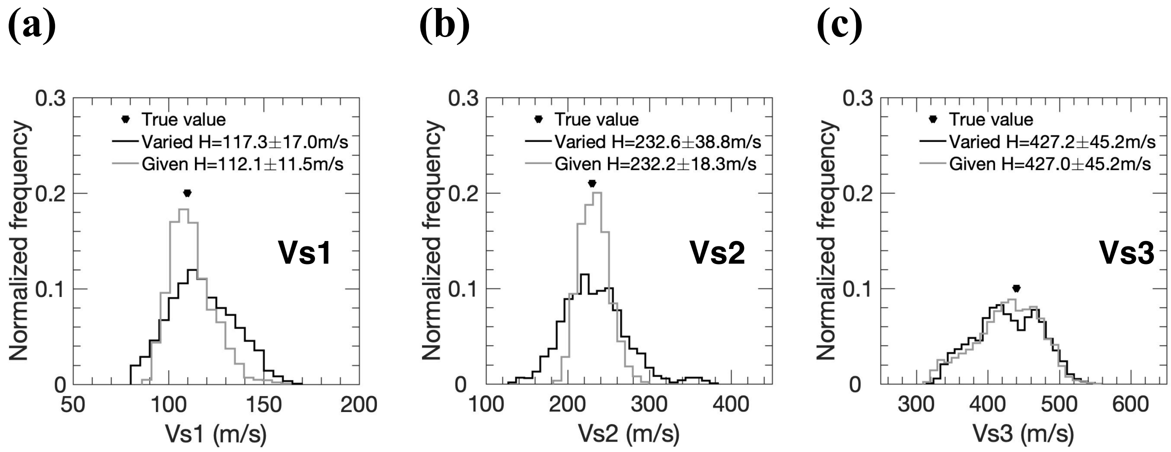

Figure 3.15 Comparison between distributions of model parameters from given (given *H*) and varied (varied *H*) thicknesses. Distributions of S-wave velocities of (a) the first, (b) the second, and (c) the third layers.

As indicated in the results in the two- and three-layer models, I could improve the resolutions of the S-wave velocity by giving information of the thickness if the S-wave velocity has a moderate/strong trade-off relationship with the thickness. Otherwise, the resolution of the S-wave velocity from the given thickness is similar to that of unknown thickness.

3.7 Effects of phase velocity at limited frequencies and different observational errors of phase velocities on uncertainties of S-wave velocity models

3.7.1 Phase velocity at limited frequencies

I here try to find out the effect of an absence of a phase velocity coverage in a low or high frequency range on uncertainties of model parameters. These difficulties are often encountered during practical microtremor measurements. The phase velocity at frequencies of 0.5 to 20 Hz in Figure 3.1(b) contains sufficient coverage for the two-layer model. I deleted some of the phase velocities to make new data that are limited in a low frequency range of 1.5 to 20 Hz or a high frequency range of 0.5 to 2.5 Hz as portrayed in Figure 3.16(a) and (b), respectively. Then, I conducted a similar sampling for the new data.

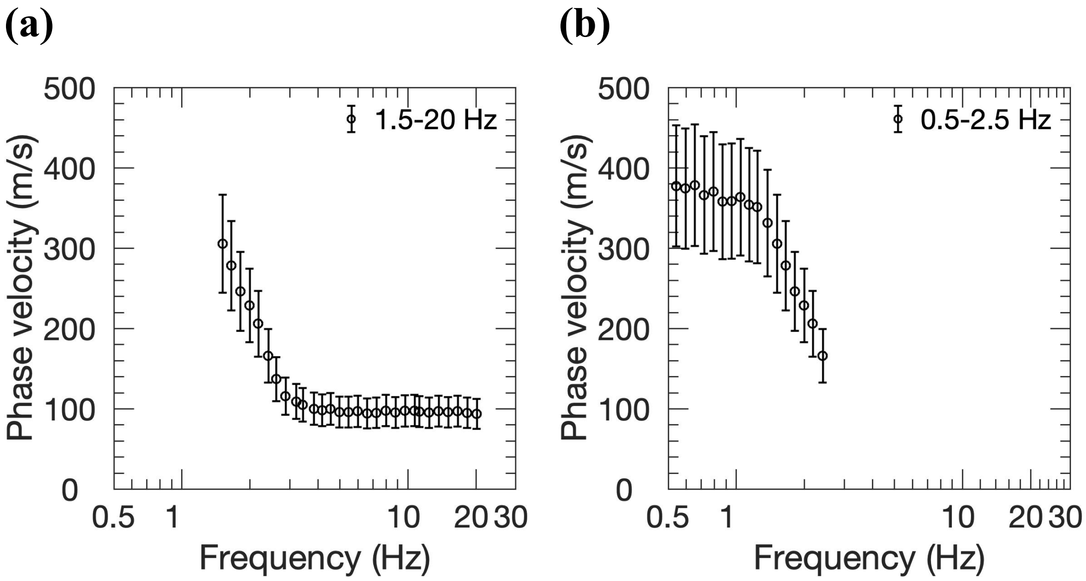

Figure 3.16 Absence of phase velocities in (a) low and (b) high frequency range from phase velocity in Figure 3.1(b).

In comparison to the phase velocity with enough information, the lack of the phase velocity at the high frequency range makes the distribution of the S-wave velocity and the thickness of the first layer wider as shown in Figure 3.17(a) and (b), respectively. Their averages shift into the higher values than those of the complete phase velocity as described in Figure 3.17(d), while fewer effects are seen in the distribution of the S-wave velocity of the second layer as presented in Figure 3.17(c) as well as its average as indicated in Figure 3.17(d). Effects of the absence of the phase velocity in the low frequency range are also shown in the figure. The distribution of the S-wave velocity of the second layer is wider as compared to that of the sufficient phase velocity as reported in Figure 3.17(c) and its average shifts into high value as stated in Figure 3.17(d). However, slight effects on the distributions of the S-wave velocity and the thickness of the first layer are identified in Figure 3.17(a) and (b). Moreover, its averages are also similar to those of the phase velocity with sufficient information as shown in Figure 3.17(d). Moreover, a non-symmetrical distribution of the S-wave velocity at the second layer as depicted in Figure 3.17(c) is caused by the incompleteness of the phase velocity at frequencies less than 1.5 Hz is shown in Figure 3.16(a).

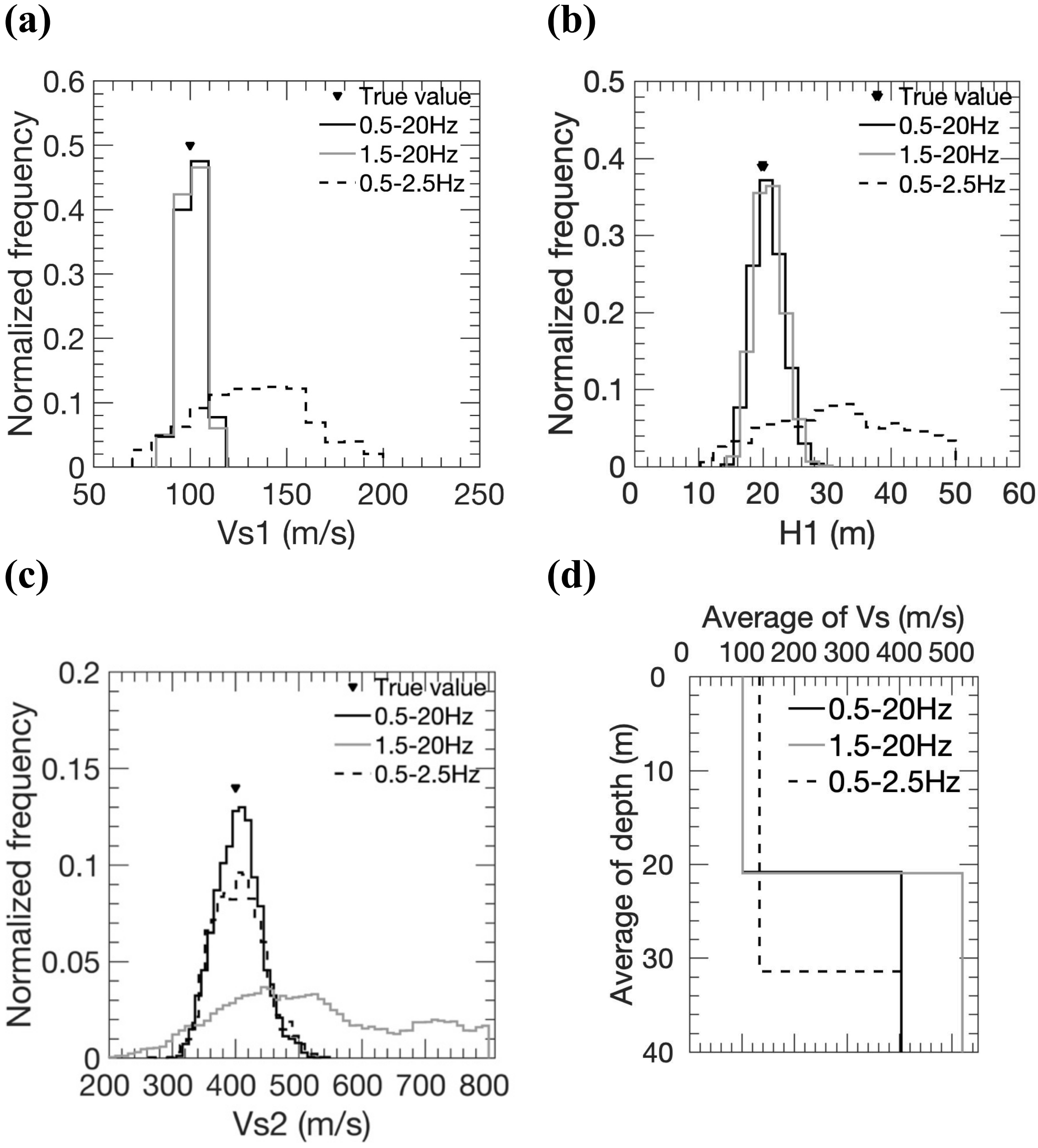

Figure 3.17 Phase velocity limited at low (gray) or high frequency range (broken black line) in the two-layer model. Comparison of distributions of (a) *Vs*1, (b) *H*1, and (c) *Vs*2. (d) Comparison of final inverted models. Black line shows the phase velocity with enough information. The triangle shows the true value of models.

3.7.2 Different observational errors of phase velocities

In this part, I discuss the effects of different standard deviations in the phase velocities on the uncertainty in the model parameters. First, I assumed synthetic observed phase velocities with variation coefficients of 5 to 40% of the true value in the two-layer model, as shown in

Figure 3.1(a). I made the phase velocities in a similar manner to that explained in the previous section. Then, similar samplings were conducted for synthetic data with different standard deviations.

Figure 3.18 shows the relationship between the variation coefficients of the observed phase velocities and variation coefficients of the model parameters. The uncertainties of the model parameters are linearly related to the accuracy of the phase velocities. The variation coefficient of the thickness of the first layer is significantly affected by the observational errors, while the S-wave velocity of the first layer is not so influenced. The model parameters with the variations of less than 10% can be obtained for the observational errors of less than 20%.

Furthermore, I also determined the average S-wave velocity for the upper 30 m ($AVS30$) from the sampled model parameters using the following Equation

$$AVS30 = \frac{30}{\sum_{i}^{n} \frac{H_i}{Vs_i}}. \qquad 3.3$$

These $AVS30$s are indicated in Figure 3.18, the $AVS30$ is also linearly correlated to the observational error. The figure also indicates the observational error has less effect on $AVS30$ as compared to H_1 and Vs_2 because $\frac{H_i}{Vs_i}$ maybe more important than H_i and Vs_i itself. It is also presented that the variation coefficients of the $AVS30$ is similar to those of $Vs1$. The uncertainty in the $Vs1$ may mostly control the uncertainty in the $AVS30$.

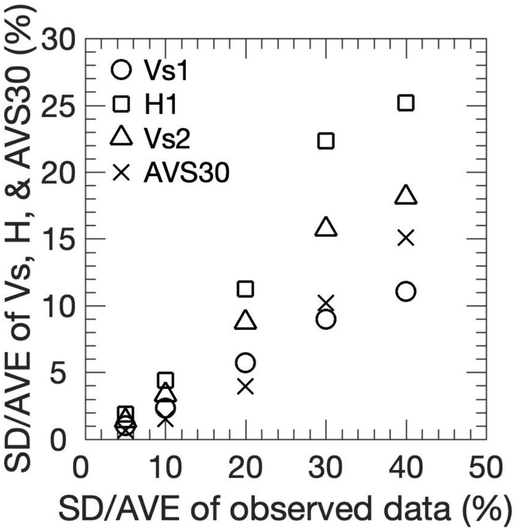

Figure 3.18 Relationship of standard deviations of synthetic observed data and variation coefficients of model parameters and *AVS*30 in the two-layer model.

Furthermore, I calculated similar samplings to the synthetic data with different standard deviations by giving information about thickness during the inversion. The variation coefficient of *Vs*1 from known *H*1 has a lower value than that of *Vs*1 from unconstrained *H*1 as shown in Figure 3.19, particularly for error higher than 20%. However, the variation coefficient of the *Vs*2 from the known *H*1 is similar to that of *Vs*2 from the unknown *H*1 for errors of 5-40%. It is caused by a weak correlation of the *H*1 and the *Vs*2 as I discussed before. These results indicate that the reduction of the uncertainty in the S-wave velocity by giving information of the thickness is not only related to observational errors of the phase velocities but also the trade-off-relationship between the thickness and the S-wave velocity at a certain layer.

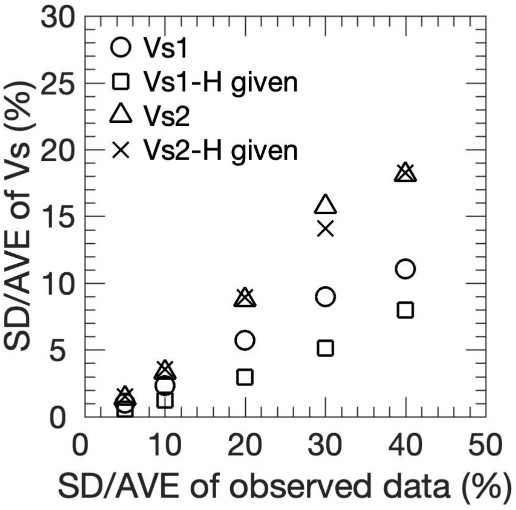

Figure 3.19 Comparison between model parameters from the MCMC inversion in cases of thickness information is not given and given in the two-layer model.

3.8 Effect of frequency-dependent error of phase velocity on uncertainty of sampling parameters

In the previous section, I have already discussed the phase velocity which has a constant error of 20% for each frequency (Case 1 in the following) as depicted in Figure 3.1(b). In this section, I examined the effect of the error of the phase velocity which depends on frequency as shown in Figure 3.20. A phase velocity with errors of 50-20% (Case 2 in the following) from low to high frequency ranges as shown in Figure 3.20(a). Furthermore, a phase velocity with errors of 20-50% (Case 3 in the following) in low to high frequency ranges is depicted in Figure 3.20(b). The errors for Cases 2 and 3 are assumed to be linearly reduce and increase as the increment of frequencies, respectively, as portrayed in Figure 3.20(c). We may face these three types of phase velocity during microtremor explorations. Here, I also conducted the MCMC sampling for Cases 2 and 3.

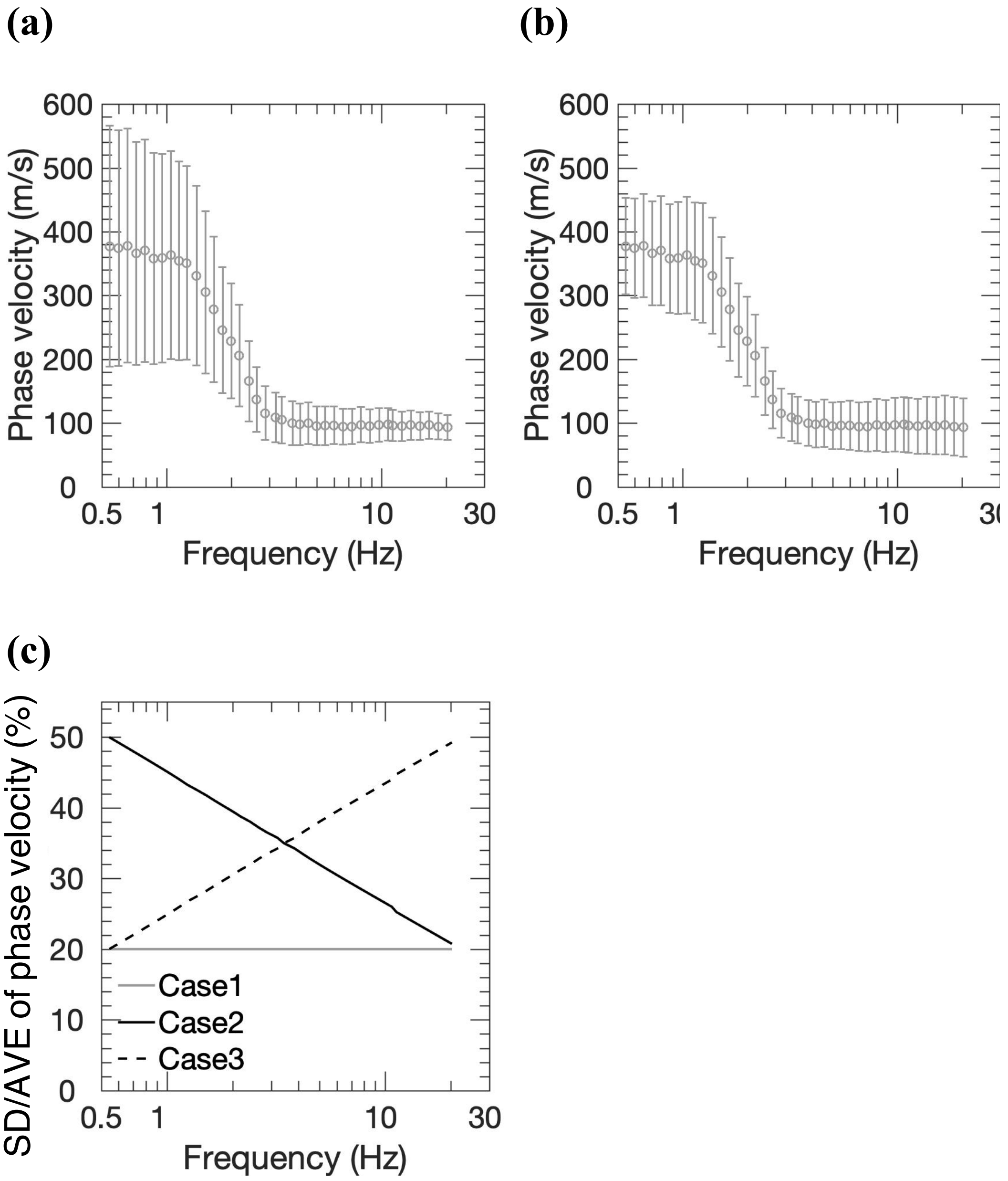

Figure 3.20 Frequency dependent error of phase velocity. Errors of phase velocities of (a) 50-20% and (b) 20-50%. (c) Given errors for different cases.

Figure 3.21 indicates distributions of model parameters for Cases 1, 2, and 3. The distribution of *Vs*1 of Case 2 has similar wide than that of Cases 1, while the distribution of *Vs*1 of Case 3 is wider than those of Cases 1 and 2 as depicted in Figure 3.21(a). However, the distributions of *H*1 from Cases 2 and 3 have wider distributions than that of Case 1 as depicted in Figure 3.21(b), because the error of the phase velocity in mid frequency range for Cases 2 and 3 are higher than that of Case 1 (Figure 3.20(c)). As previously mentioned, the phase velocity of the two-layer model in mid frequency ranges is controlled by $H1$, as shown in Figure 3.8(b). Furthermore, the distribution of $Vs2$ for Case 3 is similar to that of Case 1 while the distribution of $Vs2$ for Case 2 is wider than those of Cases 1 and 3. It is caused by the error of the phase velocity for Case 2 in low frequency ranges is higher than those of Cases 1 and 2. Moreover, non-symmetrical distributions of $H1$ of Cases 2 and 3 in Figure 3.21(b) are generated by their wide standard deviations of the phase velocities in the high frequency range as depicted in Figure 3.20(a) and (b). Additionally, a wide standard deviation in low frequency ranges of Case 2 also affects a non-symmetrical distribution of $Vs2$ as depicted in Figure 3.21(c). The inverted Vs profile for different cases can be found in Figure 3.21(d). The figure indicates average of $Vs1$ is similar while there are differences in average of $H1$ for each case. Furthermore, there are slight differences in average of $Vs2$ for each case.

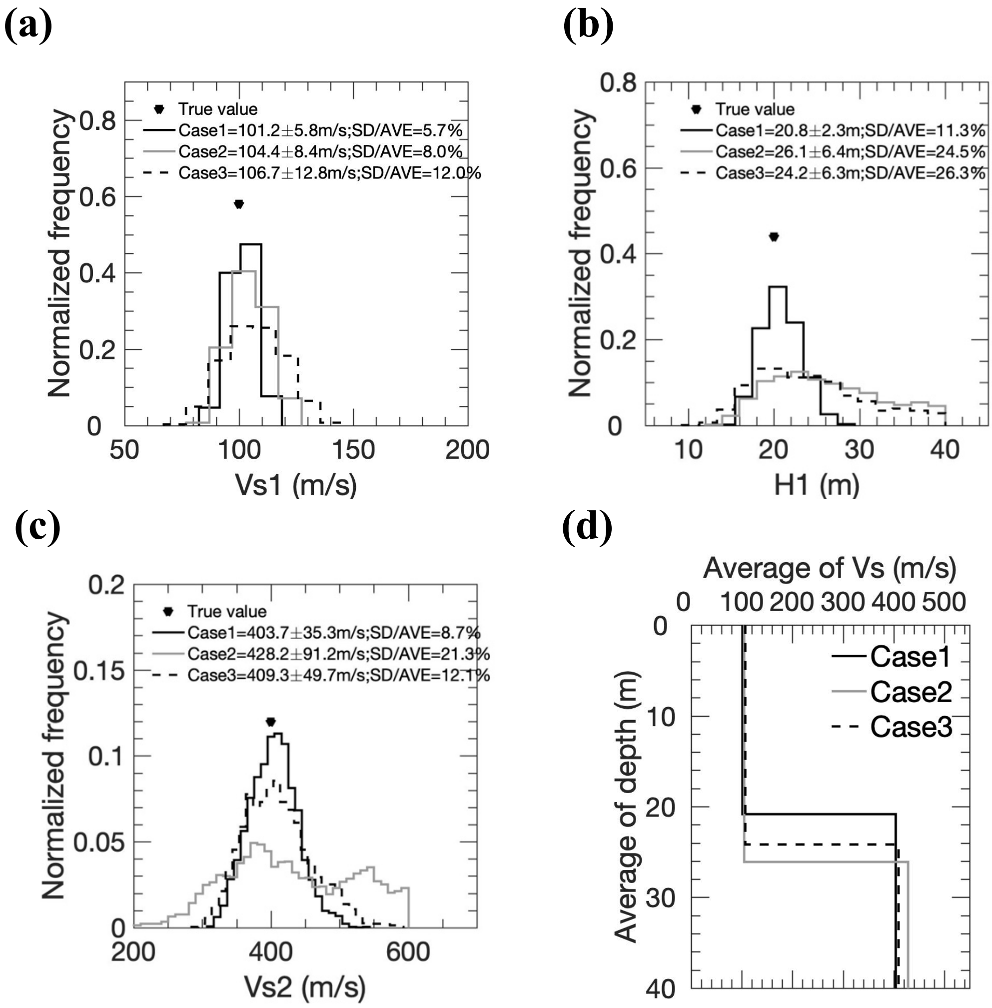

Figure 3.21 Comparison between Cases 1, 2, and 3 for (a) *Vs*1, (b), *H*1, and (c) *Vs*2. (d) comparison of final inverted models.

3.9 Summary

I have conducted numerical experiments to estimate uncertainty in an S-wave velocity profile from observational errors of phase velocity of the two- and three-layer models of shallow soil using the Markov-chain Monte Carlo (MCMC) inversion. First, I have shown the advantage of multiple chains over a single chain in the MCMC sampling. Regardless of the time calculation of the multiple chains is more costly than that of a single chain, the multiple chains could find the stationary state of sampled models faster than that of a single chain. I showed the high applicability of the MCMC method in assessing the uncertainties in the S-wave velocity and the thickness. The final inverted models and calculated phase velocity and their corresponding uncertainties portray well the true S-wave velocity profiles and phase velocities, respectively. I also showed that the sampled models can be used to estimate the trade-off-relationship between the model parameters. The trade-off-relationship indicates that the uncertainty in one parameter might be affected by other parameters. Furthermore, the resolution of S-wave velocity can be improved by giving information of thickness if the S-wave velocity and the thickness have a moderate/strong relationship.

Furthermore, I showed that the absence of the phase velocity at the high frequency increases the uncertainty in the S-wave velocity and thickness at top layer while the lack of phase velocity at the low frequency rises the uncertainty in the S-wave velocity in the half-space. Moreover, I also presented that observational errors are linearly related to the resolutions of S-wave velocity and thickness. Furthermore, the results of the given thickness for different observational errors and the frequency-dependent errors of the phase velocity indicated that uncertainty in the S-wave velocity profile is strongly related to the observational errors in the phase velocity.

Chapter 4 Estimation of variability of soil amplification

4.1 Objective

4.2 Generation of synthetic motion

4.3 Amplification for two-layer model

4.4 Amplification for three-layer model

4.5 Effects of incompleteness and different observational errors of phase velocity on variability of soil amplification

4.6 Effects of frequency-dependent errors of phase velocities on nonlinear soil amplification variability

4.7 Effects of characteristics of input motions on variability of soil amplification

4.8 Comparison with the previous studies

4.9 Summary

4.1 Objective

In this chapter, I examine sampled models from the MCMC method in Chapter 3 for estimation of variability of 1D linear and nonlinear amplifications. In this numerical experiment, I used a conventional equivalent linear technique (SHAKE91) to approximate a nonlinear soil response. Different variability of linear and nonlinear amplifications is explained using the sampled models in this chapter. I also present the variability in soil responses from sampled models of the incompleteness of phase velocity and different observational errors. Likewise, I depict effects of PGAs and phase angles of input motions to variability of nonlinear soil responses. Furthermore, I also compare my results with previous studies.

4.2 Generation of synthetic motion

I prepared a synthetic input motion to estimate responses of the soil models. I generated an acceleration wave within a frequency range of 0.1 to 10 Hz on the surface of engineering bedrock based on safety limit of spectral acceleration of Japanese building code (the Notification No. 1461 of the Ministry of Construction, Japan, May 31, 2000) in Figure 4.1(a). The synthetic wave has random phases with a PGA of 336 cm/s^2 as presented in Figure 4.1(b). Since I used the conventional equivalent linear method in my nonlinear analysis, this PGA might be too large for my soil models and the nonlinear amplification might have significant over-damping effect at a high frequency (Hartzell et al., 2004; Yoshida et al., 2002) as explained before. Therefore, by normalizing the synthetic motion with PGA of 200 cm/s^2, I made a new input motion with a PGA of 200 cm/s^2 as shown in Figure 4.1(b) and its spectral acceleration can be seen in Figure 4.1(a) as well.

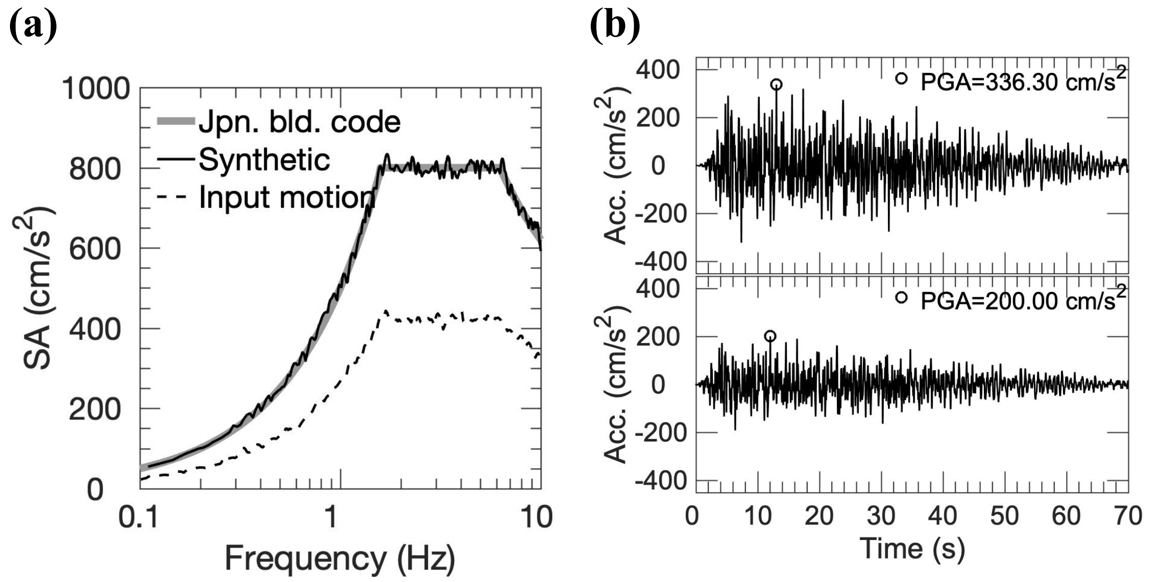

Figure 4.1. Response spectra and wave motion on the surface of engineering bedrock. (a) Response spectra of Japanese building code, synthetic, and input motion. (b) Synthetic and input motions with PGAs of 336 and 200 cm/s^2, respectively.

I assumed that the first layer of the two-layer model is a clay layer. Moreover, the first and the second layers of three-layer model are given as clay layer. Shear modulus and damping factor of the clay layer used in the estimation of the amplification were obtained from Figure 4.2. I used the shear modulus and the damping factor curves from studies by Sun et al. (1988) and Idriss (1990), respectively. The linear soil amplification was calculated by assuming the damping factor and the shear modulus at the lowest shear strain level. On the other hand, the shear modulus and the damping factor in the nonlinear amplification were determined using an iterative procedure for each layer so as to be consistent with the level of effective shear strain obtained in the layer (Schnabel et al., 1972). The effective shear strain was assumed to be 65% of the maximum shear strain. Moreover, the shear modulus and the damping factor of engineering bedrocks of the models were assumed at the lowest strain level.

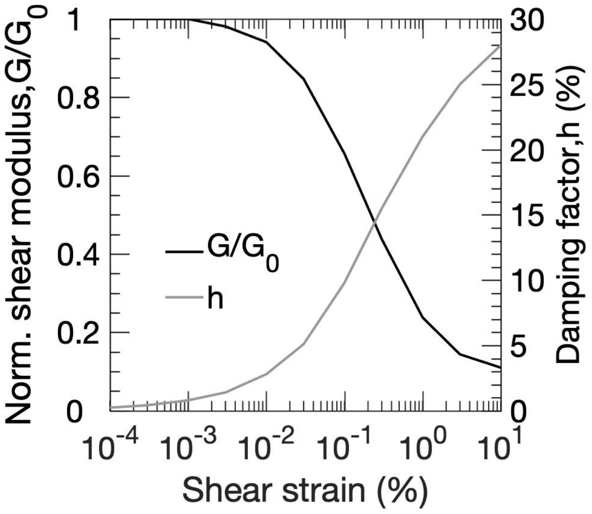

Figure 4.2. Normalized shear modulus (G/G_0) and damping factor (h) of clay.

4.3 Amplification for two-layer model

4.3.1 Estimation of amplification and spectral acceleration

After I have estimated the uncertainty of the parameters for the inverted S-wave velocity profiles in the two-layer model, the variation of the amplification can also be numerically obtained for the sampled models using the SHAKE91 code. Figure 4.3(a) shows a comparison of the linear and nonlinear amplifications for the sampled models. I expressed the average of the amplification factors and its uncertainties in the figure. In the averages of the linear responses, the maximum amplitude is about 4.0 at the fundamental frequency of about 1.2 Hz. The variation of the linear amplification is greater at a frequency range of about 3 to 10 Hz than those at frequencies lower than 3 Hz because of averaging of fluctuation of higher mode peaks that are different in the models. In term of the nonlinear response, I can observe a common phenomenon showing the reduction of the maximum amplitude of about 2.7 with a significant decrease in the peak amplitudes at frequencies greater than 1 Hz. Moreover, its fundamental frequency shifts into a lower value of about 0.9 Hz than that of the linear response. Moreover, I also notice the flat spectral amplitudes at frequencies greater than 3 Hz. Furthermore, SD/AVEs of the amplification of the nonlinear response are lower than that of the linear amplification after frequencies of about higher than 1 Hz, as depicted in Figure 4.3(b).

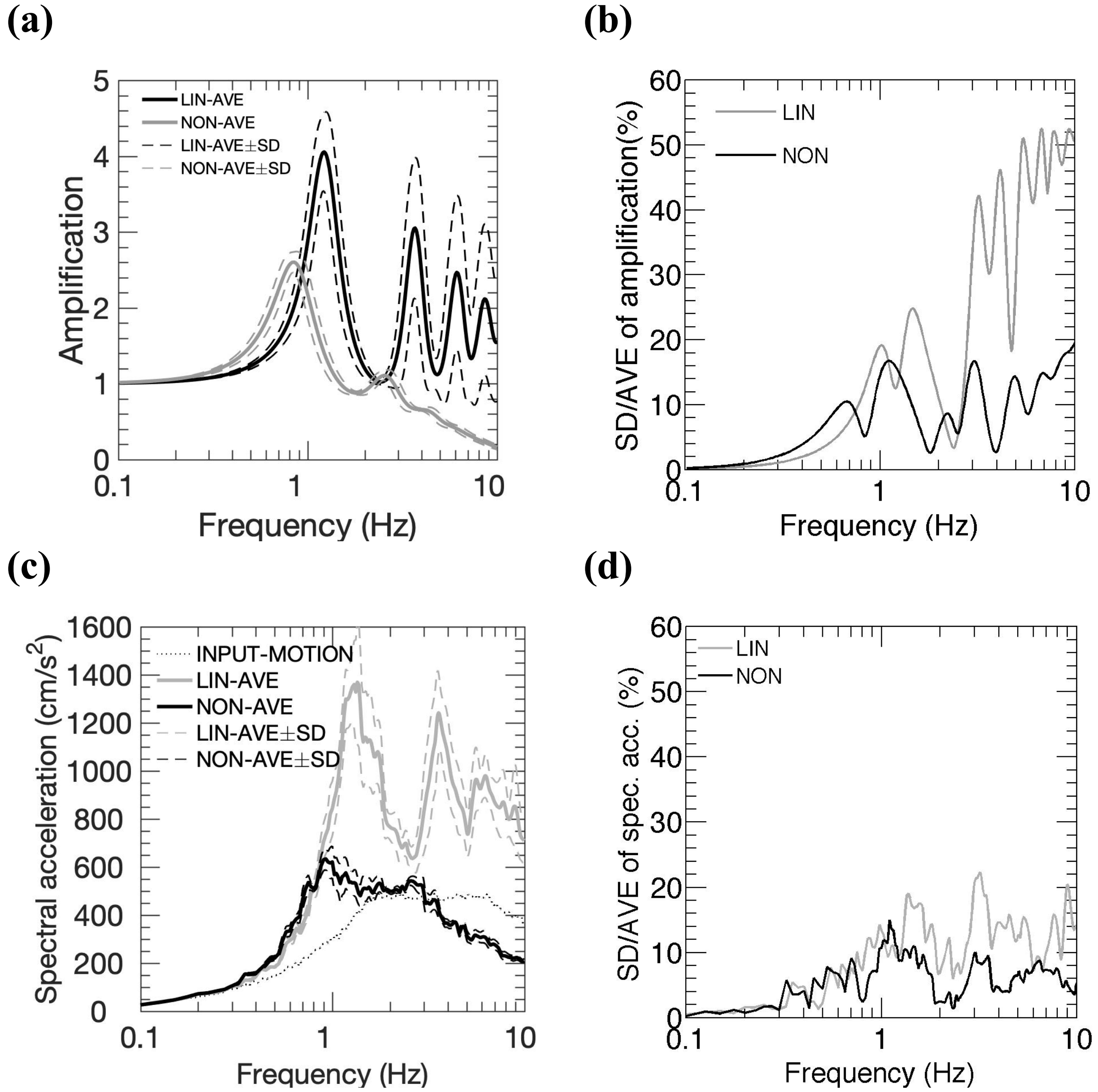

Figure 4.3. Comparisons of linear (LIN) with nonlinear (NON) cases in the two-layer model. (a) Amplifications and (b) their SD/AVEs. (c) Spectral accelerations (spectral damping of 5%) and (d) their SD/AVEs.

I, furthermore, estimated response spectra with a damping ratio of 5% for the input motion and the estimated surface motions as shown in Figure 4.3(c). The differences of the amplification control the variation of the response spectra because I used the same input motion for the sampled models. The average of the peak amplitudes in the nonlinear case is significantly smaller than that of the linear case, especially at frequencies greater than 1 Hz. Moreover, the peak of the fundamental model of the spectra in the nonlinear case also shifts into the lower frequencies at a frequency range of about 0.9 as compared with that of the linear spectral acceleration of about 1.4. Figure 4.3(d) shows SD/AVEs of the spectral acceleration of the nonlinear response are smaller than that of the linear amplification after frequencies of about higher than 1 Hz.

The differences of the spectral characteristics and variability in linear and nonlinear responses are caused by the different use of shear modulus and damping factor as presented in Figure 4.4. An effective strain level average of the nonlinear response is 0.17% for the two-layer model using SHAKE91 as shown in Figure 4.4(a). It is indicated that the strain level is lower than the upper limit of the strain level (0.3%) of SHAKE91 applicability for a nonlinear amplification analysis. Figure 4.4(a) also shows that variation of effective shear strain in the nonlinear analysis depends on the difference of the *Vs* profile. Hence, normalized shear modulus and damping of the nonlinear case are also varied based on the variation of the *Vs* profile, while the normalized shear modulus (G/G_0=1) and damping (h=0.2%) in linear response are given in advance as shown in Figure 4.4(b) and (c), respectively. The nonlinear response has normalized shear modulus reduction of about 52% in average. The reduction of the shear modulus in the first layer means the reduction of shear wave velocity in the first layer, as indicated in Figure 4.4(d), from $V_S = \sqrt{G/\rho}$. However, the widths of the distributions of the S-wave velocity at the first layer in the linear and nonlinear responses are similar as shown in the figure. The increase of the damping factor about 13% in average for the nonlinear response reduced the peaks of the amplification as compared to those of the linear response as depicted in Figure 4.3(a).

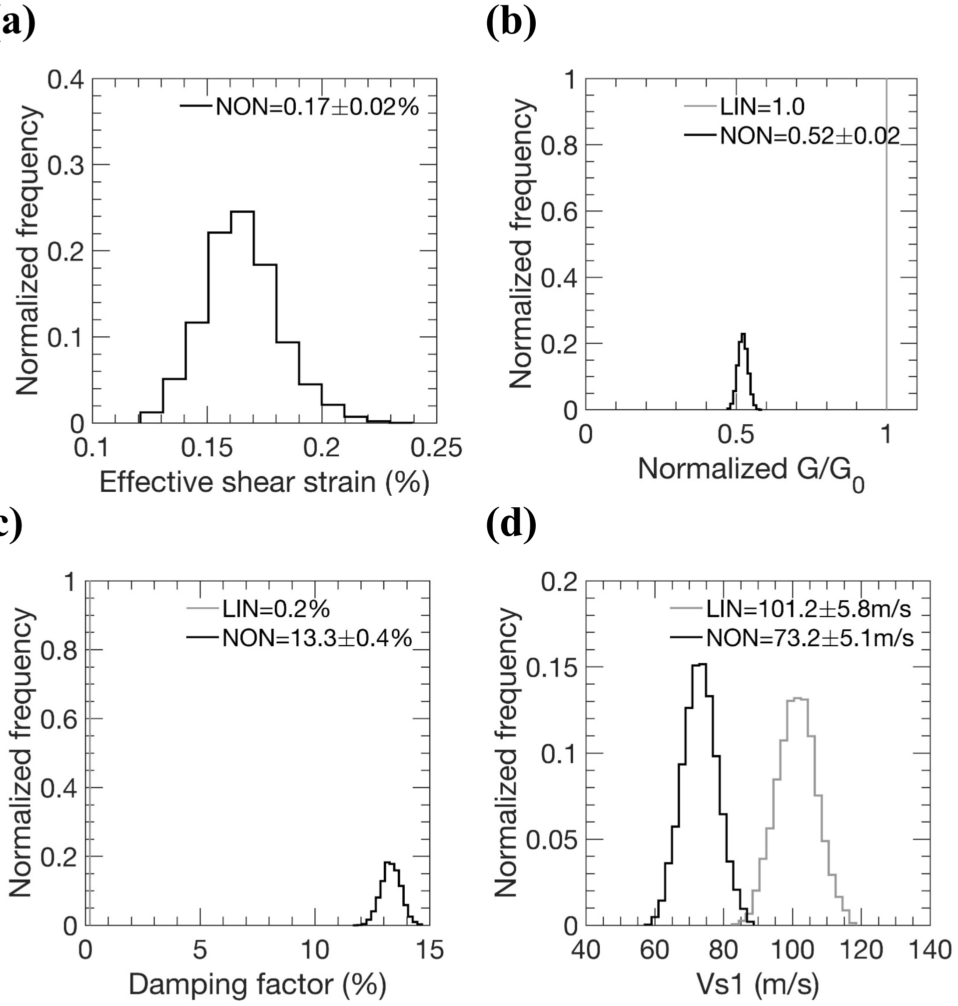

Figure 4.4 Comparison between distributions of linear (LIN) and nonlinear (NON) cases in two-layer model. (a) Effective shear strain, (b) Normalized shear modulus, (c) damping factor, and (d) S-wave velocity at the first layer.

4.3.2 Distribution of ground motion proxy

Figure 4.5 shows the distributions of ground motion proxies (e.g. fundamental frequency, maximum amplification, PGA, and PGV) of the estimated surface motion for the linear and the nonlinear cases. The final model has very similar proxies to the true values as shown in the figure. The figure indicates that all of the averages of the ground motion proxies in the nonlinear amplification have lower values than those of the linear amplification. The low value of the average of the fundamental frequencies in the nonlinear responses is caused by the reduction of the S-wave velocity in the first layer as indicated in Figure 4.4(d) while the decreases of the averages of the other ground motion proxies are affected by the increase of the damping factors in the first layer as shown in Figure 4.4(c). Most of the distributions of the ground motion proxies in the nonlinear case have narrower distributions than those of the linear case except for the fundamental frequency. The fundamental frequencies of the linear and the nonlinear cases have similar uncertainties with similar widths of the distributions as shown in Figure 4.5(a) because the distributions of the S-wave velocity at the first layer in the linear and nonlinear responses are similar, as depicted in Figure 4.4(d). Since the fundamental frequency is related to the S-wave velocity ($f_{fundamental} = {}^{V_S}\!/_{4H}$), the other ground motion proxies have narrower distributions in the nonlinear response. These results are caused by the reduction of damping factors as presented in Figure 4.4 (c).

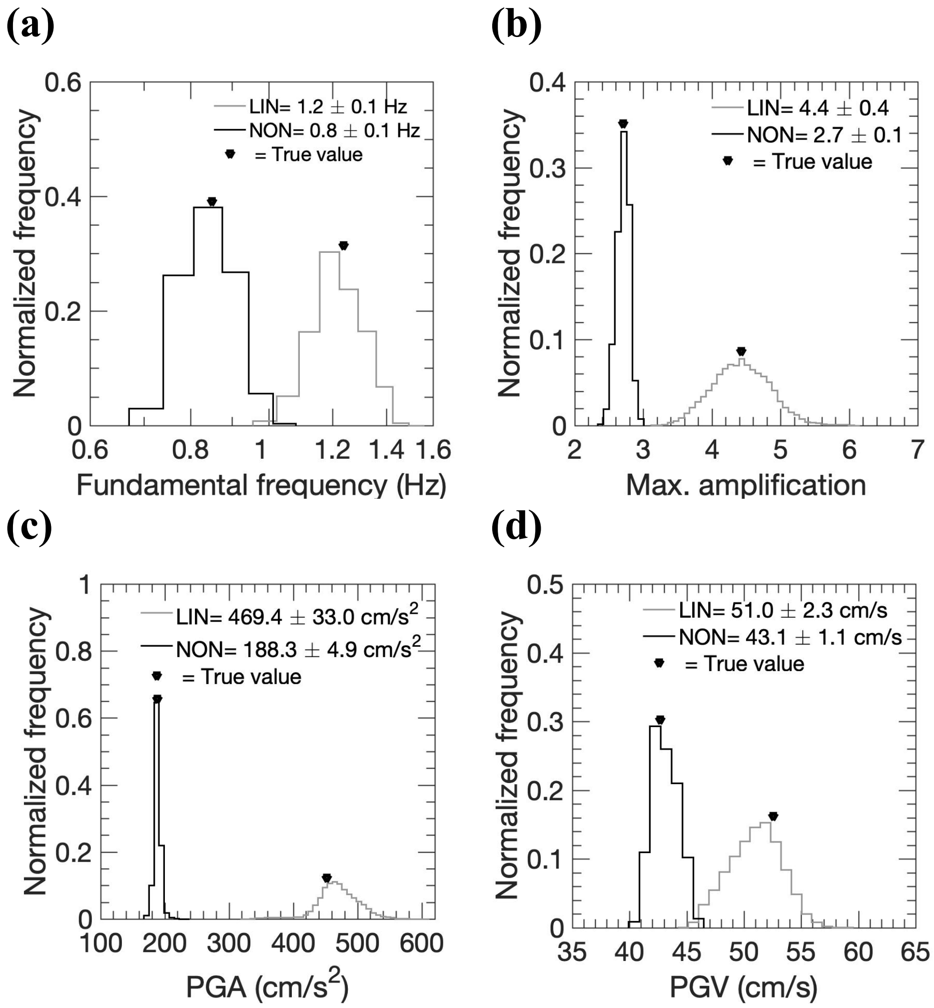

Figure 4.5 Comparison of the distributions of linear (LIN) and nonlinear (NON) cases in the two-layer model. (a) Fundamental frequency, (b) maximum amplification, (c) PGA, (d) PGV. The triangle shows true value for each parameter.

4.3.3 Effects of rigidity and damping to variability in soil amplification

In this part, I discuss more detail on effects of rigidity (shear modulus) and damping on the soil amplification. Unlike, the fundamental frequency which only depends on the rigidity while it is not affected by damping. Other ground motion proxies such as maximum amplification, PGA, and PGV are controlled by the rigidity and damping. As previously explained that the complex shear modulus (G^*) is an important parameter for estimation of soil amplification and defined as

$$G^* = G\left(1 - 2h^2 + 2ih\sqrt{1-h^2}\right) \cdot \qquad 4.1$$

Hence, this equation shows that the spectral characteristics of the amplification and other ground motions proxies, except fundamental frequency, are controlled by a combination of the rigidity (G) and damping factor (h).

Figure 4.6 shows a comparison of different rigidity and damping on the soil response. I used sampled models of the two-layer model in Figure 3.5 to estimate soil amplification variability. In the first analysis, I gave information of rigidity values of 100, 75, and 50% of G_0, while the damping factor is constant (h_0=0.2%) as depicted in Figure 4.6(a) and (b). h_0 and G_0 are the damping and rigidity at the lowest strain level. Figures indicate that the lower rigidity produces the higher peaks of the average amplification. I can also see that the fundamental frequency shifts into a lower value as a reduction of the rigidity. Moreover, the variation coefficient of amplification increase as the reduction of the rigidity is higher. In the second analysis, I changed the damping factors of 0.2, 5, and 10% with constant rigidity (G_0) as presented in Figure 4.6(c) and (d). The figures describe that the high damping factor makes the low peaks of the amplification. Furthermore, the variation coefficient is also lower as the increase of the damping. In the third evaluation, I assumed that both the rigidity and damping are varied as portrayed in Figure 4.6(e) and (f). Figure 4.6(e) shows that the higher damping is, the lower peak of amplification is. I can also see that the lower rigidity is, the lower of the fundamental frequency is. In terms of the variation coefficient of amplification, the increase of the damping and the reduction of the rigidity decrease the variation coefficient of the amplification as depicted in Figure 4.6(f). Moreover, it shows that the SD/AVE of the amplification due to reduction of the rigidity and increase of the damping have similar value to that of increase of damping with constant rigidity as shown in Figure 4.6(d) although it is different from that of reduction of rigidity with constant damping as presented in Figure 4.6(b). These results suggest that the material damping factor has more pronounced effects than material rigidity on the variability in the soil amplification due to the uncertainty in the S-wave profile from the inversion of a surface wave.

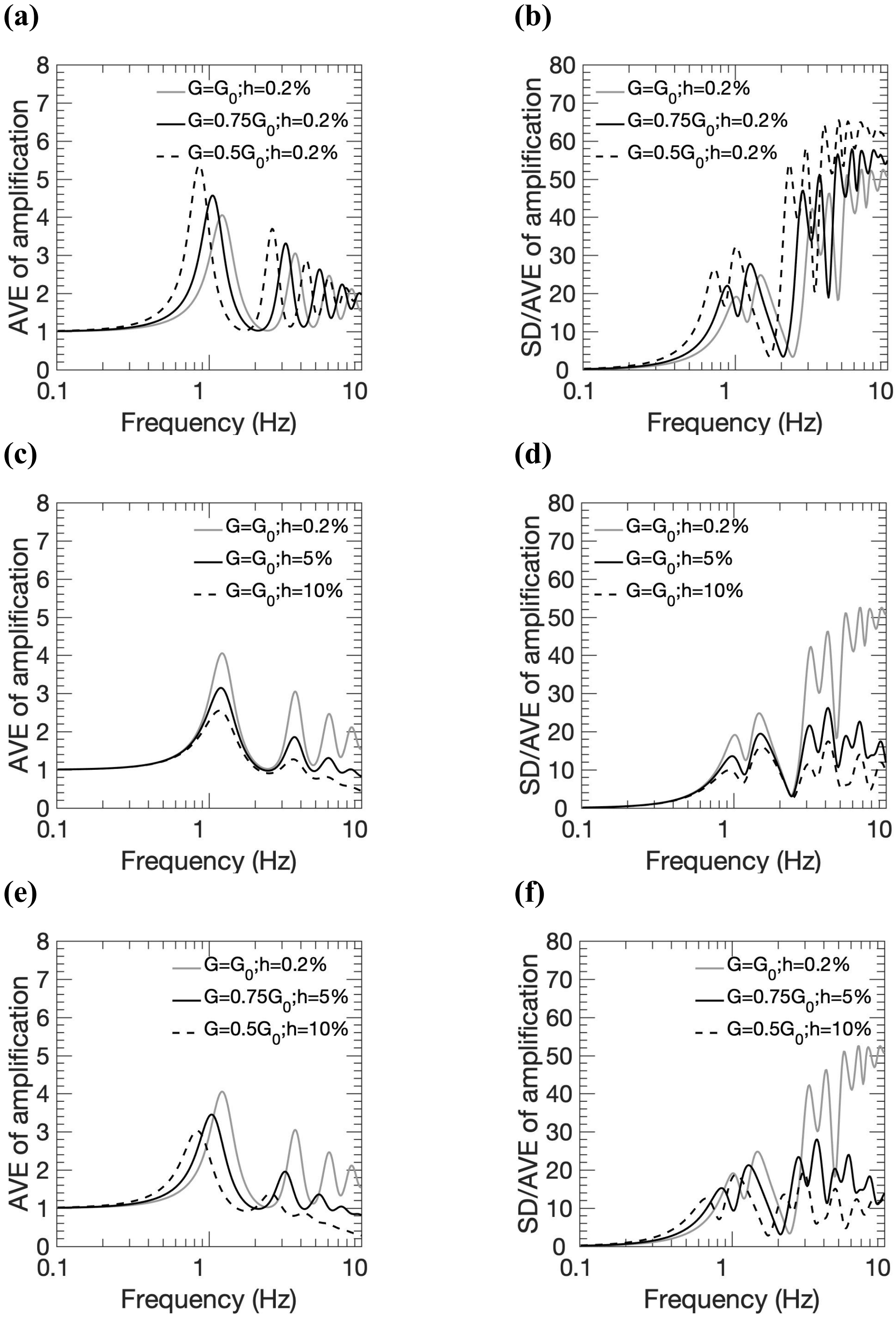

Figure 4.6 Effects of varied rigidity while constant damping on (a) average (AVE) amplification and (b) its uncertainty (SD/AVE). Effects of varied damping whereas constant rigidity on (c) average (AVE) amplification and (d) its uncertainty (SD/AVE). Effects of varied rigidity and damping on (e) average (AVE) amplification and (f) its uncertainty (SD/AVE).

4.4 Amplification for three-layer model

I also estimated soil amplification of the three-layer model as shown in Figure 4.7(a). The figure indicates that the linear and nonlinear amplifications have two peaks. The first and second peaks of the linear response are located at frequencies of about 2 and 5 Hz, respectively. Meanwhile, the first and second peak-frequencies of the nonlinear case are about 1-2 and 4 Hz, respectively. The maximum amplification of the linear case is equal to that of the second peak of the linear amplification, while the maximum amplification of the nonlinear response is the same as that of the first peak of the nonlinear amplification. It occurs due to de-amplification of the nonlinear response in high frequency range. The characteristics of spectral acceleration of the linear and nonlinear responses are similar to their corresponding amplifications, as depicted in Figure 4.7(b). SD/AVEs of the nonlinear amplification and spectral acceleration are lower than that of linear response at the frequency of about higher than 3 Hz as shown in Figure 4.7(c) and (d), respectively.

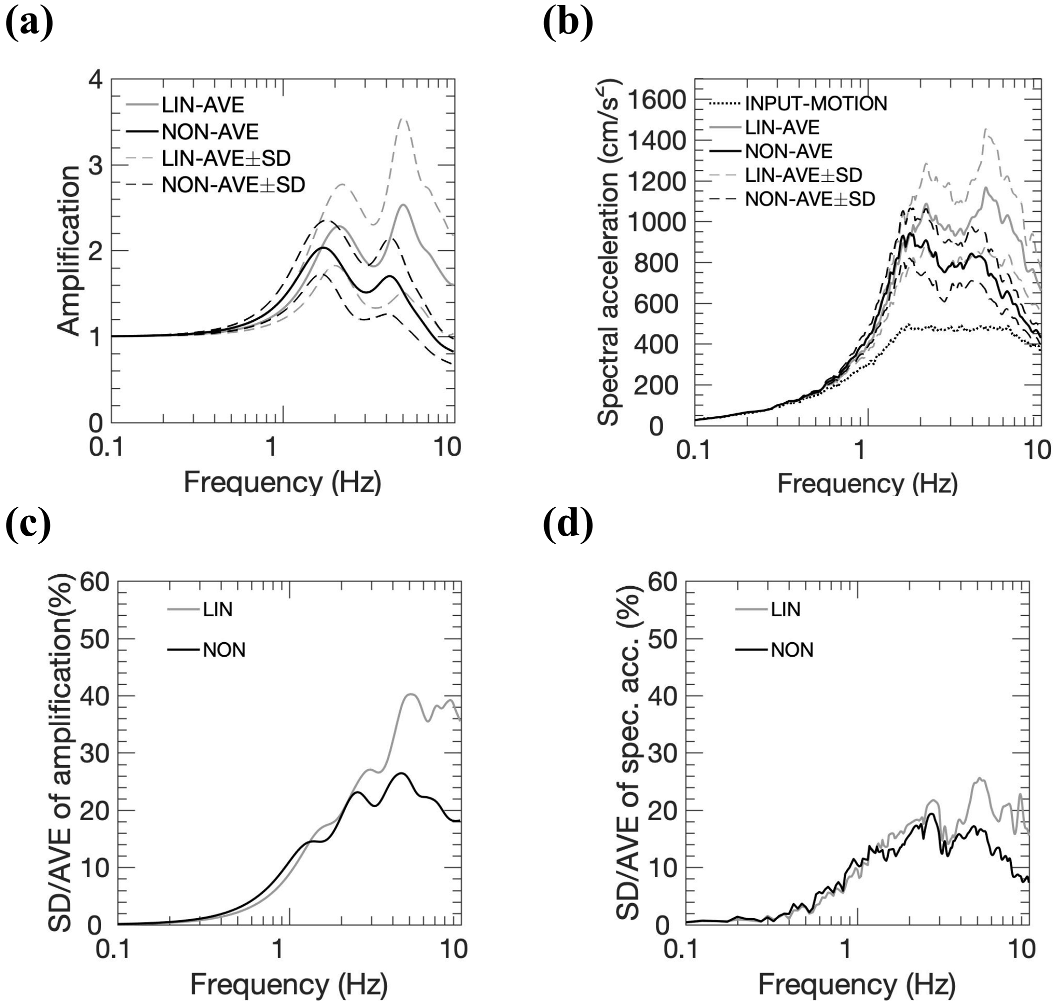

Figure 4.7 Comparisons of linear (LIN) with nonlinear (NON) cases in the three-layer model. (a) Amplifications and (b) their SD/AVEs. (c) Spectral accelerations (spectral damping of 5%) and (d) their SD/AVEs.

Figure 4.8(a) and (b) indicate the effective strain in the first and second layers have a normal distribution because the S-wave velocity and thickness at the first and second layer have also normal distribution. Moreover, the effective strain levels of the three-layer model are 0.06% and 0.05% in averages at the first and second layers, as depicted in Figures 4.8(a) and (b), respectively. It is suggested that the strain levels during the nonlinear amplification using SHAKE91 are still allowable. The comparison between the distributions of the shear moduli at the first and second layer are also presented in Figure 4.8(c) and (d), respectively. The reductions of the shear moduli of the nonlinear case are about 25 and 21% on averages at the first and second layer, respectively, although their distributions are similar to each other for each case. Figure 4.8(e) and (f) show that the damping factors the nonlinear case is different for each model corresponding to the effective strain as similar to the two-layer model.

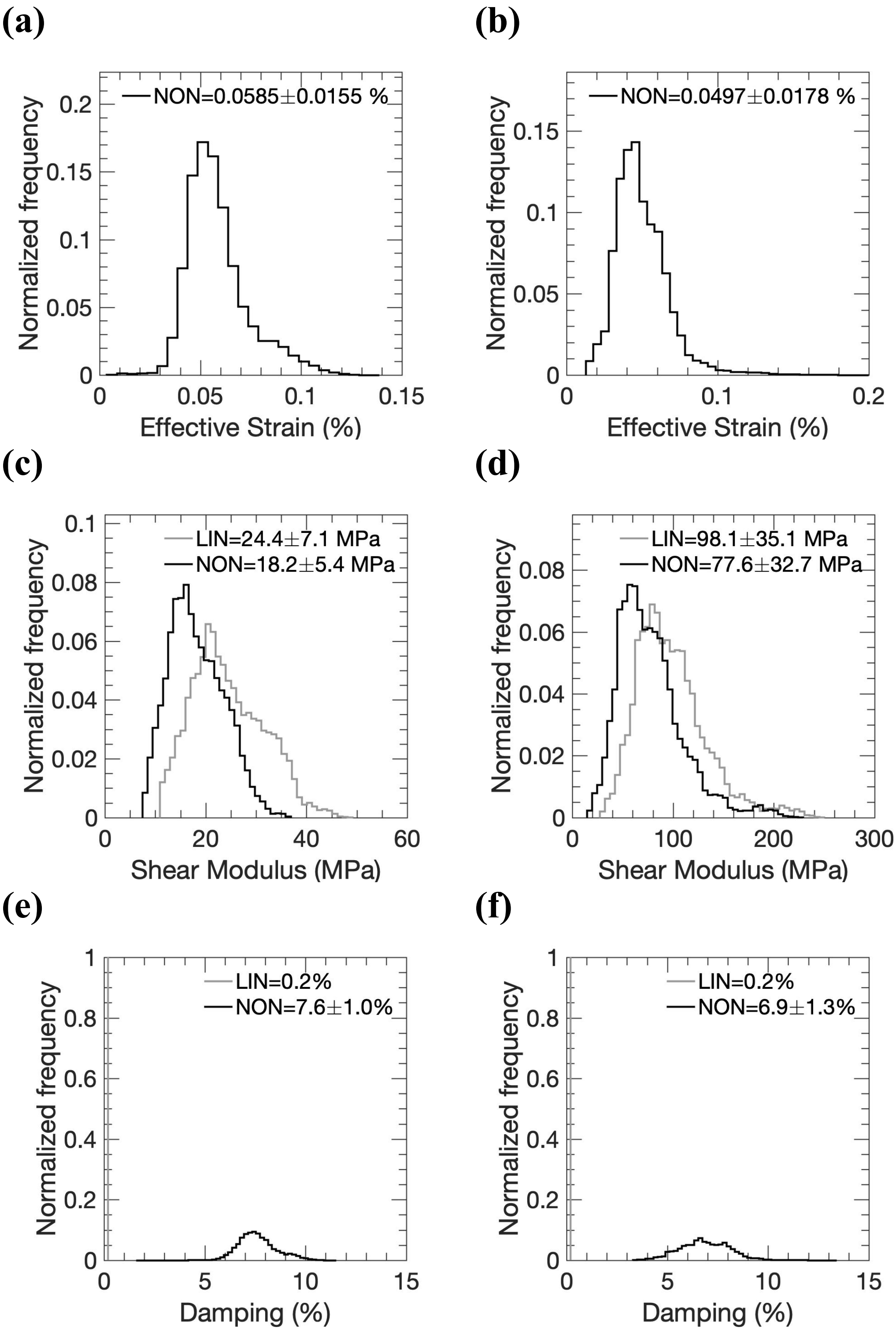

Figure 4.8 Comparison between distributions of linear (LIN) and nonlinear (NON) cases for the three-layer model. Effective shear strains in (a) the first and (b) second layers, shear moduli in (c) the first and second layers (d), and damping factors in (e) the first layer and (f) second layers.

In the three-layer model, I used a parameter of a frequency at the maximum amplification (*fmax*) instead of a fundamental frequency. As indicated in Figure 4.9(a), *fmax* has two peaks either in the distribution for the linear or nonlinear response. The peak of *fmax* for the linear case is located at its first mode, while *fmax* of the nonlinear amplification is located at the fundamental mode. However, the maximum amplifications of the linear and nonlinear responses have only a single mode as shown in Figure 4.9(b). In terms of uncertainties in ground motion proxies, the distributions of the maximum amplification and PGA of the nonlinear case are narrower than those of the linear case as portrayed in Figure 4.9(b) and (c), respectively. On the other hand, the distribution of PGV of the nonlinear response is similar to that of the linear one as indicated in Figure 4.9(d). These results occur because the uncertainty in the nonlinear response is lower than that of the linear response in high frequency range, although, the uncertainty of the nonlinear response is similar to that of the linear one in low frequency range as depicted in Figure 4.7(a). It is widely known that PGV and PGA are controlled by the soil amplification in low and high frequency ranges, respectively.

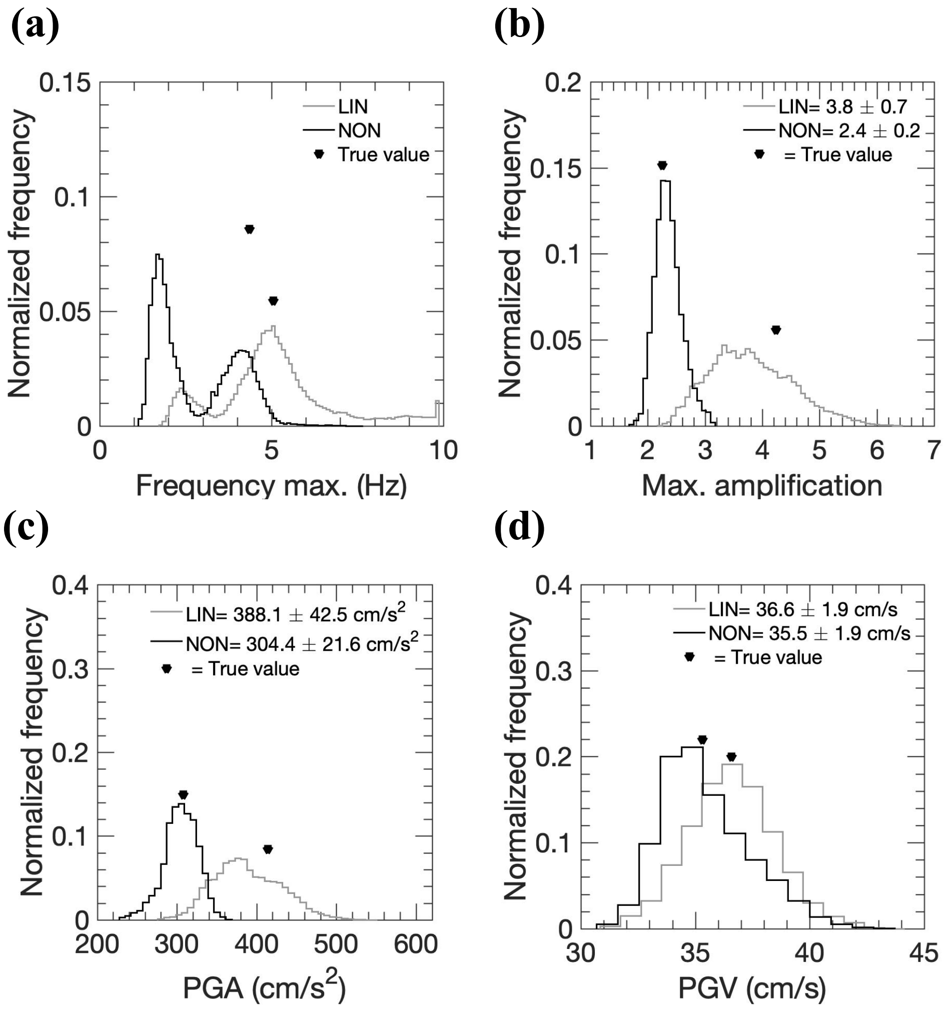

Figure 4.9 Comparison between the distributions of linear (LIN) and nonlinear (NON) cases in the three-layer model. (a) Frequency at maximum amplification, (b) maximum amplification, (c) PGA, and (d) PGV. The triangle shows true value for each parameter.

4.5 Effects of incompleteness and different observational errors of phase velocity on variability of soil amplification

4.5.1 Effects of phase velocity at limited frequencies

It is known that the velocity contrast (impedance ratio) between a top over a bedrock layer mostly controls the maximum amplification. Figure 4.10 shows a comparison of the effects of the absence of the phase velocity in the low or high frequency ranges on the variability of the linear and nonlinear amplifications with those of the sufficient coverage of the phase velocity. In the linear amplification, Figure 4.10(a) shows that the absence of the phase velocity in the low frequency range makes the higher velocity contrast resulting in a higher average of the maximum amplitude that of sufficient coverage of the phase velocity. On the other hand, the lack of the phase velocity in the high frequency range generates a low average of the maximum amplitude for the models with the lower velocity contrast that of sufficient coverage of the phase velocity. Besides the difference in the mean of the maximum amplitudes, I can also notice the differences in the mean of the peak amplitudes at frequencies of about 2.5, 6 and 8 Hz. Because of strong damping factors in the nonlinear responses, the lack of the phase velocity in the low or high frequency ranges generates not so significant to the average of the maximum amplitude as shown in Figure 4.10(b).

I compared the variation of the linear and nonlinear responses using variation coefficients as shown in Figure 4.10(c) and (d), respectively. For the linear case, the significant differences of the variation in the absence of the phase velocity in the low or the high frequency ranges can be clearly seen at around the fundamental frequency, while slight differences in the variability of the amplifications are found at frequencies greater than 3 Hz as indicated in Figure 4.10(c). For the nonlinear case, there are slight differences in the variation of the amplification at around the fundamental frequencies and almost no differences of the peak amplitudes at a high frequency as presented in Figure 4.10(d). I can also observe that the lack of the phase velocity in the high frequency ranges is much more crucial than that of the low frequency range as indicated by the high variation coefficients at around the fundamental frequencies for the linear and nonlinear responses as presented in Figure 4.10(c) and (d), respectively. These results suggest that the absence of the phase velocity in the low or high frequency ranges has less significant effects on the nonlinear response than that of the linear amplification. Furthermore, variation coefficients of ground motion proxies of the limited frequencies in low and high frequency ranges for the nonlinear case are also generally lower than those of linear case as indicated in Figure 4.11.

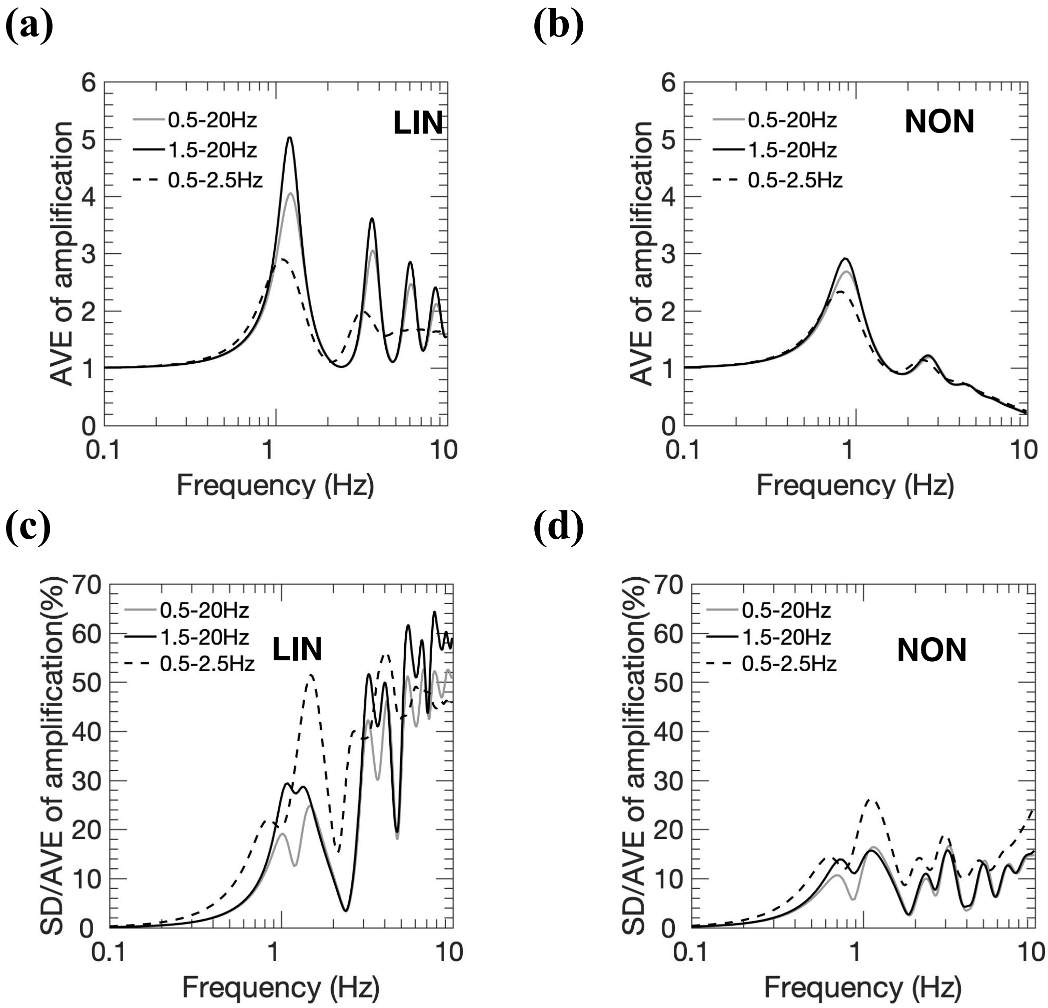

Figure 4.10. Comparison between the average of (a) linear and (b) nonlinear responses for phase velocity limited at low (black line) or high frequency range (broken black line) in the two-layer model. Comparison of variation coefficients of (c) linear with (d) nonlinear responses. The gray line shows sufficient information of phase velocity.

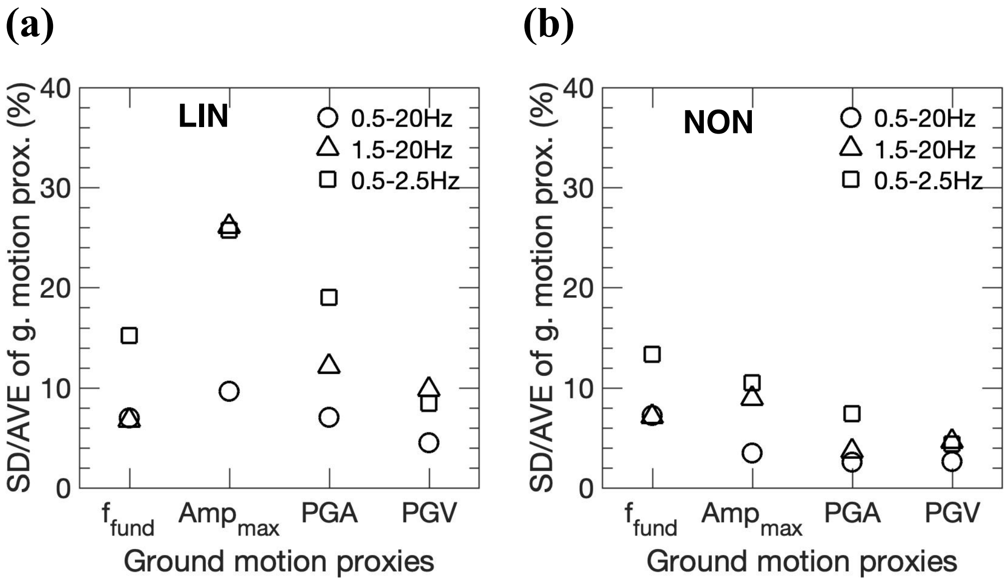

Figure 4.11 Relationship between ground motion proxies: fundamental frequency (*f_{fund}*), maximum amplification (*Amp_{max}*), PGA, PGV, and their SD/AVEs. Phase velocity limited at low (triangle) or high frequency range (trianle) in the two-layer model. Cycle shows sufficient information on phase velocity. (a) Linear and (b) nonlinear soil responses.

4.5.2 Effects of observational errors of phase velocities

In this part, I compared the variability in the linear and nonlinear responses for different observational errors of 5-40% in the phase velocity in the two-layer model as shown in Figure 4.12. The peaks of average amplifications in the linear case are lower as the observational errors are higher as depicted in Figure 4.12(a). I also see a similar pattern in the nonlinear response as presented in Figure 4.12(b). However, the effects are less profound than those of the linear one. In terms of the variation coefficients of the linear and nonlinear responses are portrayed in Figure 4.12(c) and (d), respectively. Figures indicate the higher is observational errors, the higher is variation coefficients of the linear and nonlinear cases. However, I can observe that the effects are less significant in the nonlinear response than that of the linear amplification due to a high damping factor in the nonlinear response.

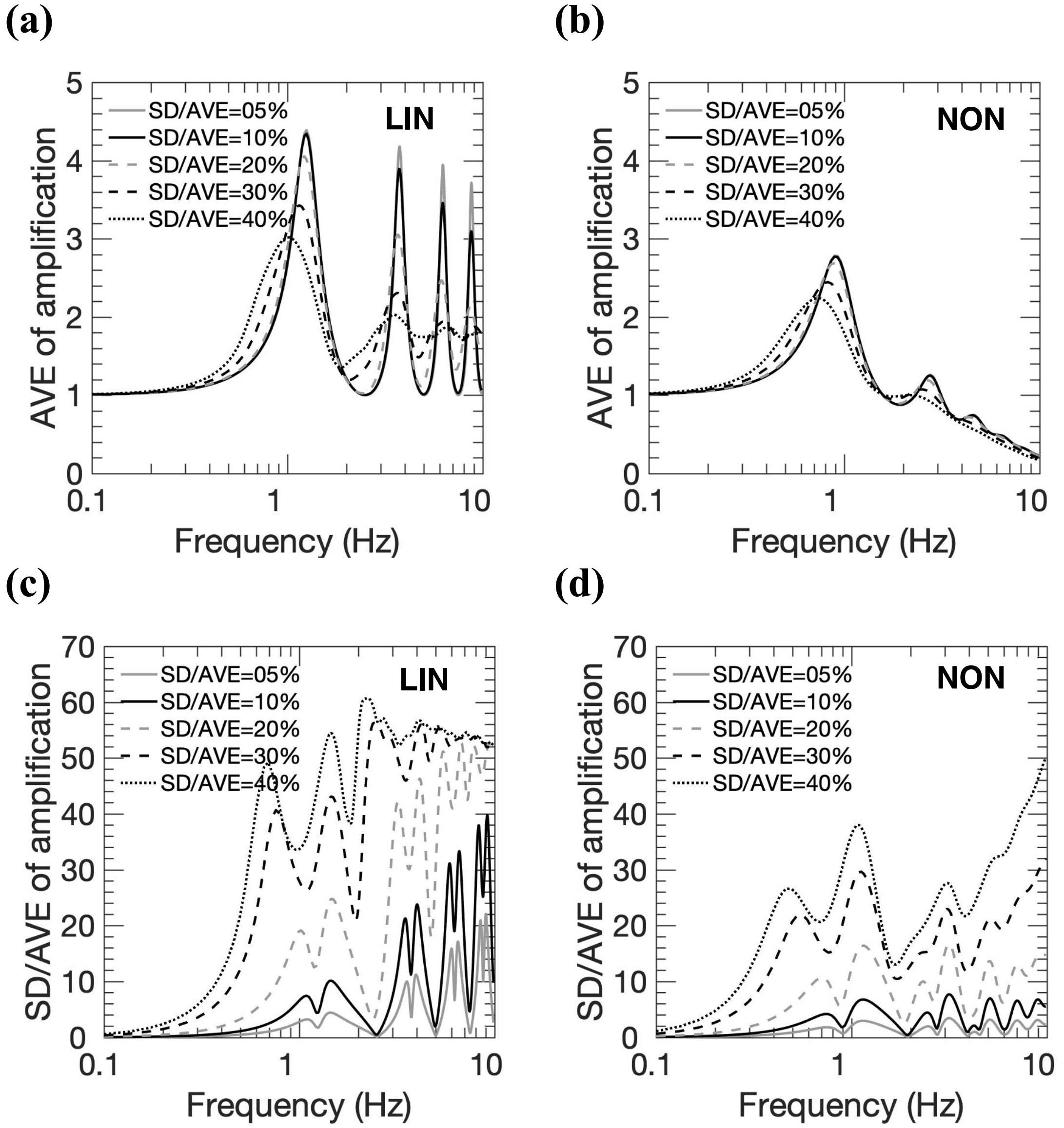

Figure 4.12 Effects of different observational errors 0f 5-40% on soil responses in the two-layer model. Comparison between the average of (a) linear and (b) nonlinear responses. Comparison of variation coefficients of (c) linear and (d) nonlinear responses.

The relationship between the observational errors of the phase velocities and the variation coefficients of the ground motion proxies of the linear and the nonlinear responses can be shown in Figure 4.13. The figure indicates that the uncertainties of the linear and nonlinear amplifications are linearly associated with observational errors. Figure 4.13(a) indicates that uncertainty in the fundamental frequency for the linear and nonlinear amplifications is similar for the different observational errors. Meanwhile, the uncertainty in other ground motion proxies of the nonlinear response is generally lower than those of the linear amplification as depicted in Figure 4.13(b) to (d).

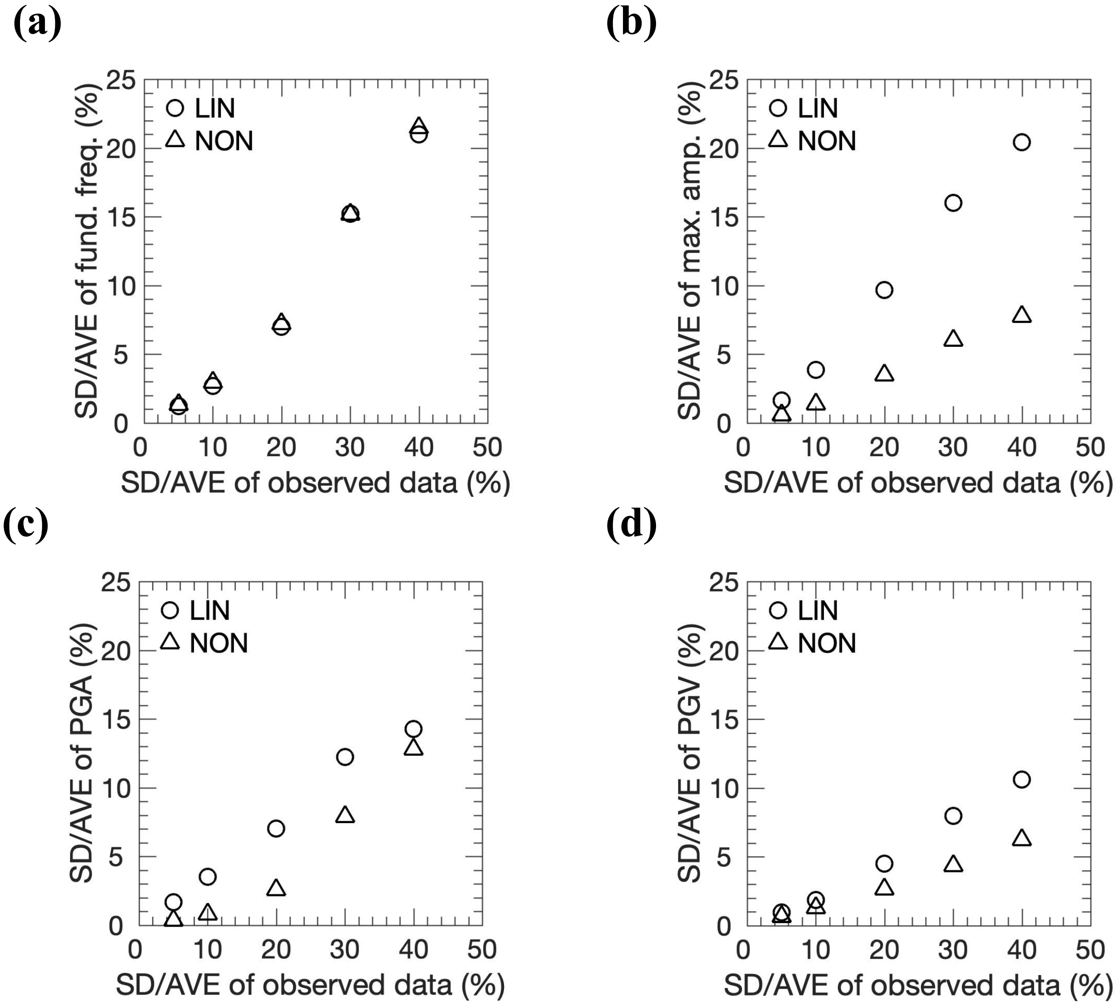

Figure 4.13. Relationship of standard deviations of synthetic observed data with variation coefficients of ground motion proxies of linear (LIN) and nonlinear (NON) in the two-layer model. (a) Fundamental frequency, (b) maximum amplification, (c) PGA, (d) PGV.

4.6 Effects of frequency-dependent errors of phase velocities on nonlinear soil amplification variability

In this section, I examine the effects of the frequency-dependent errors in the phase velocity on the variability of the nonlinear amplification. The sampled models for each case in section 3.8 is used to estimate its nonlinear soil amplification variability as depicted in Figure

4.14. The SD/AVEs of the phase velocities of Case 1, Case 2, and Case 3 are 20%, 50–20%, and 20–50%, respectively, as increasing of the frequencies. In section 3.8, I found that the distributions of *H1* and *Vs2* of Case 2 are wider than those of Case 1, while the distribution *Vs1* of Case 2 is similar to that of Case 1. On the other hand, the distributions of *Vs1* and *H1* of Case 3 are wider than those of Case 1, whereas the *Vs2* distribution of Case 3 has a similar width as that of Case 1. Figure 4.14(a) shows that the average of the nonlinear amplification is only slightly different at its peak-amplitude for each case. Meanwhile, the SD/AVEs of the amplification and the ground motion proxies for Case 2 are higher than those of Cases 1 and 3 as shown in Figures 4.14(b) and 4.15, respectively, as the results of the distributions of *Vs2* of Case 2 are wider than those of Cases 1 and 3.

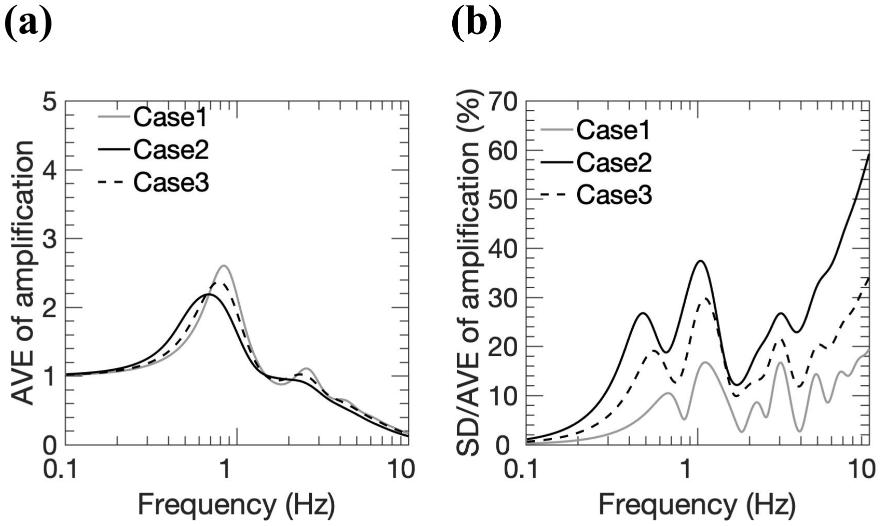

Figure 4.14 (a) Averages of and (b) SD/AVEs of amplifications for different cases. Case 1, Case 2, and Case 3 have SD/AVEs of phase velocities are 20%, 50–20%, and 20–50%, respectively, for frequencies of 0.5–20 Hz.

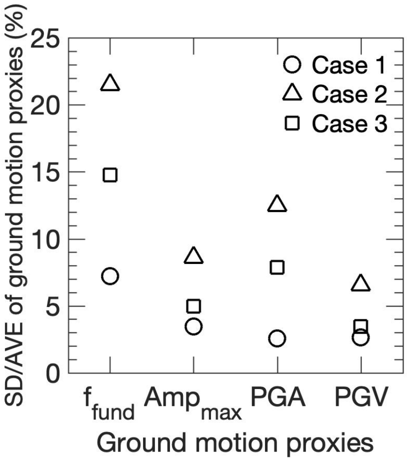

Figure 4.15 SD/AVE of ground motion proxies for various cases. Case 1, Case 2, and Case 3 have SD/AVEs of phase velocities are 20%, 50–20%, and 20–50%, respectively, for frequencies of 0.5–20 Hz.

4.7 Effects of characteristics of input motions on variability of soil amplification

4.7.1 Effects of different PGAs of input motions

I, furthermore, examine the effect of different PGAs of the input motions on the variability of the nonlinear amplification. I generated input motions with PGAs of 5 to 200 cm/s^2 based on the spectral acceleration of the Japanese building code in the same way in the earlier section. I used the sampled models from the two-layer model to estimate the nonlinear amplification for each input motion.

Figure 4.16(a) shows the peaks of the average nonlinear amplification are lower as the PGAs of the input motions are higher. Moreover, the variation coefficients of the nonlinear responses are reduced as the increase of the PGAs of the input motions as depicted in Figure 4.16(b).

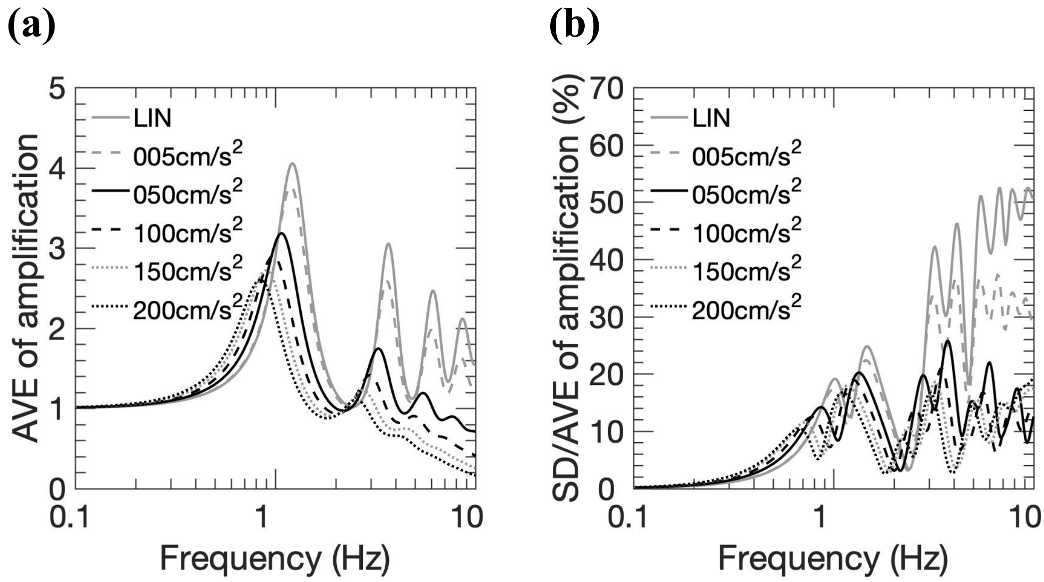

Figure 4.16 Comparison of (a) average and (b) variation coefficient of nonlinear soil amplification for different PGAs of input motions of 5-200 cm/s^2. Linear (LIN) amplification is also presented.

Effects of the different PGAs of the input motions on the ground motion proxies in the nonlinear response can be found in Figure 4.17. The ground motion proxies in the linear case are also presented for comparisons. Figure 4.17(a) shows that are variation coefficients of the fundamental frequency for the nonlinear case are similar for all the input motions. Meanwhile, the variation coefficients of the maximum amplification, PGA, and PGV are generally lower as the increase of PGAs of the input motions.

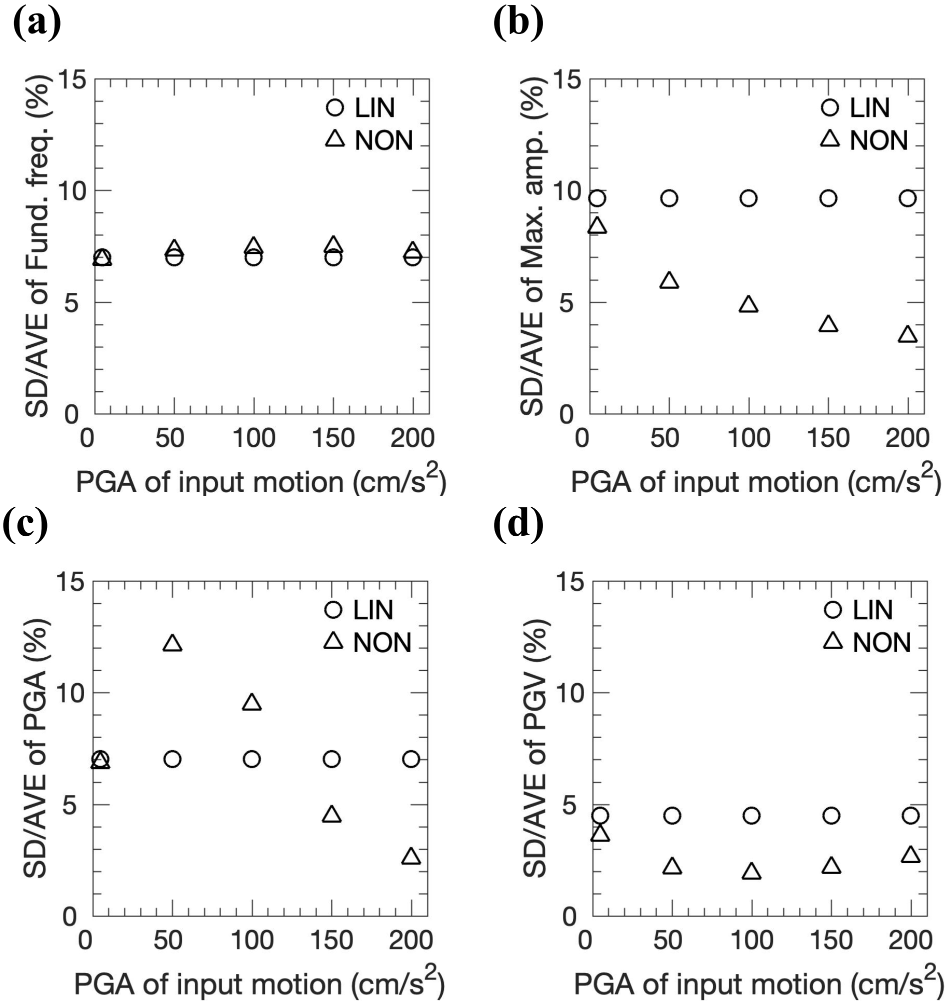

Figure 4.17. Relationship of different PGAs of input motions with variation coefficients of ground motion proxies of linear (LIN) and nonlinear (NON) in two-layer model. (a) Fundamental frequency, (b) maximum amplification, (c) PGA, (d) PGV.

Figure 4.17(c) also indicates that the variation coefficients of the surface PGA in the nonlinear case for the input motions with PGAs of 50 and 100 cm/s^2 are higher than those of the linear case, because the distributions of the PGAs of 50 and 100 cm/s^2 are non-Gaussian as presented in Figure 4.18(a). Meanwhile, the other PGA distributions of the nonlinear case for input motions with PGAs of 5, 150, and 200 cm/s^2 can be similar to the normal distribution as shown in the figure. Moreover, the distributions of PGA of the linear case for the input motions with PGAs of 5-200 cm/s^2 have also normal distributions as shown in Figure 4.18(b). To understand the reason why the distributions of the surface PGA for the input motion with the

PGA of 50 cm/s^2 has double modes, I split the distribution into two parts as indicated in Figure 4.18(c). The PGA of the first and second parts are about 60-70 cm/s^2 and 70-90 cm/s^2, respectively. Figure 4.18(d) indicates double modes in the distribution of the PGA, are not affected by the distributions of the S-wave velocity, at the first and second layers, since the distributions of the S-wave velocity at the first and second layers are similar for the first and second parts of PGA distributions. However, Figure 4.18(e) shows that the first and second parts use different distributions of the first layer's thickness. It is indicated that the first part is experiencing stronger nonlinear effect than that of the second part.

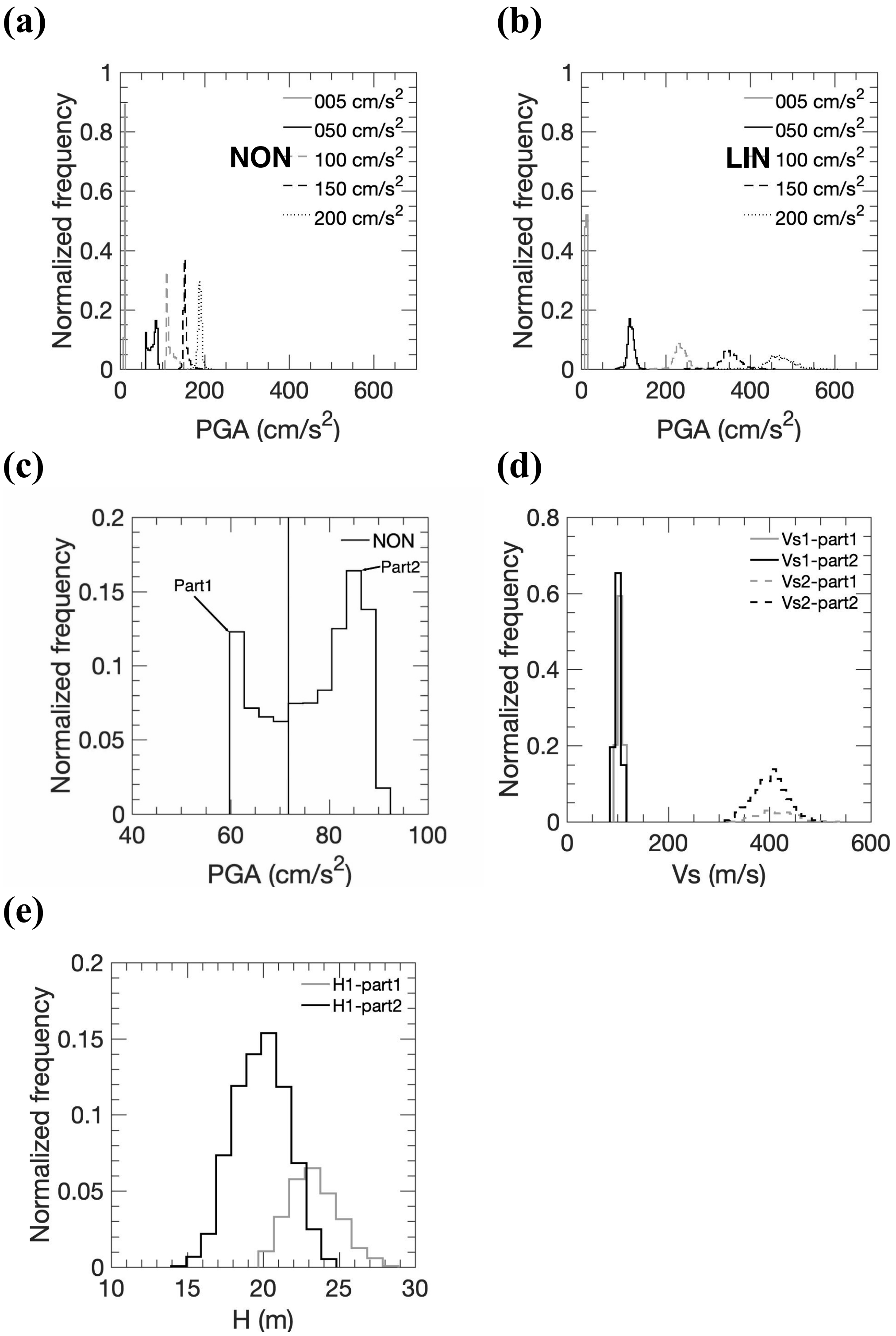

Figure 4.18 Distributions of surface PGAs for different PGAs of input motions for (a) nonlinear and (b) linear responses. (c) Distribution of surface PGA of nonlinear response for input motion with PGA of 50 cm/s^2. The vertical black line indicates boundary for first (part1) and second modes (part2) of the PGA distribution. (d) S-wave velocities and (e) thicknesses that are responsible for the first and second parts of the distribution of PGA.

4.7.2 Effects of different phase angles of input motions

In this section, I try to understand the effects of different phase angles of input motions to nonlinear soil amplification variability. Ten input motions with different phases are employed in this section. I generated other nine synthetics motions based on a spectral acceleration of the Japanese building code as similar to the first synthetics motion as shown in Figure 4.1(b). I used different random numbers to generate motions with different phases. The first synthetic motions can be found in Figure 4.1(b). Meanwhile, the other nine synthetics motions are presented in Figure 4.19.

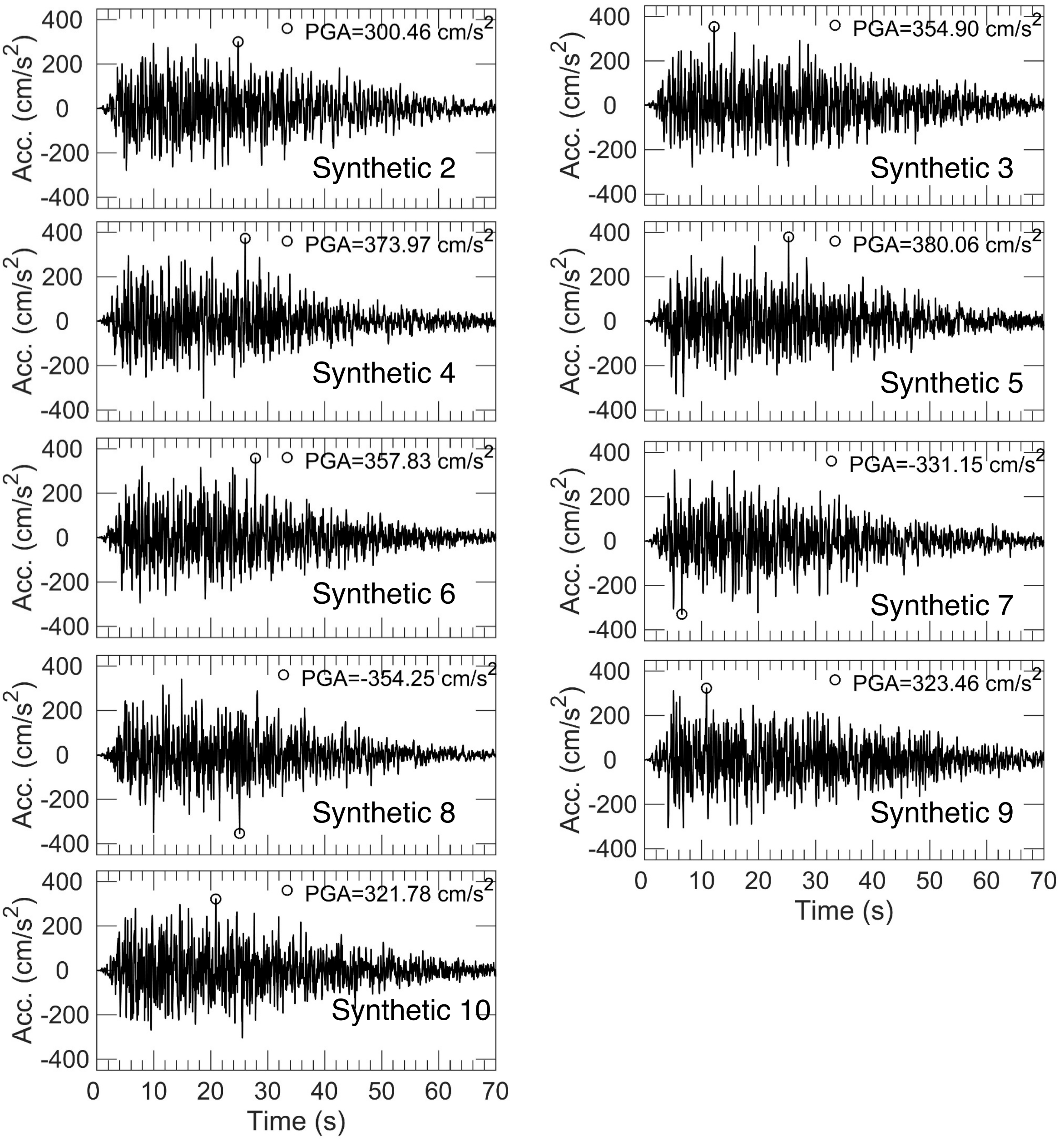

Figure 4.19 Synthetic motions with different phases generated by different random numbers based on the Japanese building code.

The nine synthetics motions are also normalized, and their PGAs are also equal to be 200 cm/s^2 as similar to the first input motion as presented in Figure 4.1(b). The other nine input motions with PGAs of 200 cm/s^2 are depicted in Figure 4.20. Each input motion was used to estimate corresponding nonlinear amplification for the sampled models of the two-layer model as depicted in Figure 3.5.

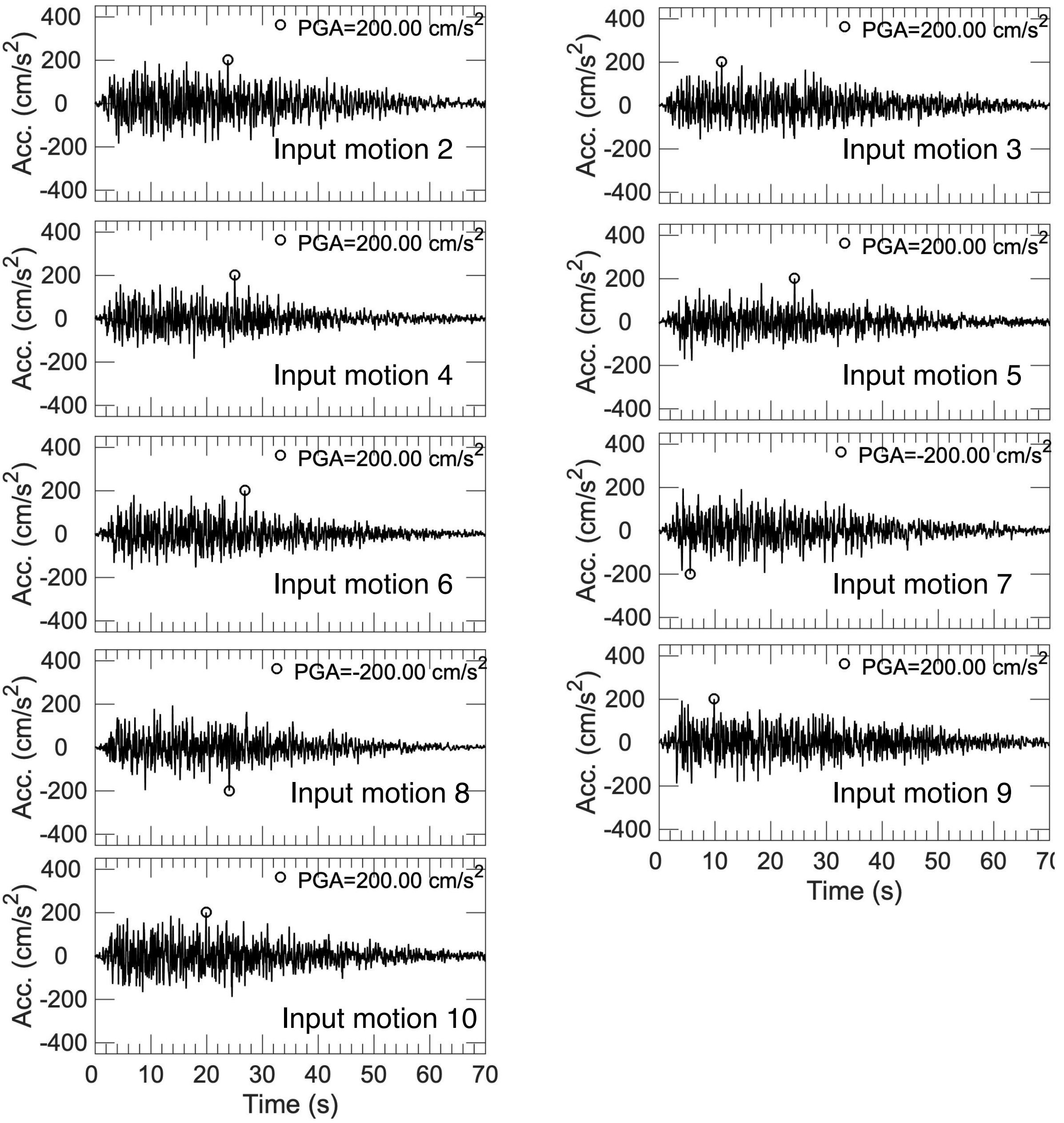

Figure 4.20 Normalized motion of synthetic motions in Figure 4.19.

Figure 4.21(a) shows that average nonlinear amplifications are similar for different input motions. Their variation coefficients of the amplification for each input motion are also slightly different at frequencies higher than 8 Hz, as depicted in Figure 4.21(b). The effects of the different input motion's phases are more noticeable in PGA and PGV than those of fundamental frequency and maximum amplification as displayed in Figure 4.21(c). The variations of input motion's phases influence the values of the effective strain, rigidity, and damping factor as depicted in Figure 4.22. The figure shows that the widths of the distributions of the effective strain, rigidity, and damping factor are different for each input motion. Therefore, it is suggested that the phase of the input motion slightly affect the variability of nonlinear soil responses, particularly PGA and PGV.

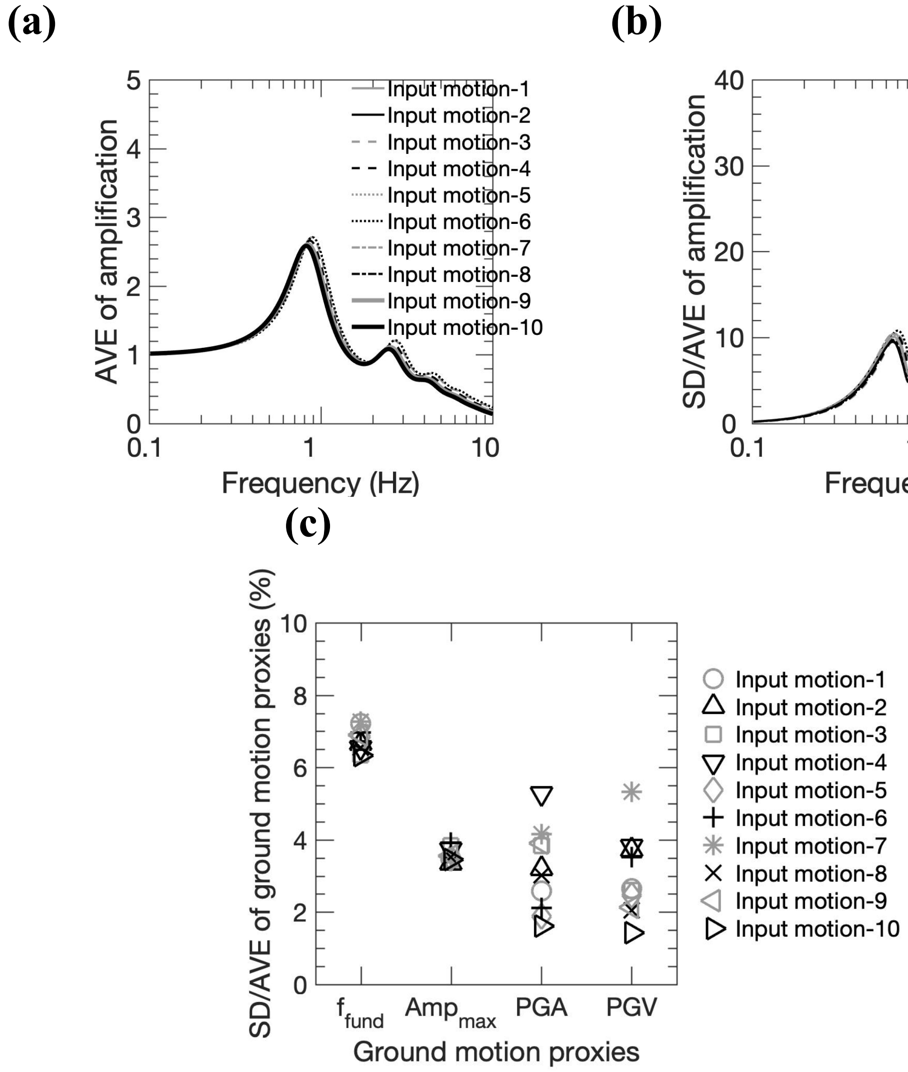

Figure 4.21 (a) Average and (b) variation coefficient of nonlinear amplification for input motions with different phases. (c) The relationship between ground motion proxies: fundamental frequency (f_{fund}), maximum amplification (Amp_{max}), PGA, PGV and their SD/AVEs in two-layer model.

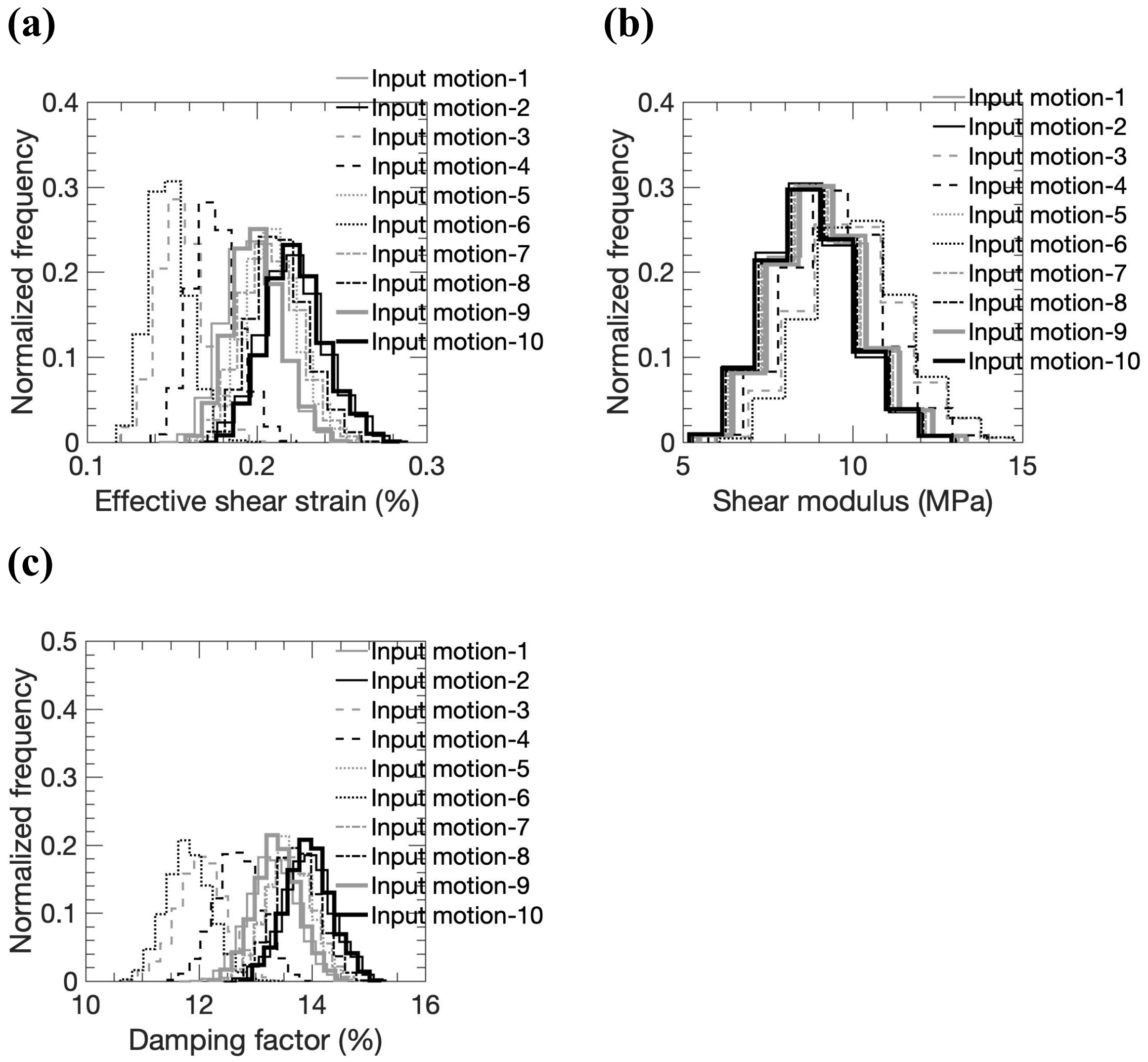

Figure 4.22. Effects of various phases of input motion on (a) effective shear strain, (b) shear modulus, and (c) damping factor.

4.8 Comparison with the previous studies

As explained earlier, the previous studies indicate the contradiction of the results on the effect of uncertainty of S-wave velocity profiles to 1D soil responses. In studies on linear soil response, the uncertainty of S-wave velocity profiles played a major role in the variation of linear soil amplification (Molnar et al., 2013; Yamanaka, 2014, 2013, 2011) which agreed with my results. My results also suggest that the linear amplification with small damping factors which lead to the broader variation of the peak amplitudes, particularly at a high frequency.

However, Foti et al. (2009) reported that the uncertainty of S-wave velocity profiles was insignificant to linear amplification. Considering my results, their result is occurred due to the fact that they used phase velocity with a standard deviation of less than 10%. Figure 4.13 (b) shows that the phase velocity having a variation coefficient of 10% has a variation coefficient of less than 5% in the maximum amplification. In the assumption of the nonlinear soil response, Foti et al. (2009) showed that the uncertainty of S-wave velocity profiles was negligible to nonlinear soil response as similar to my results. I found that the nonlinear amplification had a higher damping factor that can reduce the peak amplitudes and also flatten the spectral shape at a high frequency. Nevertheless, Jakka et al. (2014) found that the uncertainty of S-wave velocity profiles could lead to significant effects on the soil response. In their study, they used an input motion with a PGA of 100 cm/s^2 for their soil models. One of their soil models has S-wave velocities of about 200 to 250 and 300 to 500 m/s for top layer and bedrock, respectively. The PGA of the input motion might be too small to discuss the nonlinear effect as compared with ours. This result could lead to a high variation of their soil response. As can be seen in Figure 4.16(b), my results indicate that the lower PGAs of the input motions produce the higher uncertainties of the amplification. My study has clearly shown that a damping factor plays a major role in the variability of 1D soil response which was estimated from the uncertainty of S-wave velocity profiles.

4.9 Summary

In this Chapter, I have conducted numerical experiments to estimate the variability in linear and nonlinear responses due to uncertainty in a S-wave velocity profile from a Rayleigh wave phase velocity of inversion using the MCMC method. The uncertainties in the *Vs* profiles are obtained from two- and three-layer models. The *Vs* profile uncertainties smooth peak-amplitudes of the linear and nonlinear amplifications due to peak averaging, especially in high frequency range. I found that the nonlinear amplification has a higher resolution and a smoother spectral shape at high frequencies than the linear amplification. It is found that fundamental frequencies of the linear and nonlinear cases have similar widths of the distributions because the distribution of the shear modulus of the nonlinear response has a similar width to that of the linear response. It is widely known that the fundamental frequency is only affected by shear modulus, not by damping factor. Meanwhile, other ground motion proxies (e.g., maximum amplification, peak ground acceleration, and peak ground velocity) have less uncertainty in the nonlinear cases than in the linear cases. The other ground motion proxies are controlled by a combination of the shear modulus and damping. However, I found that the material damping has a more profound effect on the variability of soil amplification as compared to the material shear modulus.

I also have shown the variability of the soil amplification due to the uncertainty of S-wave velocity models in relation to the incompleteness and various observational errors of the phase velocities. Furthermore, I have presented the effects of different PGAs of input motions on the nonlinear soil amplifications. It is shown that the material damping also plays a major role in the variability of soil amplification in those cases. I also found that the input motion’s phase angles have fewer effects on the variability in the nonlinear soil response.

Chapter 5 Variability of deconvolved bedrock motion

5.1 Objective

5.2 Re-sampling model parameters from the inversion

5.3 Comparison between the variability in nonlinear soil response from SHAKE and DYNEQ codes

5.4 Deconvolution analysis

5.5 Variability of deconvolved bedrock motion due to uncertainty of S-wave velocity model from given thickness in advance in the inversion

5.6 Summary

5.1 Objective

My main goal in this chapter is to understand the effects of uncertainty in an S-wave velocity model in Chapter 3 into variability in a deconvolved bedrock motion. Deconvolution is a common technique to estimate a bedrock motion from an observed surface wave using an S-wave velocity profile at a certain site. Then, the deconvolved bedrock motion can be used to estimate ground motion characteristic for other engineering interest sites. In Chapter 4, I used SHAKE91 code to estimate nonlinear soil responses since it is the first developed code and the most used equivalent linear method worldwide, particularly for engineering purpose. Moreover, the conflicting results in the variability of soil responses by Foti et al. (2009) and Jakka et al. (2014) as I already have discussed in Chapter 4, they also used SHAKE program in their soil responses. However, since SHAKE can be only used up to moderate motion, application to large strong-motion record might be not appropriate such as strong-motion during the 2011 off Pacific Coast of Tohoku Earthquake as I will discuss in the next chapter. Therefore, in this numerical experiment, I used a frequency-dependent equivalent linear method (DYNEQ) to calculate a nonlinear soil response. In this chapter, I show variability in the bedrock motion in the two- and three-layer models. Moreover, I also show comparisons between variability in bedrock motions from given and unknown thicknesses during inversions.

5.2 Re-sampling model parameters from the inversion

Even though DYNEQ has an advantage over SHAKE to estimate nonlinear soil response for high shear strain level. However, the computational time of DYNEQ is so much slower than that of SHAKE. Therefore, to speed up the calculation in DYNEQ, I chose 200 models so as to have similar distributions of the re-sampled model parameters to that of all the models. First, I sorted all models based on their misfits, from lowest to highest misfits, then selected 200 models. I compared the distributions of all and the 200 models for the two-layer model and two three-layer models in Figure 5.1. The comparisons show that the distributions of the parameters of all the models and the 200 resampled models are quite similar indicating the re-sampled models contains similar statistical features to those of all the sampled models. I use the re-sampled models to estimate soil amplification and its variability in the following analysis.

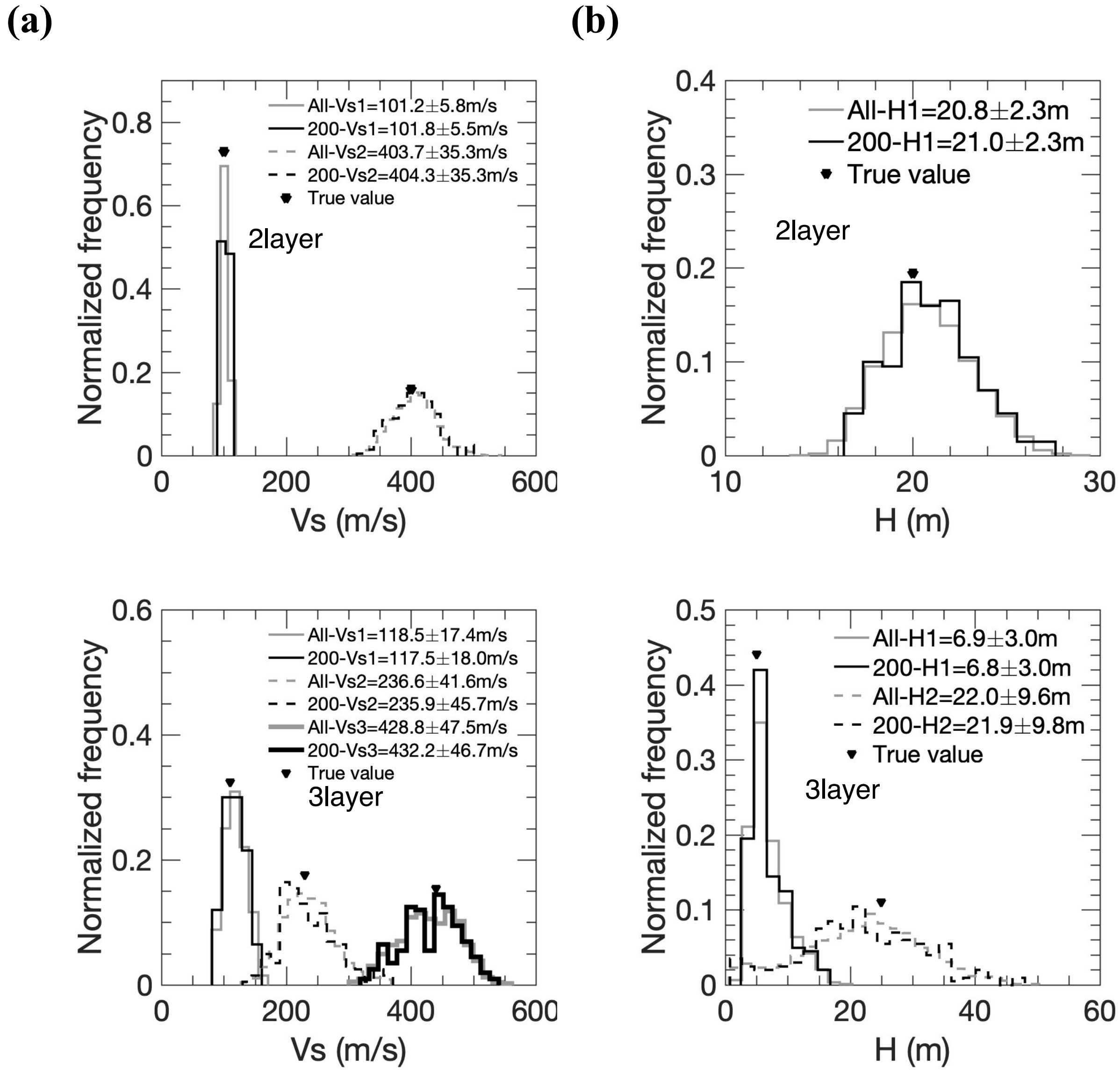

Figure 5.1 Comparison between all parameters after burn-in periods (All) and 200 re-sampled model parameters (200). (a) S-wave velocities and (b) thicknesses of the two- and three-layer models. Triangle indicates true value for each parameter.

5.3 Comparison between variability in nonlinear soil responses from SHAKE and DYNEQ codes

Before I used DYNEQ to estimate variability in bedrock motion due to uncertainty in the S-wave velocity profiles. I try to understand the difference between nonlinear amplification and its variability estimated using SHAKE and DYNEQ for the two- and three-layer models. Soil type assumption is the same as I did in Chapter 4. The first layer is assumed to be a clay layer in the two-layer model, while the first and second layers are given as clay layers for the three-layer model. Moreover, I employed the same shear modulus and damping factor curves that I used in Chapter 4 as presented in Figure 5.2(a). Moreover, an input motion with a PGA of 200 cm/s^2 is also used, as shown in Figure 5.2(b).

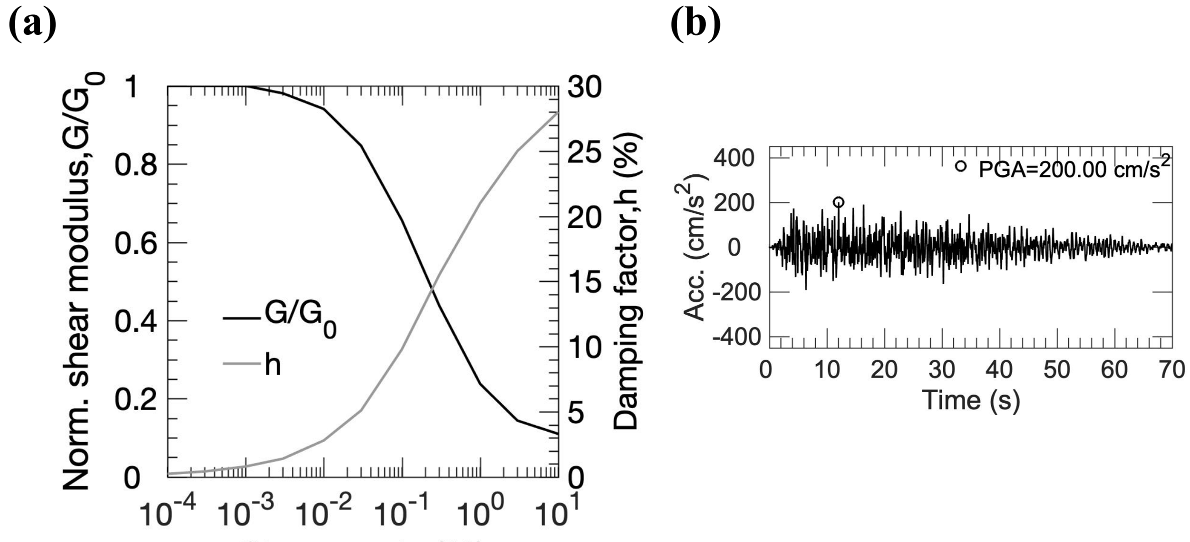

Figure 5.2 (a) Normalized shear modulus (*G*/*G*$_0$) and damping factor (*h*) of clay. (b) Input motion with PGA of 200 cm/s^2.

Figure 5.3 indicates that the amplifications and their uncertainties from SHAKE and DYNEQ are similar at frequencies of 0.1-5 Hz. The amplification from DYNEQ is higher than that of SHAKE at the frequencies of greater than 5 Hz for the two- and three-layer models as depicted in Figure 5.3. The figure also indicates that the variability of amplifications from

SHAKE and DYNEQ is similar. These results are caused by the different assumptions of the effective shear strains in SHAKE and DYNEQ as previously stated. SHAKE is assumed that the effective shear strain is constant at all frequencies, while DYNEQ treats that the effective shear strain is frequency dependent as depicted in Figure 5.4(a). Thus, the shear modulus and damping are also constant for all the frequencies in SHAKE, whereas the shear modulus and damping in DYNEQ are also frequency-dependent as portrayed in Figure 5.4(b) and (c). Moreover, Figure 5.5 depicts the effective shear strains, shear moduli, and dampings of DYNEQ and SHAKE in the three-layer model.

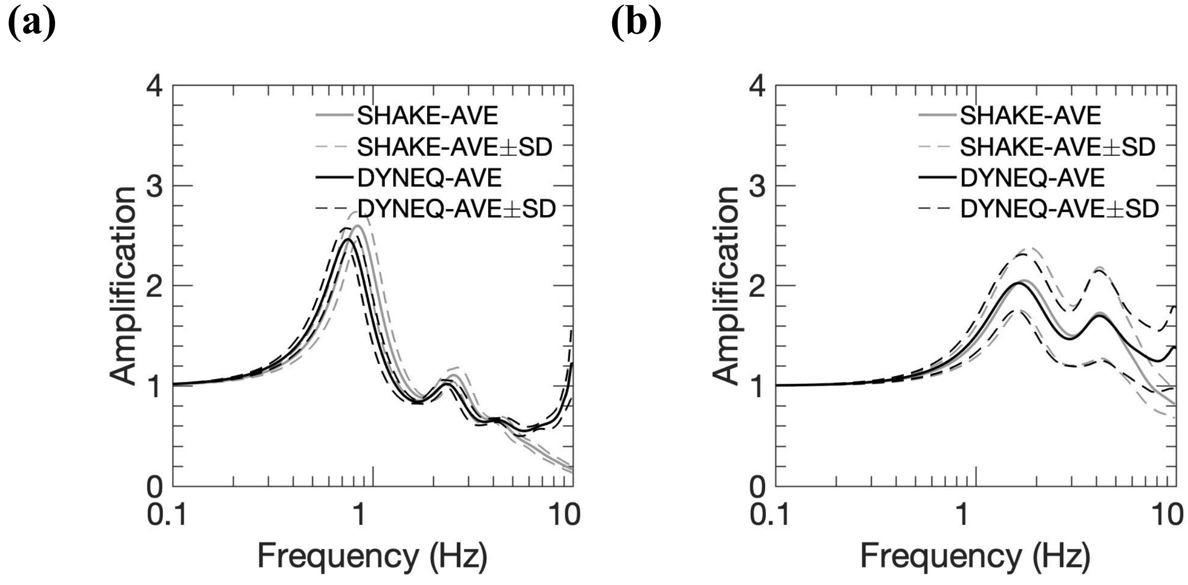

Figure 5.3 Comparison between SHAKE and DYNEQ to estimate average (AVE) nonlinear soil amplification and its uncertainty (SD) in (a) two- and (b) three-layer models.

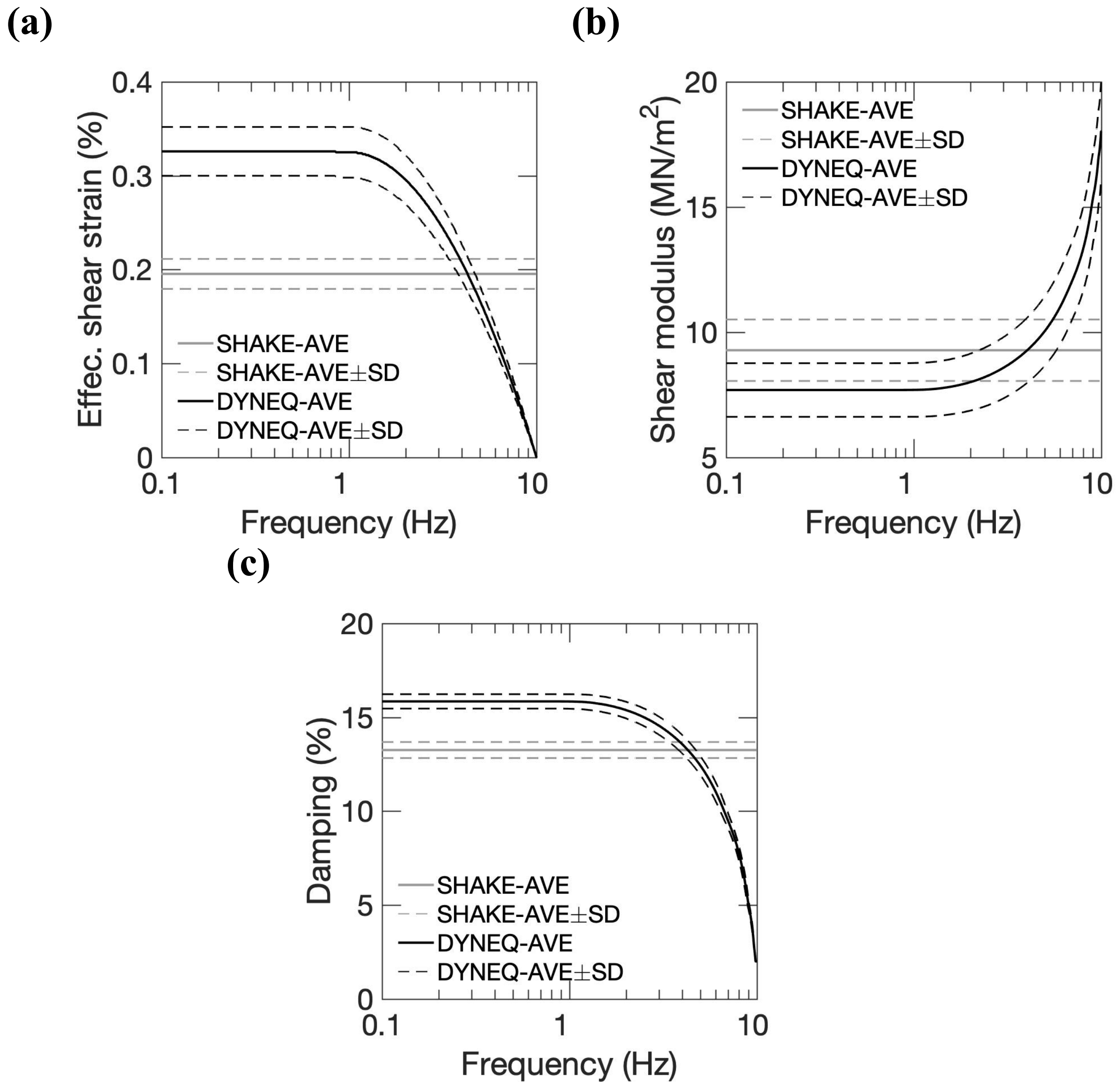

Figure 5.4 Comparison between SHAKE and DYNEQ to estimate average (AVE) nonlinear parameters and their variability (SD) of (a) effective shear strain, (b) shear modulus, and (b) damping at the first layer in two-layer model.

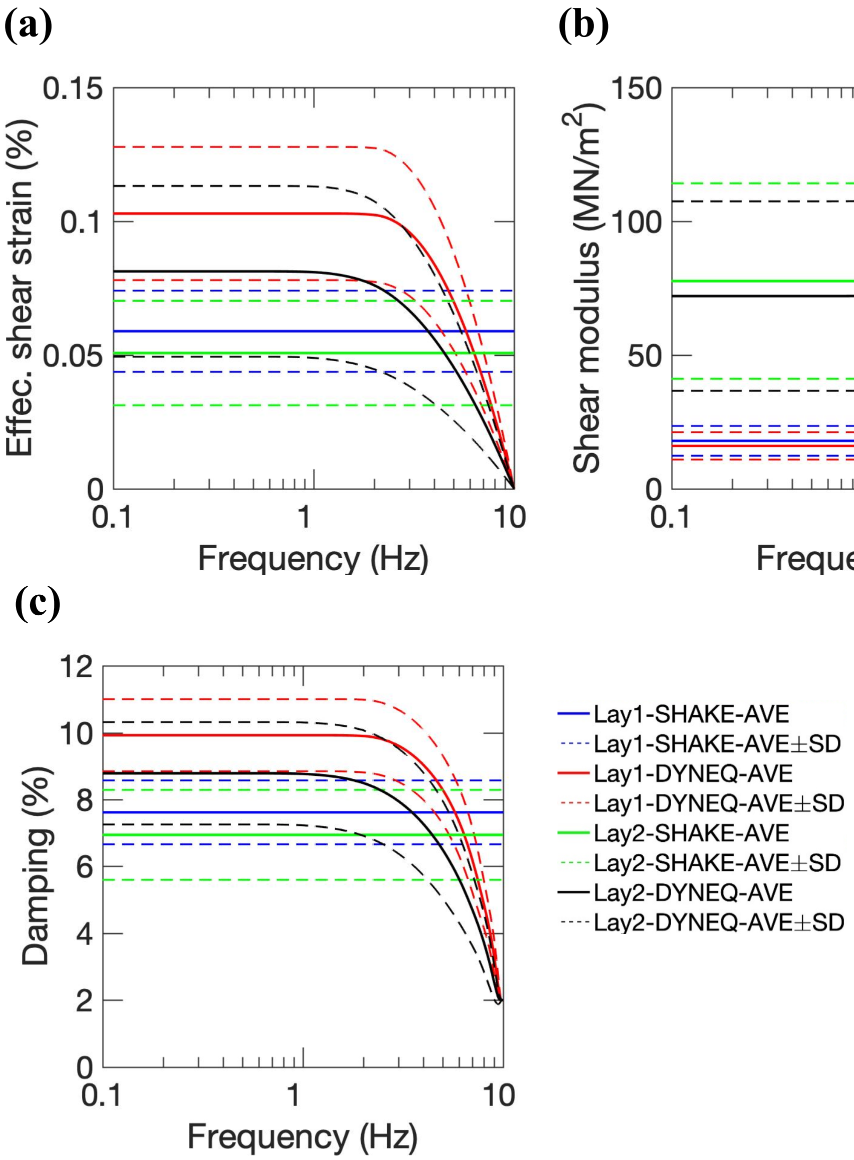

Figure 5.5 Comparison between SHAKE and DYNEQ to estimate average (AVE) nonlinear parameters and their variability (SD) of (a) effective shear strain, (b) shear modulus, and (b) damping at the first (Lay1) and second (Lay2) layers in the three-layer model.

5.4 Deconvolution analysis

5.4.1 Generation of surface motion

I used the synthetic bedrock motion with a PGA of 336 cm/s^2 to obtain a surface motion using DYNEQ. The bedrock motion is generated based on the spectral acceleration of the Japanese building code as previously discussed in section 4.1 and depicted in Figure 5.6(a).

The bedrock motion and the true S-wave profile of the two-layer model are used to generate a surface acceleration as shown in Figure 5.6(b). Their velocity waves are estimated from the acceleration waves as depicted in Figure 5.6(c) and (d). The figures also show that the PGA of the surface motion is lower than that of the bedrock motion due to a high damping factor of the first layer. I also generated surface motions for the three-layer model using the same bedrock motion used for the two-layer model as shown in Figure 5.7. The surface motion of the three-layer model has higher PGA than that of the bedrock motion because this model has a less nonlinear effect than that of the two-layer model, as depicted in Figure 5.7. Meanwhile, the surface PGV of the two- and three-layer models are higher than that of the input motion.

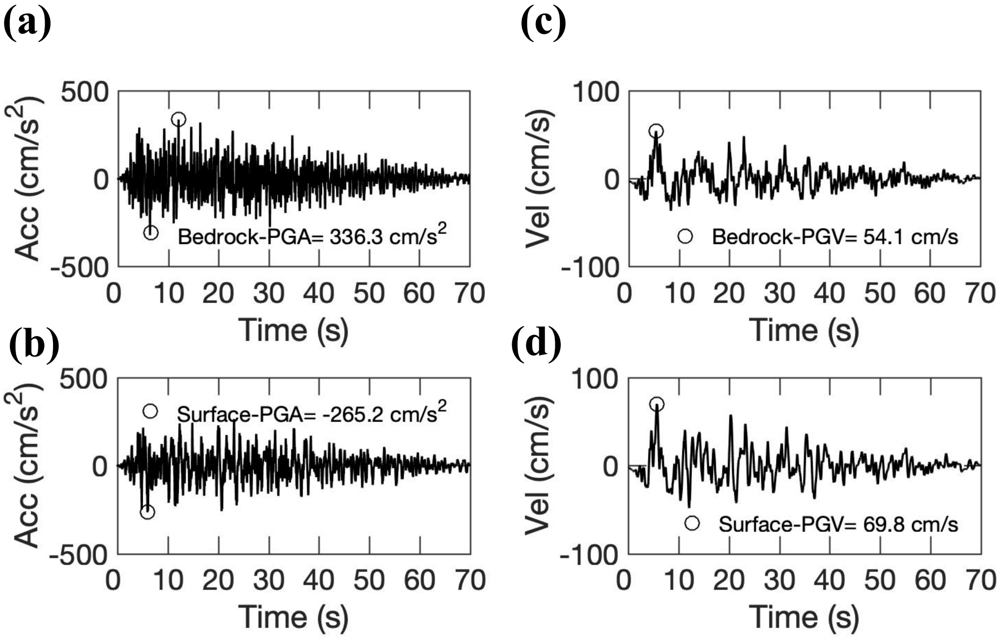

Figure 5.6 Acceleration waves at (a) bedrock and (b) surface, and velocity waves of (c) bedrock and (d) surface using true S-wave velocity profile of the two-layer model assuming nonlinear response.

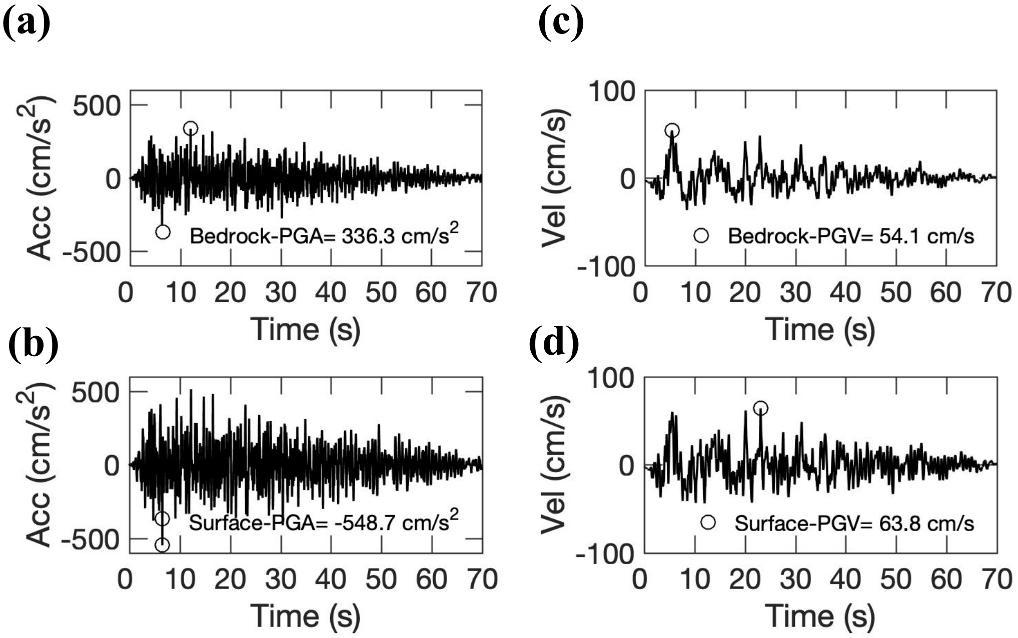

Figure 5.7 Acceleration waves at (a) bedrock and (b) surface, and velocity waves of (c) bedrock and (d) surface using true S-wave velocity profile of the three-layer model assuming nonlinear response.

5.4.2 Variation of deconvolved bedrock motion in the two-layer model

I estimate a variation of bedrock motions due to the uncertainty in the Vs profile of the two-layer model (Figure 5.1), deconvolved from a surface motion as depicted in Figure 5.6(b). Moreover, I also estimated average and the variability of spectral acceleration (SA) as shown in Figure 5.8(a) from the variation of the bedrock motions. The figure indicates that the average bedrock SA can be similar to the true bedrock SA. Coefficient variation (SD/AVE) of the deconvolved bedrock SA is presented in Figure 5.8(b). The SD/AVE has values larger than 10% at the frequencies of 1 Hz and about 3-9 Hz. Distributions of PGAs and PGVs of the bedrock motion are depicted in Figure 5.9(a) and (b), respectively. The figures indicate that the average PGA and PGV have similar values to their corresponding true values. The variation coefficient of the PGA is higher than that of the PGV as indicated in the figures.

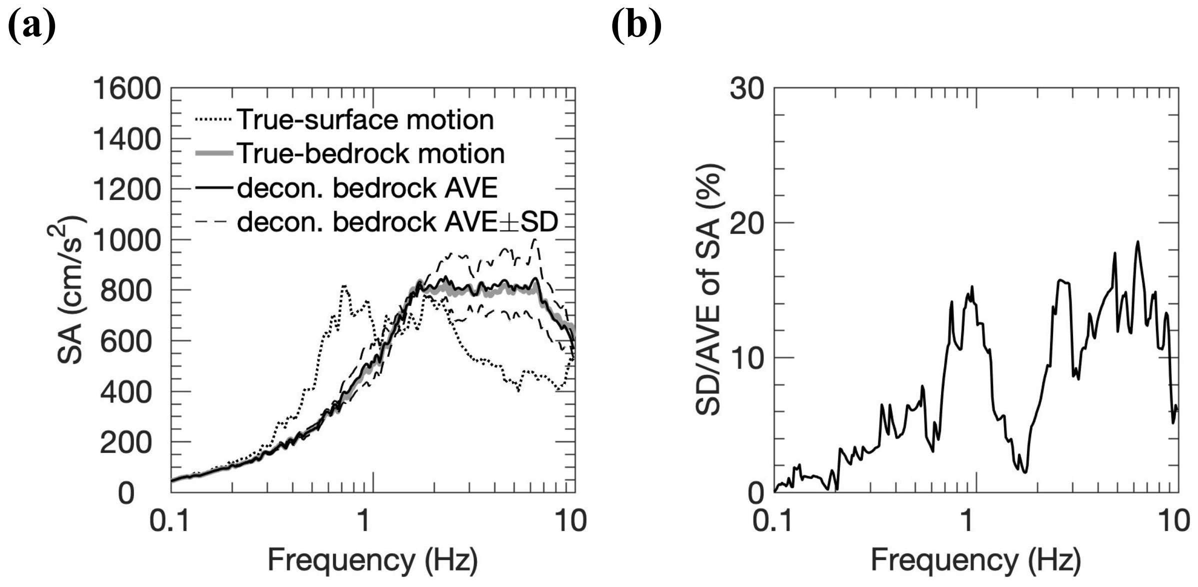

Figure 5.8 (a) Comparison between true bedrock and deconvolved bedrock SAs for two-layer model. (b) The variation coefficient of deconvolved bedrock SA. Spectral damping of 5% is used.

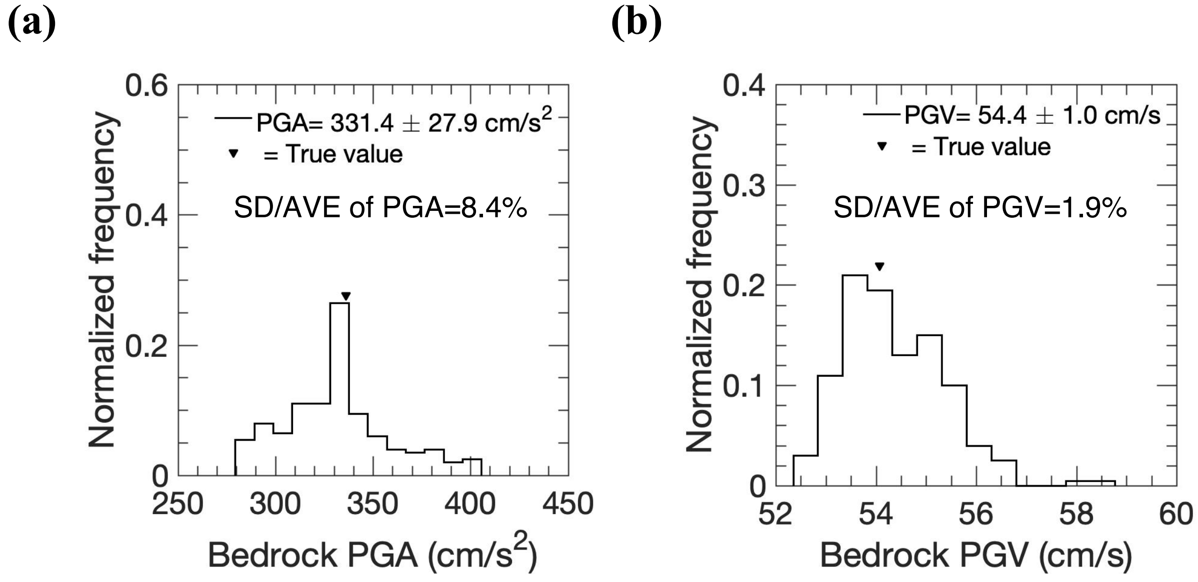

Figure 5.9 Distributions of deconvolved bedrock (a) PGA and PGV for the two-layer model. The triangle shows true value for each parameter.

I show several examples of the bedrock acceleration and the velocity waves in Figure 5.10 which have similar values as the average and the average plus/minus the standard deviation of PGA and PGV distributions in Figure 5.9. Figures indicate that the representative acceleration and velocity motions have similar shape and amplitude as compared to those of the true value.

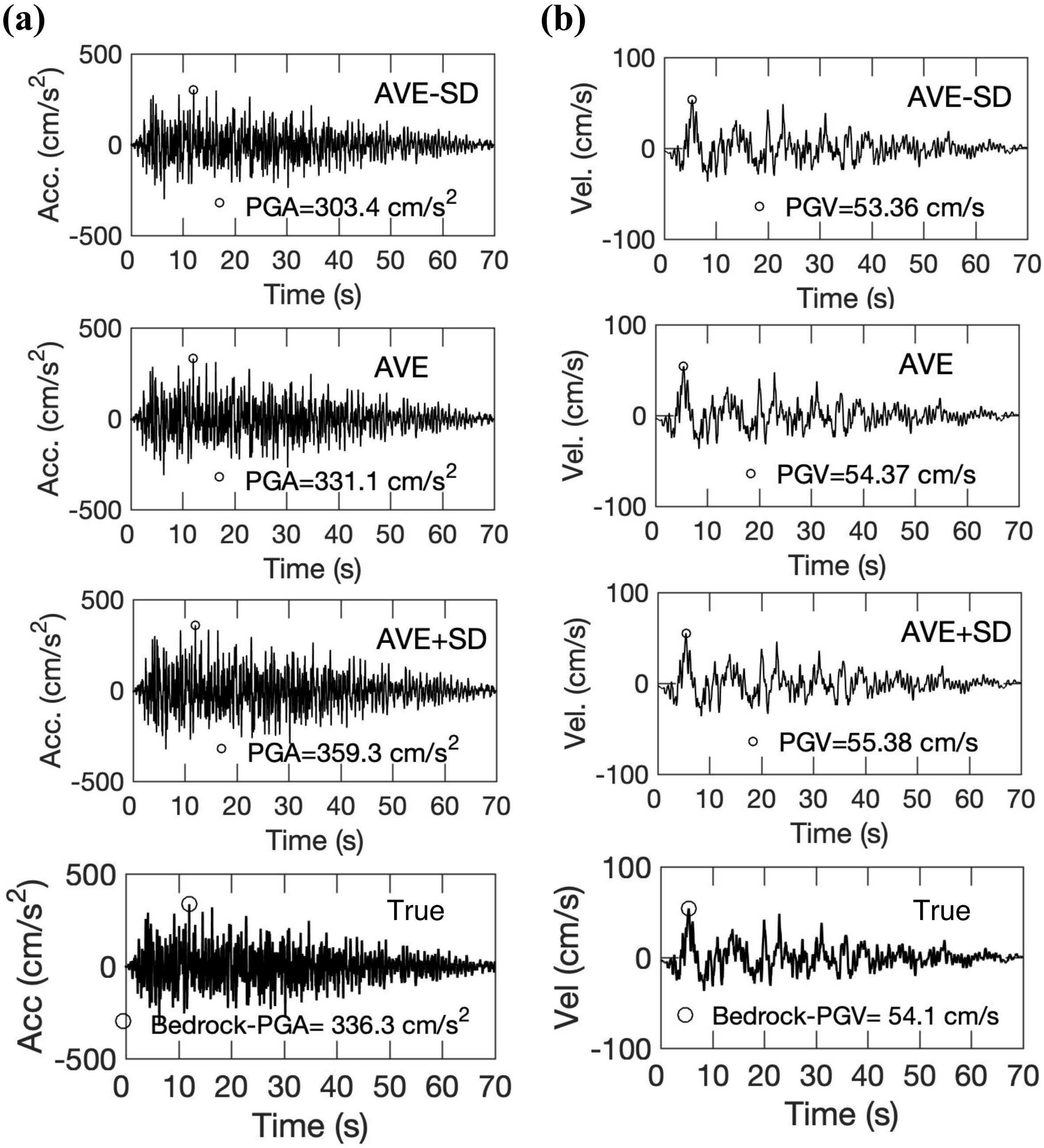

Figure 5.10 Several examples of (a) acceleration and (b) velocity waves in the two-layer model which have similar values in average (AVE), average plus/minus standard deviation (SD) of PGA and PGV distributions as depicted in Figure 5.9. True acceleration and velocity motions can be also found in the figure.

5.4.3 Variation of bedrock motion for the three-layer model

I also approximated variability in a deconvolved bedrock motion for the three-layer model. Figure 5.11(a) shows that the calculated bedrock SA considering its uncertainty generally can explain well the true bedrock SA. However, the average deconvolved SA is overestimated than that of true SA for the frequency of 3-6 Hz. The SD/AVE of the bedrock SA has higher values than 10% at frequencies about higher than 1 Hz.

Figure 5.12 indicates that the variation coefficient of the PGA is higher than that of the PGV. However, their distributions can describe well the corresponding true values as depicted in the figure.

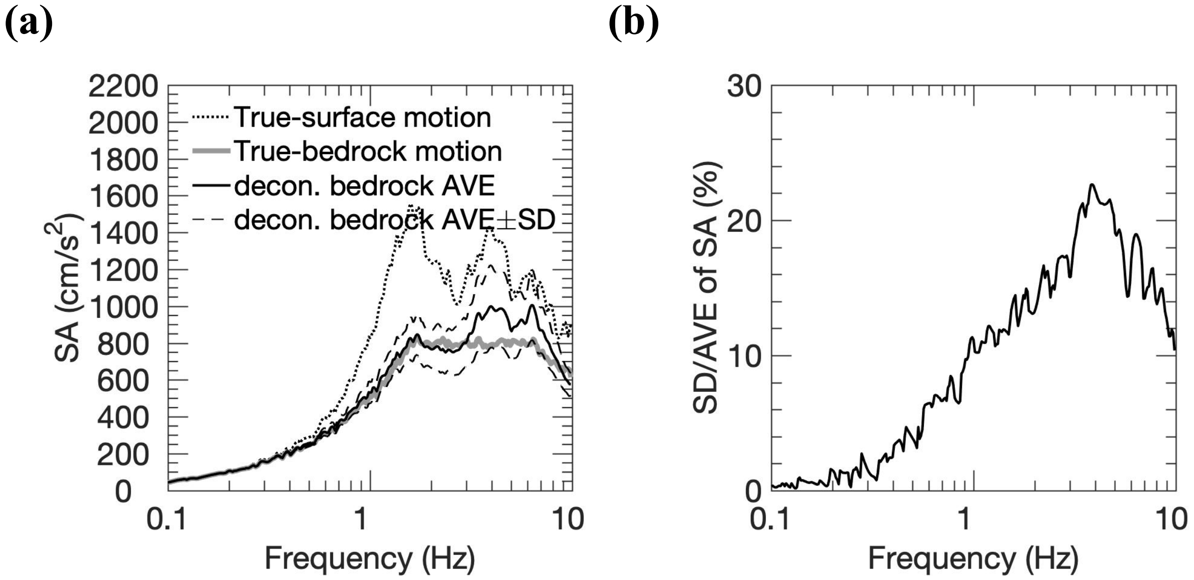

Figure 5.11 (a) Comparison between true bedrock and deconvolved bedrock SAs for the three-layer model. (b) The variation coefficient of deconvolved bedrock SA. Spectral damping of 5% is used.

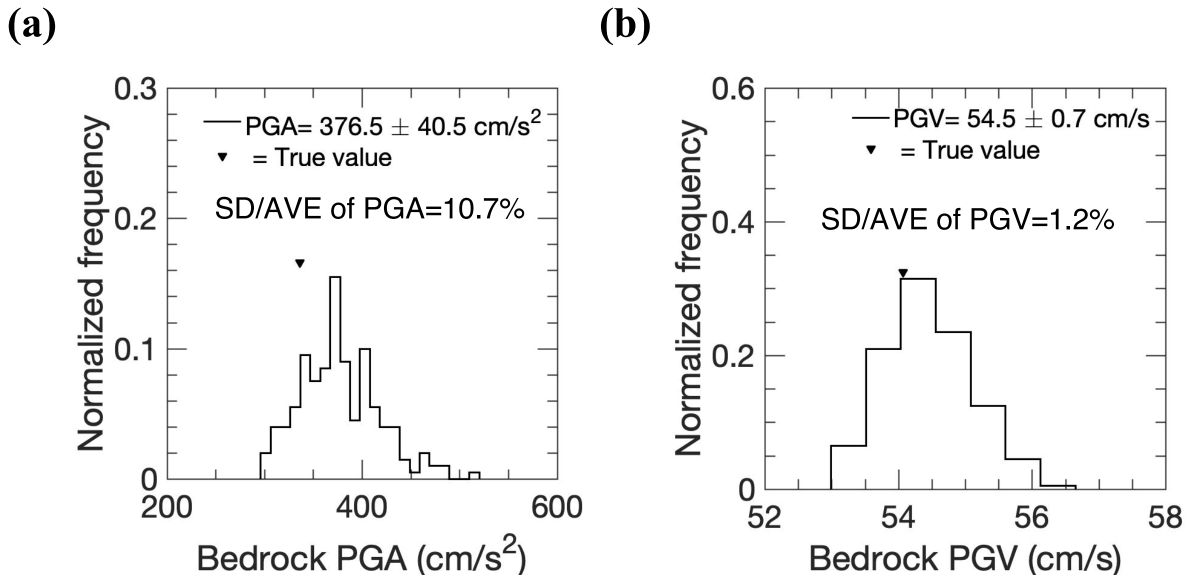

Figure 5.12 Distributions of deconvolved bedrock (a) PGA and (b) PGV for the three-layer model. The triangle shows true value for each parameter.

Comparison of calculated motions for the average or the average plus/minus the standard deviation with the true motion can be found in Figure 5.13. The figure indicates that the acceleration from the average minus the standard deviation has similar PGA as compared to that of the true value, while average and average plus standard deviation accelerations are slightly overestimated than that of true value. Overall, velocity waves for the average and the average plus/minus the standard deviation are resembling that of the true value.

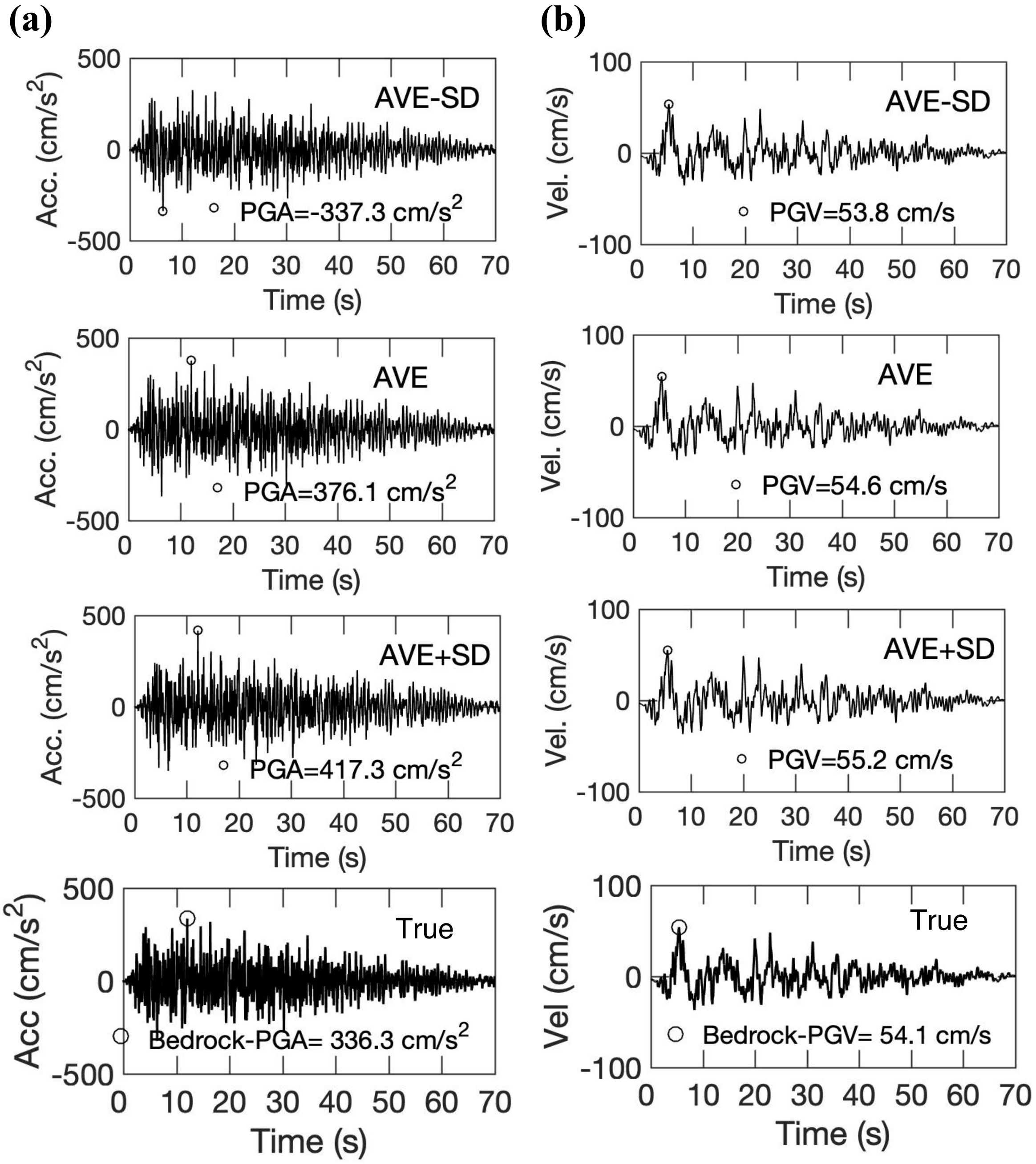

Figure 5.13 Several examples of (a) acceleration and (b) velocity waves in the three-layer model which have similar values as average (AVE), average plus/minus standard deviation (SD) of distributions of PGA and PGV as depicted in Figure 5.12.

5.5 Variability of deconvolved bedrock motion due to uncertainty of S-wave velocity model from given thickness in advance in the inversion

As previously discussed, a resolution of an S-wave velocity may be improved by giving information of layer thickness during inversion of surface-wave phase velocity. Here, I like to know the effects of uncertainty in an S-wave velocity profile of given thickness into variability of deconvolved bedrock motion. Figure 5.14(a) shows that the average bedrock SAs for the given thickness have better matching to true SA than those of unknown thickness in the two- and three-layer models. SD/AVEs of SAs for the given thickness generally lower than that of unknown thickness for both models as depicted in Figure 5.14(b), especially for the three-layer model. Furthermore, Figure 5.15 indicates that resolutions of the bedrock PGA and PGV for the given thickness are better as compared to those of the unconstrained thickness, particularly for the three-layer model.

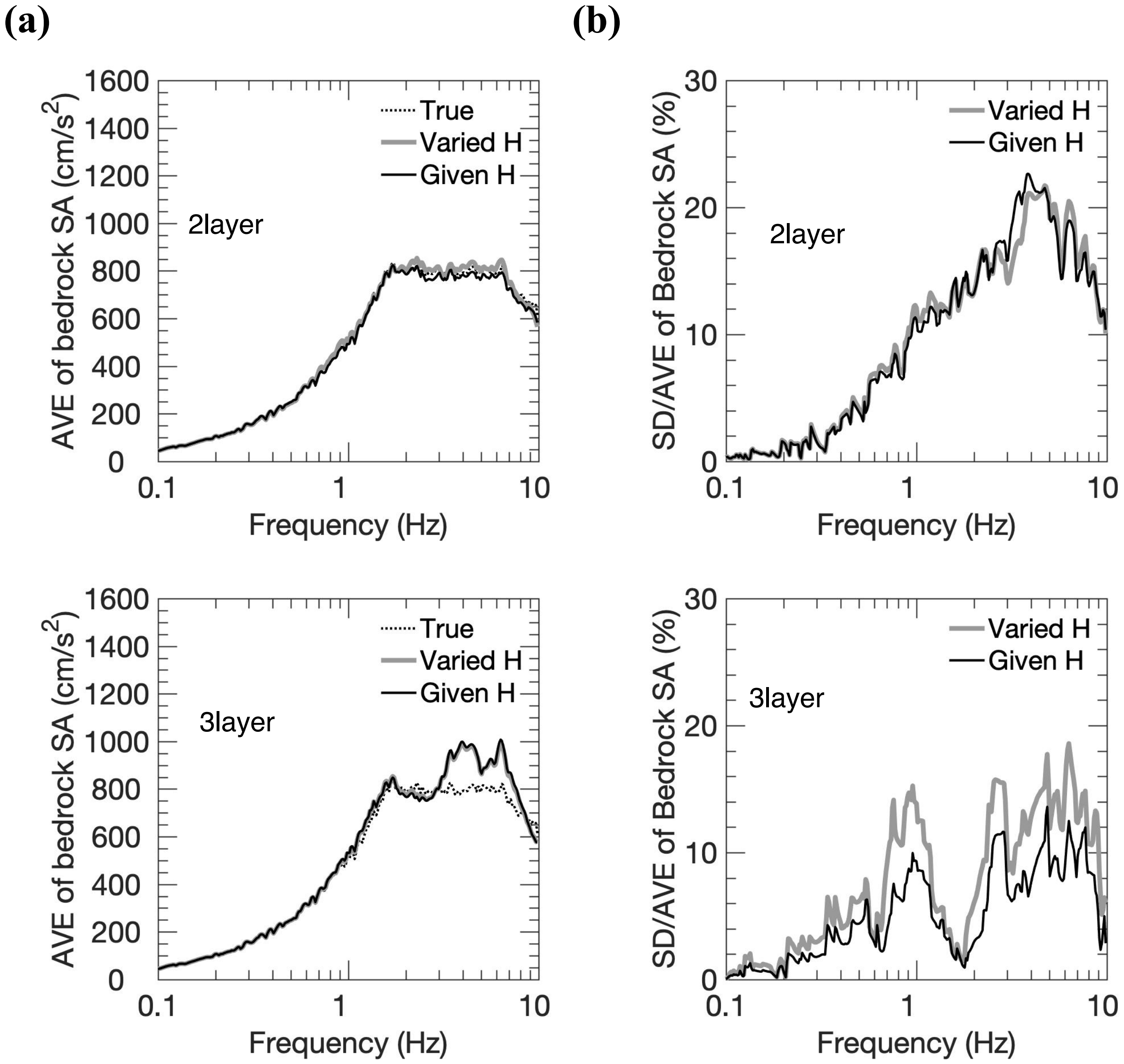

Figure 5.14 (a) Comparison between average spectral acceleration at bedrock for a varied and given thickness in two- and three-layer models. True bedrock spectral acceleration can be also found in the figure. (b) Comparison between the variation coefficient of spectral acceleration at bedrock for a varied and given thickness.

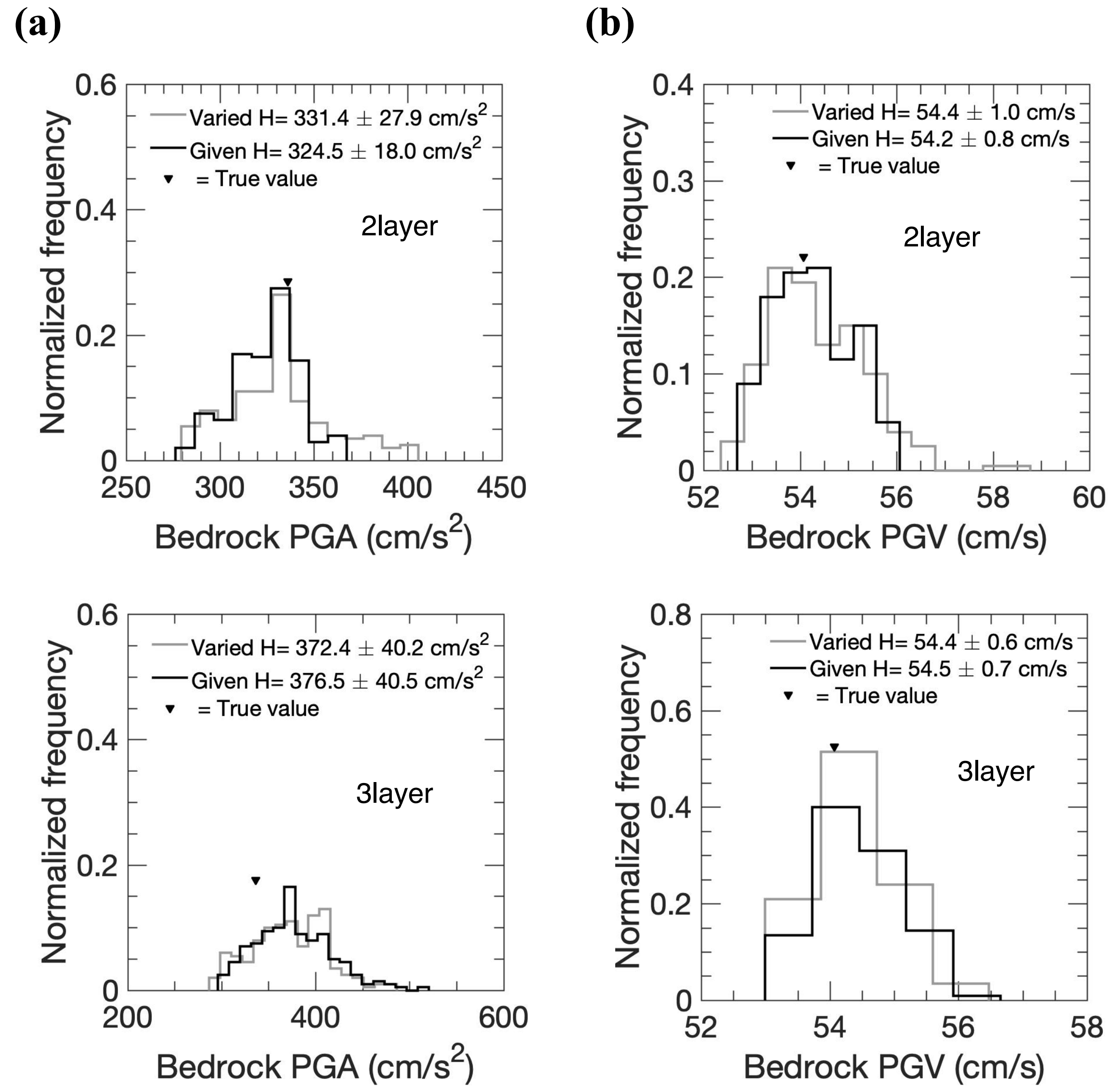

Figure 5.15 Comparison between ground motion proxies at bedrock for a varied and given thickness in two- and three-layer models. (a) PGA and (b) PGV.

5.6 Summary

I have conducted numerical experiments to estimate variability in a deconvolved bedrock motion due to uncertainty in a *Vs* profile from phase velocity inversion in the two- and three-layer models. In this experiment, I used a frequency dependent equivalent linear method (DYNEQ) instead of a conventional equivalent linear approach (SHAKE) to approximate a nonlinear response during a large motion. The spectral acceleration and distribution of ground motion proxies of deconvolved bedrock motions with their uncertainties are good agreements with the true value in the two-layer model. Furthermore, the spectral acceleration and ground motion proxies of the three-layer model with their uncertainties are decent to describe the true value. Moreover, resolution of the spectral acceleration and the ground motion proxies at the bedrock layer for a given thickness is better than those of unknown thickness, especially for the three-layer model.

Chapter 6 Application to actual data

6.1 Introduction

6.2 Strong ground motion at MYG004

6.3 Previous microtremor survey

6.4 Nonlinear soil response analysis

6.5 Results of phase velocity inversion

6.6 Deconvolution analysis

6.7 Summary

6.1 Introduction

During the 2011 off Pacific Coast of Tohoku Earthquake, with a moment magnitude (Mw) of 9.0, a large peak ground acceleration (PGA in the following) of 2700 cm/s^2 was recorded at Tsukidate station (MYG004) in Miyagi Prefecture. However, little structural damage was reported in the main part of Tsukidate Town in the north of MYG004 (e.g., Motosaka 2012). Different explanations have been proposed to describe the contradiction between the minor damage and the large ground motion. Motosaka (2012) suggested that a partially uplifting basement of the strong motion sensors was responsible for the large PGA. On the other hand, Nagashima et al. (2014) proposed that soil nonlinearity affected the large ground motion. The low damage during the main shock was explained by the ground motion's spectral characteristics at predominant periods less than 0.5 s (e.g., Irikura and Susumu 2012; Goto and Morikawa 2012). However, this suggestion was only based on the recorded waveforms at MYG004. Thus, understanding the ground motion characteristics of the main shock will help explain the contradiction between the damage and the large motion around Tsukidate Town. Yamanaka et al. (2011) proposed that local site effects caused the high ground motion, using S-wave velocity (*Vs*) profiles revealed from microtremor explorations around MYG004. Nonetheless, Yamanaka et al. (2011) did not consider observational errors in the phase velocities that may have affected the interpretation of the observed strong ground motion. Moreover, they did not estimate strong motion during the main shock in the area around MYG004, which should be considered when discussing the reasons why there was so little structural damage.

In this study, I also invert the Rayleigh wave phase velocities around MYG004, obtained by Yamanaka et al. (2011), creating a *Vs* profile with their uncertainties using the MCMC method. I apply the uncertainty in the *Vs* profiles at MYG004 to estimate the bedrock motion's variability during the main shock. Moreover, I estimate the convolved surface motion around

MYG004 to explain the contradiction between the low damage and the large acceleration in the area.

6.2 Strong ground motion at MYG004

Figure 6.1(a) shows the locations of MYG004 in the northern part of Miyagi Prefecture, the epicenters of the main shock of the 2011 Tohoku Earthquake, and moderate events with weak motion records (PGAs = 5–25 cm/s^2 at the station). In addition, the aftershock observation stations, used by Yamanaka et al. (2011), are presented in Figure 6.1(b). MYG004 was situated on a small cliff with a relatively high elevation of about 5 m (Yamanaka et al., 2011) until it was moved to a different location on December 19, 2012.

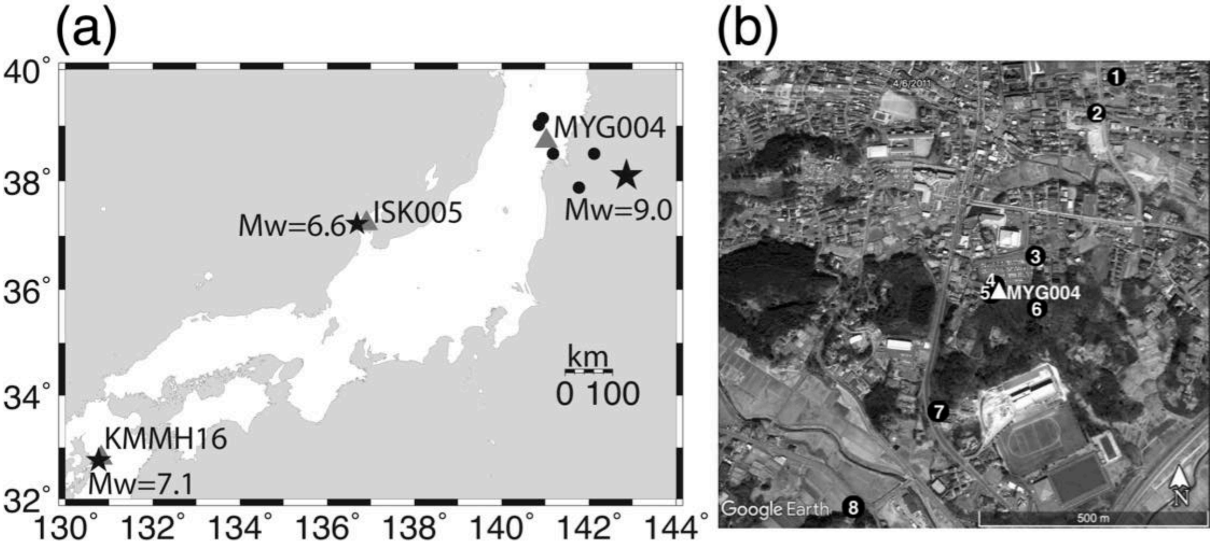

Figure 6.1 (a) Locations of MYG004 station (triangle), epicenters of the 2011 off Pacific Coast of Tohoku Earthquake (star, Mw=9.0) and moderate events (cycles) with PGAs of 5-25 cm/s^2 at MYG004. The figure also indicates the epicenters of the 2007 Noto Hanto Earthquake (star, Mw=6.6) and the 2016 Kumamoto Earthquake (star, Mw=7.1) and locations of ISK005 (triangle) and KMMH16 stations (triangle). (b) Locations of aftershock observation station (cycles with numbers) by Yamanaka et al. (2011) and MYG004 (triangle). Figure 6.1(b) is acquired from Google Earth for 6 April 2011.

The recorded surface waveforms at MYG004 gave pulse-like waveforms with PGAs of 1269 and 2700 cm/s^2 in the east-west (EW) and the north-south (NS) directions, respectively, while the vertical (UD) motion gave a PGA of 1880 cm/s^2, as shown in Figure 6.2(a). Figure 6.2(b) shows the Fourier amplitude spectra for the EW and NS directions with peaks at periods between 0.15 and 0.3 s. I selected a time window of 140 s from the original motions (Figure 6.2(a)) for spectral analysis. Then, I filtered the horizontal motions in the period range of 0.1–10 s (Figure 6.2(c)) for further deconvolution analysis, considering periods of engineering interest. Nevertheless, the filtered horizontal motions still show significant peaks with PGAs of 1009 and 2207 cm/s^2.

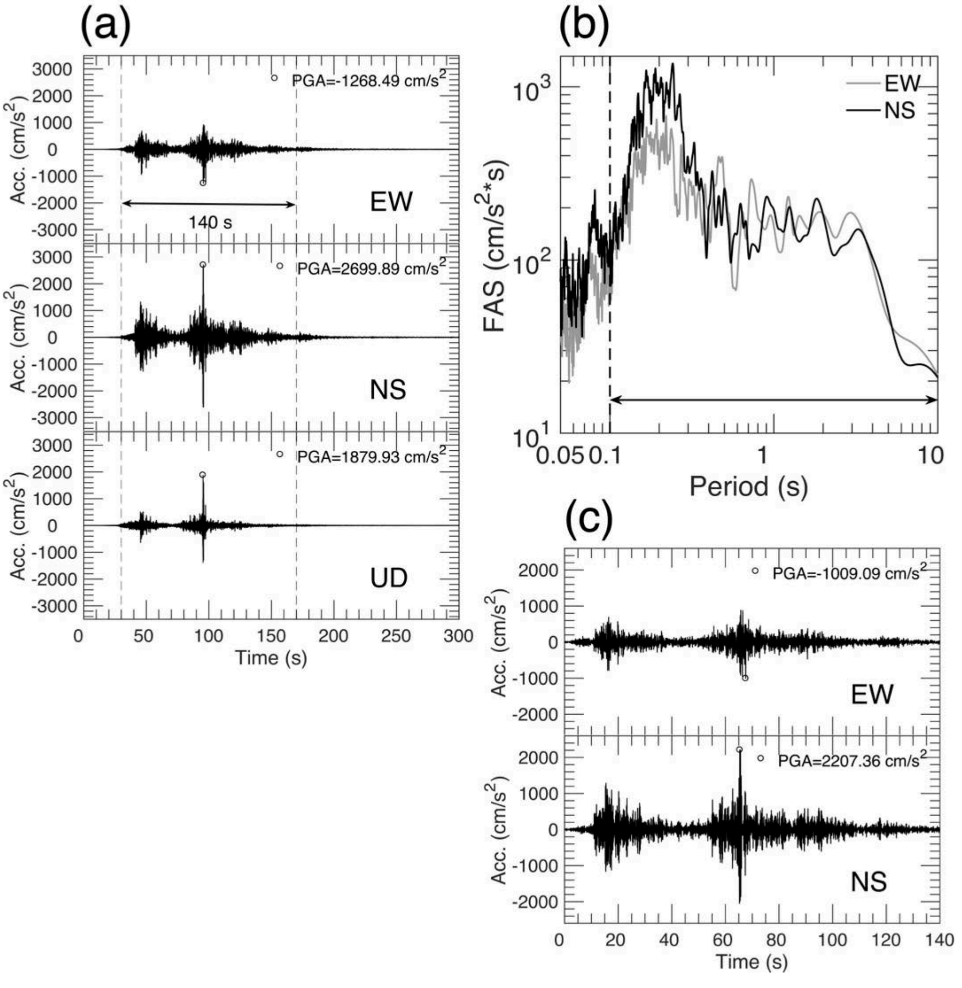

Figure 6.2 Observed strong motion. (a) Original surface motions and (b) Fourier amplitude spectra (FAS) of main shock for EW and NS directions at MYG004. (c) Filtered acceleration wave (Acc.) in a period range of 0.1-10 s for 140 seconds of time window.

6.3 Previous microtremor survey

To understand the ground motion characteristics in the area around MYG004, Yamanaka et al. (2011) observed the aftershocks recorded at sites 1 to 8 (Figure 6.1(b)). Sites 4 and 5 were located less than 30 m from MYG004. Site 4 was situated on the cut ground, while site 5 was placed on the cliff near MYG004. Sites 3 and 6 were located at the foot and at the top of the hill, respectively, where sites 4 and 5 were located. Sites 1 and 2 were placed in a flat area covered with Quaternary sediments, while sites 7 and 8 were positioned at relatively low elevations. They also conducted microtremor explorations at the aftershock observation sites, except for site 6, in order to deduce shallow Vs profiles.

In this study, I reanalyze the phase velocity of the Rayleigh waves at sites 1-5 and 8, considering observational errors. I excluded a result of a phase velocity at site 7, because the surface of this site was covered probably with a thick concrete slab at a gas station. The Vs profile at site 5 is used to estimate bedrock motions because its geological conditions were similar to those in MYG004. Meanwhile, the Vs profiles at sites 1-4 and 8 with different geological conditions are employed to estimate surface motions around Tsukidate Town.

The Rayleigh wave phase velocities were obtained by the SPAC method of microtremor array data (Yamanaka et al., 2011). They used two triangle arrays with seven vertical sensors at each site as depicted in Figure 6.3. The figure also indicates that there are ten array sizes (r) based on station pairs. The array sizes of the first measurement are $2R_1$ (3 pairs), $\sqrt{3}R_1$ (3 pairs), $2R_1/\sqrt{3}$ (3 pairs), R_1 (9 pairs), and $R_1/\sqrt{3}$ (3 pairs). The array sizes of the second measurement are $2R_2$ (3 pairs), $\sqrt{3}R_2$ (3 pairs), $2R_2/\sqrt{3}$ (3 pairs), R_2 (9 pairs), and $R_2/\sqrt{3}$ (3 pairs).

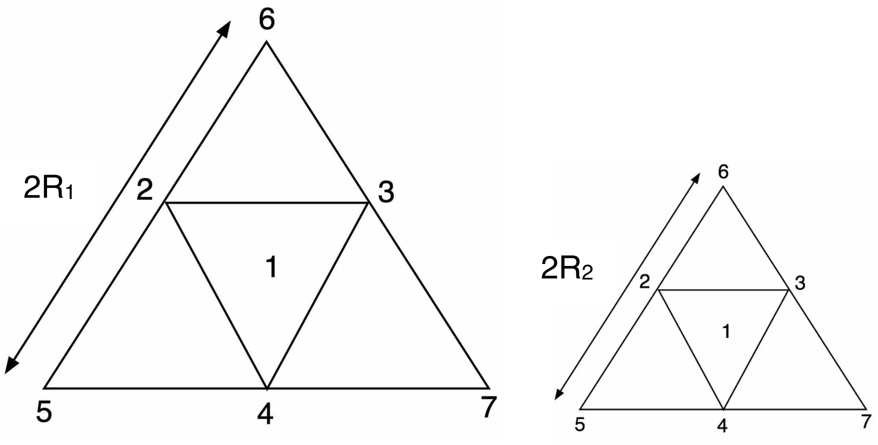

Figure 6.3 Microtremor measurements of the SPAC method using seven sensors (Sensors 1 to 7). First and second maximum array sizes of $2R_1$ and $2R_2$, respectively. $2R_1$ is larger than $2R_2$.

A phase velocity is estimated by an average of the SPAC coefficient ($\bar{\rho}(f,r)$) using ensemble average (block averaging) of power spectra and cross spectra of each segment of microtremor records (e.g., Ohori et al., 2002; Okada, 2003). The power and cross spectra are calculated for each station and pair of stations, respectively. Station pairs are indicated by *j* and *k*. $\bar{\rho}(f,r)$ is a function of frequency (*f*) and array size and defined as

$$\bar{\rho}(f,r)=\frac{\left\langle \hat{G}_{jk}(f,r)\right\rangle}{\sqrt{\left\langle \hat{G}_{jj}(f,r)\right\rangle}\sqrt{\left\langle \hat{G}_{kk}(f,r)\right\rangle}}, \tag{6.1}$$

where, $\hat{G}_{jj}(f,r)$ and $\hat{G}_{kk}(f,r)$ are power spectra at stations *j* and *k*, respectively. Meanwhile, $\hat{G}_{jk}(f,r)$ is cross-spectra at stations *j* and *k*. A hat symbol (^) over a quantity G_{jj} indicates an estimate of G_{jj} based on a finite time interval (e.g., Bendat and Piersol, 2010). Assuming x_j(t) and x_k(t) are recorded microtremors at stations *j* and *k* with the total recorded time T_r. The record can be divided into n_d continuous segments, each of length *T*. Thus, I obtain the following equation

$$T_r = n_d T \,. \qquad 6.2$$

Hence, the Fourier spectra's microtremor signals at stations *j* and *k* are $X_j(f)$ and $X_k(f)$ for length *T,* respectively. A star symbol (*) indicates a conjugate their corresponding Fourier spectrum. The expected values of power spectra and cross spectra at stations *j* and *k* are estimated by Equations 6.3-6.5.

$$\left\langle \widehat{G}_{jj}(f,r) \right\rangle = \frac{1}{n_d T} \sum_{i=1}^{n_d} \left| X_{jj}^{i}(f) \right|^2 , \qquad 6.3$$

$$\left\langle \widehat{G}_{kk}(f,r) \right\rangle = \frac{1}{n_d T} \sum_{i=1}^{n_d} \left| X_{kk}^{i}(f) \right|^2 , \qquad 6.4$$

$$\left\langle \widehat{G}_{jk}(f,r) \right\rangle = \frac{1}{n_d T} \sum_{i=1}^{n_d} X_j^{*,i}(f) X_k^{i}(f) . \qquad 6.5$$

The ensemble average reduces variance errors (Var) of the spectral power and cross spectra as an increase of n_d as depicted in Equations 6.6-6.8 (e.g., Bendat and Piersol, 2010). Therefore, I can use the average of the SPAC coefficient from ensemble averages of the power spectra and cross spectra for estimation of a phase velocity.

$$\mathrm{Var}\left[\hat{G}_{jj}(f,r) \right] = \frac{G_{jj}^2(f,r)}{n_d} , \qquad 6.6$$

$$\mathrm{Var}\left[\hat{G}_{kk}(f,r) \right] = \frac{G_{kk}^2(f,r)}{n_d} , \qquad 6.7$$

$$\mathrm{Var}\left[\left| \hat{G}_{jk}(f,r) \right| \right] = \frac{\left| G_{jk}(f,r) \right|^2}{\rho^2(f,r)\, n_d} . \qquad 6.8$$

Where $G_{jj}(f,r)$ and $G_{kk}(f,r)$ are power spectra at station *j* and *k* for the microtremor record *T_r*, respectively. Moreover, $G_{jk}(f,r)$ and $\rho(f,r)$ are cross spectra and a SPAC coefficient for the record time T_r, respectively.

Alternatively, the power spectra and the cross spectra can be also approximated by smoothing the power spectra and cross spectra (e.g., Bendat and Piersol, 2010; Okada, 2003), using Equations 6.9 and 6.10 (e.g., Bendat and Piersol, 2010),

$$b \approx \Delta f = \frac{1}{T} \; . \tag{6.9}$$

Where Δf and b are frequency resolution and bandwidth resolution. Substituting Equation into 6.9 into 6.2, I obtain following equation

$$n_d = \left(\frac{T_r}{T} \right) \approx bT_r \cdot \tag{6.10}$$

Equation 6.10 shows that the reduction of spectral variations of the power spectra and the cross spectra of due to n_d in ensemble average can be also done by smoothing the spectra with bandwidth resolution b. In this study, the cross spectra and the power spectra were smoothed by Parzen window ($W(f)$) as the following equations

$$b = \frac{1}{\int_{-\infty}^{\infty} W^2(f)\,df} \tag{6.11}$$

and

$$W(f) = \frac{3}{4} u \left(\frac{\sin \frac{\pi u f}{2}}{\frac{\pi u f}{2}} \right)^4 , \tag{6.12}$$

where u is constant in second.

Assuming, total recorded signal T_m is divided into N segments with time T_s for each segment. An average of the SPAC coefficient for each segment can be obtained from the smoothed power spectra and cross spectra. Then, the average of the SPAC coefficient with the same array size is averaged by their number of station pairs (e.g., $r = 2R_1$ has three station pairs). Hence, I can obtain the final average of the SPAC coefficient ($\bar{\rho}(f,r)$) from the average of the SPAC coefficient for different segments ($\rho_i(f,r)$) with the same array size (e.g., $r = 2R_1$) using following equation

$$\bar{\rho}(f,r) = \frac{1}{N}\sum_{i=1}^{N}\rho_i(f,r) . \tag{6.13}$$

Moreover, I can estimate the standard deviation of the SPAC coefficient ($\bar{\rho}(f,r)$) by this equation

$$\sigma_\rho(f,r) = \sqrt{\frac{1}{N}\sum_{i=1}^{N}\left(\rho_i(f,r) - \bar{\rho}(f,r)\right)^2} . \tag{6.14}$$

I can obtain the average of phase velocity ($\bar{C}(f,r)$) by fitting $\bar{\rho}(f,r)$ to a zeroth-order Bessel function ($J_0(.)$) using following equation

$$\bar{\rho}(f,r) = J_0\left(\frac{2\pi rf}{\bar{C}(f,r)}\right). \tag{6.15}$$

Equation 6.15 indicates that a phase velocity (C) also depends on a SPAC coefficient (ρ). Therefore, I can express the phase velocity as a function of the SPAC coefficient, the frequency, and the array size as following

$$C = C\left(\rho, f, r\right) \cdot \tag{6.16}$$

Hence, the standard deviation ($\sigma_C\left(\rho, f, r\right)$) of the phase velocity can be estimated from $\sigma_\rho\left(f, r\right)$ using the theory of error propagation as following

$$\sigma_C\left(\rho, f, r\right) = \frac{\partial C}{\partial \rho}\sigma_\rho\left(f, r\right) \tag{6.17}$$

assuming there are no errors for r and f. Moreover, $\frac{\partial C}{\partial \rho}$ can be estimated numerically.

I also estimated the average and standard deviation of the phase velocities for other array sizes by smoothing the cross spectra and the power spectra. The phase velocities with different array sizes are used for determination of the final phase velocity. For instance, the phase velocities with the largest array size ($2R_1$) and the lowest array size ($R_2/\sqrt{3}$) are responsible for the final phase velocity in low and high frequency ranges, respectively. In this study, for example, site 1, T_s and T_m were 40.96 s and about 20 minutes (1,200 seconds), respectively. Hence, N was about 30 samples (T_m/T_s). Moreover, the largest and the smallest array sizes were 12 and 1.5 m, respectively. b was set to be 0.05 Hz. Similar analyses were conducted for other sites.

Okada (2003) assumed that microtremors are a stochastic (random) process. The first assumption that within a certain extent of space, microtremors are both temporally and spatially a stochastic process. The second assumption is a microtremor record at a certain point over a limited period of time within the same domain can be regarded as a sample record (or sample function) of the stochastic process. The first assumption indicates that the probability density function is not dependent on either space or time. In other words, if a probability density function of the amplitude of microtremors is determined once for a point of time, then the form of the function does not vary over much larger periods of time. Moreover, I assumed partial stationarity for each segment in the analysis. This partial stationarity is also assumed to be similar to the stationarity for the mother population. Therefore, I assumed that the standard deviation of the phase velocity using only 20 minutes recorded signals can be enough instead of using very long recorded signals (e.g., 100-1000 days) based on the above assumptions. Furthermore, considering high frequency range of the phase velocities around Tsukidate city are including total waves about 4,800 (1,200 s x 4 Hz)-36,000 (1,200 s x 30 Hz) at the lowest and highest frequencies, respectively.

The observed phase velocities with their observational errors around MYG004 can found in Figure 6.4. The observational error is quite high for each site as shown in the figure. Variation coefficients (SD/AVEs) of the phase velocities in low frequency range are generally higher than that of high frequency range for site 1-3 and 8. Meanwhile, sites 4 and 5 have higher variation coefficients in the high frequency range than that of the low frequency range. Moreover, the SD/AVE of the phase velocity at site 2 is more than 200% in the low frequency range.

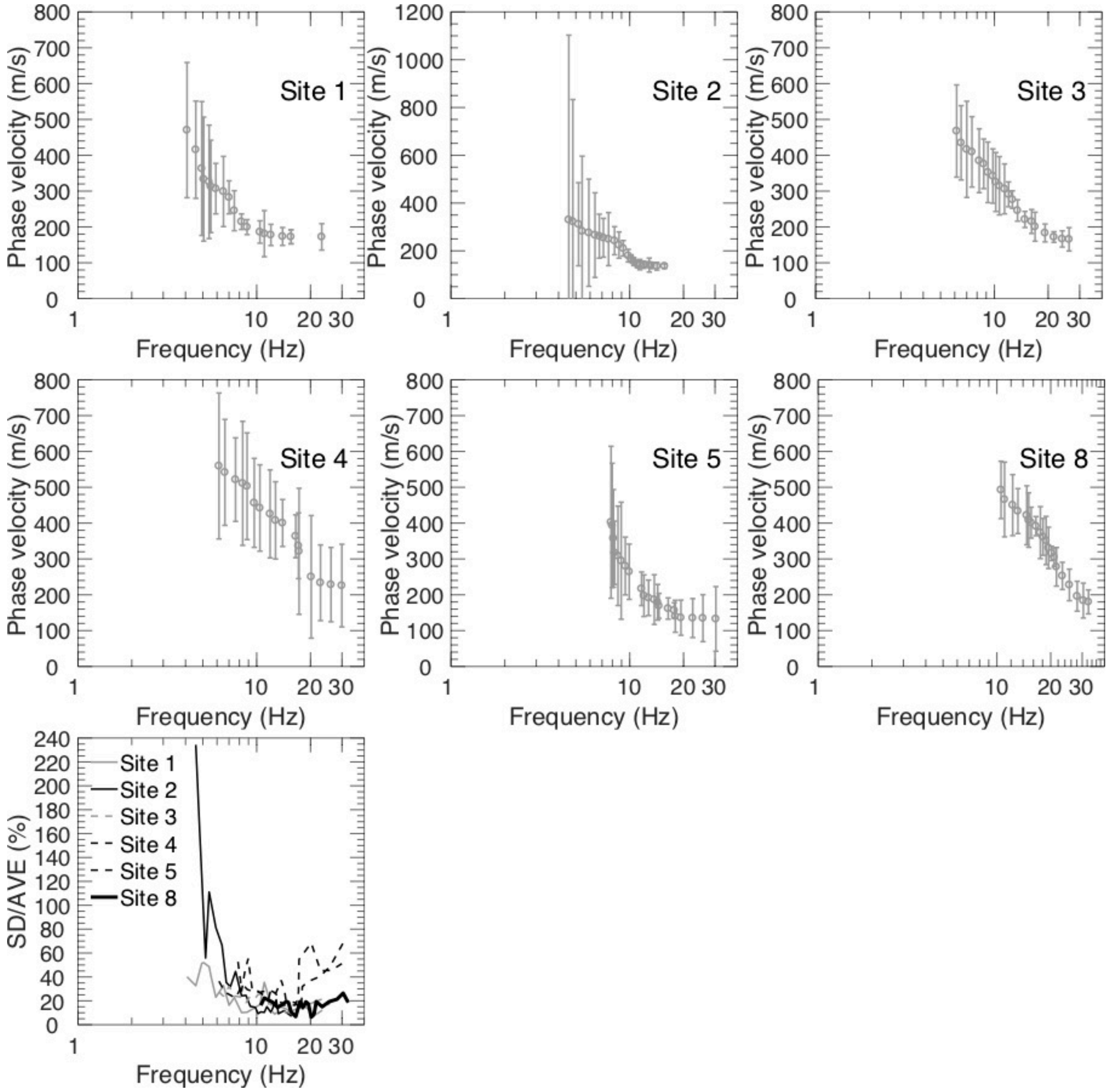

Figure 6.4 Observed phase velocities with its observational errors around MYG004. Their variation coefficient for each site can be also found in the figure.

6.4 Nonlinear soil response analysis

I used the variation of the inverted S-wave velocity models from the MCMC inversion for the deconvolution and convolution of the earthquake ground motions at sites 5 and other sites, respectively. Equivalent linear methods have been widely applied for deconvolution and convolution analyses (e.g., Di Giulio et al. 2014; Ko et al. 2009), particularly in the engineering community. In this study, I used a frequency-dependent, equivalent linear method (DYNEQ) to approximate the nonlinear soil responses for the deconvolution and convolution due to the large PGA of the surface motions at MYG004. DYNEQ has an advantage over conventional equivalent linear techniques, such as SHAKE by Idriss and Sun (1992). SHAKE significantly reduces the high frequency signal and, therefore, it is inappropriate when there are large strain motions in soft soil (e.g., Yoshida et al. 2002; Hartzell et al. 2004). To overcome this drawback, DYNEQ considers the effective strain as the frequency-dependent features of soil layers (Yoshida, 2015; Yoshida et al., 2002).

I used the filtered surface acceleration motions (Figure 6.2(c)) to estimate the deconvolved bedrock motion beneath MYG004. A three-layer model at site 5 was used in the analysis. I assumed the first layer was clay during the nonlinear analysis, whereas the second layer was assumed to be firm, as shown in Table 6.1. The nonlinear soil behavior was only modeled in the first layer, while the second layer behaved as a linear layer. In this analysis, I adopted the soil type for MYG004, as depicted in Figure 6.5(a). I used normalized rigidity (shear modulus) and a damping factor for the clay based on the Japanese standard building code (Figure 6.5(b)). During the linear analysis, the rigidity and the damping factor were assumed at the lowest strain level. Moreover, the damping and the rigidity at the engineering bedrock layer were also assumed to be the same as at the lowest strain level.

Table 6.1. Search limits for parameters in phase velocity inversions and soil type assumption

No	Search limits										ρ (g/cm^3)	Soil type assumption
	Site 1		Site 2		Site 3	Site 4	Site 5		Site 8	Site 3, 4, and 8		
	Vs (m/s)	H (m)	Vs (m/s)	H (m)	Vs (m/s)	Vs (m/s)	Vs (m/s)	H (m)	Vs (m/s)	H (m)		
1	100-250	1-15	100-200	1-10	100-220	100-350	80-250	1-8	120-220	1-10	1.64	Clay
2	220-450	1-25	150-350	10-50	220-400	220-450	220-400	1-25	220-400	1-25	1.88	Rock
3	300-750	-	250-1100	-	350-750	400-800	350-750	-	380-700	-	2.0	Engineering bedrock

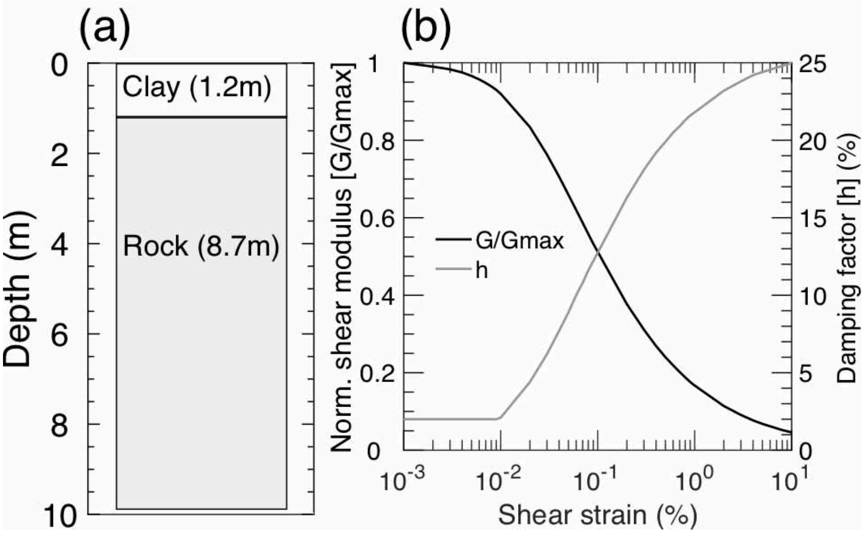

Figure 6.5 (a) Soil column of MYG004 by National Research Institute for Earth Science and Disaster (NIED). (b) Normalized shear modulus (G/Gmax) and damping factor (h) of clay in Japanese standard building code. G/Gmax and h of the clay can be found in DYNEQ code.

6.5 Results of phase velocity inversion

In the inversion of the phase velocities at sites 1-5 and 8, I assumed that the shallow profile consists of the three layers as similar to those of the logging result at MYG004 and to the previous study by Yamanaka et al. (2011). The model parameters' search limits can be seen in Table 6.1.

The sampling results for the MCMC inversion at site 5 are summarized in Figure 6.6(a). I executed five runs with 100,000 iterations using different initial values. Therefore, a total of 500,000 models were produced. The figure indicates that the chains of Vs_1 (S-wave velocity of the first layer) tend to be similar each other. On the other hand, the individual chains of Vs_2 and Vs_3 show different evolutions. The H_1 chains are fairly similar, whereas the H_2 chains vary. However, I still managed to find a stationary state for each model parameter using the Geweke's technique. The maximum Z-values of all parameters were estimated from the averages of the all parameter evolutions in Figure 6.6(a). Figure 6.6(b) shows the maximum Z-values of all parameter averages against the different burn-periods. A total of 125,000 models were discarded. Hence, I employed the 375,000 sampled models after the burn-in periods to estimate the distributions of the velocities and thicknesses as presented in Figure 6.7(a) and (b), respectively. The sampling results of sites 1-4 and 8 can be found in Appendix A.

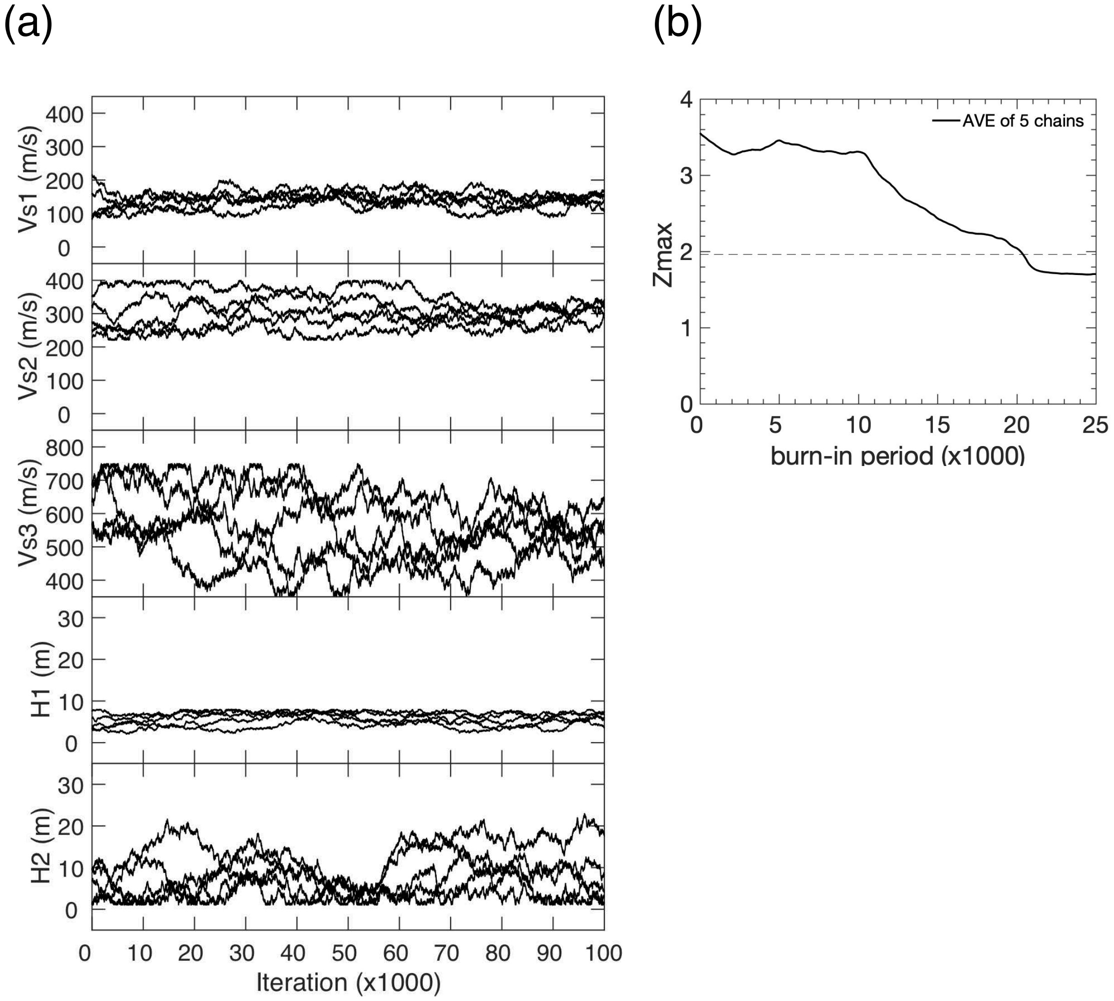

Figure 6.6 Results of the MCMC sampling in an inversion of phase velocity at site 5. (a) evolutions of S-wave velocities of first, second, and third layers, following by thicknesses of first and second layers obtained from five tests from top to bottom, respectively. The chains are averaged to estimate the maximum Z-value. (b) Relationship of the maximum Z-values and different burn-in periods. A broken horizontal line indicates a Z-value of 1.96.

I normalized each parameter's frequency distribution by its area (Figure 6.7) for a probability density function. Moreover, a final model and its uncertainty were developed from the average and standard deviation of the sampled model distributions, respectively. Furthermore, the upper and lower possible values of the model parameters in this study were defined as the average plus the standard deviation and the average minus the standard deviation, respectively. Figure 6.7 (a) indicates that the Vs_1 has the narrowest distribution compared to those of Vs_2 and Vs_3. The distribution of H_1 is also narrower than that of H_2 (Figure 6.7(b)). The narrow distributions of Vs_1 and H_1 are caused by sufficient coverage of the observed phase velocity in the high frequency range, while Vs_2 and H_2 have wide distributions due to the insensitiveness of the parameters of the second layer. Furthermore, Vs_3 has also a wide distribution, probably due to insufficient coverage of the observed phase velocity, in the frequency range below 8 Hz. The actual distribution of H_2 cannot be approximated with the normal distribution since it has a non-symmetrical distribution. It is caused by the incompleteness of the phase velocity at frequencies less than 8 Hz as depicted in Figure 6.4.

Next, I selected 200 examined models after the burn-in period, to speed up the later calculation, since the calculation of a nonlinear amplification using DYNEQ takes quite long for a large number of soil models as I mentioned in Chapter 5. The selected 200 models had similar distributions to the re-sampled model parameters. I compared the distributions of all parameters and the 200 re-sampled models for site 5 (Figure 6.7). The comparisons show that the two distributions are quite similar for all parameters, indicating that the re-sampled models contain statistical features that are similar to the sampled models. I use the re-sampled models for further analysis. I eventually estimated a final inverted model from the average of the re-sampled 200 models at site 5. Furthermore, I repeated the same process to determine the sampled models at site 1-4 and 8. The distributions of the model parameters at sites 1-4 and 8 can be found in Figure 6.8. The figure indicates that some model parameters at different sites have unsymmetrical distributions. It is mostly caused by the absences of the phase velocities in the low frequency range as depicted in Figure 6.8.

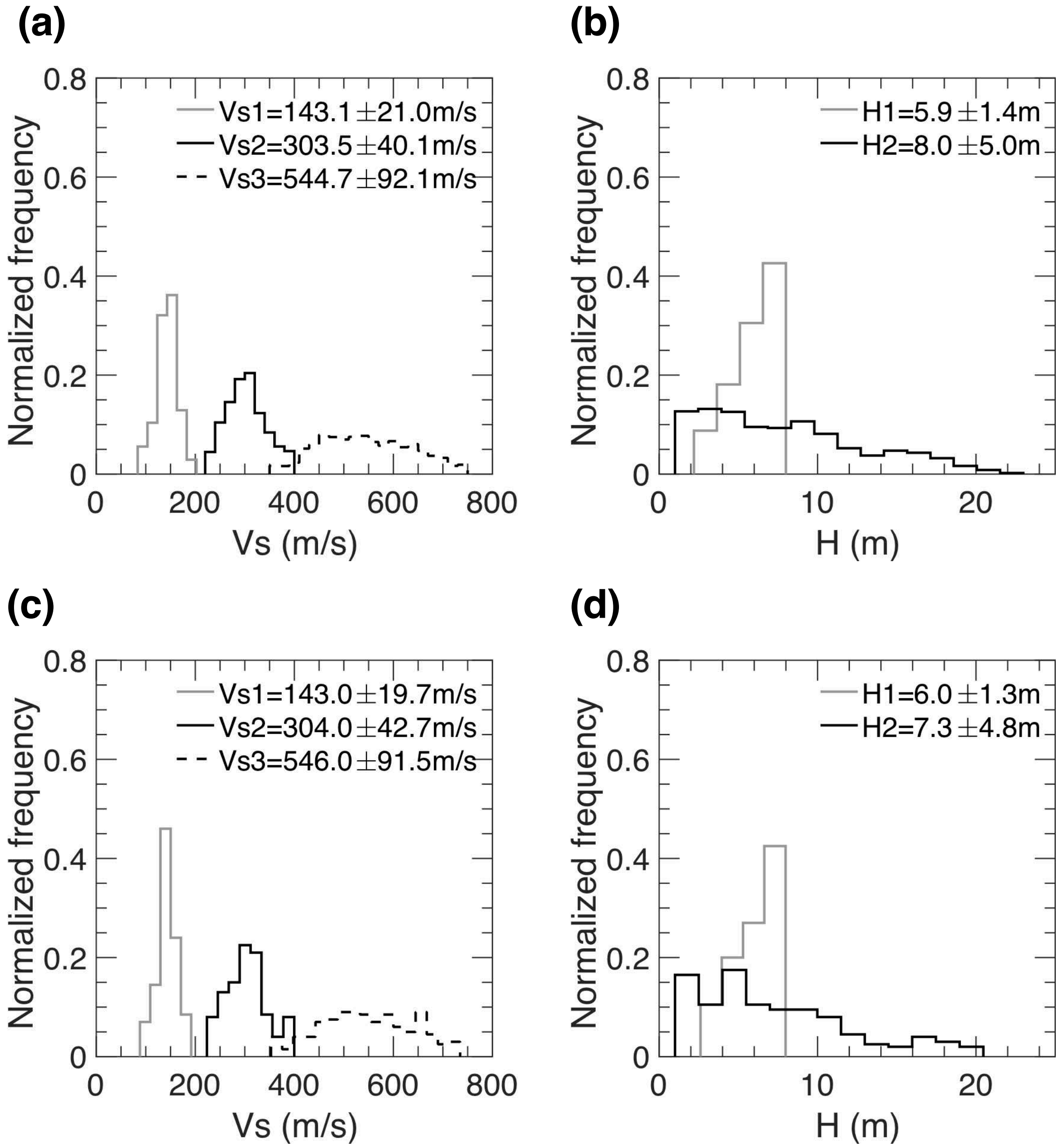

Figure 6.7 Distributions of S-wave velocities and thicknesses of sampled models at site 5. Distributions of (a) S-wave velocities and (b) thicknesses for all sampled models. Distributions of (c) S-wave velocities and (d) thicknesses for 200 resampled models.

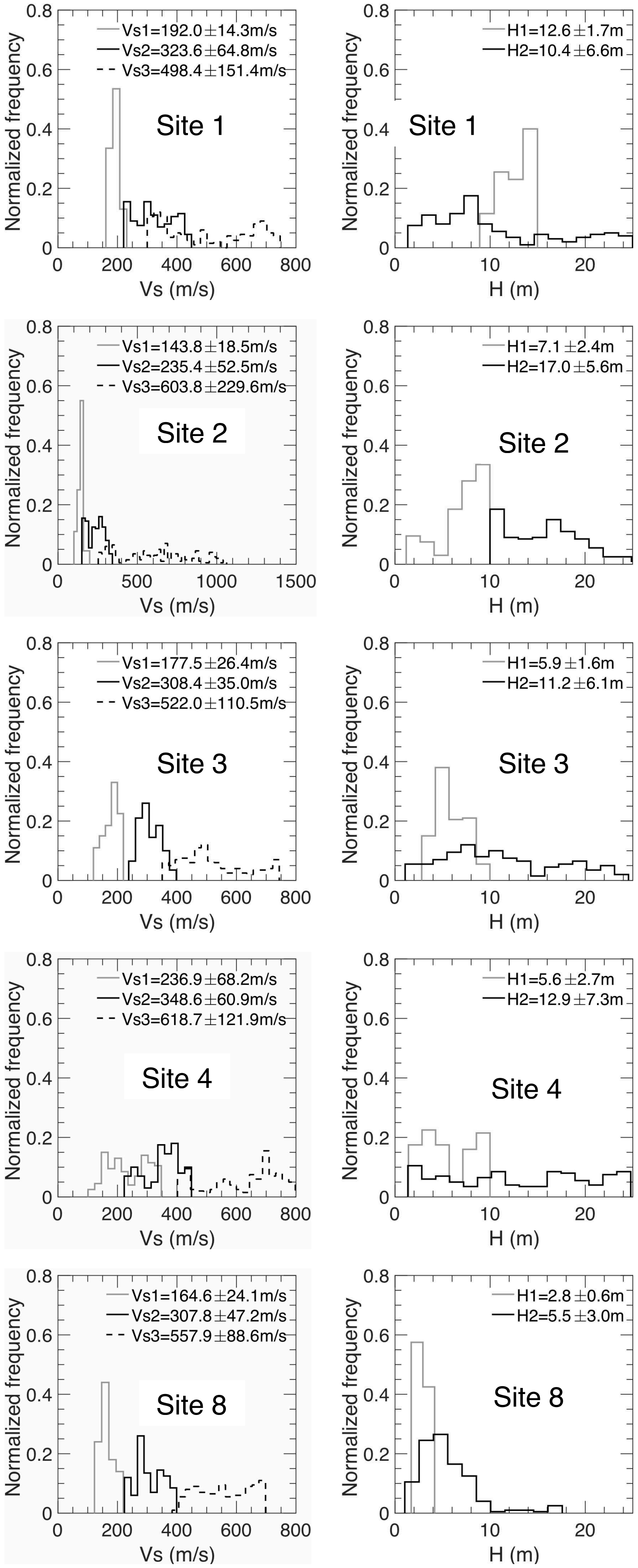

Figure 6.8 Distributions of (a) S-wave velocities and (b) thicknesses at sites 1-4 and 8.

The final S-wave velocity profiles at sites 1-5 and 8 are depicted in Figure 6.9. I also show the *Vs* profile according to Yamanaka et al. (2011) in the same figure. My *Vs* profile has similar S-wave velocities and thicknesses in the first and third layers with those of Yamanaka et al. (2011) for sites 1-5 and 8. The basement depths of the two models are also similar. Except site 3, there are slight differences in the second layer between the two models at each site. However, these are considered insignificant when taking the uncertainty in my *Vs* profiles into account. Yamanaka et al. (2011) used a hybrid of the genetic algorithm and simulated annealing (Yamanaka, 2007) in their inversions of the phase velocities. The differences in the two final inverted models occur because the hybrid heuristic method only tries to find an optimal model with the smallest misfit. Meanwhile, the MCMC inversion attempts to find a distribution of the model parameters. Then, the final model is obtained from the averages of the model distributions, which is not necessarily the same as the model with the lowest misfit. Moreover, as similar to Yamanaka et al. (2011), sites 1 and 2 have thick surface layers over the bedrock with an S-wave velocity of more than 500 m/s, while the depth to the bedrock is shallow at site 8 as depicted in Figure 6.9.

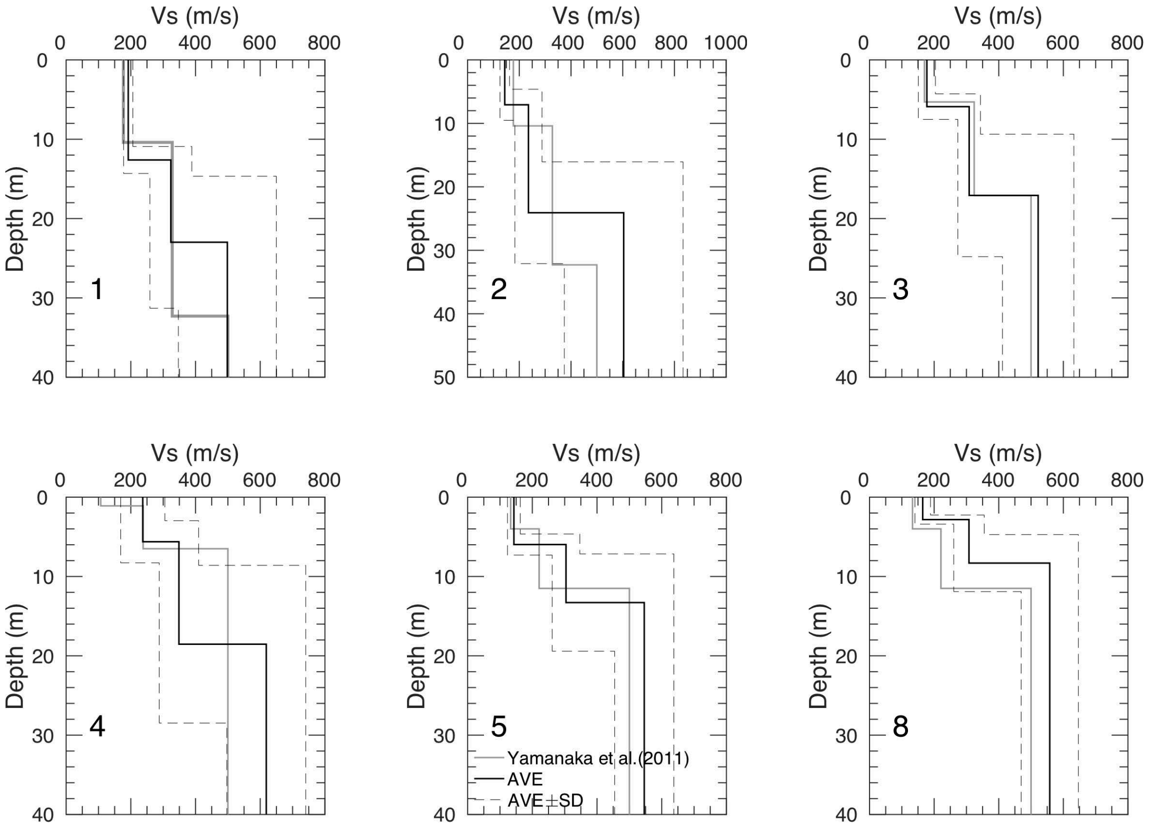

Figure 6.9 Average (AVE) and average plus/minus its standard deviation (AVE±SD) for inverted *Vs* profile at sites 1-5 and 8 for 200 re-sampled models. *Vs* profile by Yamanaka et al. (2011) are also shown in the figure.

The calculated phase velocity for my model is quite similar to that of Yamanaka et al. (2011), as shown in Figure 6.10. My average of the theoretical phase velocity could explain well the observation in high frequency ranges (>8 Hz) at each site. Meanwhile, the average calculated phase velocity is underestimated than that of the observed phase velocity in low frequency ranges (<8 Hz) due to the absence of the phase velocity in the low frequency ranges at each site. However, the theoretical phase velocities for the inverted models, with their upper and lower possible values, in this study can explain the observed phase velocities at sites 1-5 and 8

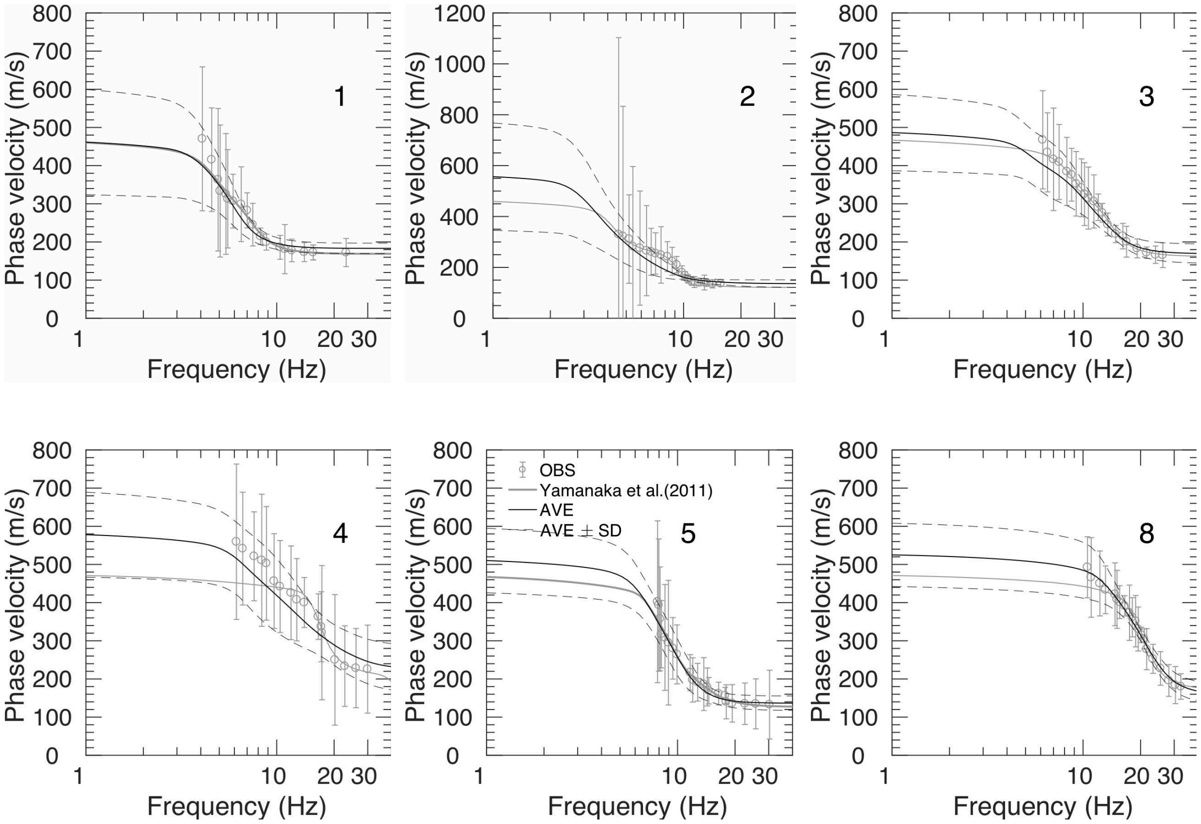

Figure 6.10 Average (AVE) and average plus/minus its standard deviation (AVE±SD) for theoretical phase velocity at sites 1-5 and 8 for 200 re-sampled models. Theoretical phase velocity by Yamanaka et al. (2011) are also shown in the figure.

6.6 Deconvolution analysis

6.6.1 Deconvolution analysis at site 5

I examine the performance of the inverted *Vs* profiles at site 5 in characterizing ground motion features by comparing their theoretical linear amplification factors to the weak motion spectra observed at MYG004. The response spectral velocities of the weak motion records during the moderate events, with PGAs ranging from 5–25 cm/s^2, are shown in Figure 6.11(a). The epicenters of these events are shown in Figure 6.1(a). The response spectra are characterized by single peaks at periods of 0.1–0.2 s. Figure 6.11(b) shows the 1D linear amplification factors for the three *Vs* profiles derived from the velocity logging, the inversions of the phase velocity by Yamanaka (2011), and this study. My amplification in the figure was achieved by averaging those of the re-sampled 200 models. These observed peaks cannot be explained by the linear amplification features for the logging profile, having peaks at periods less than 0.07 s. Even though there are differences in the amplification factors between my study and Yamanaka et al. (2011) at a high frequency, the linear amplifications can explain the observed peaks at the period of around 0.1–0.2 s. The observed spectra and the spectra from my inverted model do not contain many peaks and troughs at periods less than 0.1 s. However, the linear amplification from the logging profile and Yamanaka et al. (2011) have many peaks and troughs. Therefore, I used the *Vs* profile with its uncertainty from the MCMC inversion of the phase velocity at site 5 in the following analysis, instead of those of the velocity logging and Yamanaka et al. (2011).

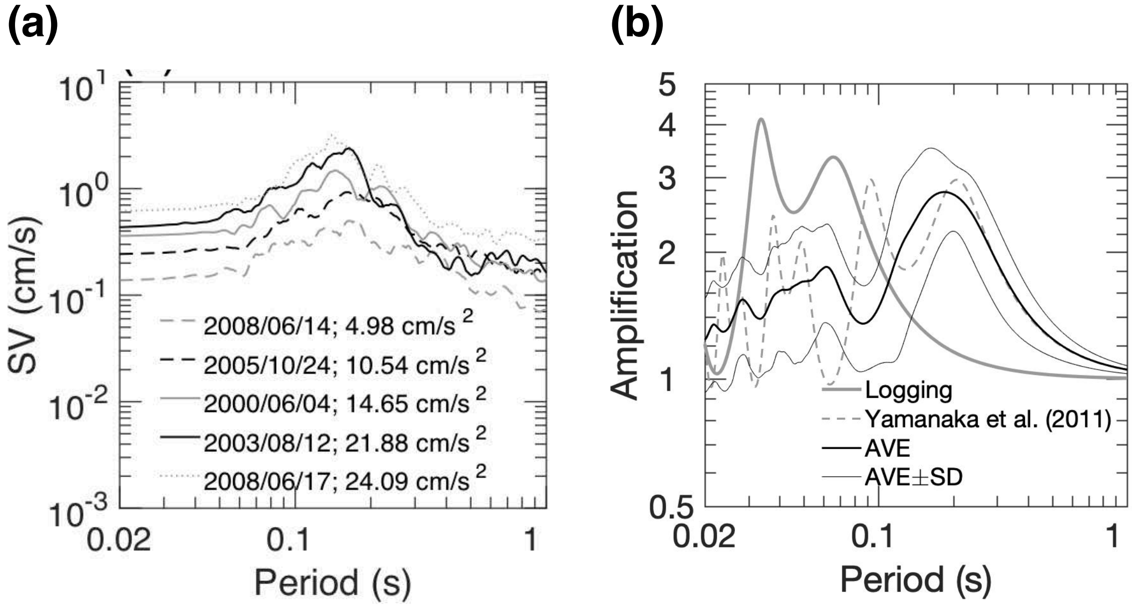

Figure 6.11 Comparison of linear amplification with the observed spectral velocity (SV) at MYG004**.** (a) SV at MYG004 for weak motion records with PGAs of 5-25 cm/s^2. Date of each earthquake is presented in a format of year/month/day. (b) Comparison between linear amplification factors for three *Vs* profiles from logging at MYG004, by Yamanaka et al. (2011), and this study. The amplification factor in this study is indicated by average (AVE) and average plus/minus standard deviation (AVE±SD).

I estimated bedrock motions from a deconvolution of the observed surface motions during the main shock using the explored *Vs* profile. A nonlinear soil response was assumed during the deconvolution. Figure 6.12(a) shows effective strains for EW and NS directions. The figure indicates that the strain levels of the EW direction is less than 1% for all frequency ranges. It is suggested that the nonlinear response estimations for EW components are within the applicability of DYNEQ. Meanwhile, the strain level of the NS direction is 2% in the average for frequencies of 0.1-5 Hz as shown in the figure. Since the upper limit of the strain level of DYNEQ applicability is not stated by Yoshida (2015) and Yoshida et al. (2002). I assumed that the strain levels of 2% are still allowable in DYNEQ. Figure 6.12(b) shows the amplification factors and their uncertainties for the EW and NS components. The deconvolution results, using the re-sampled 200 models, were averaged to the final amplification factor, and their standard deviations are also shown in Figure 6.12(b). These results indicate that the dominant periods of the average amplifications for the two horizontal directions are about 0.3 and 0.5 s. Moreover, the peak values of the two spectra are around 2. I also estimated the response spectral accelerations (SAs) with a damping of 5% from the deconvolved bedrock motions. Figure 6.12(c) shows the SA peaks with their uncertainties in the EW direction are generally higher than that of the design spectrum at periods less than 0.4 s. The design spectrum for the safety limit of the Japanese building code is based on Notification No. 1461 of the Ministry of Construction, Japan, May 31, 2000. Moreover, the SAs for the NS component are higher than that of the design spectrum at periods less than 0.6 s.

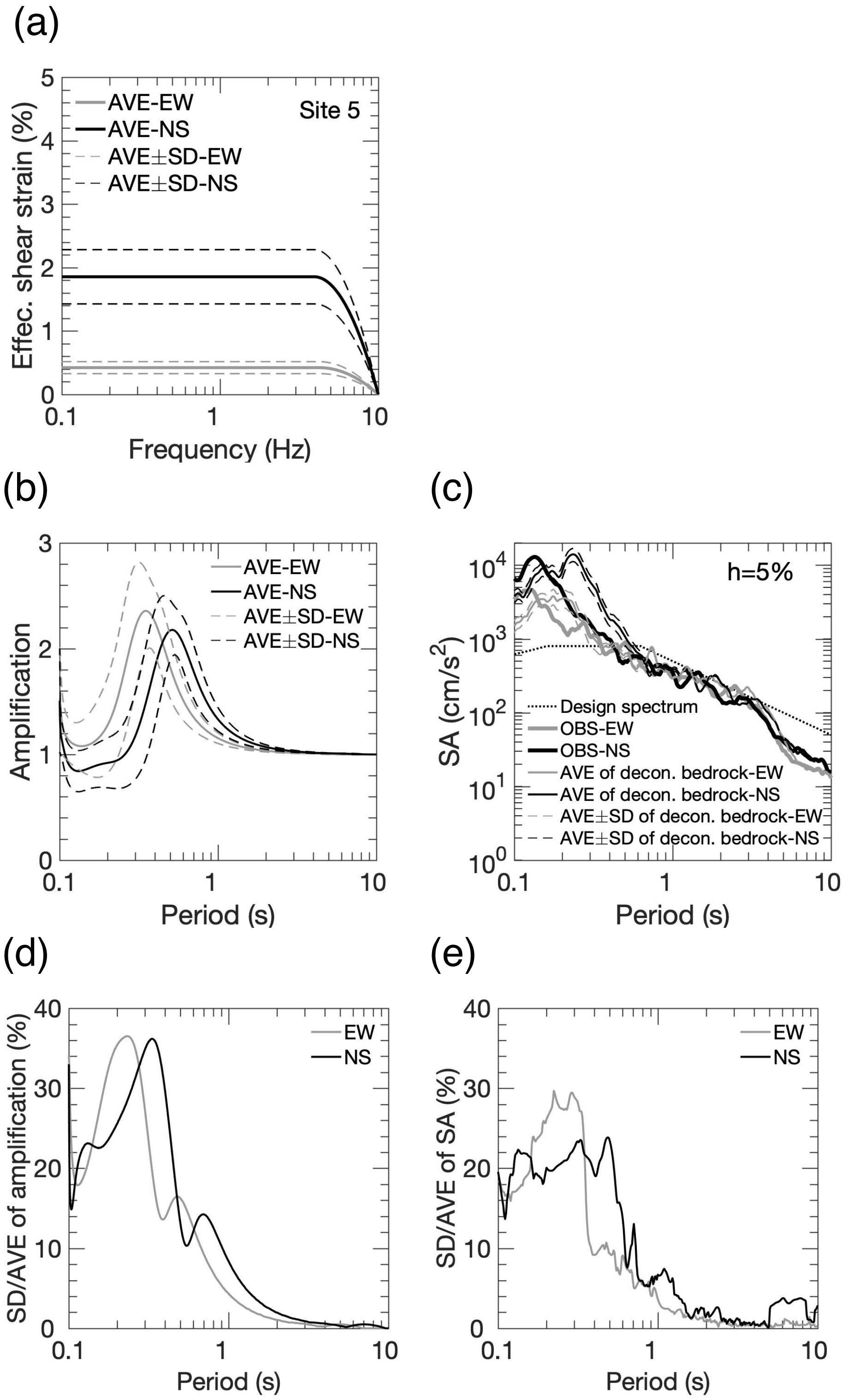

Figure 6.12 Deconvolution results at site 5. (a) Effective strain level for different motion directions. (b) Soil amplification and (c) spectral acceleration (SA) with 5% damping for EW and NS directions with their corresponding uncertainties. Variation coefficients (SD/AVE) of (d) amplification and (e) SA for two horizontal motions.

The variation coefficients (SD/AVEs in the following) of the amplification factors and the SAs are presented in Figure 6.12(d) and (e), respectively. Here, the coefficient is defined as a ratio of the standard deviation to the average of each parameter of the 200 deconvolved motions. Figure 6.12(d) shows that the SD/AVEs of the amplifications are greater than 10% at periods less than 0.7 and 1 s for the EW and NS directions, respectively. Meanwhile, the SD/AVEs of the SAs for the EW and NS components are higher than 10% at periods less than 0.6 and 0.7 s, respectively (Figure 6.12(e)). Figure 6.12(d) also indicates that the SD/AVEs of the amplification factors have peaks at periods 0.2–0.3 and 0.3–0.4 s for the EW and NS components, respectively. The results also show that the profiles' uncertainty has minor effects on the ground motion characteristics at periods longer than 1 s.

Furthermore, I estimate the distributions of the PGAs and the peak ground velocities (PGVs in the following) of the deconvolved bedrock motions in the two horizontal components, as shown in Figure 6.13(a) and (b), respectively. The PGAs have different distributions between the EW and NS directions. Probably, the nonlinear effects are more sensitive to the NS wave motion than to the EW motion. These features are pronounced in the PGVs' distributions. The possible PGA ranges are about 610–930 cm/s^2 and 2000–3100 cm/s^2 for the EW and NS directions, respectively. On the other hand, the PGV ranges are about 35–40 cm/s and 90–120 cm/s for the EW and NS components, respectively. These results clearly indicate that the estimated bedrock motion in the EW direction is more reliable than the NS component in my estimation.

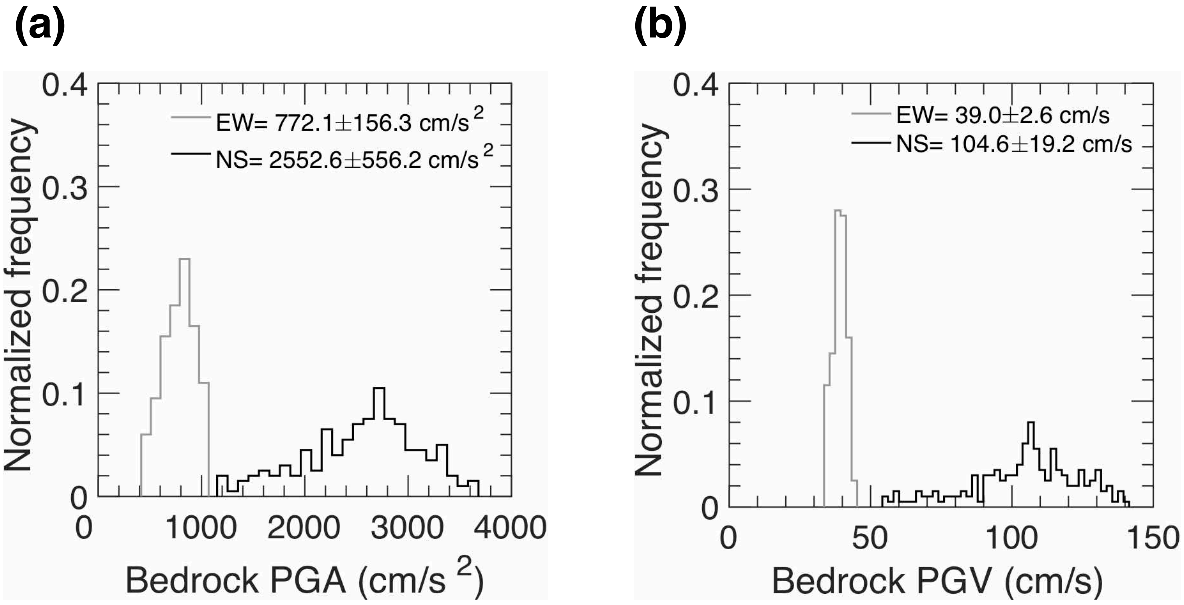

Figure 6.13 Comparison between distributions of (a) PGA and (b) PGV of estimated bedrock ground motions for EW and NS directions.

I present here some examples from the deconvolved bedrock acceleration and velocity waves for the EW and NS components, in Figure 6.14(a) and (b), respectively. The example motions were selected to have similar peak values with the average (AVE) and average plus/minus the standard deviation (AVE±SD) from the distributions (Figure 6.13). Some models generate bedrock motions with higher PGAs and PGVs in the NS component than those of the surface motion. This is caused by the strong soil de-amplification at periods shorter than 0.3 s (Figure 6.12(b)). Most models reproduce the bedrock PGAs and PGVs of the EW motion, which are generally lower than those of the surface EW component.

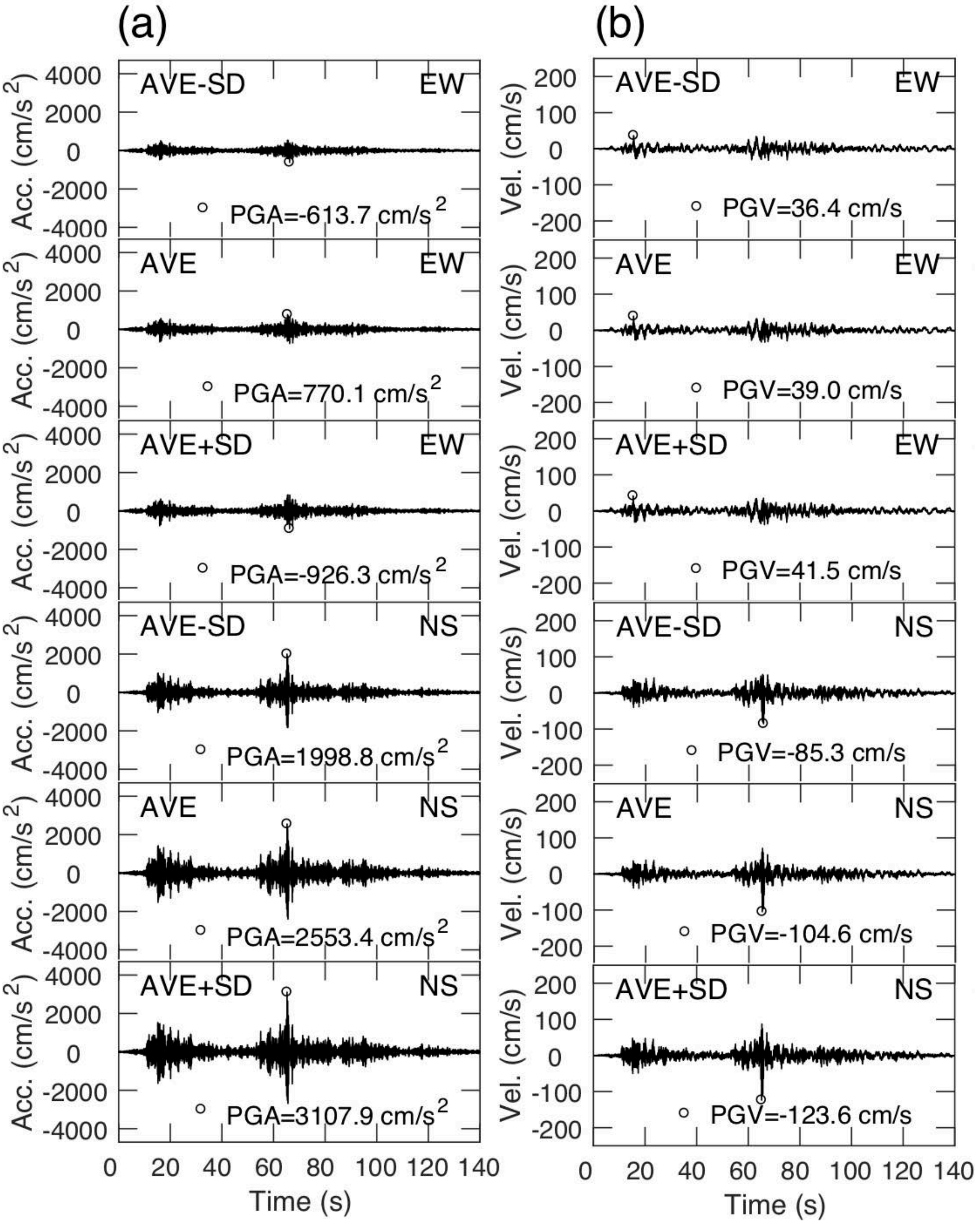

Figure 6.14 Examples of deconvolved bedrock motions with similar peak-values as average (AVE) and average plus/minus standard deviation (AVE±SD) of distributions of PGA and PGV from Figure 6.13(a) and (b), respectively. (a) Acceleration and (b) velocity waves for different motion directions.

Figure 6.14(a) also shows that the first major parts (0–40 s) of the acceleration waves for the AVE and AVE±SD have similar shapes. However, the second major parts (40–140 s) of the accelerations differ, particularly in the peak amplitudes at 65 s. Meanwhile, the variation of the peaks of velocity waves in the second major part is less than those of the acceleration waves (Figure 6.14(b)). The large PGA variations may be caused by the high SD/AVE of the amplifications in the high frequency ranges, while the minor differences in the PGVs could be attributed to the small SD/AVEs of the amplifications in low frequency ranges (Figure 6.12(c)). It is well understood that the PGAs and PGVs are controlled by amplification in the high and low frequency ranges, respectively. Therefore, the large variation of the bedrock acceleration waves, particularly in the NS direction, is caused by the high frequency pulse of the second major part of the surface motion.

6.6.2 Convolution analysis at other sites

I used 200 deconvolved bedrock motions at site 5 as input motions for calculating the surface motion at sites 1-4 and 8. As explained earlier, I also obtained the 200 re-sampled *Vs* profiles derived from the MCMC inversions of the phase velocities at each site. The 200 bedrock motions with the 200 *Vs* models produced a total 40,000 convolved surface motions at each site. Since there is no soil-type data at sites 1-4 and 8, I employed the soil-type classification of MYG004 in the nonlinear soil response analysis (Table 6.1). Effective strain levels at sites 1-4 and 8 are shown in Figure 6.15. The effective strain levels at site 1 for the EW and NS directions are less than and about 1% in averages at frequencies of 0.1-5 Hz, respectively. Moreover, the effective strain levels at sites 2-4 and 8 for the EW component are less than 1%. These strain levels are the allowable application of DYNEQ. Furthermore, strain levels for the NS motion at sites 2-4 and 8 are about 2% in average for frequencies of 0.1-5 Hz, as presented in the figure. Since the upper value of the strain level of DYNEQ applicability was not mentioned by Yoshida (2015) and Yoshida et al. (2002) as I discussed before. I also assumed strain levels of 2% are still acceptable in DYNEQ.

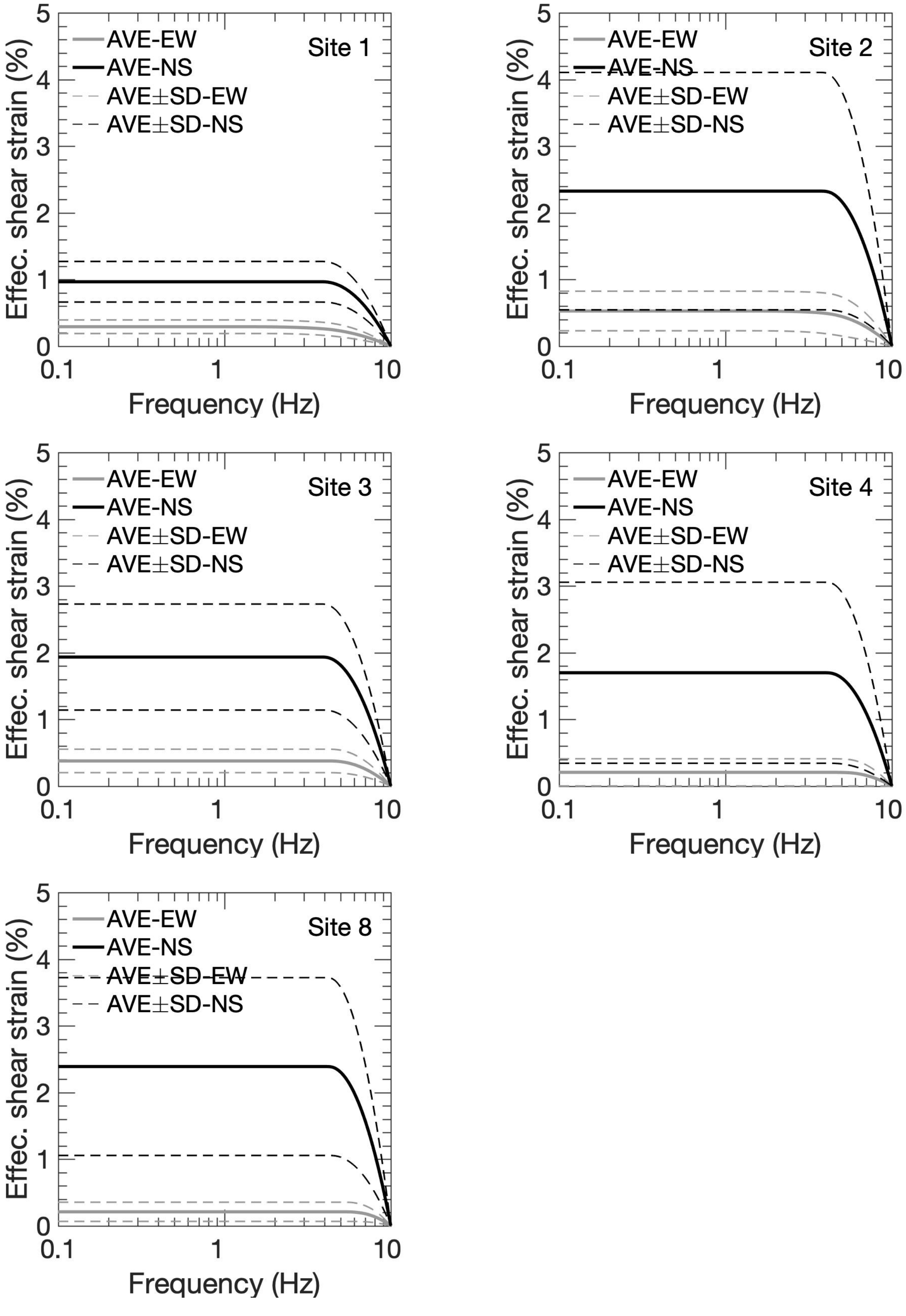

Figure 6.15 Effective strain levels at sites 1-4 and 8.

Amplifications and their SD/AVEs at sites 1-4, and 8 are presented in Figure 6.16(a) and (b), respectively. Peak-periods at sites 1 and 2 for the EW and the NS directions are about 0.5 and 0.8 s, respectively as depicted in Figure 6.16(a). The figure also shows that peak-periods for the EW and the NS components at site 3 are 0.3 and 0.4 s, respectively. Moreover, site 4 has peak-periods for the EW and the NS motions at 0.2 and 0.3 s, respectively. Furthermore, site 8 has peak-periods for the EW and the NS directions at 0.1 s due to given cut-off periods less than 0.1 s. Figure 6.16(b) shows SD/AVEs of the amplifications at sites 1 and 2 are larger than 10% for periods less than 1.5 s. Meanwhile, the SD/AVE of the amplification at sites 3-4 and 8 are more than 10% at periods less than 1 s.

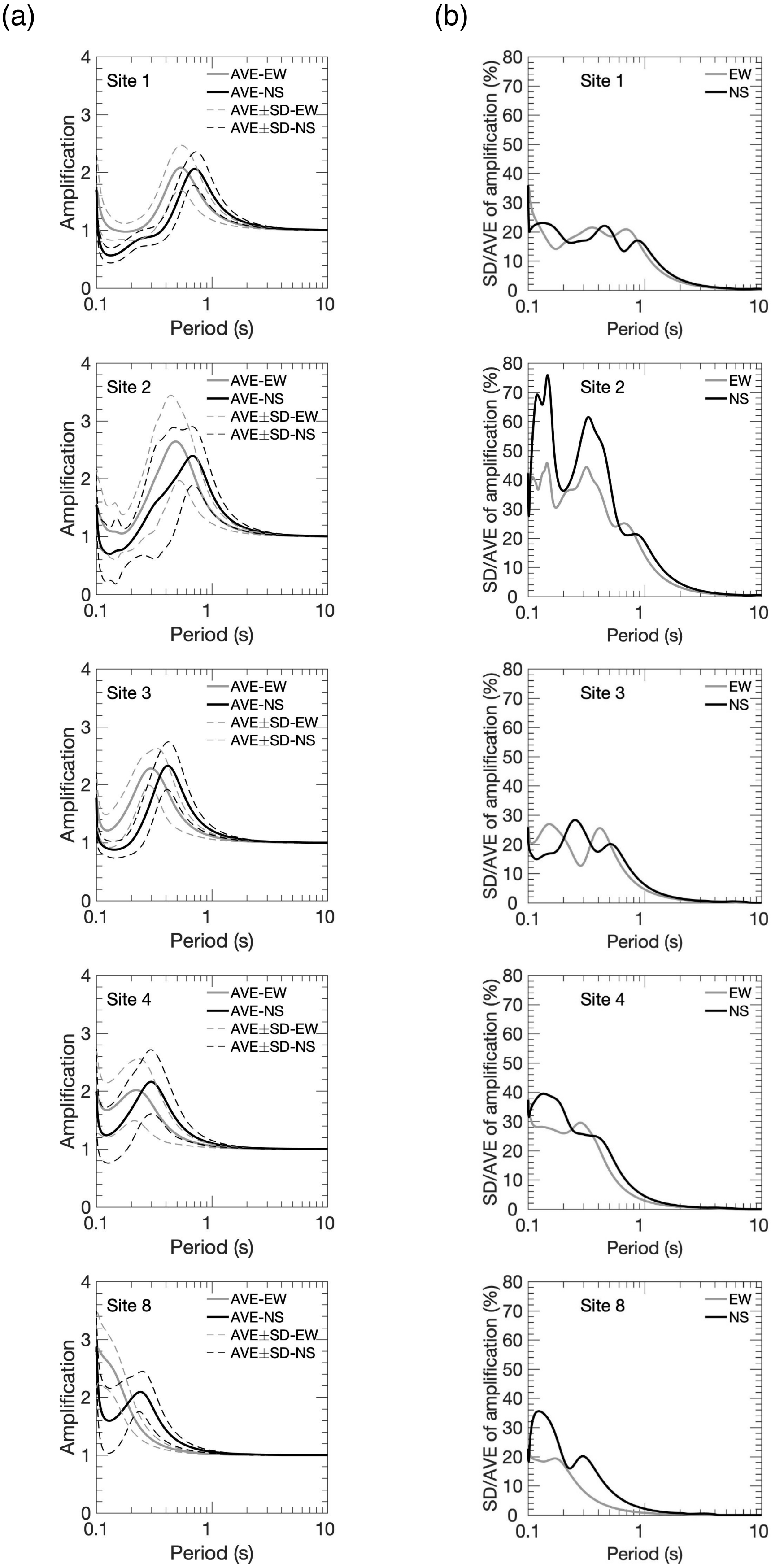

Figure 6.16 (a) Amplifications and (b) their SD/AVEs at sites 1-4 and 8.

To investigate the relationship between the PGA or PGV and the structural damages at sites 1-4, and 8, I compared the PGA or PGV averages of the convolved surface motions, considering their uncertainties, with the observed values at MYG004 and at other stations that existed during past large events, to the structural damage (Figure 6.17). I filtered the recorded acceleration waves at periods of 0.1–10 s. Then, I estimated the velocity waves from the observed acceleration waves. I compared my estimated ground motions at sites 1-4 and 8 to those observed at Anamizu station (ISK005) during the 2007 M_W 6.6 Noto Hanto Earthquake and at Mashiki station (KMMH16) during the 2016 Mw 7.1 Kumamoto Earthquake. The locations of these two earthquakes and the corresponding stations can be found in Figure 6.1(a). During these two events, many buildings were damaged in the central region of Anamizu Town (e.g., Shimizu et al. 2008) and in the downtown area of Mashiki Town (e.g., Chimoto et al. 2016). The PGAs for the EW and NS directions at sites 1 and 2 are similar to those of MYG004. Sites 3, 4, and 8 have slightly higher PGAs than MYG004 in the EW direction, while the PGAs for the NS motion are significantly higher than that of MYG004. On the other hand, all the sites have similar PGVs to that of MYG004 for the EW component. The NS motions at sites 1 and 2 have also similar PGV to that of MYG004. Conversely, sites 3, 4, and 8 have significantly higher PGVs than that of MYG004. The excessive PGAs and PGVs at some of the sites were generated because of some of the massive bedrock motion as I mentioned before. Regardless of these results, there was little damage around Tsukidate city. Thus, I should not only discuss the PGA and PGV in terms of the structural damage in this area.

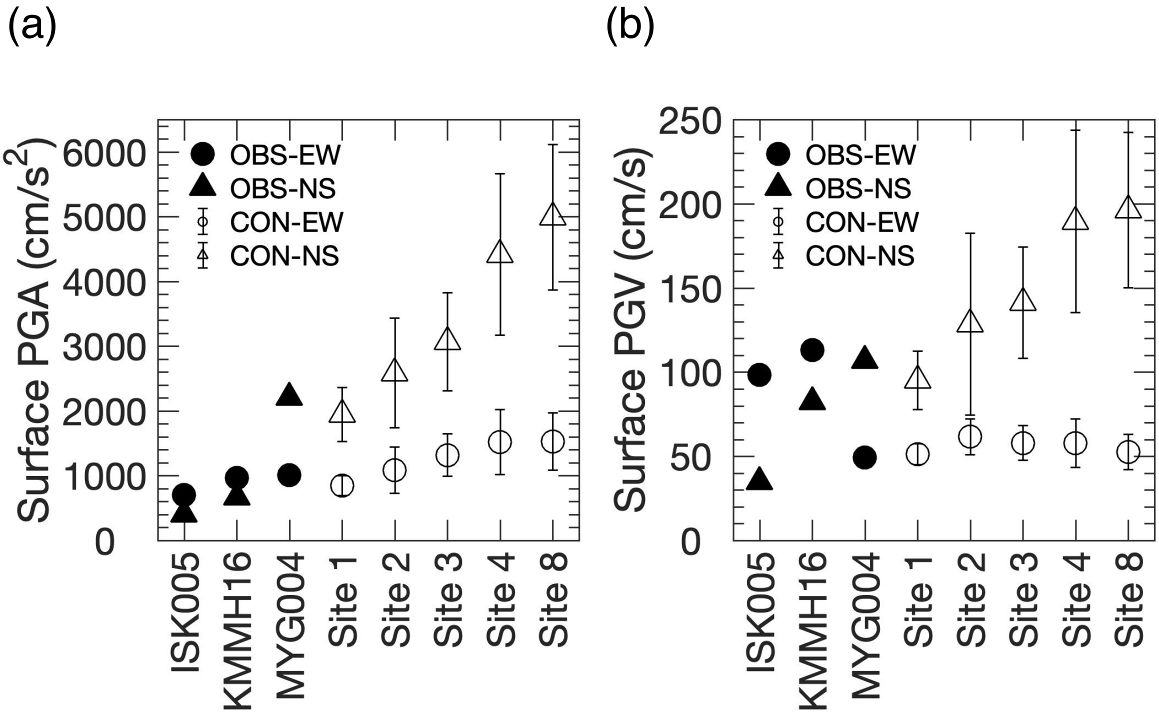

Figure 6.17 Comparison of (a) PGA or (b) PGV of observed surface motions (OBS) at ISK005, KMMH16, and MYG004 with convolved surface waveforms (CON) in EW and NS directions at site 1-4, and 8.

I compared the convolved surface ground velocity motions at sites 1-4 and 8 with the observed velocity waves at ISK005, KMMH16, and MYG004 (Figure 6.18(a)). The displayed velocity waves have PGVs similar to the values of the average (Figure 6.17(b)). I show here only the velocity waves instead of the acceleration waves in order to demonstrate the effects of the ground motions on the structural damage in the area. Figure 6.18 also indicates that several of my sites have higher PGVs than those of ISK005 and KMMH16. However, the recorded velocities at ISK005 and KMMH16 have shorter durations than those of MYG004 and sites 1-4 and 8 because of the differences in event magnitudes (Figure 6.18).

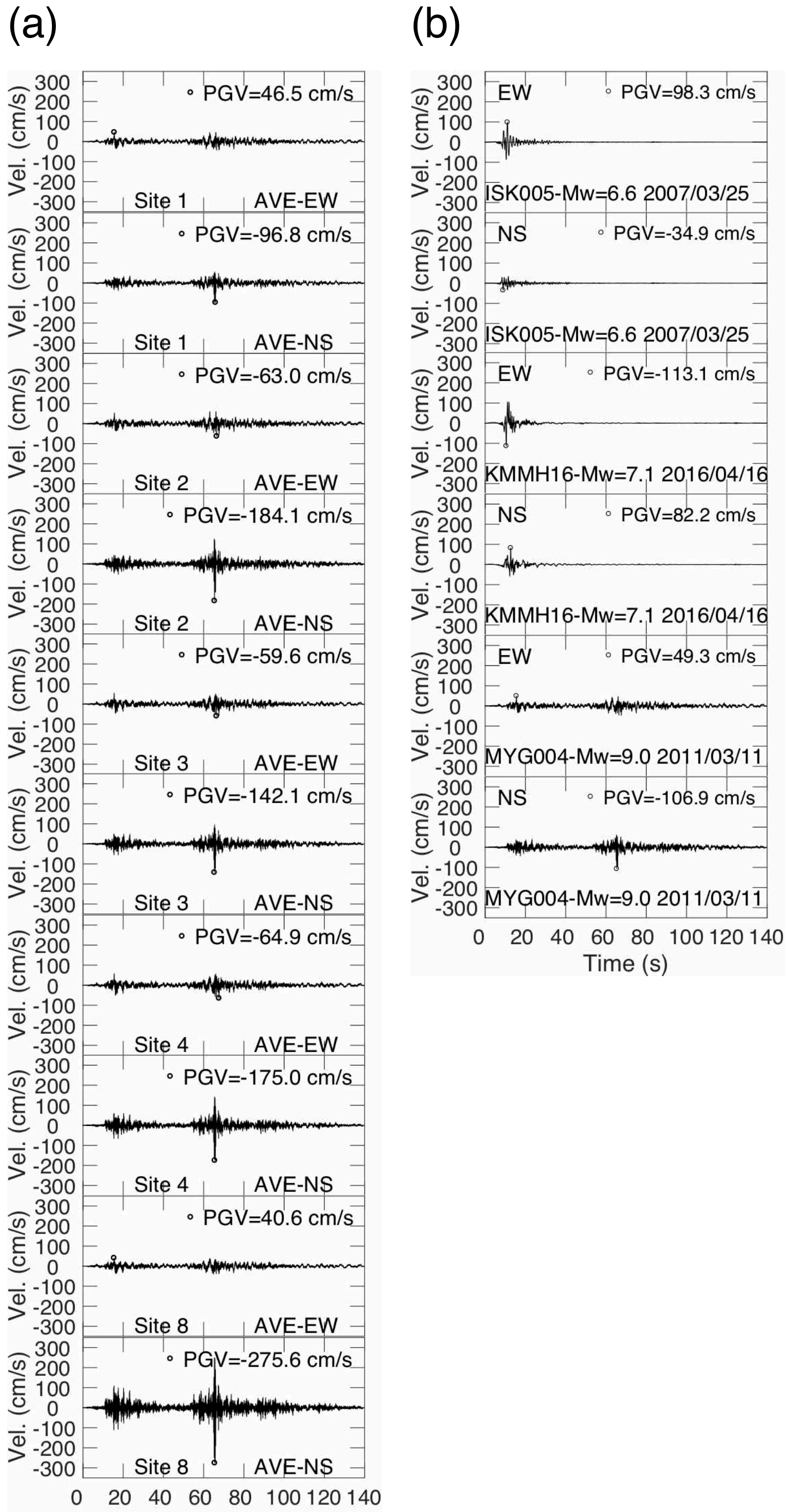

Figure 6.18 (a) Examples of surface ground velocity waves with similar PGV to AVE values from Figure 6.17(b). (b) Observed velocity waves at ISK005, KMMH16, and MYG004. Date of each earthquake is presented in a format of year/month/day.

Figure 6.19(a) and (b) depict the comparisons between the response spectral velocities (SVs in the following) with their uncertainties at the microtremor sites and the SVs at ISK005, KMMH16, and MYG004 for the EW and NS directions, respectively. These figures indicate that the peak periods of the SVs at MYG004 and all sites are about 0.2 and 0.2–0.3 s for the EW and NS directions, respectively. The peak amplitudes of the SVs at site 1-4 and 8 are generally higher than those of ISK005 and KMMH16 at periods 0.2 s and less than 0.4 s in the EW and NS components, respectively. However, their peak amplitudes are lower than those of ISK005 and KMMH16 at periods longer than 0.4 s for the two components. Furthermore, the SVs at ISK005 and KMMH16 have peaks at a period of about 1 s in both directions. Sakai (2009) suggested that strong ground motion at the periods about 1–2 s controls the structural damage. The surface SVs estimated at all sites in Tsukidate Town are lack of the powers at periods around 1–2 s. Hence, the low structural damage in the area is due to the SVs focused at periods less than 0.5 s, as suggested by previous studies using only strong motion data at MYG004 (e.g., Goto and Morikawa 2012; Irikura and Susumu 2012). Based on my results, I conclude that these features are common ground motion characteristics in the major part of Tsukidate Town.

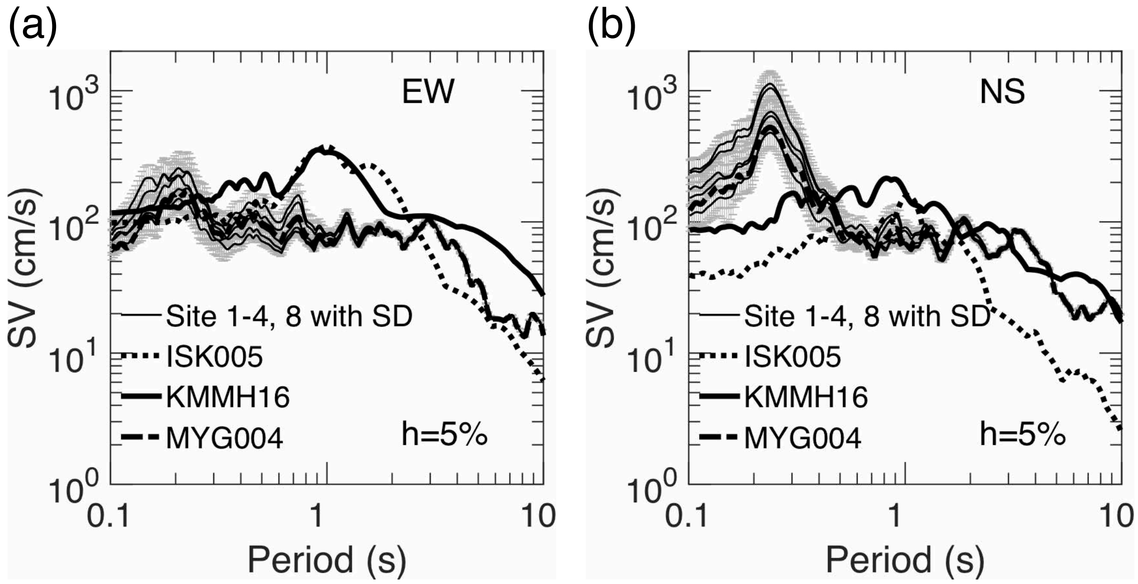

Figure 6.19 Spectral velocities (SVs) with their uncertainties of surface motions at site 1 as compared to SVs of ISK005, KMMH16, and MYG004 in (a) EW and (b) NS directions. Spectral damping ratio (h) of SV is 5%.

6.7 Summary

I have examined the effect of the uncertainty in the S-wave velocity (*Vs*) profiles on the deconvolved bedrock motions at Tsukidate station (MYG004) during the 2011 Tohoku Earthquake. The *Vs* profile uncertainty was obtained from the inversions of the Rayleigh wave phase velocities with the observational errors observed at MYG004 and a site in the central part of the area. The inversions of the phase velocities were performed by the Markov-chain Monte Carlo (MCMC) method. The observational errors in the phase velocities were attained by reanalyzing the microtremor survey result by Yamanaka et al. (2011). My S-wave velocity model, considering the uncertainty of the MCMC inversion, can explain the observed phase velocity quite well for each site. The *Vs* profile, with the uncertainty at MYG004, was used for the deconvolution analysis to estimate the bedrock motion variability. The upper and lower possible values of the deconvolved response spectral acceleration and the ground motion proxies are not only influenced by the uncertainty in the *Vs* profile. Moreover, the upper and lower possible values of the spectral acceleration and the ground motion proxies are also influenced by their nonlinear soil characteristics. The estimated bedrock peak ground acceleration ranges were 610–930 cm/s^2 and 2000–3100 cm/s^2 for the east-west (EW) and north-south (NS) directions, respectively. The peak ground velocities were also estimated in ranges of about 35–40 cm/s and 90–120 cm/s for the EW and NS components, respectively. Furthermore, the variability of the deconvolved bedrock motion was used as an input motion to obtain the convolved surface motion for other microtremor sites around Tsukidate Town. I found that the spectral velocities considering their uncertainties at the stations around Tsukidate city have predominant peaks at periods less than 0.5 s. Moreover, the spectral amplitudes for periods longer than 0.4 s are lower than those of damaged areas during past destructive earthquakes. Therefore, these ground motion characteristics in the Tsukidate Town, including MYG004, may have little effect on the structural damage, regardless of the massive acceleration.

Chapter 7 Conclusions and future works

7.1 Conclusions

7.2 Future works

7.1 Conclusions

I have conducted numerical experiments to understand effects of observational errors in surface-wave phase velocities of shallow soil into uncertainties in S-wave velocity profiles using the Markov-chain Monte Carlo (MCMC) inversion. Moreover, the uncertainties in the S-wave velocity profiles into the variability of soil amplifications were also evaluated assuming linear and nonlinear responses. Furthermore, I also estimated variability in a deconvolved bedrock motion due to uncertainty in an S-wave velocity profile from a Rayleigh wave phase velocity inversion beneath Tsukidate (MYG004) station during the 2011 off the Pacific Coast of Tohoku Earthquake.

In the numerical experiments, the estimated S-wave velocity profiles with its uncertainty and their calculated phase velocity models from the MCMC inversion can explain well corresponding the true S-wave velocity and the phase velocity, respectively. I showed that the incompleteness of the phase velocity at the high frequency rises the uncertainty in the S-wave velocity and thickness at the top layer while the absence of phase velocity at the low frequency increases the uncertainty in the S-wave velocity in the half-space. Furthermore, I also depicted that the observational errors of the phase velocities are linearly associated with the resolution of the S-wave velocity and thickness.

The sampled model parameters were also used to understand the trade-off relationship between the model parameters. Moreover, resolution of the S-wave velocity profiles could be improved by giving information of thickness during the inversion to avoid the trade-off-relationship. Additionally, the results of the given thickness during the inversion for different observational errors and the frequency-dependent errors of the phase velocities indicated that uncertainties in the S-wave velocity profiles are strongly related to the observational errors in the phase velocities.

Estimation of linear and nonlinear (equivalent linear method) soil amplifications based on the multiple reflection theory, using the sampled models, suggest that the spectral characteristics of the amplification and the ground motion proxies, except the fundamental frequency, are controlled by a combination of material rigidity (shear modulus) and damping. I found that the variability in the nonlinear soil response is lower than that of the linear amplification. Moreover, the ground motion proxies such as maximum amplification, peak ground acceleration (PGA), and peak ground velocity (PGV) of the nonlinear case also have higher resolution as compared to those of the linear case. However, the resolution of the fundamental frequency of the nonlinear case is similar to that of the linear one, because the distributions of the rigidities of the linear and nonlinear amplifications are similar. The reduction of the rigidity enlarges the variability of the nonlinear response, while the increase of the damping factor reduces the variability of the nonlinear amplification. Nonetheless, it is found that the damping plays more profound effect on the variability of nonlinear amplification than that of the rigidity. The higher resolution of the nonlinear response than that of the linear one is caused by the high damping factor in the nonlinear responses. Equivalent linear methods were used for estimation of the nonlinear soil response. Therefore, a more sophisticated nonlinear method (e.g., YUSAYUSA code by Yoshida and Towhata (2003)) can be applied during the nonlinear soil calculation for precise results.

Sufficient coverage of the phase velocity in the high frequency range should be more priority than that of the low frequency range since its variability of linear and nonlinear responses is higher than those of incompleteness of the phase velocity in low frequency. It is also found that the material damping also plays major roles in the variability of soil amplification due to the uncertainty in the S-wave velocity models in association with limited information of phase velocity, different observational errors in phase velocities, and different PGAs of bedrock motions. However, little differences were found in the variability of the nonlinear soil response for different phase angles of the bedrock motions. Furthermore, I might able to explain the reasons why conflicting results of the variability in soil responses in the previous studies (Foti et al., 2009; Jakka et al., 2014) from results of different observational errors and different PGAs of bedrock motions on the variability in soil responses. An error of phase velocity is determined from the requirement of amplification based on the accuracy (e.g., 10%) of a building response for a seismic design building.

I also numerically estimated variability in a deconvolved bedrock motion due to uncertainty in a S-wave velocity profile. It is shown that the deconvolved spectral acceleration and ground motions proxies considering its uncertainties have good agreement with the true spectral acceleration and ground motion proxies, respectively. Resolution of the deconvolved bedrock motions could be improved by giving thickness information during the inversion.

In application to real data, I estimated the S-wave velocity profile considering uncertainty from inversion of a Rayleigh wave phase velocity obtained by previous microtremor explorations around MYG004 in Miyagi Prefecture (Yamanaka et al., 2011). My inverted S-wave velocity profiles considering uncertainty at each site is similar to the inverted S-wave velocity profile by Yamanaka et al. (2011). Moreover, my calculated phase velocity with its uncertainty could also match well the observation at each site. The massive surface accelerations from a mainshock of the 2011 off the Pacific Coast of Tohoku Earthquake were used to obtain the variability in bedrock motions beneath MYG004. It is shown that the variability in the nonlinear response and the bedrock motions are affected by the S-wave velocity profile uncertainty. Moreover, their variability is also influenced by their nonlinear soil characteristics. Furthermore, the spectral velocities at all stations around MYG004 with different geological conditions in the main part of the Tsukidate city have a predominant period shorter than 0.5 s. Hence, lack of the powers at the period around 1 s are suggested to have less structural damages in spite of large peaks of acceleration.

In this study, I have shown the advantages of the MCMC method for the surface-wave phase velocity inversion in numerical experiments and the application to real data. It is understandable that the computational time of the MCMC inversion is relatively longer than those of the linearized square method, genetic algorithm, and simulated annealing. However, as a faster computer is becoming more affordable, this drawback could be minimized. Moreover, this study was mostly conducted on a Laptop or a MacBook with a reasonable computational cost. Despite this drawback, I have demonstrated the MCMC inversion could connect the observational error in the phase velocity in relation to the variability of the linear and nonlinear soil amplifications. It is not possible by using popular inversion techniques such as genetic algorithm and simulated annealing. Hence, it may be better to consider using the MCMC method over the genetic algorithm and simulated annealing during a surface-wave phase velocity inversion for further applications if variability in a soil amplification is concerned, particularly for engineering application.

7.2 Future works

I propose following future works based on the results of this thesis. Application of the MCMC inversion into more complex S-wave velocity profiles such as inverse S-wave velocity, thin or thick layer profiles, and multiple layer profiles (>= four layers) since I did not cover these types of soils in my thesis. I applied the MCMC inversion to Rayleigh wave phase velocities from microtremors in low damage area around Tsukidate city during the main shock of the 2011 Tohoku-oki Earthquake. Hence, the MCMC method can be used for Rayleigh wave phase velocity inversions in the damage area due to large earthquakes (e.g., 2016 Kumamoto Earthquake). Furthermore, the MCMC inversion can be also used in earthquake prone areas of Indonesia (e.g., Jakarta, Bandung, Yogyakarta) for seismic hazard mitigations.

In this study, I used 30 segments from 20 minutes of recorded microtremors to estimate the standard deviation of the phase velocity around Tsukidate city. From application of the method to above proposed areas, estimation of the standard deviation of a phase velocity from different number samples (e.g., 5, 10, 15, 20, 25, 30, …) can be also conducted, to find at which numbers of samples that the standard deviation is approaching convergence.

Additionally, estimation of variability of building responses for earthquake-resistant building due to soil amplification variability should be done. Therefore, an engineer may ask a geophysicist to provide *Vs* models from a surface-wave inversion with a certain uncertainty, so the building response has allowable accuracy (e.g., 10%).

Moreover, I used equivalent linear methods (SHAKE91 and DYNEQ) to estimate a nonlinear soil response. As I mentioned before, the equivalent linear is an approximation of nonlinear soil behavior and it is not a truly nonlinear method. Therefore, it is also important to understand the variability in the nonlinear soil response due to the uncertainty of S-wave velocity profile from the MCMC inversion from more advance nonlinear approach such as YUSAYUSA.

References

Aki, K., 1957. Space and time spectra of stationary stochastic waves, with special reference to microtremors. Bull. Earthq. Res. Inst. 35, 415–456.

Amrouche, M., Yamanaka, H., Chimoto, K., Dhakal, Y.P., 2014. Near-surface geophysical profiling near former location of K-NET Tsukidate strong motion station. J. Disaster Res. 9, 709–718.

Assimaki, D., Gazetas, G., Kausel, E., 2005. Effects of local soil conditions on the topographic aggravation of seismic motion: Parametric investigation and recorded field evidence from the 1999 Athens earthquake. Bull. Seismol. Soc. Am. 95, 1059–1089. https://doi.org/10.1785/0120040055

Aster, R., Borchers, B., Thurber, C., 2013. Parameter estimation and inverse problems. Elsevier. https://doi.org/10.1016/C2009-0-61134-X

Bendat, J.S., Piersol, A.G., 2010. Random data: analysis and measurement procedures. John Wiley & Sons, Inc. https://doi.org/10.2307/2289430

Beresnev, I.A., Wen, K.L., 1996. Nonlinear soil response a reality? Bull. Seismol. Soc. Am. 86, 1964–1978.

Brune, J.N., Benioff, H., Ewing, M., 1961. Long-period surface waves from the Chilean Earthquake of May 22, 1960, recorded on linear strain seismographs. J. Geophys. Res. 66, 2895–2910. https://doi.org/10.1029/JZ066i009p02895

Chimoto, K., Yamanaka, H., Tsuno, S., Miyake, H., Yamada, N., 2016. Estimation of shallow S-wave velocity structure using microtremor array exploration at temporary strong motion observation stations for aftershocks of the 2016 Kumamoto earthquake. Earth, Planets Sp. 68. https://doi.org/10.1186/s40623-016-0581-3

Dal Moro, G., Pipan, M., Gabrielli, P., 2007. Rayleigh wave dispersion curve inversion via genetic algorithms and Marginal Posterior Probability Density estimation. J. Appl.

Geophys. 61, 39–55. https://doi.org/10.1016/j.jappgeo.2006.04.002

Di Giulio, G., Gaudiosi, I., Cara, F., Milana, G., Tallini, M., 2014. Shear-wave velocity profile and seismic input derived from ambient vibration array measurements: The case study of downtown L'Aquila. Geophys. J. Int. 198, 848–866. https://doi.org/10.1093/gji/ggu162

Ewing, W.M., Jardetsky, W.S., Press, F., 1957. Elastic waves in layered media. McGraw-Hill, New York.

Foti, S., Comina, C., Boiero, D., Socco, L.V., 2009. Non-uniqueness in surface-wave inversion and consequences on seismic site response analyses. Soil Dyn. Earthq. Eng. 29, 982–993. https://doi.org/10.1016/j.soildyn.2008.11.004

Foti, S., Hollender, F., Garofalo, F., Albarello, D., Asten, M., Bard, P.-Y., Comina, C., Cornou, C., Cox, B., Di Giulio, G., Forbriger, T., Hayashi, K., Lunedei, E., Martin, A., Mercerat, D., Ohrnberger, M., Poggi, V., Renalier, F., Sicilia, D., Socco, V., 2018. Guidelines for the good practice of surface wave analysis: a product of the InterPACIFIC project. Bull. Earthq. Eng. 16, 2367–2420. https://doi.org/10.1007/s10518-017-0206-7

Foti, S., Lai, C.G., Rix, G.J., Strobbia, C., 2014. Surface Wave Methods for Near-Surface Site Characterization. CRC Press, London.

Garofalo, F., Foti, S., Hollender, F., Bard, P.Y., Cornou, C., Cox, B.R., Dechamp, A., Ohrnberger, M., Perron, V., Sicilia, D., Teague, D., Vergniault, C., 2016a. InterPACIFIC project: Comparison of invasive and non-invasive methods for seismic site characterization. Part II: Inter-comparison between surface-wave and borehole methods. Soil Dyn. Earthq. Eng. 82, 241–254. https://doi.org/10.1016/j.soildyn.2015.12.009

Garofalo, F., Foti, S., Hollender, F., Bard, P.Y., Cornou, C., Cox, B.R., Ohrnberger, M., Sicilia, D., Asten, M., Di Giulio, G., Forbriger, T., Guillier, B., Hayashi, K., Martin, A., Matsushima, S., Mercerat, D., Poggi, V., Yamanaka, H., 2016b. InterPACIFIC project: Comparison of invasive and non-invasive methods for seismic site characterization. Part I: Intra-comparison of surface wave methods. Soil Dyn. Earthq. Eng. 82, 222–240.

https://doi.org/10.1016/j.soildyn.2015.12.010

Geweke, J., 1992. Evaluating the accuracy of sampling-based approaches to the calculation of posterior moments. Bayesian Stat. 4 Oxford Univ. Press 169–193.

Ghahramani, Z., 2015. Probabilistic machine learning and artificial intelligence. Nature 521, 452–459. https://doi.org/10.1038/nature14541

Gilks, W.R., Richardson, S., Spiegelhalter, D., 1995. Markov chain Monte Carlo in practice. Chapman and Hall/CRC, New York.

Goto, H., Morikawa, H., 2012. Ground motion characteristics during the 2011 off the Pacific Coast of Tohoku Earthquake. Soils Found. 52, 769–779. https://doi.org/10.1016/j.sandf.2012.11.002

Hartzell, S., Bonilla, L.F., Williams, R.A., 2004. Prediction of nonlinear soil effects. Bull. Seismol. Soc. Am. 94, 1609–1629. https://doi.org/10.1785/012003256

Haskell, N.A., 1953. The dispersion of surface waves on multilayered media. Bull. Seismol. Soc. Am. 43, 17–34. https://doi.org/10.1029/SP030p0086

Hastings, W.K., 1970. Monte Carlo sampling methods using Markov Chains and their applications. Biometrika 57, 97–109. https://doi.org/10.2307/2334940

Horike, M., 1985. Inversion of phase velocity of long-period microtremors to the S-wave velocity structure down to the basement in urbanized areas. J. Phys. Earth 59–96.

Huang, Z., Su, W., Peng, Y., Zheng, Y., Li, H., 2003. Rayleigh wave tomography of China and adjacent regions 108. https://doi.org/10.1029/2001JB001696

Idriss, I.M., 1990. Response of soft soil sites during earthquakes, in: Proc. H. B. Seed Memorial Symposium. Univ. of California, Barkeley, California, pp. 273–289.

Idriss, I.M., Sun, J.I., 1992. SHAKE91: a computer program for conducting equivalent linear seismic response analyses of horizontally layered soil deposits. Center for Geotechnical Modeling, Department of Civil and Environmental Engineering, University of California at Davis.

Iida, M., Yamanaka, H., Yamada, N., 2005. Wave field estimated by borehole recordings in the reclaimed zone of Tokyo Bay. Bull. Seismol. Soc. Am. 95, 1101–1119. https://doi.org/10.1785/0120040010

Irikura, K., Susumu, K., 2012. Strong ground motion during the 2011 Pacific Coast Off Tohoku, Japan earthquake, in: Proceedings of the International Symposium on Engineering Lessons Learned from the 2011 Great East Japan Earthquake. Tokyo.

Ismet Kanli, A., Tildy, P., Prónay, Z., Pinar, A., Hermann, L., 2006. Vs30 mapping and soil classification for seismic site effect evaluation in Dinar region, SW Turkey. Geophys. J. Int. 165, 223–235. https://doi.org/10.1111/j.1365-246X.2006.02882.x

Jakka, R.S., Roy, N., Wason, H.R., 2014. Implications of surface wave data measurement uncertainty on seismic ground response analysis. Soil Dyn. Earthq. Eng. 61–62, 239–245. https://doi.org/10.1016/j.soildyn.2014.02.004

Kaklamanos, J., Baise, L.G., Thompson, E.M., Dorfmann, L., 2015. Comparison of 1D linear , equivalent-linear , and nonlinear site response models at six KiK-net validation sites. Soil Dyn. Earthq. Eng. 69, 207–219. https://doi.org/10.1016/j.soildyn.2014.10.016

Kaklamanos, J., Bradley, B.A., Thompson, E.M., Baise, L.G., 2013. Critical parameters affecting bias and variability in site-response analyses using KiK-net downhole array data. Bull. Seismol. Soc. Am. 103, 1733–1749. https://doi.org/10.1785/0120120166

Kanai, K., Osada, T., Tanaka, T., 1954. Measurement of the microtremors. Bull. Earthq. Res. Inst. 32, 199–209.

Karagoz, O., Chimoto, K., Citak, S., Ozel, O., Yamanaka, H., Hatayama, K., 2015. Estimation of shallow S-wave velocity structure and site response characteristics by microtremor array measurements in Tekirdag region, NW Turkey. Earth, Planets Sp. 67, 176. https://doi.org/10.1186/s40623-015-0320-1

Kitsunezaki, C., Goto, N., Kobayashi, Y., Ikawa, T., Horike, M., Saito, T., Kurota, T., Yamane, K., Okuzumi, K., 1990. Estimation of P- and S-wave velocities in deep soil deposits for evaluating ground vibrations in earthquake. Japan Soc. Nat. Disaster Sci. 9, 1-17. (in Japanese).

Ko, Y., Hsu, S., Chen, C., 2009. Analysis for seismic response of dry storage facility for spent fuel. Nucl. Eng. Des. 239, 158–168. https://doi.org/10.1016/j.nucengdes.2008.09.006

Kramer, S.L., 1996. Geotechnical Earthquake Engineering. Prentice Hall, Upper Saddle River, New Jersey, p. 376.

Kuo, C.H., Chen, C. Te, Lin, C.M., Wen, K.L., Huang, J.Y., Chang, S.C., 2016. S-wave velocity structure and site effect parameters derived from microtremor arrays in the Western Plain of Taiwan. J. Asian Earth Sci. 128, 27–41. https://doi.org/10.1016/j.jseaes.2016.07.012

Martínez-Pagán, P., Navarro, M., Pérez-Cuevas, J., Alcalá, F.J., García-Jerez, A., Sandoval-Castaño, S., 2014. Shear-wave velocity based seismic microzonation of Lorca city (SE Spain) from MASW analysis. Near Surf. Geophys. 12, 739–749. https://doi.org/10.3997/1873-0604.2014032

Menke, W., 2012. Geophysical data analysis: discrete inverse theory. Academic Press.

Molnar, S., Dosso, S.E., Cassidy, J.F., 2013. Uncertainty of linear earthquake site amplification via Bayesian inversion of surface seismic data. Geophysics 78, WB37–WB48. https://doi.org/10.1190/geo2012-0345.1

Molnar, S., Dosso, S.E., Cassidy, J.F., 2010. Bayesian inversion of microtremor array dispersion data in southwestern British Columbia. Geophys. J. Int. 183, 923–940. https://doi.org/10.1111/j.1365-246X.2010.04761.x

Montagner, J.-P., Tanimoto, T., 1991. Global upper mantle tomography of seismic velocities and anisotropies. J. Geophys. Res. Solid Earth 96, 20337–20351. https://doi.org/10.1029/91JB01890

Motosaka, M., 2012. Lessons of the 2011 Great East Japan Earthquake focused on characteristics of ground motions and building damage, in: Proceedings of the

International Symposium on Engineering Lessons Learned from the 2011 Great East Japan Earthquake. Tokyo, pp. 166–185.

Nagashima, F., Matsushima, S., Kawase, H., Sánchez-sesma, F.J., Hayakawa, T., Satoh, T., Oshima, M., 2014. Application of horizontal-to-vertical spectral ratios of earthquake ground motions to identify subsurface structures at and around the K-NET site in Tohoku, Japan 104, 2288–2302. https://doi.org/10.1785/0120130219

Nakamura, Y., 1989. A method for dynamic characteristics estimation of subsurface using microtremor on the ground surface.

Nazarian, S., Stokoe, K.H., 1984. In situ shear wave velocities from spectral analysis of surface wave, in: 8th Conference on Earthquake Engineering,. San Francisco.

Ohori, M., Nobata, A., Wakamatsu, K., 2002. A comparison of ESAC and FK methods of estimating phase velocity using arbitrarily shaped microtremor arrays. Bull. Seismol. Soc. Am. 92, 2323–2332. https://doi.org/10.1785/0119980109

Okada, H., 2003. The microtremor survey method. Society of Exploration Geophysicists.

Özmen, Ö.T., Yamanaka, H., Alkan, M.A., Çeken, U., Öztürk, T., Sezen, A., 2017. Microtremor array measurements for shallow S-wave profiles at strong-motion stations in Hatay and Kahramanmaras Provinces, Southern Turkey. Bull. Seismol. Soc. Am. 107, 445–455. https://doi.org/10.1785/0120160218

Park, C.B., Miller, R.D., Ryden, N., Xia, J., Ivanov, J., 2005. Combined Use of Active and Passive Surface Waves. J. Environ. Eng. Geophys. 10, 323–334. https://doi.org/10.2113/JEEG10.3.323

Pearl, J., 1984. Heuristics: Intelligent search strategies for computer problem solving. United States: N. P.

Pramatadie, A.M., Yamanaka, H., Chimoto, K., Pagacancang, A., Koketsu, K., Sakaue, M., Miyake, H., Sengara, W., Sadisun, I.A., 2016. Microtremor exploration for shallow S-wave velocity structure in Bandung Basin, Indonesia. Explor. Geophys.

https://doi.org/10.1071/EG16043

Rathje, E.M., Bachhuber, J., Dulberg, R., Cox, B.R., Kottke, A., Wood, C., Green, R.A., Olson, S., Wells, D., Rix, G., 2011. Damage patterns in Port-au-Prince during the 2010 Haiti Earthquake. Earthq. Spectra 27, S117–S136. https://doi.org/10.1193/1.3637056

Richardson, R.M., Zandt, G., 2003. Inverse Problems in Geophysics.

Sakai, Y., 2009. Reinvestigation on period range of strong ground motions corresponding to buildings damage. J. Struct. Constr. Eng. 74, 1531-1536. (in Japanese).

Satoh, T., Kawase, H., Iwata, T., Higashi, S., Sato, T., 2004. S-wave velocity structures of sediments estimated from array microtremor records and site responses in the near-fault region of the 1999 Chi-Chi , Taiwan earthquake 545–558. https://doi.org/10.1007/s10950-004-2644-3

Satoh, T., Kawase, H., Marsushima, S., 2001. Estimation of S-Wave velocity structures in and around the Sendai Basin, Japan, using array records of microtremors. Bull. Seismol. Soc. Am. 91, 206–218. https://doi.org/10.1785/0119990148

Schnabel, P.B., Lysmer, J., Seed, H.B., 1972. SHAKE: a computer program for earthquake response analysis of horizontally layered sites. Report No. EERC 72-12. University of California at Barkeley.

Semblat, J.F., 2006. Modeling seismic wave propagation and amplification in 1D / 2D / 3D linear and nonlinear unbounded media 1–12. https://doi.org/10.1061/(ASCE)GM.1943-5622.0000023

Shimizu, R., Maeda, T., Saito, G., 2008. Ground motion simulation in Anamizu town during the 2007 Noto-Hanto Earthquake, in: 14th World Conference on Earthquake Engineering (14WCEE). Beijing.

Socco, L.V., Foti, S., Boiero, D., 2010. Surface-wave analysis for building near-surface velocity models — Established approaches and new perspectives. GEOPHYSICS 75, 75A83-75A102. https://doi.org/10.1190/1.3479491

Sun, J.I., Golesorkhi, R., Seed, H.B., 1988. Dynamic moduli and damping ratios for cohesive soils. Report No. UCB/EERC-88/15. Earthquake Engineering Research Center, University of California at Barkeley.

Trampert, J., Woodhouse, J.H., 1995. Global phase velocity maps of Love and Rayleigh waves between 40 and 150 seconds. Geophys. J. Int. 122, 675–690. https://doi.org/10.1111/j.1365-246X.1995.tb07019.x

Villaseñor, A., Ritzwoller, M.H., Levshin, A.L., Barmin, M.P., Engdahl, E.R., Spakman, W., Trampert, J., 2001. Shear velocity structure of central Eurasia from inversion of surface wave velocities 123, 169–184.

Wen, K.L., Beresnev, I.A., Yeh, Y.T., 1994. Nonlinear soil amplification inferred from downhole strong seismic motion data. Geophys. Res. Lett. 21, 2625–2628. https://doi.org/10.1029/94GL02407

Wiggins, R.A., 1972. The general linear inverse problem: Implication of surface waves and free oscillations for Earth structure. Rev. Geophys. 10, 251. https://doi.org/10.1029/RG010i001p00251

Xia, J., Miller, R.D., Park, C.B., Hunter, J.A., Harris, J.B., Ivanov, J., 2002. Comparing shear-wave velocity profiles inverted from multichannel surface wave with borehole measurements. Soil Dyn. Earthq. Eng. 22, 181–190. https://doi.org/10.1016/S0267-7261(02)00008-8

Yamanaka, H., 2014. Estimation of model uncertainty of S-wave velocity profile from inversion of surface-wave phase velocity using MCMC method. J. Struct. Constr. Eng. 79, 1795-1803. (in Japanese). https://doi.org/10.3130/aijs.79.1795

Yamanaka, H., 2013. Surface-wave phase velocity inversion using Markov Chain Monte Carlo method. Butsuri-Tansa 66, 97-110. (in Japanese). https://doi.org/10.3124/segj.66.97

Yamanaka, H., 2011. Application of Markov Chain Monte Carlo method in inversion of surface-wave phase velocity. 4th IASPEI/IAEE International Symposium, University of

California Santa Barbara, California.

Yamanaka, H., 2007. Inversion of surface-wave phase velocity using hybrid heuristic search method. Butsuri-Tansa 60, 265-275. (in Japanese). https://doi.org/doi.org/10.3124/segj.60.265

Yamanaka, H., 2005. Comparison of performance of heuristic search methods for phase velocity inversion in shallow surface wave method. J. Environ. Eng. Geophys. 10, 163–173. https://doi.org/10.2113/JEEG10.2.163

Yamanaka, H., Ishida, H., 1996. Application of genetic algorithms to an inversion of surface-wave dispersion data. Bull. Seismol. Soc. Am. 86, 436–444. https://doi.org/10.1144/gsjgs.155.2.0323

Yamanaka, H., Tsuno, S., Chimoto, K., Yamada, N., Fukumoto, S., Eto, K., 2011. Estimation of site amplification from observation of aftershocks of the 2011 off the Pacific coast of Tohoku earthquake and microtremor explorations in the vicinity of K-NET Tsukidate station, Miyagi prefecture, Japan. Geophys. Explor. 64, 389-399. (in Japanese).

Yoshida, N., 2015. Seismic ground response analysis, Geotechnical, Geological and Earthquake Engineering. Springer Netherlands, Dordrecht. https://doi.org/10.1007/978-94-017-9460-2

Yoshida, N., Kobayashi, S., Suetomi, I., Miura, K., 2002. Equivalent linear method considering frequency dependent characteristics of stiffness and damping. Soil Dyn. Earthq. Eng. 22, 205–222. https://doi.org/10.1016/S0267-7261(02)00011-8

Yoshida, N., Towhata, I., 2003. YUSAYUSA-2 Theory and practice.

Yuan, D., Nazarian, S., 1993. Automated surface wave method: inversion technique. J. Geotech. Eng. 119, 1112–1126. https://doi.org/10.1061/(ASCE)0733-9410(1993)119:7(1112)

Zor, E., Özalaybey, S., Karaaslan, A., Tapirdamaz, M.C., Özalaybey, S.Ç., Tarancioĝlu, A., Erkan, B., 2010. Shear wave velocity structure of the Izmit Bay area (Turkey) estimated from active-passive array surface wave and single-station microtremor methods. Geophys.

J. Int. 182, 1603–1618. https://doi.org/10.1111/j.1365-246X.2010.04710.x

Appendix A

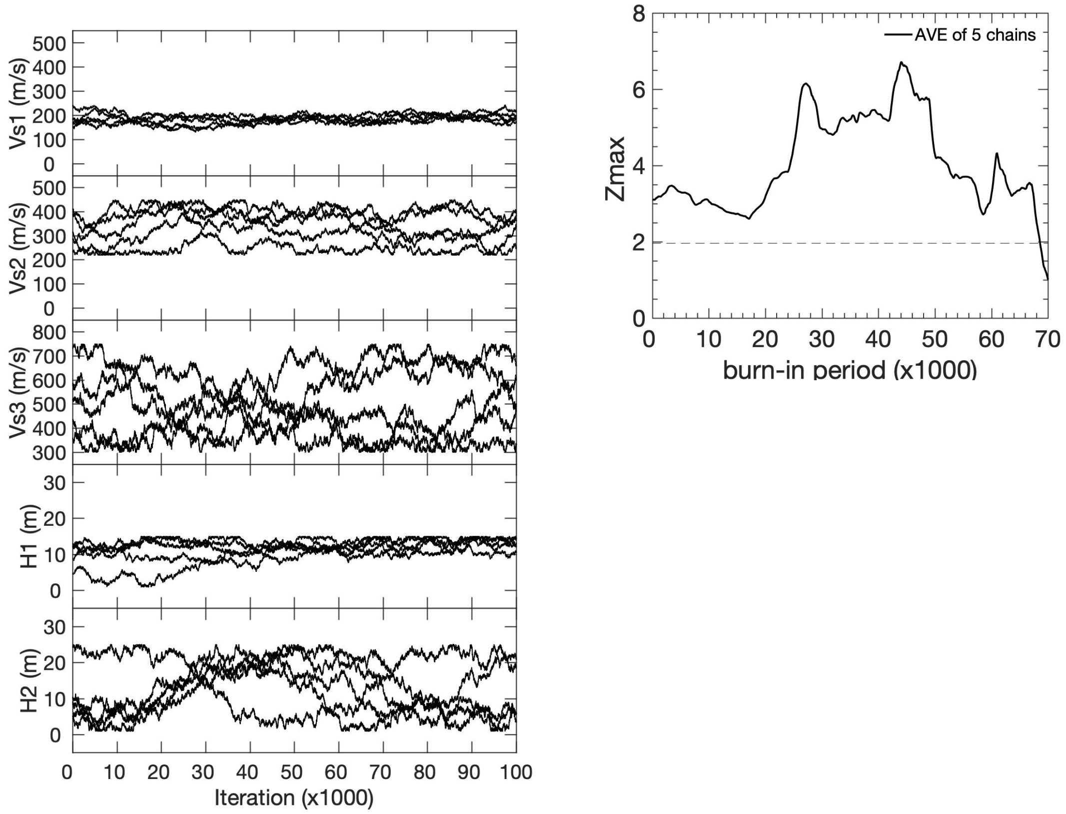
(a)

(b)

Figure A.1 Results of the MCMC sampling in an inversion of phase velocity at site 1. (a) evolutions of S-wave velocities of first, second, and third layers, following by thicknesses of first and second layers obtained from five tests from top to bottom, respectively. (b) Relationship of the maximum Z-values and different burn-in periods. A broken horizontal line shows a Z-value of 1.96.

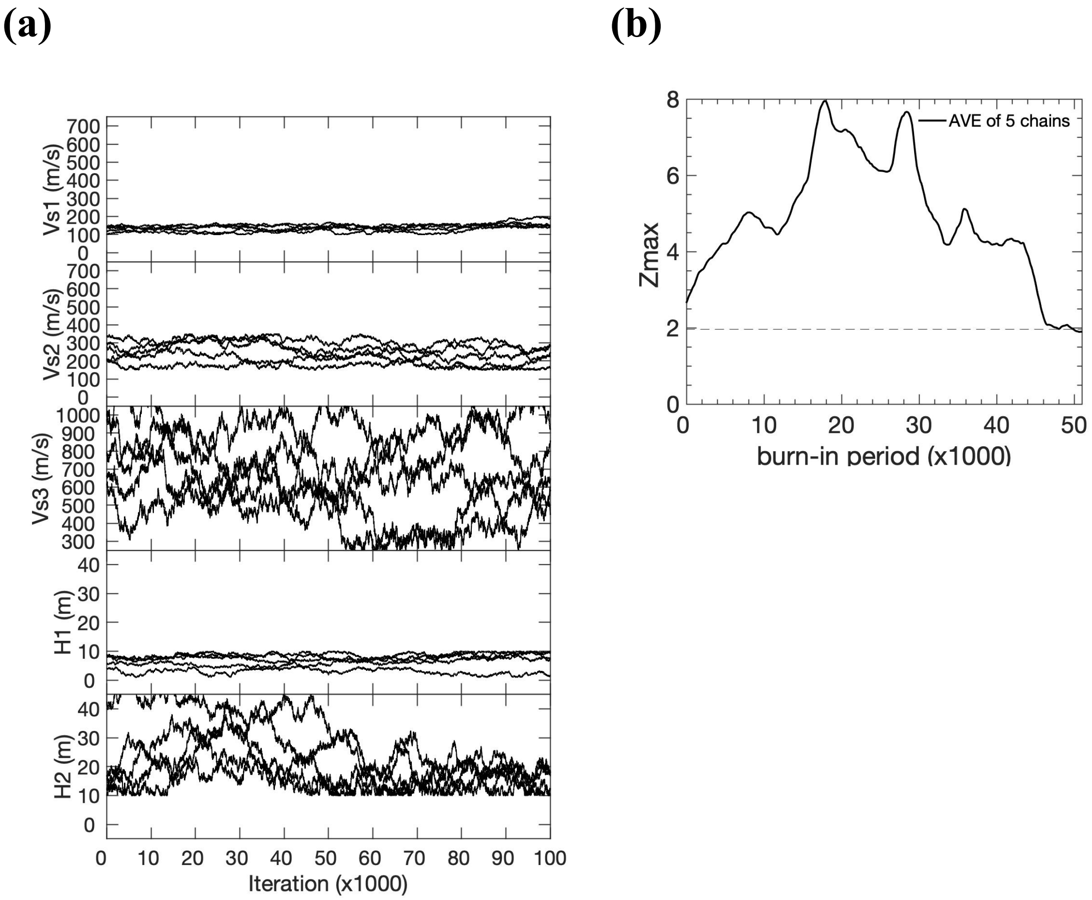

Figure A.2 Results of the MCMC sampling in an inversion of phase velocity at site 2. (a) evolutions of S-wave velocities of first, second, and third layers, following by thicknesses of first and second layers obtained from five tests from top to bottom, respectively. (b) Relationship of the maximum Z-values and different burn-in periods. A broken horizontal line shows a Z-value of 1.96.

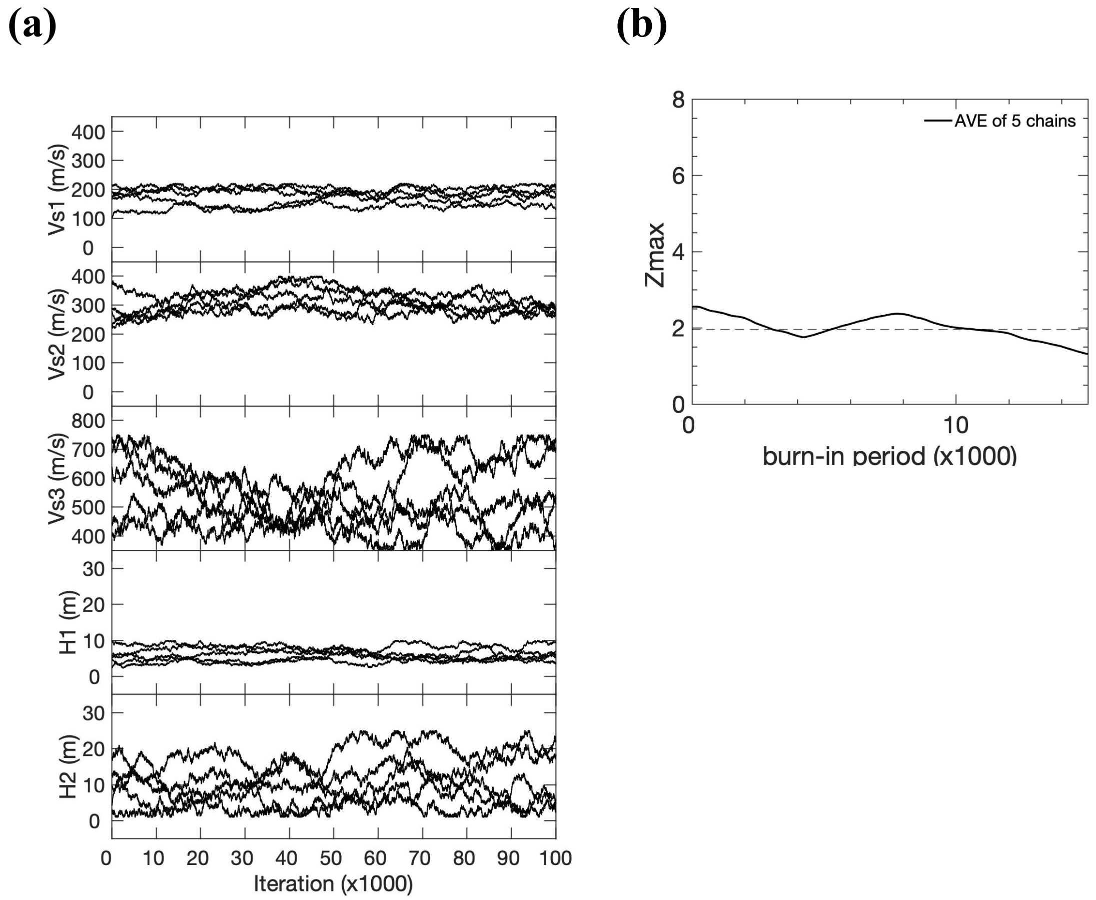

Figure A.3 Results of the MCMC sampling in an inversion of phase velocity at site 3. (a) evolutions of S-wave velocities of first, second, and third layers, following by thicknesses of first and second layers obtained from five tests from top to bottom, respectively. (b) Relationship of the maximum Z-values and different burn-in periods. A broken horizontal line shows a Z-value of 1.96.

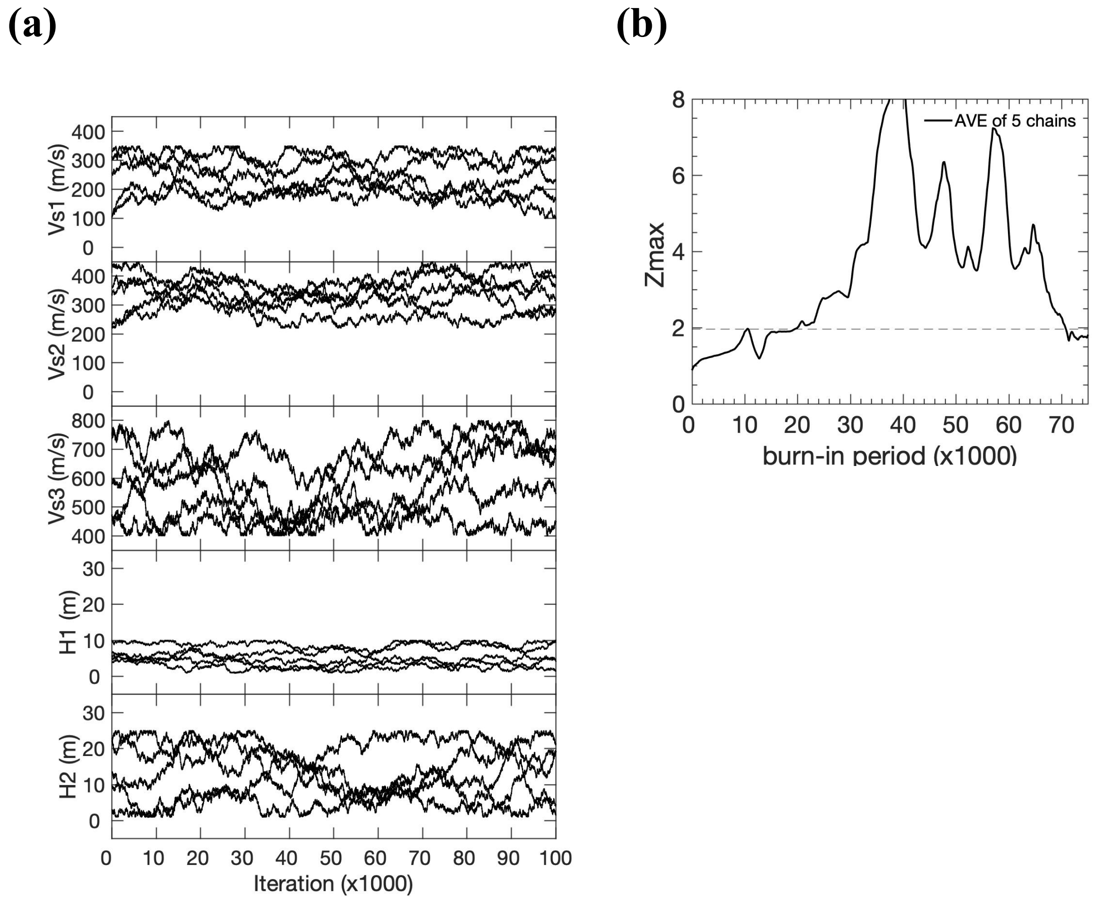

Figure A.4 Results of the MCMC sampling in an inversion of phase velocity at site 4. (a) evolutions of S-wave velocities of first, second, and third layers, following by thicknesses of first and second layers obtained from five tests from top to bottom, respectively. (b) Relationship of the maximum Z-values and different burn-in periods. A broken horizontal line shows a Z-value of 1.96.

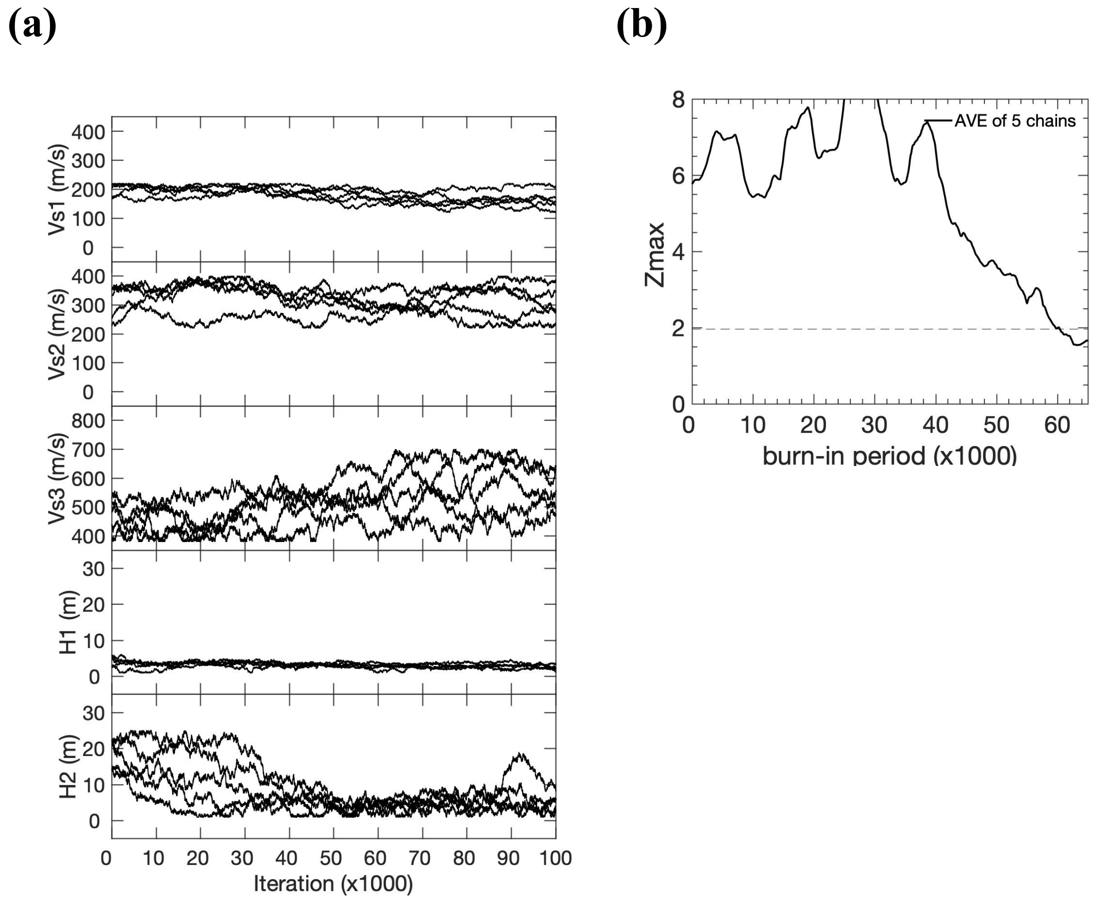

Figure A.5 Results of the MCMC sampling in an inversion of phase velocity at site 8. (a) evolutions of S-wave velocities of first, second, and third layers, following by thicknesses of first and second layers obtained from five tests from top to bottom, respectively. (b) Relationship of the maximum Z-values and different burn-in periods. A broken horizontal line shows a Z-value of 1.96.